A COMPUTATIONAL MICROMECHANICS INVESTIGATION OF LONGITUDINAL STRENGTH IN UNIDIRECTIONAL FIBRE REINFORCED COMPOSITES

Mostafa Barzegar

Universitat de Girona

DOCTORAL THESIS

A computational micromechanics investigation of longitudinal strength in unidirectional fibre reinforced composites

Mostafa Barzegar

2022

Universitat de Girona

DOCTORAL THESIS

A computational micromechanics investigation of longitudinal strength in unidirectional fibre reinforced composites

Mostafa Barzegar

2022

Doctoral Program in Technology

Supervisors:

Prof. Josep Costa Balanzat

Prof. Carlos Daniel González Martínez

Dr. Claudio Saúl Faria Lopes

Thesis submitted to the Universitat de Girona for the degree of Doctor of Philosophy

Mostafa Barzegar

A computational micromechanics investigation of longitudinal strength in unidirectional fibre reinforced composites

DOCTORAL THESIS, 2022
Doctoral Program in Technology
Supervisors: Prof. Josep Costa Balanzat, Prof. Carlos Daniel González Martínez and Dr. Claudio Saúl Faria Lopes

Universitat de Girona
AMADE Research Group
Escola Politècnica Superior
Dept. d'Enginyeria Mecànica i de la Construcció Industrial
Carrer Universitat de Girona, 4. Campus de Montilivi
17003 Girona

To my beloved parents and sister.

> *If I have seen further than others, it is by standing upon the shoulders of giants.*

— Isaac Newton
(1676 AD)

Preface

The work contained in this Ph.D. thesis was conducted in the AMADE Research Group (Escola Politècnica Superior, Dept. d'Enginyeria Mecànica i de la Construcció Industrial, Universitat de Girona, Spain). The thesis was carried out with FPI grant BES-2016–076544 from the the Spanish Ministerio de Economía, Industria y Competitividad (MINECO).

Girona, 2022

Mostafa Barzegar

Acknowledgements

The completion of this thesis would not have been possible without the support and encouragement of several special people. Hence, I would like to take this opportunity to express my gratitude to those who have assisted me along the way.

First and foremost, I have to thank my beloved parents and sister for their love and support throughout my life. Thank you for giving me the strength to reach for the stars and pursue my dreams.

I would like to sincerely thank my supervisors, Prof. Josep Costa and Prof. Carlos Gonzalez, for their guidance, patience, availability and support throughout this study.

I would also like to thank the AMADE group at the University of Girona, especially Jose M. Guerrero and Daniel Trias, for all the support and the opportunity to collaborate with such a wonderful team.

I would like to thank everyone at IMDEA Materials for their trust, gratitude and kindness they have shown me since the first day I set foot there.

I would like to thank and remember all of my friends who supported me not just scientifically and technically, but also spiritually: Miguel, M. Marvi, Ali, M. Elahi, Abrar, Andrea, Ehsan, Reza, Marjan. I could not list all the names here, but you are always on my mind.

Finally, I'd like to dedicate the remaining space to the late Dr. Claudio Lopes. I'd like to express my gratitude for all of his support during my PhD. Aside from his exceptional scientific credentials, he was a wonderful person and friend. He will live on in our memories forever.

List of Publications

This section lists all journal and conference publications related to this thesis.

Journal papers

- **M. Barzegar**, J. Costa, C.S. Lopes. High-fidelity computational micromechanics of first-fibre failure in unidirectional composites: Deformation mechanisms and stress concentration factors. *International Journal of Solids and Structures* 204–205 (2020) 18-33.
  doi: https://doi.org/10.1016/j.ijsolstr.2020.08.005.

Other publications derived from this thesis but not belonging to this thesis and not included in this document are listed below:

- D. M. Peeters, P. Sardar Abadi, A. Baluch, T. Sebaey, **M. Barzegar**, C. Lopes. Dispersed-ply design and optimization to improve the brittle flexural behaviour of composite laminates, *Composites Part A: Applied Science and Manufacturing*, accepted.

Conference papers

- **M. Barzegar**, J. Costa, D. Trias, J. M. Guerrero, C. S. Lopes, C. Gonzalez. Stress Intensity Factor of a fibre embedded in a matrix. *the 20th European Conference on Composite Materials (ECCM 2022)*. Lausanne (Switzerland), 2022.

- **M. Barzegar**, J. Costa, D. Trias, J. M. Guerrero, C. S. Lopes, C. Gonzalez. In Situ Stress Intensity Factor of an Embedded Fiber. *10th International Conference on Composites Testing and Model Identification (COMPTEST)*. France, 2021.

- **M. Barzegar**, C. S. Lopes, J. Costa. Effects of dynamic fibre failure in unidirectional composites. *Materiales Compuestos 4 (1), 24-29*. Vigo

(Spain), 2020. ISSN: 2531-0739.

- **M. Barzegar**, C. S. Lopes, J. Costa. Effects of Local Peak Stress in UD Composites. *FibreMod conference*. KU Leuven (Belgium), 2019.

- **M. Barzegar**, C. S. Lopes, J. Costa. Effects of Dynamic Fibre Failure in Unidirectional Composites. *7th ECCOMAS Thematic Conference on the Mechanical Response of Composites (COMPOSITES)*. Girona (Spain), 2019.

- **M. Barzegar**, C. S. Lopes, J. Costa. Longitudinal tensile failure mechanism in unidirectional fibre composites using computational micromechanics. *13th national congress of composite materials (MATCOMP)*. Vigo (Spain), 2019.

- **M. Barzegar**, F. Montas, C. S. Lopes, C. Gonzalez, J. Costa. Analysis of longitudinal tensile failure of unidirectional composites by means of computational micromechanics. *4th International Conference on Mechanics of Composites (MECHCOPMP)*. Madrid (Spain), 2018.

Some sections of this thesis have not been published yet, but will be in the near future.

Declaration

Universitat de Girona

Prof. Josep Costa Balanzat, Professor of AMADE Research Group, Dept. d'Enginyeria Mecànica i de la Construcció Industrial at Universitat de Girona, and **Prof. Carlos Daniel González Martínez**, Professor of Escuela Técnica Superior de Ingenieros de Caminos, Canales y Puertos at Universidad Politécnica de Madrid,

WE DECLARE:

That the thesis entitled *A computational micromechanics investigation of longitudinal strength in unidirectional fibre reinforced composites*, presented by **Mostafa Barzegar** for obtaining a doctoral degree, has been completed under our supervision in accordance with the code of good practice and does not contain plagiarized elements, and meets the criteria required for obtaining the Doctorate title.

For all intents and purposes, we hereby sign this document.

Prof. Josep Costa Balanzat

Prof. Carlos Daniel González Martínez

Girona, 2022

List of Symbols

In general, the superscripts ^{f}, ^{m}, and ^{c} are referred to the components of the fiber, matrix and fiber/matrix cohesive interface, respectively. Whereas the subscripts $_{t}$ and $_{c}$ indicate tensile and compressive quantities. The subscripts $_{1}$, $_{2}$, $_{3}$ indicate the direction of the axes including longitudinal, transverse, and through-the-thickness, respectively.

List of acronyms

FRP	Fibre Reinforced Polymer
CFRP	Carbon Fibre Reinforced Polymer
RVE	Representative Volume Element
SCF	Stress Concentration Factor
SIF	Stress Intensity Factor
LEFM	Linear Elastic Fracture Mechanics
EPFM	Elasto-Plastic Fracture Mechanics
FPZ	Fracture Process Zone
UD	Unidirectional
CZM	Cohesive Zone Model
CDM	Continuum Damage Mechanics
WD	Weibull distribution
GLS	Global Load Sharing
LLS	Local Load Sharing
SEM	Spring Element Model
PFM	Progressive Failure Model
FEM	Finite Element Method
FE	Finite Element
XFEM	Extended Finite Element Method
CMM	Computational Micromechanical Modelling
CMOD	Crack Mouth Opening Displacement
PBC	Periodic Boundary Conditions
MN	Master Node
BK	Benzeggagh-Kenane

UMAT	User Material Subroutine in Abaqus/Standard
VUMAT	User Material Subroutine in Abaqus/Explicit

Mechanical and statistical symbols

E	Longitudinal Young's Modulus (with different sub-indices)
G	Shear modulus (with different sub-indices)
ν	Poisson's ratio (with different sub-indices)
V_f	Fiber volume fraction
x_1	Longitudinal direction
x_2	Transverse direction
x_3	Through-the-thickness direction
σ	Nominal stress tensor
$\tilde{\sigma}$	Effective stress tensor
ε	Strain tensor
$\Delta\varepsilon$	Strain increment tensor
$\tilde{\varepsilon}_t^{pl}$	Equivalent plastic strain under tension
$\tilde{\varepsilon}_c^{pl}$	Equivalent plastic strain under compression
ε^0	Strain at damage initiation
ε^u	Strain at ultimate failure
$\mathbf{S}$	Compliance tensor
$\mathbf{Q}$	Stiffness tensor
$\mathbf{I}$	Identity tensor
$\mathbf{C}_T$	Tangent constitutive tensor
$\mathbf{M}$	Damage evolution tensor
P	Load
H	Hardness
E^m	Elastic modulus of the matrix
ν^m	Poisson ratio of the matrix
c^m	Cohesion parameter of the matrix
ϕ^m	Internal friction angle of the matrix
σ_t^m	Uniaxial tensile strength of the matrix
G_t^m	Fracture energy of the matrix under uniaxial tension
σ_{yc}^m	Uniaxial compressive yield strength of the matrix
σ_{uc}^m	Uniaxial ultimate compressive strength of the matrix
D_t^m	Damage variables of the matrix under tension
D_c^m	Damage variables of the matrix under compression

ψ^m	Dilation angle of the material model of the matrix
ε^m	Eccentricity parameter of the material model of the matrix
σ_{b0}/σ_{c0}	Biaxial to uniaxial compressive ratio of the matrix
K_c^m	Tensile and compressive meridian yield condition ratio of the matrix
μ^m	Viscosity of the material model of the matrix
α^m	Coefficient of thermal expansion of the matrix
N^c	Normal tensile strength of the cohesive interface
S^c	Shear strength of the cohesive interface
G_n^c	Fracture energies under modes I of the cohesive interface
G_s^c	Fracture energies under modes II of the cohesive interface
μ^c	Friction coefficient of the cohesive interface
t_n	Normal cohesive traction
t_s	Longitudinal shear cohesive traction
δ_n	Normal displacement jump
δ_s	Longitudinal shear displacement jump
δ_0	Separation at damage initiation
δ_u	Separation at ultimate failure
k_{nn}^c	Penalty stiffness in the normal direction of the cohesive interface
k_{ss}^c	Penalty stiffness in the shear direction of the cohesive interface
η_{BK}^c	Benzeggagh-Kenane power exponent of the cohesive interface
D^c	Damage variable of the cohesive interface
V_f	Fiber volume fraction
E_1^f	Longitudinal elastic modulus of the fiber
E_1^{0f}	Initial longitudinal elastic modulus of the fiber of the nonlinear model
E_2^f	Transverse elastic modulus of the fiber
G_{12}^f	Longitudinal shear modulus of the fiber
G_{23}^f	In-plane shear modulus of the fiber
c_f	Nonlinear parameter of the longitudinal elastic modulus
ν_{12}^f	Longitudinal Poisson ratio of the fiber
ν_{23}^f	In-plane Poisson ratio of the fiber
X_t^f	Fibre strength under longitudinal tension
X_c^f	Fibre strength under longitudinal compression
G_t^f	Fibre fracture energy under longitudinal tension
G_c^f	Fibre fracture energy under longitudinal compression
α_1^f	Coefficient of thermal expansion in the longitudinal direction of the fiber

α_2^f	Coefficient of thermal expansion in the transverse direction of the fiber
D	Fiber diameter
R	Fiber radius
L_0	Reference length in the Weibull distribution for fiber strength
σ_0	Weibull strength
m	Weibull shape parameter
F	Weibull cumulative density function
a	Crack length
a_0	Initial crack length
Δa	Crack propagation length
K_I	Stress intensity factor under mode I
K_{II}	Stress intensity factor under mode II
K_{III}	Stress intensity factor under mode III
K_{IC}	Critical stress intensity factor under mode I
K_{IC}^f	Mode I fracture toughness of the fiber
σ_∞	Remote stress
G_I	Energy release rate under Mode I
G_{IC}^f	Energy release rate under Mode I
W	Elastic strain energy density
$\vec{t}$	Traction vector
$\vec{u}$	Displacement vector
Γ	J-integral contour
E^*	Effective elastic modulus
l_p	Plastic process zone length
ρ	Volumetric density
λ	Linear density
$\dot{\varepsilon}$	Strain rate
σ_c	Compressive stress
ε_c	Compressive strain
ΔT	Temperature drop during the cool down process
$\vec{U}_k$	Displacement of master node k
u_i	Displacement in the i direction
l^*	Characteristic element length
D	Damage variable
F_{1+}	Damage activation functions under longitudinal tension

F_{1-}	Damage activation functions under longitudinal compression
ϕ_{1+}	Loading functions under longitudinal tension
ϕ_{1-}	Loading functions under longitudinal compression
r_{1+}	Elastic domain thresholds under longitudinal tension
r_{1-}	Elastic domain thresholds under longitudinal compression

Contents

Preface iii

Acknowledgements v

List of Publications vii

Declaration ix

List of Symbols xi

List of Figures xxi

List of Tables xxxi

Abstract xxxiii

Resum xxxv

Resumen xxxix

1 Introduction 1

1.1 Composite materials 2

1.2 Multiscale modelling approaches 4

1.2.1 Top-down strategy 4

1.2.2 Bottom-up strategy 5

1.3 Failure in FRP composites 7

1.3.1 Failure criteria in FRP composites 9

1.4 Thesis motivation 12

1.5 Objectives of this thesis 13

1.6 Structure of the thesis 14

2 State-of-the art: Current understanding of longitudinal failure in UD composites 17

2.1 Statistical distribution for fibre strength 19

2.1.1 Standard Weibull distribution 19

2.1.2 Modified Weibull distributions 20

2.2 Size scaling effects 21
2.3 Stress redistribution around a broken fibre 22
2.4 Critical cluster size 24
2.5 Effects of matrix and interface properties 25
2.6 Thermal residual stress 26
2.7 Tensile failure models of UD composites 26
2.7.1 Analytical fibre bundle models 27
2.7.1.1 Global load sharing model 27
2.7.1.2 Local load sharing models 31
2.8 Modeling Strategies based on Continuum Micromechanics . . 32
2.8.1 Analytical micromechanics 34
2.8.1.1 Mean-field approaches 34
2.8.1.2 Variational bounding methods 38
2.8.1.3 Micromechanics fibre bundle models 39
2.8.2 Spring element models 42
2.9 Computational micromechanics 44
2.9.1 Embedded cell models 45
2.9.2 Periodic microfield approaches 47
2.9.3 Concluding remarks 49

3 Methodology: Computational micromechanics 51
3.1 Constitutive models of fiber, matrix and interface 52
3.1.1 Carbon fiber 52
3.1.2 Epoxy matrix 53
3.1.3 Fibre-matrix interface 65
3.2 Representative volume element 71
3.2.1 RVE generation 71
3.3 Micromechanics modelling frameworks 73
3.3.1 Boundary conditions 73
3.3.2 Methodology 74
3.4 Results and discussion 80
3.5 Concluding remarks 89

4 Effect of first-fiber failure: Deformation Mechanisms and Stress Concentration Factors 91
4.1 Introduction 92

4.2 Micromechanics modeling framework 95
4.2.1 Periodic RVE approach 96
4.2.2 Model constituents 100
4.2.3 Post-processing of results 102
4.3 Results and discussion 104
4.3.1 Relevant micromechanisms associated with first-fibre breakage 104
4.3.1.1 Progressive fibre breakage and recoil 104
4.3.1.2 Fibre/matrix interface debonding 111
4.3.1.3 Matrix inelastic deformation 114
4.3.1.4 Residual curing stresses 116
4.3.2 Influence of microstructural parameters on failure mechanisms and SCFs 117
4.3.2.1 Fibre volume fraction 120
4.3.2.2 Fibre-to-matrix stiffness ratio 122
4.3.2.3 First-fibre breaking strength 124
4.3.2.4 Fibre/matrix interface strength 124
4.4 Concluding remarks 127

5 Implications of matrix on fibre failure mechanisms: Stress Intensity Factor and Ultimate Strength 131
5.1 Introduction 132
5.2 Linear elastic fracture mechanics 134
5.2.1 Stress intensity factor 136
5.2.2 SIF determination methods 139
5.2.2.1 Compounding method 139
5.2.2.2 Displacement extrapolation 140
5.2.2.3 Force method 140
5.2.2.4 J-integral 141
5.2.2.5 Finite crack extension method 142
5.3 Methodology 146
5.3.1 Numerical evaluation of SIF 146
5.3.2 Non-dimensional Parametric Analysis 149
5.3.3 Micromechanical Progressive Failure Model 151
5.4 Finite element model validation 152

5.4.1 Free fibre model 152
5.4.2 Embedded fibre model with very low stiffness matrix . 153
5.4.3 Comparison with an analytical model 154
5.5 Results and discussion 155
5.5.1 Isotropic fibre embedded in a matrix 155
5.5.2 Orthotropic free fibre 158
5.5.3 Orthotropic fibre embedded in a matrix 161
5.5.4 Effect on the fibre strength 164
5.5.5 Progressive failure and cluster development 167
5.6 Concluding remarks 170

6 In situ stress intensity factor of a carbon fibre embedded in an epoxy matrix 173
6.1 Introduction 174
6.2 Methodology 176
6.2.1 Finite element micromechanics modelling 176
6.2.2 Numerical evaluation of SIF 178
6.2.3 Model constituents 179
6.2.3.1 Fibre and matrix 179
6.2.3.2 Fibre/matrix interface 180
6.3 Results and discussion 180
6.3.1 Effect of isotropy and orthotropy 180
6.3.2 Orthotropic carbon fibre embedded in a matrix 181
6.3.3 Fibre/matrix interface debonding 183
6.3.4 Fibre/matrix interface strength 186
6.3.5 Matrix plasticity 187
6.3.6 Matrix yield stress 190
6.3.7 Matrix plasticity and interface debonding 191
6.4 Concluding remarks 191

7 Conclusions and future work 195
7.1 Conclusions 196
7.2 Future work 198

Bibliography 199

List of Figures

1.1 Multiscale simulation strategies to carry out virtual mechanical tests of composite materials and structures [1]. 6

1.2 Schematic of the different failure micromechanisms in unidirectional composite as a function of the loading conditions. (a) Longitudinal tension. (b) Longitudinal compression. (c) Transverse tension. (d) Transverse compression. (e) Transverse shear. (f) Longitudinal shear [2]. 8

1.3 Three-dimensional stresses on a UD composite element. The axes 1,2, and 3 (coordinate system) are fixed to fiber direction (axis 1), transverse (axis 2) and thickness direction (axis 3). The coordinate system is rotated by the fracture angle θ_{fp}, against the thickness direction. 10

1.4 Predictive failure curve derived from Puck's criterion under matrix failure modes and their fracture angles. 11

1.5 Schematic of LaRC principal failure modes. 12

2.1 Schematic illustration of fibre packings: (a) 1D regular packing, (b) 2D regular packing (c) 1D random packing and 2D random packing [36]. 23

2.2 Demonstration of stress distribution in a broken fiber. 30

2.3 Schematics of the stress redistribution used by Swolfs [36]: a) stress concentration around a single broken fibre, b) SCF around two broken fibres is summed up by linear superposition and c) SCF around two broken fibres by enhanced superposition. Black fiber represents broken fiber. 41

2.4 Representation of the node lattice of the spring element model showing the fibres (green lines) connected by matrix shear springs (grey dashed lines). 42

2.5 Schematic of the embedded cell model to simulate the three-point bend test on a notched beam. The microstructure is considered as the core region with a high level of detail (including the matrix, fibres and interfaces) embedded in the homogeneous material (in gray) whose constitutive equation is provided by a suitable homogenization model. 46
2.6 The periodic microstructure generated by the repetition of the unit cell, which contains an RVE of 30 fibers, randomly distributed in a square domain. 48

3.1 Schematic of the Mohr-Coulomb failure criterion: shear band created by a uniaxial compression stress and Mohr's circle. . . . 55
3.2 Drucker–Prager and Mohr-Coulomb yield surfaces. 57
3.3 Matching between the Mohr-Coulomb and Drucker-Prager yield surfaces in the deviatoric plane 58
3.4 Types of fracture according to the FPZ relative dimensions. From left to right: brittle, ductile and quasi-brittle material. Stress distribution along the crack line is shown at the bottom. From Bazant and Planas [138]. 60
3.5 Yield surface in plane stress. 62
3.6 Response of quasi-brittle material to uniaxial loading in: a) tension and b) compression. 63
3.7 Schematic of the stress-strain curves used to model the epoxy uniaxial tension and compression response. Damage modes are highlighted in red. 64
3.8 Schematic of the pure-mode bilinear traction– separation law used to model the cohesive zone interface. 66
3.9 Schematic of bilinear traction– separation law for mixed-mode loading based on the BK fracture criterion 69
3.10 Schematics of the shear response of the damage-friction model for fiber/matrix interfaces. 70
3.11 Schematic of the periodic fiber distribution generation based on the RSA algorithm. The black fibres guarantee the periodicity of the RVE. 73
3.12 Diagram depicting the position of the master nodes used to implement the periodic boundary conditions within the RVE. 75

3.13 Reference RVE section with $V_f = 51\%$, contains 107 fibers. The location and number of each fiber are specified. 76
3.14 Extruded 3D RVE model. 77
3.15 An example of the distribution of fracture planes and cohesive surface-based interactions in a fiber. The parameter d denotes the distance between fracture planes. 78
3.16 A section of the micromechanical model detailing the location of cohesive surfaces in the fiber and at the fiber/matrix interface. . . 78
3.17 Distributions of tensile strength of the 2140 fracture planes in the fibres of the RVE, based on Weibull distribution. 80
3.18 Stress-strain curves for the AS4/8552 carbon-epoxy matrix under longitudinal tension. The number of broken fibers at various strains is represented. The blue color represents broken fibers, while the red color represents intact fibers. 81
3.19 Longitudinal stress and failure at $\varepsilon = 2\%$: a) the full RVE, b) the RVE in the absence of a matrix for better illustration. 82
3.20 Fracture sequence in the group of broken fibers with respect to longitudinal strain. The matrix and intact fibres have been removed for better visibility. 84
3.21 The sequence of fiber failure and cluster formation at various strains. 85
3.22 Stress distribution in the RVE prior to and after the first fibre breakage. 85
3.23 The superposition effects of stress distribution around several broken fibres. 86
3.24 The progression of damage at the fiber/matrix interface as a result of longitudinal strain. a) fibre 28, b) fibre 30, c) fibre 101, and d) fibre 116. 87
3.25 Evolution of matrix plasticity as a result of longitudinal strain. A section of the matrix is cut to improve visibility. 88

4.1 a) Reference RVE section with $V_f = 60\%$. The pre-broken or failing fibre (indicated in black) is always located at the center. Intact neighboring fibres are numbered, based on the distance from broken fibre, for reference in the text. b) Extruded 3D RVE model with details of boundary and initial conditions. The fracture plane of the breaking fibre is always located at $z = L/2$. 97

4.2 Bi-linear cohesive law used to model progressive fiber breakage. The maximum traction is a stochastic value given by the Weibull fibre failure probability distribution function (here σ_f= 2.7 GPa). 98
4.3 Weibull probability of failure distribution of AS4 carbon fibres [119]. Five discrete values are marked (2.0, 2.4, 2.7, 3.1 and 3.4 GPa) corresponding, respectively, to probabilities of failure of 10%, 25%, 50%, 75% and 90%. The reference gauge length is equal to 20 *mm*. 102
4.4 Evolution with time of average stress in the nearest intact fibre (fibre 1 in Figure 4.1a) for the dynamic case. 106
4.5 a) Evolutions of SCFs with applied strain for nearest intact fibre (fibre 1 in Figure 4.1a) in static and dynamic analyses. b) Behaviour of SCFs for several neighboring intact fibres in static and dynamic cases. Marks 1 and 2 indicate the strain levels at which SCF profiles are extracted for static and dynamic cases. 107
4.6 a) SCF profiles corresponding to maximum stress concentrations in static and dynamic analyses (marks 1 and 2 in Figure 4.5b). Each data point represents one intact fibre. b) Stress recovery profiles in broken fibres for static and dynamic cases. 108
4.7 a) Broken-fibre/matrix interface damage predictions by static and dynamic simulations at respective moments of maximum SCF values ($\varepsilon \approx 0.3\%$ and $\varepsilon \approx 1.2\%$ for static and dynamic models, respectively). b) Broken fibre debonding length vs. applied strain for static and dynamic cases. 110
4.8 Comparison of matrix plasticity levels in the plane containing the fibre break between (a) static and (b) dynamic analyses, for respective maximum SCF values ($\varepsilon \approx 0.3\%$ and $\varepsilon \approx 1.2\%$ for static and dynamic cases, respectively). 111
4.9 a) Maximum SCF values predicted by simulations considering perfect and imperfect fibre/matrix interfaces. b) Broken-fibre stress recovery profiles for both cases. 112

4.10 a) Sectional view of the integrity of the interfaces of broken-fibre neighbors (fibre debonds indicated in red) at the moment of maximum SCFs ($\varepsilon \approx 1.2\%$). b) Longitudinal view of fibre debonding on the same fibres (approximate debonding lengths of $11.2R$, $10.8R$, $10.6R$, $9.2R$, $5.4R$ and $1.1R$ for fibres 1 to 6, respectively). 113
4.11 Correlation of matrix plastic deformation levels ($\varepsilon \approx 1.2\%$) for simulations a) without interface debonding and b) with interface debonding. 114
4.12 a) Maximum SCF values for simulations with elastic and inelastic matrices. b) Ineffective and interface debonding lengths, corresponding to maximum SCFs, for both cases. 115
4.13 Maximum matrix plasticity levels predicted by the reference simulation ($\varepsilon \approx 1.2\%$). The numbered fibres are those most affected by matrix inelastic deformation. 116
4.14 a) Maximum SCF values for simulations with and without residual curing stresses. b) Levels of ineffective and interface debonding lengths, corresponding to maximum SCFs, for both cases. 118
4.15 Matrix plasticity levels, corresponding to maximum SCFs ($\varepsilon \approx 1.2\%$), in the absence (a) and inclusion (b) of curing residual stress. 119
4.16 Longitudinal strain (a) and stress (b) fields, at maximum SCFs, in the case including residual curing stresses. 119
4.17 a) Maximum SCF values for five statistically representative microstructures with V_f = 50%, 60% and 70%. b) Corresponding stochastic predictions of broken-fibre ineffective lengths ($z/R = [12 \pm 1.1, 10.7 \pm 1.1, 10.2 \pm 1]$) and debonding lengths ($z/R = [12 \pm 1.1, 10.7 \pm 1.1, 10.2 \pm 1]$), respectively, for $V_f = [50\%, 60\%, 70\%]$. 121
4.18 Matrix plasticity levels, for maximum SCF values, for representative microstructures with V_f = 50%, 60% and 70%. 122

4.19 a) Maximum statistical SCF values (five outcomes) for first-fibre breakage in AS4/8552 and S2/MTM44-1 composites (applied strains $\varepsilon \approx 1.2\%$ and $\varepsilon \approx 3.3\%$, respectively). b) Corresponding predictions of broken-fibre ineffective lengths ($z/R = [14.7 \pm 1.4, 9.2 \pm 0.8]$) and debonding lengths ($z/R = [10.7 \pm 1.1, 7.6 \pm 1.4]$), respectively, for [AS4/8552, S2/MTM44-1] material systems. 123
4.20 a) SCF vs. strain in nearest intact fibre for different fibre strengths. b) SCF profiles transverse to the broken fibre for different fibre strengths. 125
4.21 a) Broken-fibre ineffective and interface debonding lengths as function of strength. b) Evolution of peak matrix plasticity levels with fibre strength. 126
4.22 Matrix plasticity levels corresponding to maximum SCF values, and for different fibre strengths : a) σ_f = 2.0 GPa, b) σ_f = 2.4 GPa, c) σ_f = 2.7 GPa, d) σ_f = 3.1 GPa and e) σ_f = 3.4 GPa . . . 127
4.23 a) Maximum SCF predictions for weak and strong fibre/matrix interfaces. b) Corresponding broken-fibre ineffective and debonding lengths. 128
4.24 Matrix plasticity levels, corresponding to maximum SCF values, for a) weak and b) strong fibre/matrix interfaces. 129

5.1 Definition of the variables r and θ and the crack tip local coordinate frame. 138
5.2 Two steps crack closure technique. 144
5.3 FE model with details of the boundary conditions and finite-element meshing of the crack tip region. 145
5.4 A notched fibre with straight-fronted edge crack (indicated in grey) embedded in a matrix. a) 3D geometry of the model and b) the fibre cross-section at crack plane. 147
5.5 FE model with details of the boundary conditions and finite-element meshing of the crack tip region. 147
5.6 Definition of the contour path around the crack tip to compute the J-integral. 148

5.7 Schema of the progressive failure model. a) 3D view and b) cross-section view. Fibres are denoted by $q \in [1, ..., N_q]$, while planes are denoted by $p \in [1, ..., N_p]$, where N_q and N_p are the number of fibres and planes, respectively. 151
5.8 Comparison of the non-dimensional stress intensity factor of an isotropic free fibre subjected to uniform tension obtained in this work (FEM), with Astiz [227], Daoud et al. [190] and Ogihara et al. [189]. 153
5.9 Non-dimensional SIF of an isotropic free fibre resulting from a computational model of the isolated fibre (line) and with embedding material of nearly zero stiffness (dots). 154
5.10 Geometric illustration of a model consisting of a broken fibre embedded in a matrix as a solid cylinder with central circular crack. The fibre is broken in the middle ($x_1 = L/2$) and shown as the grey area. 155
5.11 Non-dimensional SIF for an isotropic fibre embedded in a matrix for different fibre/matrix stiffness ratios, α. The dots refer to the FEM results and the dashed lines to the fitting curves according to Equation 5.32. The continuous grey curve corresponds to the SIF for a free fibre ($\alpha = 1$). 156
5.12 3D surface plot of non-dimensional SIF for an isotropic fibre embedded in a matrix for different fibre/matrix stiffness ratios (α) and crack lengths (a/D). 156
5.13 Relative reduction of the non-dimensional SIF for an isotropic fibre embedded in a matrix with respect to the free fibre (continuous grey line). 157
5.14 Non-dimensional CMOD for an isotropic fibre embedded in a matrix for different fibre/matrix stiffness ratios, α. The continuous grey curve corresponds to the CMOD for a free fibre ($\alpha = 1$). . . 158
5.15 Comparison of non-dimensional stress intensity factor of an orthotropic free fibre for different longitudinal/transverse stiffness ratio, β. The dots refer to the FEM results and the dashed lines indicate the fitting results. 159

5.16 3D surface plot of non-dimensional SIF for an orthotropic free fibre for different longitudinal/transverse stiffness ratios (β) and crack lengths (a/D). 159
5.17 Percentage of non-dimensional stress intensity factor changes of an orthotropic free fibre for different longitudinal/transverse stiffness ratio, β. The percentage change was calculated with respect to the model with $\beta = 0$ ($E_1 = E_2$) as the reference. . . . 160
5.18 Comparison of non-dimensional stress intensity factor of an orthotropic fibre embedded in a matrix, for different fibre longitudinal/transverse stiffness ratios (β) and fibre/matrix stiffness ratios (α). a) $\alpha = 0.95$ and b) $\alpha = -0.95$. 162
5.19 The histograms of the tensile strength distribution of the fibres: (a) free fibres, (b) fibres embedded in an elastic matrix. 166
5.20 Logarithmic Weibull plot diagram (P is the probability of failure), for eighty-nine $34 - 700WD$ carbon fibers being either free or embedded in a matrix. 166
5.21 Ultimate average failure strain and stress, and stress-strain curve predicted by the PFM from 50 runs (using the Weibull distribution from single fibre tests, and the distribution modified by SIF), compared with the experimental data. 168
5.22 Average fibre break density as a function of the applied stress predicted by the PFM from 50 runs (using the Weibull distribution from single fibre tests, and the distribution modified by SIF), compared with the experimental data of two specimens (indicated as Exp1 and Exp2). 168
5.23 Average max cluster size, formation of 2-plet and 3-plet as a function of the applied stress predicted by the PFM from 50 runs (using the Weibull distribution from single fibre tests, and the distribution modified by SIF), compared with the experimental data of two specimens (indicated as Exp1 and Exp2). 170

6.1 Geometrical illustration of the finite element model. a) A notched carbon fiber with a straight-fronted edge crack (indicated in grey) embedded in an epoxy matrix and b) the FE model with details of boundary conditions and finite-element meshing. 177

6.2 Non-dimensional SIF of a free carbon fibre with isotropic or orthotropic elastic properties. 181
6.3 Comparison of the non-dimensional SIFs of an orthotropic carbon fibre embedded in a linear-elastic matrix for different matrix thicknesses (t). The results of a free carbon fibre are added as the reference for comparison. The parameter D is the fibre diameter. The markers represent the FE results and dashed lines represent the fitting results. 182
6.4 Comparison of the non-dimensional SIFs of an embedded orthotropic carbon fibre with interface debonding and perfect adhesion. Free fibre curve added for comparison reference. 184
6.5 Evolution of non-dimensional CMOD for the model with interface debonding and the model without interface debonding, as a function of the relative crack length (a/D). 185
6.6 Evolution of the interface debonding as a function to the relative crack length (a/D). Only half of the interface debonding is depicted as the model is symmetric. The approximate debonding lengths (relative to the fibre radius) are 0.11R, 0.17R, 0.35R, 0.56R, 0.82R, and 1R from left to right, respectively. 186
6.7 Comparison of non-dimensional SIFs of an orthotropic carbon fibre embedded in a elastic matrix for different interface strengths including strong, standard, and weak interface. 187
6.8 Non-dimensional interface debonding length for an orthotropic carbon fibre embedded in a matrix for the different interface strength. Where parameter z is the debonding length and R is the fibre radius. 188
6.9 Non-dimensional SIFs of an orthotropic carbon fibre embedded in an elasto-plastic epoxy matrix. The results of a model with linear-elastic matrix is added as the reference for comparison. . . 189
6.10 Evolution of the matrix plastic strain around the cracked area, with respect to the relative crack length: a) $a/D = 0.07$, b) $a/D = 0.1$, c) $a/D = 0.2$, d) $a/D = 0.3$, e) $a/D = 0.4$, and f) $a/D = 0.45$. Due to the symmetry of the model, only half of the model is presented. 189

6.11 Comparison of non-dimensional SIFs for an orthotropic carbon fibre embedded in an non-linear inelastic matrix for different matrix yield stress (σ_{yt}). 190
6.12 Non-dimensional SIFs of an orthotropic carbon fibre embedded in a non-linear inelastic matrix in the presence of interface debonding. The model is compared with a model with perfect interface adhesion. 192
6.13 Comparison of the size of the interface debonding and matrix inelastic deformation area around the crack region for $a/D = 0.45$. 192

List of Tables

3.1 Mechanical properties of AS4 carbon fiber [119–121] 53
3.2 Input parameters of the matrix damaged/plasticity model for the plastic flow and yield surface evolution [146]. 65
3.3 Parameters of the damaged/plasticity model of the 8552 epoxy matrix under uniaxial tension and compression [146]. 65
3.4 Material properties of AS4/8552 fiber/matrix interface [156]. . . 71
3.5 Comparison of predicted micromechanical and experimental results for a AS4/8552 carbon-epoxy. 82

4.1 Mechanical properties of materials used throughout the present work: E is the elastic modulus; ν is the Poisson ratio; α is the thermal conductivity; σ_{t0} is the tensile strength; G_t is the fracture energy under tension; σ_{yc} is the compression yield limit; σ_{uc} is the compression strength; N and S are the normal and shear interface strengths; k_{nn} and k_{ss} are the normal and shear interface penalty stiffness values; G_n and G_s are the normal and shear interface fracture energies; η_{BK} is the Benzeggagh Kenane fitting parameter. In general, superscripts ^{f,m} refer to quantities of the fibre and matrix respectively, while subscripts $_{1,2}$ indicate longitudinal and transverse properties. 103

5.1 Coefficients for the fitting equation given in Equation 5.32. . . . 158
5.2 Coefficients for the fitting of equation given in Equation 5.33. . . 161
5.3 Material properties for the 34-700WD carbon fibre. 167

6.1 Mechanical properties of materials used throughout the simulations. 179

Abstract

The use of Fibre Reinforced Polymers (FRP) composites has grown in popularity over the last few decades. They offer outstanding mechanical properties combined with a low density, making them an excellent solution for many lightweight applications. However, their low fracture toughness translates into brittle behaviour that often leads to catastrophic failure without prior damage symptoms. Moreover, there is a lack of reliable tools for the design of FRP with mitigated brittleness because of the complexity of the micromechanisms involved and the difficulties of experimental validation. These two factors constitute a serious drawback that limits the application of FRP to a wider engineering space.

As a result, virtual testing of composite materials emerges as a promising strategy for reducing experimental programs devoted to the characterization of these materials. Nonetheless, because FRP failure is controlled by microscale phenomena, there is a need for a multiscale scheme that captures them using micromechanical models. In this thesis, the capability of computational micromechanics to make virtual predictions of failure processes in unidirectional FRP composites is extended with respect to the state of the art. Towards this end, several computational micromechanics methods are developed, each with its own challenge and research objective.

A high-fidelity computational micromechanics framework was developed in order to accurately predict the failure and longitudinal behavior of UD composites. The fracture of fibers was explicitly reproduced to capture the longitudinal failure of the microstructure. To accomplish this, a sequence of fracture planes are introduced in the longitudinal direction of each fiber via cohesive surface-based interactions. A cohesive zone model with a traction separation law is used to represent fiber/matrix interface debonding, whereas a pressure dependent, elasto-plastic model with tensile and compressive damage is used to capture the nonlinear behavior of the polymer matrix.

Taking advantage of the computational micromechanics models, the failure process that occurs in each constituent of RVE, including fiber, matrix, and interface, when a unidirectional ply is loaded under longitudinal tension is

analyzed beyond the state of the art. For this purpose, a RVE consisting of 107 carbon fibers ($D = 7.09$) embedded in an 8552 epoxy matrix with dimensions of $25R \times 25R \times 113R$ (R is the radius of fibre) is used. The micromechanics model output was compared to experimental results from the literature as well as the manufacturer (Hexcel) data sheet. The predicted tensile strength agreed very well with the experimental measurements.

Subsequently, stress redistribution and damage phenomena in the vicinity of the first-fibre break in unidirectional composites under longitudinal tensile loads were thoroughly studied by means of high-fidelity computational micromechanics based on experimentally characterised material constituents. In this framework, periodic microstructures with statistically representative random fibre packings were analysed, and transient dynamic analyses were performed to take into account the progressive failure and recoiling of a breaking fibre. This study extends our understanding of the mechanisms that govern the longitudinal tensile failure of unidirectional composites. The findings indicate that dynamic fiber failure can more accurately reproduce the failure process and provide a more realistic stress distribution.

Finally, a micromechanical finite element model is employed to investigate the stress intensity factor of a single fiber with a straight-fronted edge crack embedded in a matrix. Embedding a fibre in an elastic matrix reduced the SIF over the free fibre case. It was discovered that the presence of the matrix enhances the apparent strength of the fibers and alters the Weibull strength distribution characteristics, resulting in the fibers failing at higher strains. A modified Weibull distribution taking into account such effect due to the presence of the matrix was computed. The progressive failure of a unidirectional carbon composite was simulated using this Weibull distribution. The fibre break density predicted by the model became significantly closer to the experimental observations, showing that the presence of the matrix must be included for obtaining the strength of the fibres.

Resum

L'ús de materials compostos de polímers reforçats amb fibra (FRP) ha guanyat popularitat en les darreres dècades. Ofereixen excel·lents propietats mecàniques combinades amb una baixa densitat, cosa que els converteix en una excel·lent solució per a moltes aplicacions de pes lleuger. Tot i això, la seva baixa tenacitat a la fractura es tradueix en un comportament fràgil que sovint condueix a falles catastròfiques sense símptomes previs de dany. A més, hi ha una manca d'eines fiables per al disseny de FRP amb fragilitat mitigada a causa de la complexitat dels micromecanismes involucrats i les dificultats de validació experimental. Aquests dos factors constitueixen un inconvenient seriós que limita l'aplicació de FRP a sectors més amplis de l'enginyeria.

Com a resultat, l'assaig virtual de materials compostos sorgeix com una estratègia prometedora per reduir els programes experimentals dedicats a la caracterització d'aquests materials. No obstant això, pel fet que la falla de FRP està controlada per fenòmens a microescala, hi ha la necessitat d'un esquema multiescala que els capturi utilitzant models micromecànics. En aquesta tesi s'amplia respecte a l'estat de l'art la capacitat de la micromecànica computacional per fer prediccions virtuals de processos de falla en compostos unidireccionals de FRP. A aquest efecte, es desenvolupen diversos mètodes de micromecànica computacional, cadascun amb el seu propi desafiament i objectiu de recerca.

Es va desenvolupar un marc de micromecànica computacional d'alta fidelitat per predir amb precisió la falla i comportament longitudinal dels compostos UD. La fractura de les fibres es va reproduir explícitament per capturar la falla longitudinal de la microestructura. Per aconseguir-ho, s'introdueix una seqüència de plans de fractura a la direcció longitudinal de cada fibra a través d'interaccions cohesives basades en la superfície. S'utilitza un model de zona cohesiva amb una llei de separació per tracció per representar el despreniment de la interfície fibra/matriu, mentre que s'utilitza un model elastoplàstic depenent de la pressió amb danys per tracció i compressió per capturar el comportament no lineal de la matriu polimèrica.

Aprofitant els models de micromecànica computacional, s'analitza més enllà de l'estat de l'art el procés de falla que passa a cada constituent de RVE, incloent-hi

fibra, matriu i interfície, quan una capa unidireccional es carrega sota tensió longitudinal. Per això s'utilitza un RVE compost per 107 fibres de carboni ($D = 7,09$) incrustades en una matriu epoxi 8552 de dimensions $25R \times 25R \times 113R$ (R és el radi de la fibra). El resultat del model de micromecànica es va comparar amb els resultats experimentals de la literatura, així com amb el full de dades del fabricant (Hexcel). La resistència a la tracció predita va coincidir molt bé amb les mesures experimentals.

Posteriorment, la redistribució de tensions i els fenòmens de dany al veïnat del trencament de la primera fibra en materials compostos unidireccionals sota càrregues de tracció longitudinal es van estudiar a fons mitjançant micromecànica computacional d'alta fidelitat basada en propietats de materials caracteritzades experimentalment. En aquest marc, es van analitzar microestructures periòdiques amb empaquetadures aleatòries de fibres estadísticament representatives i es van fer anàlisis dinàmiques transitories per tenir en compte la falla progressiva i la reculada d'una fibra que es trenca. Aquest estudi amplia la nostra comprensió dels mecanismes que governen la falla per tracció longitudinal dels materials compostos unidireccionals. Les troballes indiquen que la falla dinàmica de la fibra pot reproduir amb més precisió el procés de falla i proporcionar una distribució de tensió més realista.

Finalment, es fa servir un model micromecànic d'elements finits per investigar el factor d'intensitat de tensions d'una sola fibra amb una esquerda de vora recta incrustada en una matriu. Incrustar una fibra en una matriu elàstica va reduir el SIF sobre el cas de fibra lliure. Es va descobrir que la presència de la matriu augmenta la resistència aparent de les fibres i altera les característiques de distribució de la resistència de Weibull, cosa que fa que les fibres fallin amb deformacions més altes. Es va calcular una distribució de Weibull modificada tenint en compte aquest efecte a causa de la presència de la matriu. La falla progressiva d'un compost de carboni unidireccional es va simular fent servir aquesta distribució de Weibull. La densitat de trencament de fibres predita pel model es va acostar significativament a les observacions experimentals, mostrant que la presència de la matriu s'ha d'incloure per obtenir la resistència de les fibres.

Resumen

El uso de materiales compuestos de polímeros reforzados con fibra (FRP) ha ganado popularidad en las últimas décadas. Ofrecen excelentes propiedades mecánicas combinadas con una baja densidad, lo que los convierte en una excelente solución para muchas aplicaciones de peso ligero. Sin embargo, su baja tenacidad a la fractura se traduce en un comportamiento frágil que a menudo conduce a fallas catastróficas sin síntomas previos de daño. Además, existe una falta de herramientas confiables para el diseño de FRP con fragilidad mitigada debido a la complejidad de los micromecanismos involucrados y las dificultades de validación experimental. Estos dos factores constituyen un serio inconveniente que limita la aplicación de FRP a sectores más amplios de la ingeniería.

Como resultado, el ensayo virtual de materiales compuestos surge como una estrategia prometedora para reducir los programas experimentales dedicados a la caracterización de estos materiales. No obstante, debido a que la falla de FRP está controlada por fenómenos a microescala, existe la necesidad de un esquema multiescala que los capture utilizando modelos micromecánicos. En esta tesis se amplía con respecto al estado del arte la capacidad de la micromecánica computacional para realizar predicciones virtuales de procesos de falla en compuestos unidireccionales de FRP. Con este fin, se desarrollan varios métodos de micromecánica computacional, cada uno con su propio desafío y objetivo de investigación.

Se desarrolló un marco de micromecánica computacional de alta fidelidad para predecir con precisión la falla y el comportamiento longitudinal de los compuestos UD. La fractura de las fibras se reprodujo explícitamente para capturar la falla longitudinal de la microestructura. Para lograr esto, se introduce una secuencia de planos de fractura en la dirección longitudinal de cada fibra a través de interacciones cohesivas basadas en la superficie. Se utiliza un modelo de zona cohesiva con una ley de separación por tracción para representar el desprendimiento de la interfaz fibra/matriz, mientras que se utiliza un modelo elastoplástico dependiente de la presión con daños por tracción y compresión para capturar el comportamiento no lineal de la matriz polimérica.

Aprovechando los modelos de micromecánica computacional, se analiza más

allá del estado del arte el proceso de falla que ocurre en cada constituyente de RVE, incluyendo fibra, matriz e interfaz, cuando una capa unidireccional se carga bajo tensión longitudinal. Para ello se utiliza un RVE compuesto por 107 fibras de carbono ($D = 7,09$) incrustadas en una matriz epoxi 8552 de dimensiones $25R \times 25R \times 113R$ (R es el radio de la fibra). El resultado del modelo de micromecánica se comparó con los resultados experimentales de la literatura, así como con la hoja de datos del fabricante (Hexcel). La resistencia a la tracción predicha coincidió muy bien con las medidas experimentales.

Posteriormente, la redistribución de tensiones y los fenómenos de daño en la vecindad de la rotura de la primera fibra en materiales compuestos unidireccionales bajo cargas de tracción longitudinal se estudiaron a fondo mediante micromecánica computacional de alta fidelidad basada en propiedades de materiales carcaterizadas experimentalmente. En este marco, se analizaron microestructuras periódicas con empaquetaduras aleatorias de fibras estadísticamente representativas y se realizaron análisis dinámicos transitorios para tener en cuenta la falla progresiva y el retroceso de una fibra que se rompe. Este estudio amplía nuestra comprensión de los mecanismos que gobiernan la falla por tracción longitudinal de los materiales compuestos unidireccionales. Los hallazgos indican que la falla dinámica de la fibra puede reproducir con mayor precisión el proceso de falla y proporcionar una distribución de tensión más realista.

Finalmente, se emplea un modelo micromecánico de elementos finitos para investigar el factor de intensidad de tensiones de una sola fibra con una grieta de borde recto incrustada en una matriz. Incrustar una fibra en una matriz elástica redujo el SIF sobre el caso de fibra libre. Se descubrió que la presencia de la matriz aumenta la resistencia aparente de las fibras y altera las características de distribución de la resistencia de Weibull, lo que hace que las fibras fallen con deformaciones más altas. Se calculó una distribución de Weibull modificada teniendo en cuenta dicho efecto debido a la presencia de la matriz. La falla progresiva de un compuesto de carbono unidireccional se simuló utilizando esta distribución de Weibull. La densidad de rotura de fibras predicha por el modelo se acercó significativamente a las observaciones experimentales, mostrando que la presencia de la matriz debe incluirse para obtener la resistencia de las fibras.

Introduction

1

1.1 Composite materials

Composite materials are formed by combining two or more different constituents or phases that remain separate and distinct within the composite microstructure. The combination of the various mechanical properties of each individual constituent allows for the creation of a specific material with the required properties for a given application. As a result, composite materials are now playing a crucial role in technological areas such as aerospace, car, construction, energy, and biomedical. Good examples of technological applications include ceramic matrix and metal matrix composites in cutting tools, armors for military vehicles, disc brakes for sports automobiles, and gas turbine components.

Although composite materials are perceived as the materials of the future, they are abundant in nature and have been used by humans since the dawn of civilization. Muscles are an example of a fibrous material in the human body. The arrangement of muscular fibers with varying orientations enables the development of a highly adaptable material with exceptional properties in a preferred direction. Wood is another example of a composite material, in which the arrangement of cellulose fibres provides the required strength, while the matrix (lignin) provides the necessary connection between the fibres and confers compressive resistance to the material.

Fibre reinforced polymers (FRP) are the most widely used lightweight structural materials out of all the high-performance composite materials. FRPs are made up of a polymer matrix that is reinforced with stiffer and stronger continuous fibers (carbon, glass, aramid, etc.) that can be woven, knitted, or braided to create a textile sheet that will make the manufacturing process easier. However, for high-end applications that require high strength and stiffness, composite laminates made by stacking several unidirectional (UD) plies are still the reference configuration, because larger fiber volume fractions and thus better properties can be achieved. Millions of fibers run in a single direction through each ply, resulting in a highly anisotropic material. The fibers are the load-bearing phase, while the matrix is primarily used to keep the fibers oriented in the design direction. The properties of the final laminate will be determined by the stacking sequence of the individual plies. As a result, specific laminates can be tailored to achieve the desired properties.

As an example, the new Boeing 787 Dreamliner and the Airbus A350 XWB are approximately 80 percent composite by volume, demonstrating the growing use of FRPs in the modern aircraft industry. In particular, their wings and fuselage are constructed primarily of carbon fiber reinforced polymers (CFRP). As a result, predicting the mechanical properties and failure mechanisms of CFRPs has become necessary in order to demonstrate the safety of structures whose integrity human lives rely on. This task, however, is enormous in terms of cost, time, and human resources.

The recent advances in computational techniques have also contributed to the increased use of composite materials. The ability to simulate a material's or component's behavior without having to fabricate and test it helped reduce the cost and time of the design process, allowing the development of new and better materials for specific uses. Computational simulations can be performed at various scales. Macromechanical simulations required the least computational effort. These simulations allow the designer to simulate the behavior of a full component and study the stresses and deformations in the component; however, the material is assumed to be homogeneous, which is a simplification from the complex geometry of a composite material.

At a finer scale, mesomechanical simulations can be performed in which the composite material is considered to be composed of several plies (laminas) that are homogeneously stacked together with different orientations. Although the laminas are still considered homogeneous, this type of simulation allows for a more detailed analysis and study of various failure mechanisms such as delaminations, providing a better understanding of the behavior of composite materials.

However, composite materials are non-homogeneous as they made up of multiple macroscopic material. Micromechanical simulations must therefor be used to model their microstructure. Micromechanical simulations take into account the different behaviors of the constituents and allow for accurate simulation of the interfaces between them. Despite being more computationally demanding, these simulations provide a comprehensive understanding of the influence of constituent properties on composite behavior, as well as the mechanisms that lead to composite material failure.

1.2 Multiscale modelling approaches

There are currently two main multi-scale modeling strategies in the computational modeling research field: i) the standard top-down approach long used in industrial structural engineering, and ii) a relatively new bottom-up approach, primarily proposed and developed by research centers and university labs.

The hierarchical structure of FRP composite materials makes them ideal candidates for using multiscale strategies in their analysis. It is well understood that the constituent properties and distribution of the reinforcement fibers, whose cross section is of the order of micrometers, control their mechanical properties.

1.2.1 Top-down strategy

This strategy tackles multi-scale problems starting from a numerical analysis of the entire structure, usually through finite element methods, in a global-to-local approach, where material testing begins studying the composite structure and identifying the weakest parts (hot spots) where the damage is most likely to appear. Then, these regions are subjected to further refined analysis using non-linear constitutive models to predict the material response up to the final fracture. However, this strategy mainly relies on phenomenological models where the constitutive relations at certain levels will depend directly on calibration tests performed on upper scales, where complexity and costs are higher. Due to the phenomenological nature of these models, input parameters have to be obtained for each material. This means that the results obtained for a given material system cannot be extrapolated to materials with different fiber volume fraction, ply thickness, or laminate stacking sequence.

In conclusion, this multiscale approach requires a large number of parameters that must be identified and a massive investment on experimental testing in case of considering different material systems, manufacturing processes, loading conditions, composite configurations and architectures, etc.

1.2.2 Bottom-up strategy

Recent developments in multiscale simulations, together with increased computational power and improvements in modeling tools, are enabling an alternative strategy that overcomes the limitations of the top-bottom approach. A more efficient strategy is the bottom-up multiscale strategy [1] which takes the reverse way, starting from micro- and nano-mechanical informations (fiber, matrix and interfaces) and climbing up through the different length scales, each time using the lower-scale behavior as an ingredient of the constitutive model for the higher-scale response, as shown in Figure 1.1. In case of clear separation of length-scales, homogenization schemes can be applied and used to transfer information from one scale to the other. This transfer of information through the lengthscales is the main difference with top-down approach where couplings of different simulation techniques are used instead.

This new multiscale strategy takes advantage from the fact that composite structures are made up of laminates which in turn are obtained by stacking individual plies with different fiber orientation. This leads to three different entities (ply, laminate and component) whose mechanical behavior is characterized by three different length scales, namely fiber diameter, ply and laminate thickness, respectively. Fiber diameters are of the order of 5-20 μm, while ply thicknesses are in the range 100-300 μm and standard laminates are several mm in thickness and above. This clear separation of length scales is very useful to carry out multiscale modeling by computing the properties of one entity (e.g. individual plies) at the relevant length scale, homogenizing the results into a constitutive model, and passing this information to the simulations at the next length scale to determine the mechanical behavior of the larger entity (e.g. laminate). Thus, multiscale modeling is carried out through the transfer of information between different length scales rather than by coupling different simulation techniques.

Virtual testing of composites up to the component level is thus carried out in three successive steps within the framework of the finite element method, assuming that continuum mechanics describes the behavior even for the smaller scales. In the first one, computational micromechanics is used to predict the ply properties from the thermo-mechanical properties of the constituents (fiber, matrix and interfaces), together with the volume fraction and spatial distribution of the

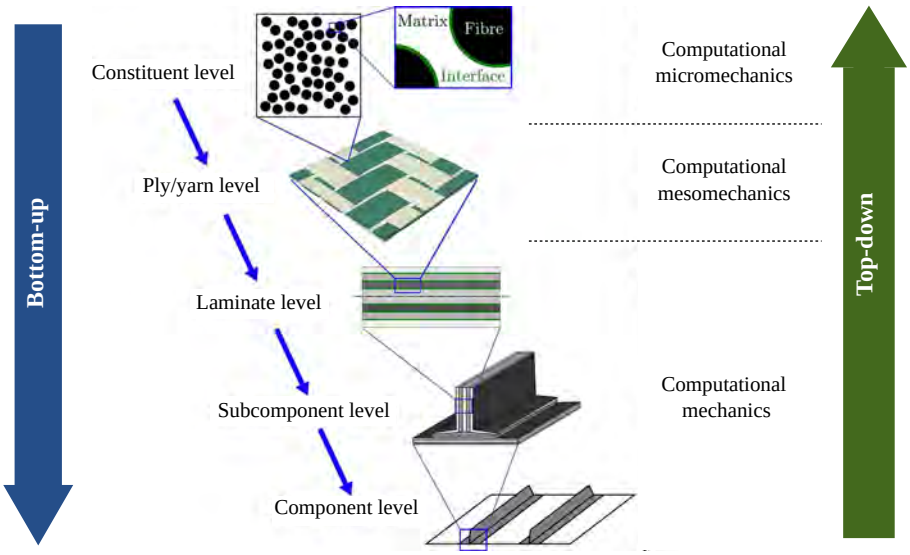

Figure 1.1: Multiscale simulation strategies to carry out virtual mechanical tests of composite materials and structures [1].

fibers within an individual ply. Fiber properties (stiffness, strength, coefficients of thermal expansion) are usually provided by the fiber manufacturer, which carries out a thorough characterization of the fiber properties as part of the optimization process. On the contrary, matrix and interface properties depend on the consolidation process (time, pressure and temperature, effect of fiber dispersion) and have to be characterized in situ by means of nanomechanics. Starting from the homogenized ply properties and information about the laminate lay-up as well as the interply behavior, computational mesomechanics is then used to determine the homogenized behavior of laminates. These results are finally used within the framework of computational mechanics to obtain the response until fracture of structural components made of composites.

This thesis focuses on the initial stages of the bottom-up multiscale strategy (constituent level), in order to develop micromechanical models for the analysis of various failure mechanisms in UD fiber reinforced composites.

1.3 Failure in FRP composites

Most structural materials present one dominant physical failure process upon deformation (e.g., void nucleation, growth and coalescence in ductile metals or shear bands formation in polymers) and the simulation of failure only has to include this micromechanism. On the contrary, FRP composites show totally different and many more failure mechanisms. Despite all existing information and current knowledge about UD FRPs, the accurate prediction of the failure stress of composite materials and structures has been a difficult task due to the complexity of the failure mechanisms involved. In order to predict the failure of UD composite materials, it is necessary to know which stress state causes which specific failure mode, respectively. Six different physical uniaxial failure mechanisms can be identified in UD composites depending on the loading direction, as shown in Figure 1.2.

Failure due to tensile stresses parallel to the fibers is controlled by the brittle fracture of the fibers, while compressive stresses along the fibers lead to fracture by fiber kinking in compression, a mechanism which mainly depends on the fiber misorientation and the matrix shear strength. Tensile fracture perpendicular to the fibers is brittle and controlled by the fracture of the polymeric matrix and of the fiber-matrix interface, while fracture caused by compressive stresses perpendicular to the fibers or by shear is accompanied by large deformations as a result of the non-linear response of the matrix when subjected to compression and/or shear. Finally, interply delamination is another typical failure mechanism in FRPs due to the thermo-elastic mismatch between adjacent plies with different orientation. Hence, accurate models of fracture of FRPs have to include all these micromechanisms and the complex interaction among them because they coexist in the same laminate subjected to one type of load as a result of the different orientation of the fibers in each ply. For instance, intraply matrix cracks (which propagate parallel to the fibers) are very often the origin of interply delaminations, while it is well known that the compressive strength parallel to the fibers is severely reduced in the presence of shear stresses.

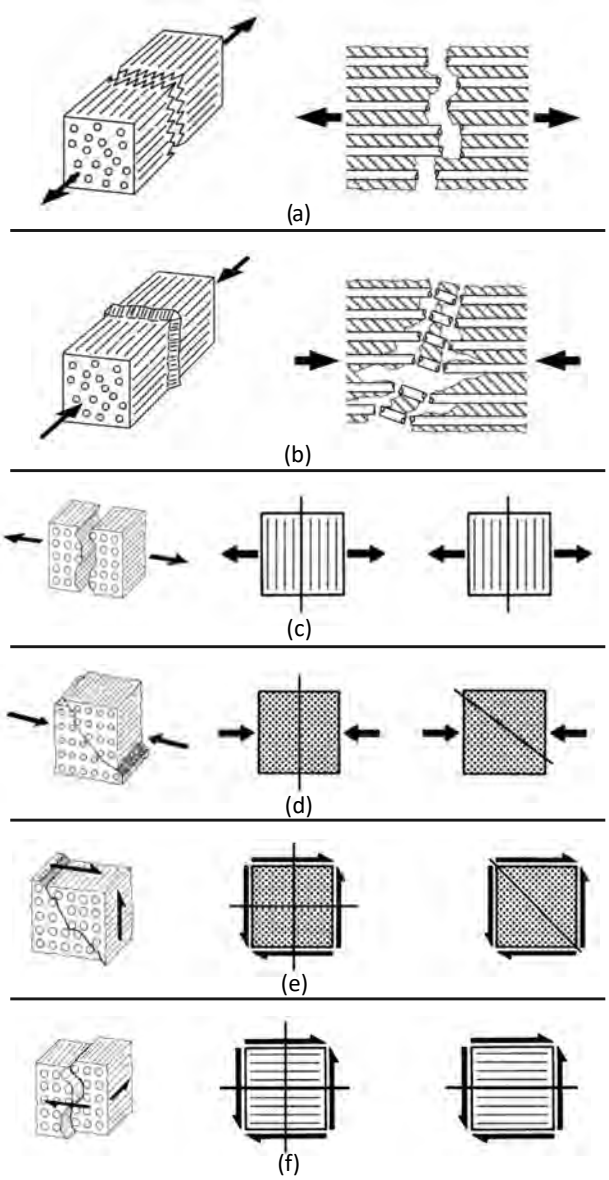

Figure 1.2: Schematic of the different failure micromechanisms in unidirectional composite as a function of the loading conditions. (a) Longitudinal tension. (b) Longitudinal compression. (c) Transverse tension. (d) Transverse compression. (e) Transverse shear. (f) Longitudinal shear [2].

1.3.1 Failure criteria in FRP composites

The failure criteria for composites are often used just in the initial calculations to size a component. Beyond that point, experimental tests on coupons or structural elements are required to determine the global design allowable. These failure criteria are made up of the intersection of different smooth surfaces, which correspond to the different physical failure modes depicted in Figure 1.2. In order to reduce the manufacturing time and the costs of new components, there is a need to establish the level of confidence in the methods for failure prediction of FRPs. To this end, Hinton et al. [3] carried out the worldwide failure exercise, assessing nineteen different theoretical approaches for predicting the deformation and failure response of FRPs. The experimental results for the strength of the FRPs subjected to complex stress states showed significant differences with the predictions of many theories, even when analyzing simple laminates.

Failure in composite structures is commonly predicted through phenomenologically based failure criteria implemented in the finite element analysis of the structure. Hashin [4] in 1980 was the pioneer in the identification of the different failure mechanisms in unidirectional laminates and incorporate them separately in a piecewise smooth failure surface. He considered two different failure mechanisms, one related to the fiber and one for the matrix, assuming a quadratic interaction between normal and shear traction on the failure plane. Hashin pointed out that a failure criterion cannot be smooth but piecewise smooth, consisting of smooth branches each of which models a distinct failure mode. In addition, he suggested that identifying the failure mode (matrix tension, matrix compression, fiber tension or fiber compression) was crucial to capture not only the damage initiation but also its propagation. The criteria assumed a quadratic interaction between tractions acting on the plane of failure (Figure 1.3). However, Hashin's model was not able to determine the actual orientation of the fracture plane for matrix and fiber compression failure modes observed in the experiments [5].

In 1998, Puck and Schurmann [6] proposed modifications to Hashin's model to improve its predictive capabilities and was able to capture the evolution of the angle of the fracture plane under matrix failure modes. The key element of

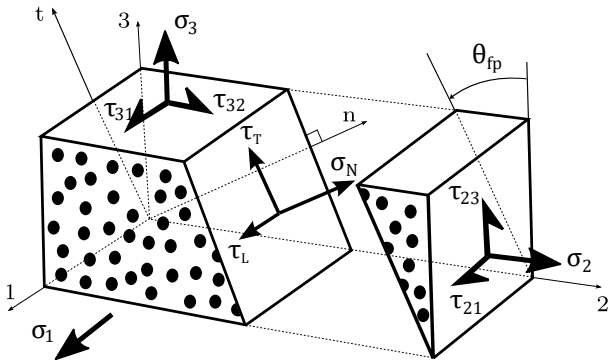

Figure 1.3: Three-dimensional stresses on a UD composite element. The axes 1,2, and 3 (coordinate system) are fixed to fiber direction (axis 1), transverse (axis 2) and thickness direction (axis 3). The coordinate system is rotated by the fracture angle θ_{fp}, against the thickness direction.

Puck's criteria is the calculation of the angle of the fracture plane in the case of matrix failure modes. Thus, transverse tension loads produce a fracture in a plane which is normal to the loading direction and parallel to the fibers. Puck's stated that under matrix failure modes, fracture is caused by the combination of normal and shear stresses acting on a plane parallel to the fibers that he called the action plane.

The criterion distinguishes between three different failure modes (I, II and III) for matrix failure cases. For matrix tension, the criterion predicts a failure plane parallel to the fibers and perpendicular to the loading direction, whereas, under matrix compression the fracture plane is inclined at an angle of θ_{fp} ranging between 0° and 54° depending on the in-plane shear (Figure 1.4).

Puck's predictions correlated very well with the experimental assessments in the worldwide failure exercise. However, it still presents some limitations, specially when dealing with longitudinal compression loading. In addition, Puck's failure criterion uses non-physical material parameters (as shown in Figure 1.4) that may be difficult to determine for non-conventional material systems. To overcome these limitations, Dávila et al. [7, 8] proposed a non-empirical set of failure criteria, denoted as LaRC03. It was based on the fracture mechanics analysis of cracked plies [9] and Puck's action plane concept.

The LaRC characterizes four different failure modes, as shown in Figure 1.5.

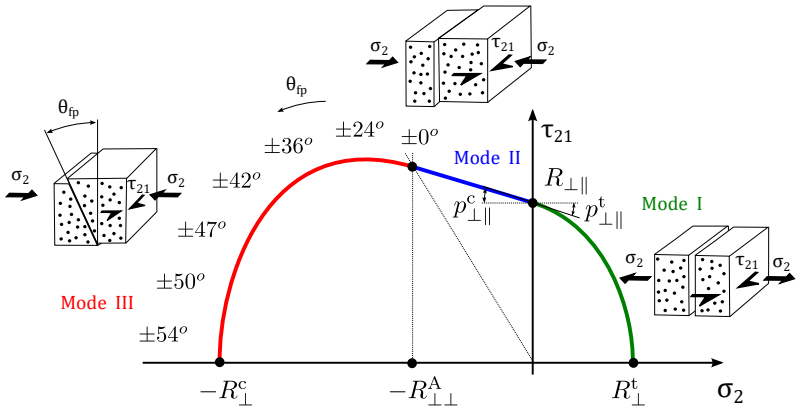

Figure 1.4: Predictive failure curve derived from Puck's criterion under matrix failure modes and their fracture angles.

The longitudinal tensile and compressive failure, are assumed to be fiber dependent modes, whereas the transverse failure modes are controlled by the matrix. These criteria are able to predict the angle of the fracture plane under matrix compression (transverse compression loading) as do Puck's criteria. Nevertheless, the criteria are also able to deal effectively with longitudinal compression loading including the fiber kinking failure mechanism, which is predicted by calculating the fiber misalignment under load and applying the matrix failure criterion in the coordinate frame of the misalignment. Originally formulated for plane stress states, the LaRC predicts effectively the transition between the different failure modes and hence, the failure envelope. In addition, instead of using non-physical material parameters, the LaRC failure criteria lead to the determination of the fracture angle using material properties. In particular, using the Mohr-Coulomb failure criterion to model the ply behavior under transverse loading and maximizing the effective shear stresses respect to the angle of the failure plane.

In addition, instead of using non-physical material parameters, the LaRC failure criteria lead to the determination of the fracture angle using material properties. In particular, using the Mohr-Coulomb failure criterion to model the ply behavior under transverse loading and maximizing the effective shear stresses respect to the angle of the failure plane. The LaRC criteria were extended by Pinho et al. [10, 11] for in-plane shear non-linear behavior and further combined with a pressure-dependent constitutive law to predict tri-axial failure envelopes for

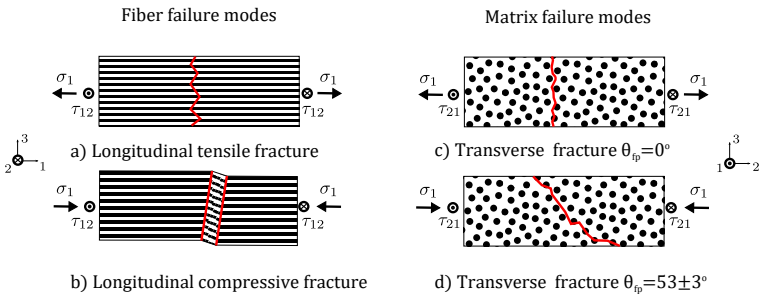

Figure 1.5: Schematic of LaRC principal failure modes.

different laminated composites, as LaRC04 criteria.

Although both Puck and LaRC failure criteria are able to handle the different matrix and fiber failure modes, the failure locus are obtained by means of phenomenological or physically-based parameters, whose accuracy has to be verified through costly and time-consuming experimental techniques. In addition, results obtained for a unidirectional ply could not be extrapolated to materials with different fibre volume fraction or constituent properties. Finally, the failure of unidirectional plies also depends on the energy dissipated by each damage mode, which has to be measured by means of complex mechanical tests or estimated by comparison with experiments [12, 13].

1.4 Thesis motivation

FRPs are now widely used in applications that require good mechanical properties as well as weight savings. However, their low fracture toughness translates into brittle behaviour that often leads to catastrophic failure without prior damage symptoms. Moreover, there is a lack of reliable tools for the design of FRP with mitigated brittleness because of the complexity of the failure micromechanisms involved (due to strong anisotropy and heterogeneity) and the difficulties of experimental validation. These two factors constitute a serious drawback that limits the application of FRP to a wider engineering space.

Computational micromechanics and Finite Elements (FE) analysis provide a novel approach to understanding material deformation and fracture mechanisms. It has demonstrated high accuracy in prediction of mechanical behavior, including fracture mechanisms, in the case of unidirectional fiber-reinforced

composites under complex multiaxial loading cases [14–16].

1.5 Objectives of this thesis

Recent advances in computational micromechanics have demonstrated that numerical simulations of the composite microstructure can be used to obtain the mechanical behavior of a composite lamina while knowing the mechanical properties of its constituents. This could be the first step in the development of a new multiscale modeling strategy for predicting the strength of composite structures.

The main goal of this research is to develop computational micromechanical models that can predict the tensile behavior of unidirectional FRP composites. These numerical models should be consistent with the main deformation and failure processes that occur at the microscale. However, in order to develop high-fidelity computational models, a deep understanding of the mechanical properties of the FRPs constituents (including matrix, fiber, and interfaces) as well as the failure mechanisms developed in the microstructure is required.

To successfully achieve the main objective, the following specific objectives have been derived and addressed in this thesis:

A) Development of computational micromechanical models to predict the tensile behavior of unidirectional FRP composites.

B) Study the deformation micromechanisms and stress redistribution in the vicinity of the first fibre break in unidirectional composites subjected to longitudinal tensile loads by means of high-fidelity computational micromechanics supported by experimentally characterised material constituents. Transient dynamic analyses were adopted to take into account the progressive failure and recoiling of a breaking fibre.

C) Investigation of effects of embedding dry fibers in a matrix has on the stress intensity factor and ultimate strength.

D) Evaluation of the in-situ effect of dry carbon fibre embbeded into a epoxy matrix.

1.6 Structure of the thesis

This thesis is divided into chapters that address various topics related to the overall goal of understanding the tensile failure of unidirectional FRP composites. Each of these chapters focuses on a different topic, each with its own set of challenges. As a result, each chapter begins with a description of the current state of the art for that particular topic. The introductory sections, already mentioned in this chapter, are followed by:

Chapter 2 discusses the state of the art in the tensile failure of UD composite materials. Various topics are covered, such as size effects in composite materials, critical cluster size, and matrix effects in tensile failure. The various statistical distributions to characterize the tensile strength of the fibers, which is important in the formation of the cluster of broken fibers prior to failure, are also presented. Furthermore, this chapter addresses the topic of modeling the tensile failure of UD composites, where different models with different backgrounds are presented and analysed in order to better understand the controlling factors in the tensile failure of UD composites.

Chapter 3 presents a computational micromechanics framework in order to predict the failure and longitudinal behavior of a unidirectional AS4/8552 composite. This chapter discusses in detail the constitutive principles used to simulate fiber, matrix, and interfaces, as well as the RVE generation procedure and boundary conditions. Ultimately, the failure processes in the fibers, matrix, and interface are analyzed, and the results are compared to experimental observations from the literature.

Chapter 4 presents a comprehensive study of the deformation micromechanisms and stress redistribution in the vicinity of the first fibre break in unidirectional composites subjected to longitudinal tensile loads by means of high-fidelity computational micromechanics supported by experimentally characterised material constituents. Transient dynamic analyses is adopted to take into account the progressive failure and recoiling of a breaking fibre. Periodic microstructures with statistically representative random fibre packings are analysed. The relevance of several phenomena on the SCF, such as curing residual stresses, fibre–matrix debonding, matrix inelastic deformation, and their effects are investigated.

Chapter 5 presents a micromechanical finite element model to analyse the stress intensity factor of a single fibre with a straight-fronted edge crack. The fibre is considered elastic and either isotropic or orthotropic, and free or embedded in an elastic material of different stiffness. The study is performed using non-dimensional variables for the fibre/matrix stiffness ratio and fibre longitudinal/transverse stiffness ratio. The J-integral is used to evaluate the stress intensity factor. The finite element model results are then used as input to calculate the Weibull parameters and the rate of change in the ultimate strength of the embedded fibres compared to the dry fibers. Finally, a semi-analytical progressive failure analysis is performed to show how these changes affect the tensile failure and damage development of a unidirectional carbon composite material.

Chapter 6 extends the findings of Chapter 5 by focusing on the impact of mechanisms such as matrix plasticity and interface debonding on the stress intensity factor of carbon fibre. This capter presents a computational micromechanics analysis of the stress intensity factor of a single carbon fibre with a straight-fronted edge crack. The fibre is considered linear-elastic and either free or embedded in an epoxy matrix. Carbon fibre reinforced plastic AS4/8552 was used as the reference material for this study.

Finally, chapter 7 contains the main conclusions of the work carried out during this thesis as well as proposals for future developments.

2

State-of-the art: Current understanding of longitudinal failure in UD composites

Modelling of composite materials is a difficult task due to the complexity of its microstructure and interactions between constituents such as fibre, matrix, and interface. However, in order to optimize their design, models that can predict the behavior of these materials are required. The mechanisms of longitudinal failure of UD composites under longitudinal loadings are well understood. They are controlled by two main factors: i) statistical fiber strength [17], and (ii) after a fibre fractures, the stress is redistributed among the intact fibers in a complicated manner [18].

When a composite is subjected to longitudinal tension, final failure is governed by the failure of unidirectional plies aligned along the loading direction. Such failure usually starts with an individual fiber breaking at its weakest location, leading to the stress redistribution along fiber axis as well as stress enhancement in nearby intact fibers. With the further increase of applied load or load cycles, more fibers break, along with other forms of damage such as fiber/matrix debonding and matrix cracking. At this stage, fibres are no longer able to carry stresses. As the matrix is loaded, it transfer the load back to the broken fibre, making it able to carry stress away from the point of fracture. The stress is redistributed to the remaining intact fibres by the matrix, which leads to stress concentrations in the intact fibres, increasing their probability of failure. At low applied stresses the fibres break appear in random locations and there is nearly no interaction between breaks.

The stress along the fiber depends on the applied external stress, but also on precisely how stress is transferred from a broken fiber to the surrounding intact fibers and in the matrix environment. This stress transfer is governed by the elastic properties of the constituents and by the fiber/matrix interface, and is difficult to obtain in the presence of more than one broken fiber. Afterwards, the stress concentration in the intact fibres will cause the creation of a cluster of broken fibres. These clusters will grow, when other fibres fail and, when a cluster reaches a certain critical size, it will propagate unstably leading to the separation of the entire composite. The tensile failure of a UD composite is, therefore, of statistical nature and function of the mechanics of load redistribution around broken fibres. In this chapter we will review the different models to predict the tensile failure of UD composites.

2.1 Statistical distribution for fibre strength

The strength of a single fibre cannot be represented by a single average value. Due to fibre brittle nature, the tensile strength is governed by surface or volume flaws [15] and exhibits weak-link characteristics. This means they break as soon as the weakest link is overloaded. The probability of failure is thus linked to the presence of weak links. There are several statistical distributions used to characterize the strength of fibres such as Weibull distribution, proposed by the Swedish mathematician Waloddi Weibull in 1951 [19]. Weibull is the most widely used statistical distribution for representing the strength of brittle fibres. Weibull distribution is available in two forms: standard and modified.

2.1.1 Standard Weibull distribution

The standard Weibull probability distribution as:

$$P(\sigma_f) = 1 - \exp\left(-\left(\frac{L}{L_0}\right)\left(\frac{\sigma_f}{\sigma_0}\right)^m\right), \tag{2.1}$$

is the most widely used statistical distribution for representing the strength of brittle fibres. Where P is the cumulative probability of failure of a fibre of length L at a stress level of σ^f, σ_0 is the characteristic Weibull fibre strength, L_0 is the reference gauge length, and m is the shape parameter or Weibull modulus. The shape parameter (m) is also known as the Weibull slope as it is equal to the slope of the line in a probability plot. Different values of the shape parameter (m) can have significant effects on the behavior of the distribution. Very high Weibull modulus leads to a low strength variability and a low Weibull modulus leads to high strength dispersion. Moreover, a longer length L reduces the strength, since the probability of having a weak link is greater.

This distribution is highly dependent on the statistical parameters and usually leads to the overestimation of the fibre strength at short gauge lengths L [20–27]. The inconsistency between the standard Weibull distribution and the experimental results for short gauge lengths can be attributed to several reasons including diameter variation between fibres [24, 28], variations of the Weibull distribution from fiber to fiber [24, 26, 27, 29] large-scale fluctuation of the density of defects in fibres [28, 30, 31]. According to Curtin [29], this distribution is not the

most accurate method to describe the strength distribution of fibres, however is still the most used to characterize the tensile strength of technical fibres. Other downside of this distribution is that there is no threshold stress below which the failure probability is zero.

2.1.2 Modified Weibull distributions

As described in the previous section the standard Weibull distribution is not the most accurate method to describe the strength distribution of fibres as it considers just one defect population to model the distribution of the fibres strength. Recent studies, however, have found that the fibres strength is governed by more than one flaw population [23, 32]. To consider more than one flaw population in the fibres, multimodal Weibull distributions were developed [23, 32–34], from which the bimodal Weibull distribution is the most common:

$$P(\sigma_f) = 1 - \exp\left(-\left(\frac{L}{L_0}\right)\left(\frac{\sigma_f}{\sigma_{01}}\right)^{m_1} - \left(\frac{L}{L_0}\right)\left(\frac{\sigma_f}{\sigma_{02}}\right)^{m_2}\right), \tag{2.2}$$

where σ_{01} and σ_{02} are the scale parameters and m_1 and m_2 the Weibull moduli for the both populations of flaws. The second population flaw of this bimodal Weibull distribution characterizes the strength of the fibres with short gauge lengths. This distribution puts an upper limit into the strength at short gauge lengths, and thus may be more realistic compared to the traditional Weibull distribution [35]. The rate at which the strength decreases at short gauge lengths depends on the magnitude of the Weibull modulus m_2 [36]. The main issue with the bimodal distribution is that many different parameters must be determined.

Another modified version of the Weibull distribution function presented in the literature [22, 24, 26] is known as the 'Power Law Accelerated Weibull distribution'. As mentioned before, the traditional Weibull distribution fails to characterise the fibre strength at short gauge lengths. This distribution is an updated version of standard distribution with an extra correction factor (α) which can characterise the fibre strength at short gauge lengths without overestimating the strength:

$$P(\sigma_f) = 1 - \exp\left(-\left(\frac{L}{L_0}\right)^{\alpha}\left(\frac{\sigma_f}{\sigma_0}\right)^{m}\right), \tag{2.3}$$

This equation leads to the traditional Weibull distribution when α equals 1. This distribution has mainly been employed in micromechanical simulations where the gauge length, L, tends to be small. The α parameter, usually lower than 1 (commonly varies between 0.6 and 0.9), allows the strength distribution to be less sensitive to length scaling, therefore, reducing the overestimation usual of the traditional Weibull distribution at very short gauge lengths. The disadvantage of this distribution is its physical background since it is based on pure fitting.

As a result, there are several distribution to characterize the failure probability of fibres, among which the traditional Weibull distribution (Eq. 2.1) is the most used. The determination of the parameters governing for these distributions is not simple, meaning that large set of samples need to be tested in order to obtain representative parameters. The problems in obtaining the statistical parameters for fibre strength makes it hard to get a single distribution to characterise this property and, therefore, many statistical parameters can be found in the literature for the same type of fibre [37].

2.2 Size scaling effects

Size scaling is defined as the change in properties with changing dimensions. Size scaling influences not only the strength of individual fibers, but also the failure process and the longitudinal strength of composite structures [38]. Because the elastic modulus is an average property, it should not change with specimen size. Strength, on the other hand, is typically determined by the weakest location or the largest defect. As a result, increasing size increases the likelihood of a large defect and decreases composite strength. This is especially important for industrial applications, as most strength predictions are based on small coupon tests.

The size scaling effect of composite strength is now well established due to the abundance of experimental evidence [22, 38–40] as well as modelling evidence [41–44]. Mahesh et al. [43] demonstrated that the size effect is strongly influenced by the Weibull modulus of the fibers. Pimenta and Pinho [41] applied their hierarchical scaling law to predict the size scaling of the longitudinal strength of composites with 1 to 1 million fibers. Their model accurately captures the size scaling effects.

There are several factors that contribute to this size effect, with most authors agreeing that fiber strength statistics are essential [38]. The size effect is influenced not only by statistical factors, but also by deterministic factors such as the effects of the damage process zone and the change of failure modes [45]. This means that in order to achieve a good design of composite structures based on coupon testing, it's important to remember that the coupons should be representative of the large-scale component's manufacturing process, and that larger structures have lower strength because critical defects are more likely to occur [38]. Manufacturing contributes to the size effect due to the presence of larger fibre waviness and overall defects in larger components.

2.3 Stress redistribution around a broken fibre

Once the first weak fibre breaks, the stress in the composite needs to be redistributed. The broken fibre locally loses its load transfer capacity and the nearby fibres are subjected to stress concentrations. If a global load sharing rule is considered, then the stress that the fractured fibre carried is transferred equally to all the remaining intact fibres. This type of load sharing rule is able to predict the failure of lubricated tows, where the fibre interaction is low [46], but it's not accurate for composite materials where the fibres are bonded by a matrix, where their is high interaction between fibres.

The interaction between the fibres and the matrix results in a non uniform stress redistribution to the intact fibres, which is highly dependent on the composite geometry [42]. The models that consider a non uniform stress redistribution are known as local load sharing rule. The stress redistribution in composite materials is a complex process that depends on several parameters, including the fibre/matrix interface, the fibre to matrix moduli ratio, the matrix yield stress, and the distribution and distance of fibers from each other [47]. This stress redistribution is often characterised by two parameters: the stress concentration factor (SCF) and the ineffective length. The stress concentration factor is defined as the longitudinal stress in an intact fibre due to fibre breaks divided by its nominal value in the absence of fibre breaks. The SCF can be expressed as an absolute value or as the percentage by which it exceeds unity.

After a fibre breaks it locally looses the ability to carry stress, even so, away from the failure plane it is still able to carry loads, which means that a fibre does

not fully loose the ability to carry stress after it breaks. The ineffective length is a measure of this stress recovery length of the broken fibre. Typically, this length refers to the length over which the longitudinal fibre stress is below 90% of its nominal value [48]. These parameters are crucial in modelling composite materials as they will affect the stress redistribution and, therefore, the damage accumulation and the formation of clusters of broken fibres.

The type of fibre packing affects the stress redistribution around fibre breaks. There are several types of fibre packings based on two important features: dimensionality and regularity (Figure 2.1).

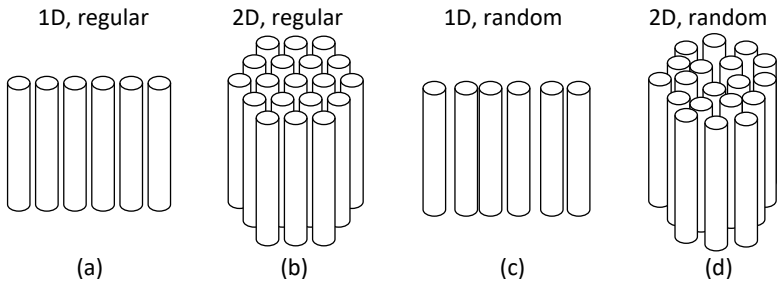

Figure 2.1: Schematic illustration of fibre packings: (a) 1D regular packing, (b) 2D regular packing (c) 1D random packing and 2D random packing [36].

A 1D packing consists of a single row of fibres that can be equally or randomly spaced and hence greatly simplifies the analysis. However, 1D packing fails to give an accurate representation of the composite behaviour and leads to an overestimation of the stress concentration factors [49, 50]. 2D packings are, however, a more realistic representation of micro-structure of composite materials. Batdorf and Ghaffarian [51] noticed a significant discrepancy between experimental and modelling results of strength of unidirectional composites. They hypothesised that variations in fibre spacing are the major cause for this discrepancy. Most models use regular packings and hence have deterministic fibre spacings. Incorporation of statistical variations in fibre spacing reduced the discrepancy between experiments and models. A 2D packing with random distribution of fibres is the model that most accurately represents the microstructure of a composite material, as it better relates with the real distribution of fibres in these materials [52].

Random distribution of fibers instead of regular packing changes the distance between the fibers and thus changes the stress distribution. Obtaining this random distributions is more difficult and computationally expensive than regular ones. Another problem of using random fibre packings especially in FE analysis, is that the variations of fibre spacing lead to some problems with the meshing. Nonetheless, the use of a random distribution is essential to have accurate results, as it translates into more realistic microstructures and behaviour of fibrous composites.

2.4 Critical cluster size

A UD composite fails under tensile loads due to the unstable propagation of a cluster of broken fibres. As a result, a proper understanding of cluster formation is required to model the failure mechanism of UD composites. The clusters form as a result of stress concentrations in intact fibres that are adjacent to a broken one. This increase in SCF causes stress to build up in intact fibres, increasing their likelihood of failure and making it more likely that fibres will fail in clusters. When one of those clusters reaches the critical cluster size, it propagates in an unstable manner, resulting in composite failure.

Ibnabdeljalil and Curtin [53] investigated the critical cluster size, assuming that composites have regions that are intrinsically weaker than others. They developed equations to predict the likelihood of such weaker regions and the critical cluster size (n^{crit}):

$$n^{crit} = 403\, m^{-1.28} \tag{2.4}$$

where m stands for the Weibull modulus. For example, the equation predicts critical clusters of 51 to 28 fibres for typical carbon fibres (m in the range of 5 to 8) [54]. The presence of a few strong fibers near a group of weak fibers can significantly slow down the progression of the cluster's propagation. This distribution of strong and weak fibers is statistical in nature. As a result, Ibnabdeljalil and Curtin [53] concluded that significant differences in critical cluster size can be expected from sample to sample.

Furthermore, several authors have observed that the critical cluster is not constrained within a single plane, but rather spans several layers within the inef-

fective length [55–57]. Therefore, the ability to detect the critical cluster size experimentally is required for the validation of composite UD strength models. Unfortunately, such attempts are doomed to fail because the critical cluster leads to immediate failure. Observing clusters immediately before failure is challenging since the strength of a composite sample is unknown prior to testing.

Scott et al. [58] discovered a 14-plet cluster size in T700/epoxy composites using synchrotron computed tomography. This was discovered at 94% of the final failure strain, implying that the critical cluster size is most likely larger. Similar research has been conducted by other authors. As an example, Aroush et al. [59] discovered critical cluster sizes ranging from 9 to 33 for quartz fiber/epoxy composites with only 125 fibers. However, Aroush et al. did not specify how close these clusters were to final failure.

Despite massive interest, there is a scarcity of experimental data on the critical cluster size. Accurately modeling the critical cluster size is also difficult because it requires an accurate prediction of the SCFs around multiple fibre breaks.

2.5 Effects of matrix and interface properties

The tensile failure of composite materials is a fibre dominated phenomena, however, the stress recovery in the broken fibre is attributed to shear stress transfer in the matrix. Most analytical models such as shear lag models typically neglect the axial stresses carried by the matrix. Xia et al. [60] proved that this negligence causes a discrepancies between analytical and FE results, especially for the models with low fibre volume fractions. This decrease could not be addressed by shear lag models that waives the matrix effect. As a result, these models were developed by adding the matrix to carry axial stresses and revealed that SCFs decrease if the matrix stiffness increases [47, 61, 62]. In fact, the SCF decreases with increased ratio of matrix to fibre modulus and decreased fibre volume fraction.

Another simplification of analytical models is that they consider the fibres and matrix to be perfectly bonded, which leads to a infinite stress concentration factor in the matrix around a fibre break for elastic materials. The matrix and the interface is unable to support such a high stress. In this case three scenarios or combinations of them can occur: (1) the matrix yields [49, 63], (2) the interface

debonds [47, 64], and (3) the matrix cracks in the break plane [65, 66].

Swolfs et al. [67] studied the impact of matrix cracks on both the SCF and the ineffective length. They used a model with a random distribution of fibres and concluded that the matrix cracking increases the ineffective length, drastically changing the stress recovery profile. It was observed in the absence of crack in the matrix, stress in the broken fibre increases rapidly, however, in the model with a crack, the stress increases slowly. Swolfs et al. [67] study further showed that matrix cracks not only increase the ineffective length, but also increase the stress concentration factor, which leads to a higher failure probability of the intact fibres.

2.6 Thermal residual stress

Thermal residual stresses are inherent to FRP composites due to the heterogeneity of the thermo-mechanical properties of fibre and matrix. These stresses generate during cooling process from the processing temperature to the test temperature. Residual stresses will be present in laminates constructed from layers with different orientations on both the micro- and macro-scales. It is widely recognised that these stresses can not be neglected because they may be high enough to initiate delaminations and microcracking inside the matrix even before loading [68–72].

Thermal residual stresses are able to initiate transverse microcracks in composite laminates. If the thermal residual stress in the matrix exceeds the yield strength of the resin and/or the fiber–matrix bond strength, matrix cracking or fiber–matrix shearing will occur. Generally, the polymer matrix is very weak and consequently after cooling from the curing condition to the room temperature, a solid composite with several microcracks is formed. Low bond strengths at the fiber/matrix interfaces lead to crack propagation along the interphase region.

2.7 Tensile failure models of UD composites

This section provides an overview of the most important models presented in the literature that are able to predict the tensile failure of UD composite materials. According to Mishnaevsky and Brondsted [73], the modeling approaches can be classified into four categories: i) analytical models, ii) fibre bundle models, iii)

fracture mechanics models, and iv) continuum damage mechanics models.

Composite materials can be studied at three levels: micromechanical, mesomechanical and macromechanical. At the micromechanical level, the fibre and matrix are represented separately so that their interaction can be investigated. However, at the mesomechanical level, the fibres and matrix are considered as a unique material with homogeneous mechanical properties at the layer level. This allows the interaction between layers, but not between fibres and matrix, to be captured. Finally, at the macromechanical level, the full laminate thickness is homogenized. Since the failure of composite materials is a micromechanical problem, the focus here is on the different micromechanical models published in the literature.

2.7.1 Analytical fibre bundle models

Fibre Bundle Models (FBM) take into account a bundle of of parallel fibres loaded under uniaxial tension and stochastic strength [74]. When one of the fibers fails, the load is redistributed to the remaining intact fibres. The procedure is repeated until the final criterion is met. The main difference between the models is how the load of a broken fibre is redistributed among the intact fibers. In some models, this is calculated using known data from a finite element simulation run a priori, while in other models it is calculated either with an analytical equation, or inherently from the equilibrium equations of the model. These models can be divided into two types based on the stress distribution rule: global load sharing (GLS) and local load sharing (LLS).

2.7.1.1 Global load sharing model

In a global load sharing model, once a fiber is broken, the load is redistributed among all the fibers placed on the fracture plane in an homogeneous way, neglecting local effects arising around the broken fiber. In other words, the fracture of a fiber is independent of where previous fractures have taken place. Under these conditions, the composite failure process can be understood by studying the failure of a single fiber embedded in the matrix under a uniform remote stress. First GLS model was developed by Daniels [75] by considering an RVE consisting of N parallel fibres (uniformly distributed) with length L, in the absence of matrix. He assumed that the strength of the fibres follows

a Weibull distribution (Equation 2.1), while the tensile strength of a bundle with infinite fibres may be represented by a normal distribution. Daniels [84] determined the stress in the bundle (σ^{∞}) using the following equation:

$$\sigma^{\infty} = E_f \varepsilon^{\infty} \cdot S(\sigma_f), \tag{2.5}$$

where E_f is the fibre longitudinal modulus, ε^{∞} is the applied strain, σ_f is the stress in the intact fibres and $S(\sigma_f)$ represents survival probability under the stress σ_f of a fibre with length L. He concluded that the tensile strength of a bundle with a large number of fibres can be represented by a normal distribution, while the strength of the fibres follows a Weibull distribution, and the strength of the bundle can be obtained by:

$$X_b = \frac{\sigma_0 \left(\frac{L}{L_0}\right)^{-\frac{1}{m}}}{m^{\frac{1}{m}} e^{\frac{1}{m}}}, \tag{2.6}$$

σ_0, L_0 and m are the characteristic parameters of the Weibull distribution. Daniels model was not accurate due to several shortcomings. Firstly, the contribution of the matrix to the load carrying capacity has been neglected, which is not realistic. Secondly, the model is based on the regular distribution of fibres. In real composite, however, the fibers are randomly distributed. Thirdly, it cannot deal with hybrid composites nor predict the failure curve of composite materials. Finally, as this model was developed for dry bundles it considers that a broken fibre is no longer able to carry load, which is not accurate in the presence of a matrix.

Rosen [48] improved Daniels model further by considering the influence of the matrix through a shear-lag model. Rosen stated that the the breakage of a single fiber in a group of N fibres, is enough to trigger the failure of the composite. According to Rosen's model, the composite longitudinal strength X_T can be predicted as:

$$X_T = V_f \sigma_0 \left[\frac{L_0}{NL}\right]^{\frac{1}{m}} + \sigma_t^m (1 - V_f), \tag{2.7}$$

where σ_t^m is the matrix tensile strengths and V_f is the fibre volume fraction. Rosen model considers that when a fibre breaks, the stress is transferred back to

the broken fibre, by the matrix that is loaded in shear. This means that there is a stress recovery in the axial direction of the broken fibre. This stress recovery length is defined as the ineffective length (L_{inef}) which is equal to the distance from the break to where the fibre recovers a percentage (e.g. 90%) of the applied stress. The following expression was formulated by Rosen to calculate the ineffective length:

$$L_{inef} = \frac{d_f}{2}\sqrt{\frac{1-\sqrt{V_f}E_f}{\sqrt{V_f}G_m}}\ln\left[\frac{1}{1-\zeta}\right], \tag{2.8}$$

where E_f is the fibre Young's modulus, d_f is the fibre diameter, G_m is the shear modulus of the matrix and ζ is the percentage of recovered stress.

Rosen model was based on a bundle of parallel fibres with length L divided into a chain of bundles with lengths L/L_{inef} and assumed that the longer bundle will fail as soon as one of the sub-bundles fails, according to the weakest link theory. Rosen reached a similar solution to that obtained by Daniels except that it accounted for the ineffective length. According to Rosen model, the failure strength of the bundle with length L is given by:

$$X_T = \frac{\sigma_0\left(\frac{L_{inef}}{L_0}\right)^{-\frac{1}{m}}}{m^{\frac{1}{m}}e^{\frac{1}{m}}}, \tag{2.9}$$

This means that while Daniels model considers the full length of the bundle (L), Rosen's model considers only the ineffective length (L_{inef}). Although Rosen model is more realistic and accurate than that of Daniels, it is still not enough to accurately capture the strength due to the inability to capture size effects.

Curtin [76] developed a model based on chain of bundles with a global redistribution of stress. The matrix was hypothesised to break into short slabs relative to the fibre fragments lengths. The load of a broken fibre was then transferred by frictional shear coupling through these matrix slabs into all the surviving fibres. Curtin's model states that the broken fibres recover stress linearly along a distance called the transference length δ, according to the shear lag model with a constant shear stress τ. This shear stress can be considered in different ways such as the matrix shear yield stress, the interfacial shear strength, or a debonded frictional shear stress. Figure 2.2 shows where the fiber is broken, the

stress increases linearly from zero up to the uniform remote stress value at δ. The transference length δ has the same meaning as ineffective length and can be calculated by:

$$\delta = \frac{\sigma_f R_f}{2\tau}, \tag{2.10}$$

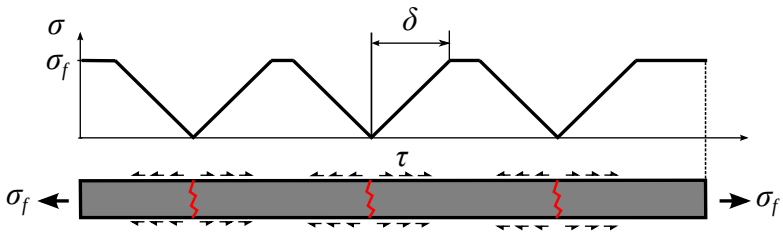

Figure 2.2: Demonstration of stress distribution in a broken fiber.

where R_f and σ_f are the fiber radius and fibre stress, respectively. The average stress in the broken fiber ($\bar{\sigma}_f$) can be approximated as:

$$\bar{\sigma}_f = \sigma_f \left[1 - \frac{1}{2}\left(\frac{\sigma_f}{\sigma_c}\right)^{\frac{1}{m+1}}\right], \tag{2.11}$$

where the parameter σ_c is the reference strength:

$$\sigma_c = \left[\frac{\sigma_0^m \tau L_0}{R_f}\right]^{\frac{1}{m+1}}, \tag{2.12}$$

Considering the overall force equilibrium of the composite material, the fibre volume fraction and adding the matrix contribution, the composite longitudinal strength X_T can be predicted as:

$$X_T = V_f \sigma_c \left[\frac{2}{m+2}\right]^{\frac{1}{m+1}} \left[\frac{m+1}{m+2}\right] + \sigma_t^m (1 - V_f), \tag{2.13}$$

Curtin's model is more accurate compared to Rosen's model as it accounts for the stress of the broken fibres in the tensile strength and considers an ineffective length that is not constant but scales with the applied stress, allowing the strength and the entire stress-strain curve of a composite to be estimated. It provides a simple solution to the fiber fragmentation problem corresponding to a GLS

model and has been successfully applied to predict the longitudinal fracture of ceramic matrix composites. However, Curtin's model represents an upper limit when it is applied to FRPs, where damage is often localized in a narrower band.

The models presented in this section are based on the global load sharing rule, which is considered to be unaccurate and therefore limits the application of these models. The main issue of GLS models is that they can not capture the formation of clusters. Furthermore, the majority of GLS models do not consider a finite number of fibres, nor the size effects. These drawbacks limits the GLS models to composites with a very low interaction of fibre breaks. The advantage of these models is that they require low computing power which makes them suitable for huge models or for performing multiple parametric analysis.

2.7.1.2 Local load sharing models

In order to improve the longitudinal strength prediction in FRPs, a new type of methods based on the local load sharing (LLS) model, have been developed. These models incorporates the influence of a fiber breakage into the failure probability of the adjacent ones. LLS is used in different approaches including shear-lag models, FE analysis, variational mechanics and fracture mechanics.

The non-uniform redistribution of stress was addressed first by Hedgpeth [77] in 1961. He calculated the stress concentration factor in the neighbouring fibres as a function of the number of broken fibres, using a shear lag model and uniformly distributed parallel fibres. Later, this model was extended by Hedgepeth and Dyke [49] for a 2D arrangement of fibres.

Harlow and Phoenix [78, 79] developed a fibre bundle model based on local load sharing. This model considers a bundle consisting of N fibres, with a length L, in which the fibres strength is characterized by the Weibull distribution. They calculated the stress concentration factor (SCF) due to a cluster of n broken fibres as:

$$\mathrm{SCF}_n = 1 + \frac{n}{2}, \tag{2.14}$$

Then, the probability of bundle failure was obtained by considering all the different sequences of fibre breaks leading to the failure. This model achieved the following important results:

- As the number of fibers increases, the size effects decrease.
- At high loads, the bundle failure probability follows the weakest link theory, leading to a Weibull distribution with a shape parameter similar to that of fibre distribution. On the contrary at low loads, the probability of failure follows a Weibull distribution with a higher shape parameter than the fibre distribution, resulting in less dispersion of the bundle strength.
- As the bundle size increases, the asymptotic behaviours mentioned begin to govern the strength distribution.
- By increasing the bundle size, the asymptotic behaviours begin to control the strength distributions.
- The strength distribution for large bundles conforms the Weibull distribution, within an appropriate probability range.
- The equivalent single-fibre strength distribution can be determined through the weakest link theory based on the strength distribution of a large number of fibres.

Harlow and Phoenix fibre bundle model is one of the most leading LLS models. The results obtained from this model are extremely accurate and are supported by many recently developed models.

Later, other LLS models were developed using different stress redistribution methods than Harlow and Phoenix model. For example, Curtin and Ibnabdeljalil [53] developed a different LLS model that considers the stress redistribution based on Green's function. Curtin and Ibnabdeljalil used a 3D lattice Green's function model to calculate the stress field, damage evolution, and failure in composites under LLS conditions in which the stress from broken fibres is transferred predominantly to the nearby unbroken fibres.

2.8 Modeling Strategies based on Continuum Micromechanics

Continuum mechanics or mechanics of continuous media provides an appropriate mathematical framework for continuous and homogeneous materials, where

the fields vary smoothly over the vicinity of a given material point. Downward movement in the hierarchical structure of FRPs, it can be realized how considering the fiber and polymer matrix as the building blocks of the composite seems to be the first step along the multiscale bottom-up approach. These micro-constituents, including the fiber, the polymer matrix, and the interfaces between them represent the smallest FRPs entities described by continuum mechanics.

To study the micromechanical behaviour of a composite, a Representative Volume Element (RVE) must first be defined. The RVE (also called as the unit cell) represents the minimum material volume that is statistically representative of the overall volume. Apparently, for computational efficiency, one will be naturally interested in the minimum size of the RVE. Any volume of the material of a size smaller than that will no longer be representative. The minimum size of RVE may vary from material to material, from discipline to discipline, and sometimes from one effective property of interest to another.

Once this RVE size has been defined, the effective or macroscopical response of the composite can be obtained from the mechanical properties of the individual micro-constituents. This computational homogenization process of the thermo-mechanical properties of the composite together with the development of new constitutive equations to study the damage onset and propagation are the main topics covered by micromechanics of FRPs.

Several micromechanical methods have been developed during the last years to accomplish such a complex task. According to Bohm [80], micromechanical methods can be classified into two main categories including analytical and computational homogenization. Several criteria must be taken into account when choosing a solution method such as: arrangement and periodicity of the microstructure, computational cost, desired information on the local fields, accuracy of the predictions, etc. A brief discussion of the various micromechanical models is presented in this section.

2.8.1 Analytical micromechanics

2.8.1.1 Mean-field approaches

Semi-analytical mean-field homogenization schemes are an efficient way to predict the behavior of heterogeneous materials. These methods are based on some assumptions for the interaction between constituents and consider that the stress and strain fields for each constituent of the composite material can be represented by means of their corresponding volumetric averages. In fact, mean-field approaches approximate the microfields within each constituents by their volume phase averages i.e., uniform strain and stress fields on each phase are used. The main geometrical characteristics of each phase, given by the volume fraction of each constituent, phase topology, and aspect ratio of inclusions are considered by using statistical descriptors.

Mean-field homogenization techniques are commonly based on the pioneer work of Eshelby [81], who analyzed the stress distribution in an elastic and isotropic ellipsoidal inclusion embedded in an elastic, isotropic and infinite matrix which is subjected to a remote strain. Eshelby model is valid for ellipsoidal inclusions only and assume a perfect bonding between constituents. In the case of two-phase materials such as FRPs, the fields can be named as $\bar{\sigma}_f$ and $\bar{\varepsilon}_f$ for the fibers and $\bar{\sigma}_m$ and $\bar{\varepsilon}_m$ for the matrix. Equations 2.15 and 2.16, show the expression of the stress and strain fields averages over the volume for each individual phase:

$$\bar{\sigma}_i = \frac{1}{V_i} \int_{Vi} \sigma_i(x)\, dV \tag{2.15}$$

$$\bar{\varepsilon}_i = \frac{1}{V_i} \int_{Vi} \varepsilon_i(x)\, dV \tag{2.16}$$

where V_i is the volume occupied by each phase, V is the total volume $(V_m + V_f)$ and x is the vector which indicates the position of a material point. The subscript i denotes f and m. The average stress $\bar{\sigma}$ and average strain $\bar{\varepsilon}$ fields can be written as:

$$\begin{aligned} \bar{\sigma} &= \xi\, \bar{\sigma}_f + (1-\xi)\, \bar{\sigma}_m \\ \bar{\varepsilon} &= \xi\, \bar{\varepsilon}_f + (1-\xi)\, \bar{\varepsilon}_m \end{aligned} \tag{2.17}$$

where ξ stands for the volume fraction of the fibres and $1-\xi$ for the volume fraction of the matrix. By considering the elastic behavior for both phases, the relation between the average stresses and strains can be described as:

$$\bar{\sigma}_i = \mathbf{L_i}\bar{\varepsilon}_i \tag{2.18}$$

where $\mathbf{L_i}$ is the fourth-order elastic stiffness tensor for each constituent phase i $(= f, m)$. Now, the mean fields of stress and strain of the different phases can be determined with the average stress and strain fields as:

$$\begin{aligned} \bar{\varepsilon}_i &= \mathbf{A_i}\bar{\varepsilon} \\ \bar{\sigma}_i &= \mathbf{B_i}\bar{\sigma} \end{aligned} \tag{2.19}$$

where $\mathbf{A_i}$ and $\mathbf{B_i}$ are fourth order tensors known as mechanical strain and stress concentration tensors (or influence functions) [82] and represent the complete solution of the respective boundary value problems. These concentration tensors should fulfill the following relations:

$$\begin{aligned} \xi\mathbf{A_f} + (1-\xi)\mathbf{A_m} &= \mathbf{I} \\ \xi\mathbf{B_f} + (1-\xi)\mathbf{B_m} &= \mathbf{I} \end{aligned} \tag{2.20}$$

where $\mathbf{I}$ is the fourth-order identity tensor. The effective elasticity and compliance tensors of the composite in the case of a two-phase composite can be obtained from the phases and from the mechanical concentration tensors. By replacing the stress and strain fields of the matrix in Equation 2.18, the effective elasticity ($\mathbf{L}$) and compliance ($\mathbf{M}$) tensors can be obtained as:

$$\begin{aligned} \mathbf{L} &= \mathbf{L}_m + \xi\left[(\mathbf{L}_f - \mathbf{L}_m) : \mathbf{A}_f\right] \\ \mathbf{M} &= \mathbf{M}_m + \xi\left[(\mathbf{M}_f - \mathbf{M}_m) : \mathbf{B}_f\right] \end{aligned} \tag{2.21}$$

In this particular case, only it is necessary to know one concentration tensor for describing the full elastic behavior of the inhomogeneous material within the meanfield methods. $\mathbf{A}$ and $\mathbf{B}$ tensors depend on the volume fraction of the constituents, the shape and spatial distribution of the reinforcement. These methods are also known as estimation methods.

Eshelby [81] determined the stress distribution and the average strain in an

elastic and isotropic ellipsoidal inclusion embedded in an elastic, isotropic and infinite matrix, determining the exact solution for the strain concentration tensor. Eshelby's result show that if an elastic homogeneous ellipsoidal inclusion (i.e., an inclusion is made of the same material as the matrix) in an infinite matrix is subjected to a homogeneous strain, the stress and strain states in the constrained inclusion are uniform and do not depend on the microscopic coordinate x.

Eshelby's model makes good predictions under dilute conditions, where the inclusion volume fraction is below 10%. Further, Eshelby's result is based on the assumption of a homogeneous inclusion. However, for mean field descriptions of dilute matrix-inclusion composites, the interest is focused on the stress and strain fields in inhomogeneous inclusions that are embedded in a matrix. Such cases can be handled on the basis of Eshelby's theory for homogeneous inclusions, by means of the concept of equivalent homogeneous inclusions. To overcome this limitation, several new micromechanical models were developed based on Eshelby's model with different methods for estimating the stress and strain concentration tensors such as:

- **Classical Self-Consistent model** [83] is based on the existence of a sufficient distance among the inhomogeneities embedded in a homogeneous matrix. This self-consistent method approximates the interaction between the different phases by assuming that each inhomogeneity is embedded in an infinite volume of an effective medium, whose properties coincide with the ones of the composite (which are not known in advance). The defect is subjected to the macroscopic strain or macroscopic stress and the boundary problem is computed by solving an implicit nonlinear system of equations for the unknown elastic tensors, which describe the behavior of the effective medium.

- **Mori-Tanaka model** [84, 85] is based on the Eshelby model for a non-interacting dilute defect distribution. In this case, interactions between inhomogeneities are introduced by means of approximating the stress acting on an inhomogeneity by an appropriate average matrix stress. This method maintains the same approach that was developed for dilute inhomogeneities and the interactions among the inclusions are considered through the modification of the stress or strain fields acting on each inhomogeneity.

Mori-Tanaka is one of the most used method in micromechanics when one implements an analytical method, since it is an explicit method that can be implemented into computer programs in a very straight-forward way and provides enough accuracy for the effective properties in some common materials.

- **Generalized Self-Consistent model** or Three-phase model was developed by Christensen and Lo [86] in 1979 and it can be considered as an improved version of the Classical Self-Consistent method. This method, which cannot be considered strictly as a Mean-Field Analysis (as it is not based on the volumetric averages of the strains and stresses in each phase.), was developed to compute the effective properties of a composite material reinforced with spheroidal inclusions or aligned fibers.

  This method is based on an energy approach in which the related elasticity problem is solved. The model leads to a set of differential equations, which describe the behavior of the three-phase material and should be solved in order to obtain the value of the effective properties of the composite. This method provides excellent results for inhomogeneous materials with matrix-inclusion topologies and is a highly appropriated method to compute the material characterization of heterogeneous materials reinforced by spherical or equiaxed particles or aligned continuous fibers.

- **Differential scheme** is based on a succession of infinitesimal steps and was developed by Roscoe [87] and Hashin [88]. In each step, small concentrations of inhomogeneities are added to a composite material and then homogenized. This differential scheme is not widely used in the study of the mechanical behavior of composite materials due to their mathematical complexity compared to other models. Differential scheme, as is the case with the Self-Consistent methods and Mori-Tanaka method, does not consider neither the distribution of the inclusions nor the interaction among them, therefore it provides only accurate results for low values of the volume fraction of the inhomogeneities.

These methods have been highly successful in describing the elastic response of homogeneous/inhomogeneous materials. Their use for modeling nonlinear composites is nowadays a subject of active research [89–92].

2.8.1.2 Variational bounding methods

These methods use variational principles, based on the principle of a minimum potential energy, to obtain upper and lower bounds on the overall elastic and physical properties of inhomogeneous materials. Bounds are important tools for assessing other micromechanical approaches. Furthermore, in many cases one of the bounds provides by itself good estimates for the physical property under consideration.

- **Voigt and Reuss bounds**

  The uniform stress and strain conditions lead to the simplest variational bounding expressions, which are also known as the Hill bounds [93]. Hill bounds comprise the isostrain Voigt (principle of minimum potential energy) lower bound and the isostress Reuss (principle of minimum complementary energy) upper bound. These bounds, which are based on simple expressions, do not contain any information on the microgeometry beyond the phase volume fractions and therefore are too weak for practical purposes.

- **Hashin-Shtrikman bounds**

  Hashin-Shtrikman bounds [94] are based on a variational principle and provide much more information since the bounds are tighter. This variational method narrowed the Hill bounds [93] providing tighter bounds due to the inclusion of additional information in the microstructure. Hashin-Shtrikman bounds can also be employed when modeling materials that do not contain matrix-inclusion topologies, since the method holds for any phase arrangement of the appropriate symmetry and phase volume fraction, because is based on energetic principles.

  In this context, the bounds obtained through this variational principle are the tightest bounds that can be obtained using only the geometrical information provided by the volume fraction and the overall symmetry. When complex phase patterns are to be considered, numerical methods must be used in order to evaluate correctly the stress polarization tensor.

- **Improved Bounds**

  Some improved version of the variational methods have been developed

in recent years. These methods use more complex trial functions and the required optimization, which is necessary to obtain the bounds of the effective properties for a inhomogeneous materials, needs some statistical information on the phase arrangement in the form of n-point correlations. Using a bigger amount of information allows to generate variational bounds that are significantly tighter than Hashin-Shtrikman estimates, although at a significantly larger computational cost.

One of the most important methods is the so-called Three-point bounds for isotropic two-phase materials, which use the reinforcement volume fraction (ξ), as well as statistical information about the distribution of the different phases in the composite material. This information is incorporated to the method by means of some micromechanical parameters admitting closed-form solutions for some particular cases, such as random dispersion of hard spherical particles with isotropic and homogeneous distributions. Among all the three-point bounds available in the literature, it is worthy to mention the work developed by Torquato [95], whose models for two phases materials provide most probably the best analytical solution to calculate the elastic constants of composite materials reinforced with elastic inclusions.

2.8.1.3 Micromechanics fibre bundle models

This model combines superposition rules and fibre bundle models, which are derived from the analytical fibre bundle models (as explained in section 2.7.1), but take into account more precise stress redistribution rules. These models are based on three elements:

- A deterministic model for stress redistribution to the neighbouring fibres after a fibre breaks.
- A super-position rule to account for the effect of multiple fibre breaks in the stress redistribution.
- A Monte-Carlo simulation of the fibre bundle model. These models are not purely analytical due to the complexity of the stress redistribution.

Several models have been developed using this type of analysis, by considering

different stress concentration factors and different super-position techniques [55, 64, 96, 97]. Fukuda and Chou [96] proposed one of the first FBM models for an RVE containing a 1D packing of parallel fibres, that could be used for both non-hybrid and hybrid composites.

Later, Curtin et al. [97] developed a more advanced model. They considered a 3D RVE with a square or hexagonal fibre packing. The fibres are divided into elements of length l, provided that l is much smaller than the ineffective length of the fibers. Then, a stochastic strength is applied to each element according to their length l. Unlike the model of Fukuda and Chou [96], Curtin's model [97] captures the stress recovery of broken fibres. Moreover, since the transverse and longitudinal directions are decoupled, stress redistribution around breaks can be changed without having to reformulate the model. Finally, a more realistic packing of fibres was considered, together with a plastic or debonded matrix.

Behzadi et al. [98] used a finite element model to calculate both the ineffective length and the SCF around multiple broken fibres, considering the matrix yielding. The FE results were then used as input data in an FBM consisting of parallel fibres with length equal to the ineffective length. This is an interesting approach because it allows the accuracy of finite elements to be exploited while still using a simple, high-efficiency model. They found that matrix yielding reduces the SCF in the fibres and the presence of an elasto-plastic matrix surrounding the fibres leads to an increase in the composite failure strain compared to the elastic matrix case.

The most recent FBM was developed by Swolfs [36, 99, 100]. Swolfs model uses FE to determine the stress redistribution profiles around a broken fibre. The FE model consisted of a circular RVE with a broken fibre in the center, with the remaining fibres arranged in a random packing for either a hybrid or a non-hybrid composite. The fibres were divided into elements of length l along the fibre longitudinal direction. The stress concentration factors were studied as a function of distance to the broken fibre. Swolfs model studied the effect of various mechanisms including matrix cracks, volume fraction, fibre/matrix stiffness ratio, isotropic and anisotropic fibres [18, 67]. However, dynamic effects and thermal residual stresses were ignored. He concluded that the stress concentration depends mainly on the distance to the broken fibre and the effect of other parameters is minimal.

The stress concentration profiles obtained from FE were used as input in the FBM. Swolfs considered a bi-modal Weibull fibre strength along with a random fibre packing. The interaction between breaks was taken into account with an enhanced superposition method, which takes into account the interaction between all fibre breaks, as can be seen in Figure 2.3. His model first considers a linear superposition of stress fields due to the broken fibres, which does not guarantee the force equilibrium. In order to implement this, the stress that the broken fibers put on each other must be redistributed. This redistribution is performed proportionally to the original SCF in the linear superposition which leads to a stress redistribution that ensures the balance of force. Although the SCF is calculated taking the number of breaks into account, the ineffective length is not considered. This means that the model neglects the increase of ineffective length with the increase of cluster size.

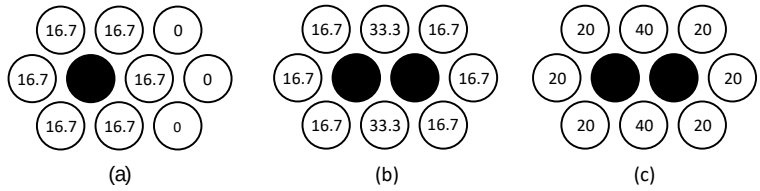

Figure 2.3: Schematics of the stress redistribution used by Swolfs [36]: a) stress concentration around a single broken fibre, b) SCF around two broken fibres is summed up by linear superposition and c) SCF around two broken fibres by enhanced superposition. Black fiber represents broken fiber.

The FE stress redistribution results are then used as inputs to the FBM, based on Rosen's approach [48] as explained in section 2.7.1.1, to predict the material behaviour and failure. This model considers 2000 UD fibres with length of 10 mm, divided into 35 μm segments to which is attributed a strength based on a Weibull distribution. Failure was assumed to occur when, at least, 10% of the fibres in the same axial segment with a length of 35 μm had failed. Swolfs compared the experimental data against the modelling results given by the FBM and observed some discrepancies. For example, the failure strain predicted by the model slightly overpredicted the experimental failure strain. The model only predicted between 20-30% of co-planar clusters, while 70% of the clusters were co-planar in the experiments (a cluster is assumed to be co-planar if the axial distance between fibre breaks is less than 3.5 μm, otherwise it is considered to be diffuse). In addition, the fibre break density was too high compared to the

experiment.

According to Swolfs [36] the discrepancies are due to several reasons such as: 1) lack of dynamic effects, 2) errors in the Weibull distribution, and 3) averaging of the SCFs over the cross section of the fibre. The Swolfs model offers several good features such as simplicity and computationally efficiency, and yet it has good accuracy due to the combination with the finite element model. Nevertheless, it also has its drawbacks. First of all, running the finite element model to obtain the stress fields is time consuming. Secondly, the ineffective length does not grow with the applied strain or the cluster size. Third, the model could not capture the stiffness loss due to broken fibres. Nonetheless, the flexible formulation of the model allows such missing features to be implemented along with other phenomena such as dynamic effects.

2.8.2 Spring element models

Spring Element Models (SEM) consider a lattice of nodes that are longitudinally connected by fibre springs and transversely by matrix springs, as illustrated in Figure 2.4. Thus in the SEMs, unlike FBMs, the matrix is physically represented by shear springs. The fibre springs can only support longitudinal load and their strength is stochastic. Further, the matrix springs are considered to only being able to support shear stress. The movement of the nodes is limited to longitudinal displacement, which means that there is only one degree of freedom.

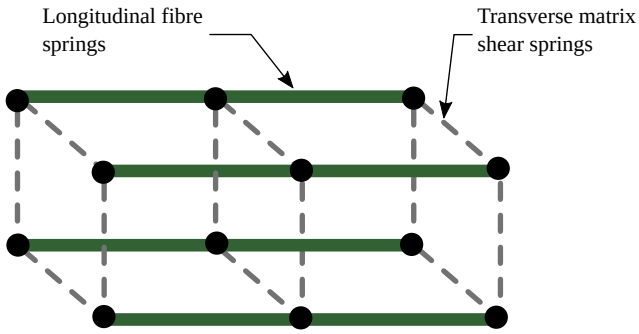

Figure 2.4: Representation of the node lattice of the spring element model showing the fibres (green lines) connected by matrix shear springs (grey dashed lines).

The SEM was first developed by Okabe et al. [101, 102]. The model can be

considered as an evolution of the Green's function model [56], which is similar to the quadratic influence superposition technique and shear lag based models. The Okabe's model considers a hexagonal arrangement of nodes, connected longitudinally by N^f linear elastic fibre spring elements with a stiffness E_f, the random strength X_f and length of l. The stiffness matrix for the fibre elements (K_f) can then be calculated as a function of the area of fiber cross-section (A_f), length (l), stiffness of the fibres (E_f) and nodal connectivities by:

$$K_f = \frac{A_f E_f}{l} \begin{bmatrix} 1 & -1 \\ -1 & 1 \end{bmatrix} \tag{2.22}$$

In the transverse plane the nodes are connected by N^m linear elastic shear matrix springs, which can be arranged into the stiffness matrix (K_m), as function of the matrix properties, including the thickness by:

$$K_m = \frac{G_m \left(A_{m2} - A_{m1}\right)}{\left(d_c - R_f^1 - R_f^2 \ln\left(\frac{A_{m2}}{A_{m1}}\right)\right)} \begin{bmatrix} 1 & -1 \\ -1 & 1 \end{bmatrix} \tag{2.23}$$

where A_{m1} and A_{m2} are the associated matrix area of the two different fibres connected by the transverse spring and d_c is the centre-to-centre distance between the two fibres. These areas can be estimated as a function of the number of fibres connected to the two fibres and their respective fibre radius, R_f^1 and R_f^2. The nodes have only longitudinal displacements which can be arranged in the matrix $\boldsymbol{u}$.

The fibre fails when the applied stress reaches its tensile strength, and recovers stress linearly according to the shear lag models with perfectly plastic matrix. At a given stress state there are N_{fb} broken fibre elements and N_{fSL} fibre elements whose stress is lower than the applied stress due to a nearby break in that fibre. Therefore, the overall equilibrium can be written as:

$$\left[\sum_{N_{f\,int}} \mathbf{K}_f + \sum_{N_m} \mathbf{K}_m\right] .\mathbf{u} + \sum_{N_{fSL}} A_f \int_{x_i}^{x_i+l} \mathbf{B}_f \, \sigma_{SL}\left(x\right) dx = \mathbf{f} \tag{2.24}$$

where $\mathbf{B}_f$ is the deformation matrix of the fibre elements, N_{fint} is the number of intact fibre elements in the model, and $\mathbf{f}$ is the matrix of nodal applied forces. At each increment of applied stress/strain it is checked if any fibre fractures. If

so, a new equilibrium is calculated. This process is repeated until failure of the composite.

The model developed by Okabe is very robust, since it inherently captures the effect that the different material parameters (such as matrix and fibres) have on the stress redistribution around breaks from the equilibrium equations. However, it is limited to regular fibre packings. Compared to experimental results, the model overpredicted the fibre break density and underpredicted the formation of larger clusters as well as the number of co-planar clusters.

Later, Tavares et al. [103, 104] developed one of the most robust and advanced SEM for a random fibre distribution. This model captures the stress fields around broken fibres inherently from the equilibrium equations, and takes into account dynamic effects. In addition, it can capture the entire stress-strain curve and the stiffness loss of a composite material. They found that the maximum SCF is always larger in the dynamic model than in the static one, this increase being dependent on the material. It was observed that if an elastic matrix is considered, the dynamic effects affect the tensile behaviour and final failure of the material. Nonetheless, with a plastic matrix the effect was not significant. Including dynamic effects led to an earlier formation of clusters than with the static model, making the results closer to the experimental ones. The model is computationally more demanding in comparison with other simpler models. For example, solving RVEs with a large number of fibres is not feasible unless a supercomputer is used.

2.9 Computational micromechanics

Extending the analytical models to the non-linear regime, including plasticity, damage and cracks, can be extremely inaccurate due to the impossibility to account for large strain gradients in analytical methods. In addition, including manufacturing conditions, such as thermal residual stresses and porosity, and dealing with anisotropic microstructures will make the problem almost infeasible. Computational Micromechanics (CM) has emerged in recent years as a powerful tool to predict the influence of the constituent properties and complex non-linear behaviors, such as damage and plasticity as well as finite strains on the composites behaviour under different loading conditions. This approach is based on the numerical simulation of the mechanical response of models

where the constituents of the material are explicitly represented. Computational micromechanics strategy considers detailed information of the microstructure and constituent properties, inherited from micromechanical characterization of the fiber, matrix and interface.

In addition, CM can capture the evolution of the stress and strain microfields, and thus, it is possible to track the nucleation and growth of damage during the analysis, which is a key aspect to model the localization of damage and fracture. Finally, CM can deal with complex multiaxial stress states that is very difficult to achieve in laboratory conditions or in analytical models, to obtain the failure spot of the heterogeneous material. For these reasons and thanks to the rapid advance in computational resources, CM models are becoming more and more popular these days.

The computational micromechanics modelling uses two different strategies to simulate the behavior of a discrete microstructure: i) the embedded cell method and ii) the periodic microfield approach. The former is mainly used to model the evolution of the stress and strain field when damage is localized along a well defined region, whereas the latter is devoted to predict the effective response of the heterogeneous material up to the onset of damage propagation. The advantages and disadvantages as well as and the specific ranges of applicability of both methods are outlined along the next subsections.

2.9.1 Embedded cell models

The embedded cell is a method that represents a material or specimen with two different microstructural descriptions [105, 106]. First, the core region where the microstructure is resolved with a high level of detail (including the matrix, fibers and interfaces). This region is embedded in an outer region where the microstructure is roughly resolved or even considered as a homogeneous domain. The outer region is responsible for transmitting the far-field loads, applied on the boundaries, to the core region where the stress and strain fields are resolved at the microstructure level. Therefore, these models are not devoted to predict the effective response of the material but the evolution of the stress-strain fields and damage mechanisms within the fracture process zone. The main advantage of the embedded cell approach is that the periodicity of the microstructure is no longer required, simplifying the pre-processing tasks considerably. The

schematic of an embedded cell for simulation of fracture is plotted in Figure 2.5, where the high stress and strain region (crack region) is modeled in detail while the remaining area is considered to be an homogeneous material.

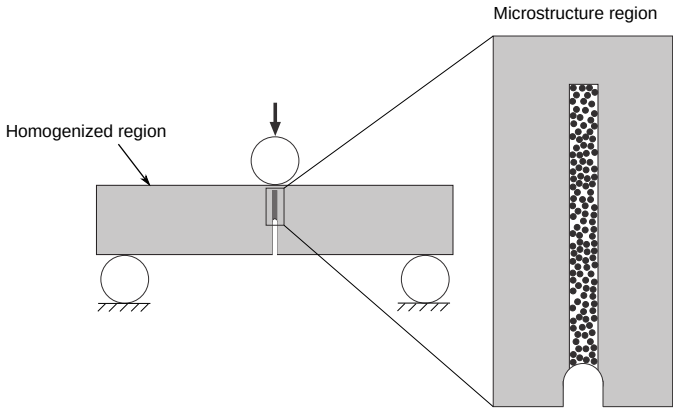

Figure 2.5: Schematic of the embedded cell model to simulate the three-point bend test on a notched beam. The microstructure is considered as the core region with a high level of detail (including the matrix, fibres and interfaces) embedded in the homogeneous material (in gray) whose constitutive equation is provided by a suitable homogenization model.

Bohm [80] classified the embedded cell approaches into three types, based on the consideration of the outer region:

- First type models which both the core and the outer region are represented as an heterogeneous material providing a highly detailed description of the microstructure, but discretized with different element size [107]. This model can easily reproduce a full sample with a refined mesh in some regions of interest, avoiding the usual layer effects generated at the interfaces between the core and the outer region. Nevertheless, this strategy is extremely expensive from a computational point of view, even with a very coarse mesh in the outer region.

- Second type models which the outer region is modeled as an homogeneous material whose properties can be approximated using one of the mean-field methods. These models are specially suited to study the localization and growth of cracks in inhomogeneous materials [105, 108, 109] or the stress concentrations near the crack tips [110] or around local defects

[111]. However, the transition between the core and the outer region is not always smooth. In FRPs, this strategy is normally limited to 2D intraply failure studies, unless very large FE models can be used.

- Finally, models which use an homogeneous outer region with unknown properties and solving the problem in an iterative way, in a similar manner as for the self consistent method. In a first step, trial properties are impose to the outer region, the stress and strain fields are computed in the microstructure of the core. Next, the homogeneous response of the core is used for the constitutive behavior of the outer region. This process is repeated until the convergence is achieved. These models have been mainly employed for material characterization [112, 113]. These models are easily used in the elastic regime, however, extending this approach to the non-linear regime is still problematic. Therefore, the second option is considered as the better balance between predictive capabilities and computational requirements.

2.9.2 Periodic microfield approaches

In these methods, the inhomogeneous material is modelled by an infinite model made by a suitable statistically representative periodic RVE to approximate the mechanical response of an infinite composite lamina. The resulting periodic microfields are evaluated by analyzing the repeating cells of the microstructure describing microgeometries ranging from rather simplistic to highly complex representations of the real microstructure of the composite. Constitutive equations for composite materials in the nonlinear range are frequently obtained using periodic microfield approaches. This approach at the microscale can also be suitable to study the onset and progression of damage within the microstructure [14, 114].

Several strategies based on periodic microfield have been developed to handle the analysis of heterogeneous materials at the microlevel. The pioneer approach was the Method of cells introduced by Aboudi [115]. It enables the computation of microscopic and macroscopic properties of heterogeneous inelastic materials subjected to multiaxial mechanical loadings as well as spatially constant thermal loading. The method divides a repeating unit cell into an arbitrary number of generic cells, which are then divided into 4 or 8 (rectangular or parallelepipedal)

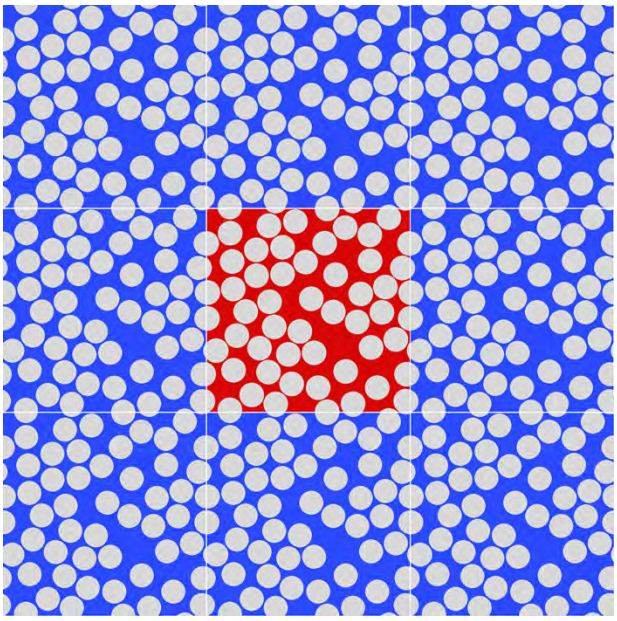

Figure 2.6: The periodic microstructure generated by the repetition of the unit cell, which contains an RVE of 30 fibers, randomly distributed in a square domain.

subcells. Each subcell only contains a homogeneous material, which is different from one cell to each other. The global response of the material is calculated using a classical volume average and assuming that the displacement vector on each subcell varies linearly with the local subcell coordinates.

Some authors have developed improvements of the generalized method of cells in order to apply it to nonlinear problems, transformation field analysis [116] and high-fidelity generalized cell methods [117, 118]. The high-fidelity general method of cells, which employs higher order displacement fields, results in significantly higher computational costs (though still lower than an equivalent finite element simulation). Despite the fact that these analytical approximations use highly idealized microstructures and provide limited information about microscopic fields, they can be used to obtain constitutive models at a low computational cost, which is required for the mechanical analysis of large composite structures. Besides the previous simplistic approximations, the analysis of composites through periodic microfield approaches is usually tackled with more complex and realistic cells which are solved by numerical tools such as the finite differences and the finite elements method.

2.9.3 Concluding remarks

This chapter has presented several models for tensile failure of UD composites. Each model represents a unique balance of computational efficiency and simplicity. It is widely acknowledged that the failure of UD composites is progressive, with the fiber fracturing progressively, forming clusters that grow until a critical size is reached. As a result, the propagation becomes unstable, leading to failure. This process is primarily governed by fiber strength statistics and micromechanical stress redistribution, which has been shown to be affected by a number of parameters.

Most models fail to account for a cluster's increased influence area in comparison to a single broken fiber, as demonstrated by experimental data. The dynamic effects are another aspect that most models overlook. When a fiber fails, the dynamic effects are also present, resulting in dynamic stress concentrations that vary over time. Another important element that most models, especially analytical ones, overlook is interface debonding.

To choose the best approach for this dissertation, we must keep in mind that the chosen method should be able to meet the following criteria:

- Capable of extending a comprehensive understanding of the failure in UD composites.
- Capable of simulating all micromechanical interactions between composite components and capturing all failures.
- The failure development has to be realistic and accurate.

Considering the foregoing criteria, the computational micromechanics was chosen as the primary method of investigation in this thesis.

3

Methodology: Computational micromechanics

FRPs are now widely used in applications that require excellent mechanical properties as well as weight savings. In most cases, their best selling point is their specific longitudinal properties, and quick ways to determine them are an advantage in the composite design process. Despite the numerous analytic models developed to predict longitudinal ply behavior, longitudinal deformation mechanisms such as fiber distribution, polymer plasticity and damage, as well as fiber/matrix debonding and friction, are difficult to simulate.

To investigate this problem, micromechanical models that can account for damage mechanisms in the longitudinal failure of composite materials must be developed. These models must accurately represent the behavior of each constituent of the composite, including fibre, matrix, and fibre/matrix interface. As the fibers and matrix have different characteristics and behaviors, two damage models must be implemented to illustrate both fiber breakage and matrix damage. To connect these constituents, the interface must be also defined, as the interfacial separation is an important failure mechanism.

The goal of this chapter is to develop a reliable and accurate computational approach to predict the longitudinal failure in UD composites based on the analysis of a statistically representative volume element of the material.

3.1 Constitutive models of fiber, matrix and interface

Computational micromechanics models represent explicitly the constituents of composite materials. Capturing the deformation and damage mechanisms is difficult and requires proper models. To this end, specific constitutive equations are used and implemented to model the behavior of each constituent, such as fibers, matrix, and fiber/matrix interfaces. In this section, all these models are explained in detail.

3.1.1 Carbon fiber

Carbon fibers, with a measured average diameter $D = 7.09\mu m$, were modeled as linear elastic and transversely isotropic solids. The elastic modulus of AS4 carbon fibers in the longitudinal direction was measured experimentally through single fiber tensile tests by Herraez et al. [119]. A transverse cracking model

was used to obtain properties in the transverse direction by Naya et al. [120]. The thermoelastic properties of AS4 carbon fibers used in the computational models are reported in Table 3.1.

Table 3.1: Mechanical properties of AS4 carbon fiber [119–121]

E_1 [GPa]	E_2 [GPa]	ν_{12} [-]	ν_{23} [-]	G_{12} [GPa]	G_{23} [GPa]	α_1 [10^{-6}°C^{-1}]	α_2 [10^{-6}°C^{-1}]
231	13	0.3	0.46	11.3	4.45	-0.9	7.2

3.1.2 Epoxy matrix

Epoxy polymers are strain rate sensitivity solids. Although, as a first approximation, strain rate effects are usually neglected when dealing with quasi-static applications, modeling the behavior of polymers in the quasi-static regime is still a complex task. The yield behavior of polymers depends on temperature and strain rate. However, the conventional yield criteria can accurately describe the plastic behavior of polymers by controlling the test conditions. Following this strategy, many studies of the yield behavior of epoxies have bypassed the question of strain rate and temperature and sought to establish a yield criterion [122, 123].

Under tensile loading, epoxy resins usually fail in a brittle manner at very low strain prior to any yielding, whereas, under compression, they exhibit yielding and large plastic deformation, even at relatively low temperatures [124]. The yield stress in these materials is often defined as the point of maximum load, at which the subsequent deformation occurs without further increase in stress [125]. In addition, the yield behavior of polymers is pressure-sensitive, which means that the yield stress decreases with hydrostatic tension and increases with hydrostatic compression. In view of this, capturing the evolution of the yield stress requires a proper yield criterion such as the Mohr-Coulomb [126] or the Drucker-Prager [127]. Originally developed to establish the yield behavior of soils and rocks, these pressure-dependent yield criteria have been adopted in the literature [109, 114, 124, 128, 129]. These plasticity criteria are summarized along the next paragraphs.

Mohr-Coulomb yield criterion

The Mohr-Coulomb failure criterion relates the shear stress required to produce material yielding (τ_t) to the applied normal stress (σ_n) by means of a linear relationship that can be mathematically expressed as:

$$\tau_t = c - \sigma_n \tan\phi \tag{3.1}$$

where c and ϕ stand for the cohesion and the friction angle, respectively, two materials parameters which control the plastic behavior of the material. The friction angle ϕ accounts for the influence of the normal stress σ_n in the evolution of the yield surface. The material cohesion c corresponds to the intersection of the failure envelope with the τ axis. The model is based on Coulomb's friction hypothesis and relies on Mohr's theory to determine the combination of shear and normal stresses producing the material failure. The yield surface of the Mohr-Coulomb model can be rewritten in terms of principal stresses (σ_1, σ_2 and σ_3) as:

$$\sigma_1 - \sigma_3 = 2c\cos\phi - (\sigma_1 + \sigma_3)\sin\phi \tag{3.2}$$

The value of c and ϕ parameters for an epoxy can be approximated from the tensile (σ_{yt}) or compression strength (σ_{yc}), and the orientation of the shear bands, θ, in uniaxial tensile or compression tests by:

$$\begin{aligned} \sigma_{yt} &= 2c\frac{\cos\phi}{1+\sin\phi} \\ \sigma_{yc} &= 2c\frac{\cos\phi}{1-\sin\phi} \end{aligned} \tag{3.3}$$

Under uniaxial compression, the shear band inclination plane of a solid, which follows the Mohr-Coulomb criterion, forms an angle θ, respect to plane perpendicular to the loading axis, that can be related to ϕ based on $\theta = \pi/4 + \phi/2$ (Figure 3.1).

It should be noticed that when $\phi = 0$ the Mohr-Coulomb model reduces to the pressure-independent Tresca model while $\phi = \pi/2$ leads to the tension cut-off Rankine model.

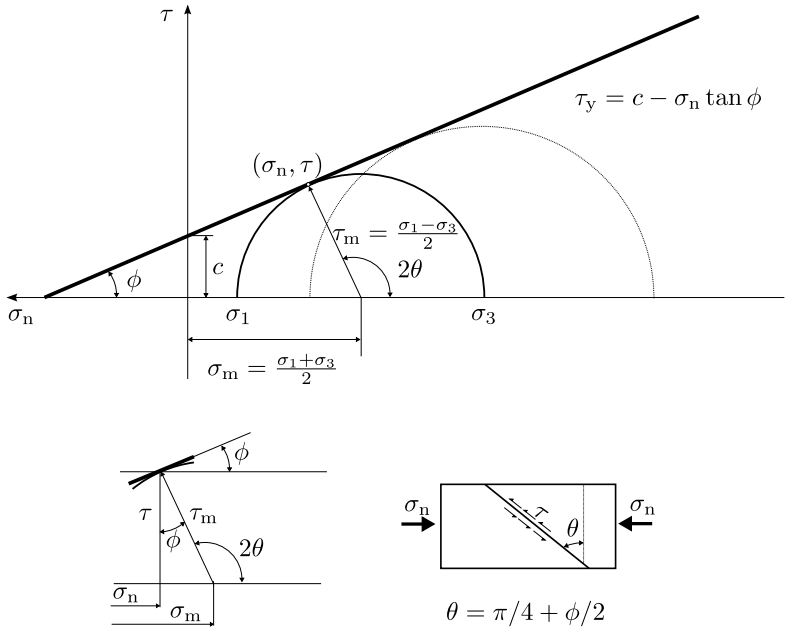

Figure 3.1: Schematic of the Mohr-Coulomb failure criterion: shear band created by a uniaxial compression stress and Mohr's circle.

Drucker-Prager yield criterion

The Mohr-Coulomb criterion has been widely used to model the behavior of soils, sands and, more recently, polymers. However, it has several downside. First, it does not depend on the intermediate principal stress, which can underestimate the strength of the material in many cases [130]. Second, the yield surface shows sharp corners, as shown in Figure 3.2, which leads to numerical issues related to the evolution of the plastic flow. A common way to avoid such inconvenient consists of smoothing the yield surface, changing the evolution of the plastic flow in both the meridian and the deviatoric planes. Among the different failure criteria devoted to this end, perhaps the Drucker-Prager stands out due to its relative simplicity and ease matching the Mohr-Coulomb behavior.

Drucker-Prager yield criterion was initially proposed by Drucker and Prager in 1952, to deal with the plastic deformation of soils [127]. However, this yield criterion and its subsequent modifications have been extensively applied to other pressure-dependent materials such as rocks [131], concrete [132] or polymers [133]. This failure criterion is very often formulated in terms of shear and normal pressure as it was done for the Mohr-Coulomb. However, despite its close relation to the Mohr-Coulomb, the Drucker-Prager yield criterion can be seen as an evolution of the popular von Mises criterion, including the effect of the hydrostatic pressure in the plastic evolution. The linear Drucker-Prager yield function can be expressed as:

$$f\left(J_1, J_2', \alpha\right) = \sqrt{\frac{3}{2}J_2'} + \alpha J_1 - d = 0 \tag{3.4}$$

where J_1 is the first invariant of the stress tensor, J_2' is the second invariant of the deviatoric stress tensor, d is the yield stress of the material under pure shear loading, and α is the pressure sensitivity parameter, which, according to experimental results, is in the range 0.10-0.30 for polymers [123]. The Drucker-Prager yield criterion can also be rewritten in terms of the principal stresses, as

in the case of the Mohr-Coulomb criterion:

$$f(\sigma_1,\sigma_2,\sigma_3) = \sqrt{\frac{(\sigma_1-\sigma_2)^2+(\sigma_2-\sigma_3)^2+(\sigma_3-\sigma_1)^2}{2}} + (\sigma_1+\sigma_2+\sigma_3)\alpha - d = 0 \tag{3.5}$$

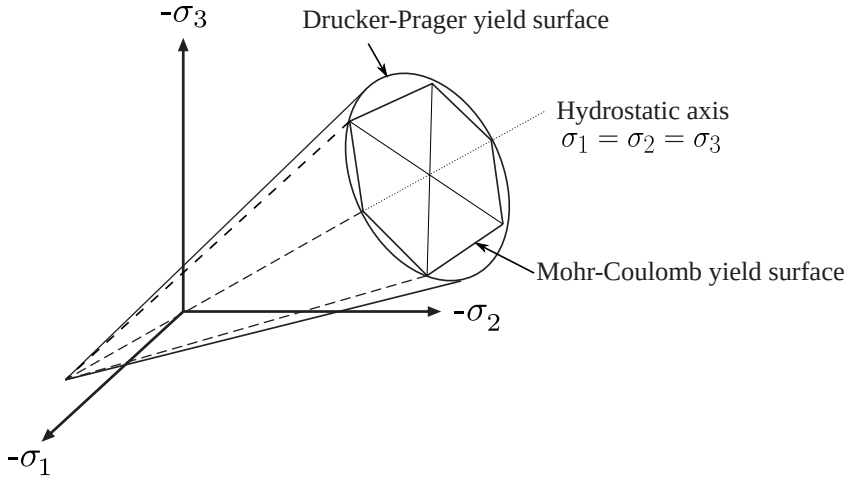

Figure 3.2: Drucker–Prager and Mohr-Coulomb yield surfaces.

Mohr-Coulomb and Drucker-Prager criteria are commonly used to describe the yield behavior of granular materials. In many cases, the available experimental data are given for one of such criterion, being necessary to obtain the relation between them. In this situation, the Drucker-Prager yield surface can be matched with the Mohr-Coulomb surface by the selection of the parameters α and d as:

$$\alpha = \frac{-\sin\phi}{\cos\eta - (1/\sqrt{3})\sin\eta\sin\phi}$$
$$d = \frac{c\cos\phi}{\cos\eta - (1/\sqrt{3})\sin\eta\sin\phi} \tag{3.6}$$

where η is the Lode angle, which is controlled by the relationship of the intermediate principal stress and the major and minor principal stresses, providing different possibilities to match the Drucker-Prager and Mohr-Coulomb criteria, as shown in Figure 3.3.

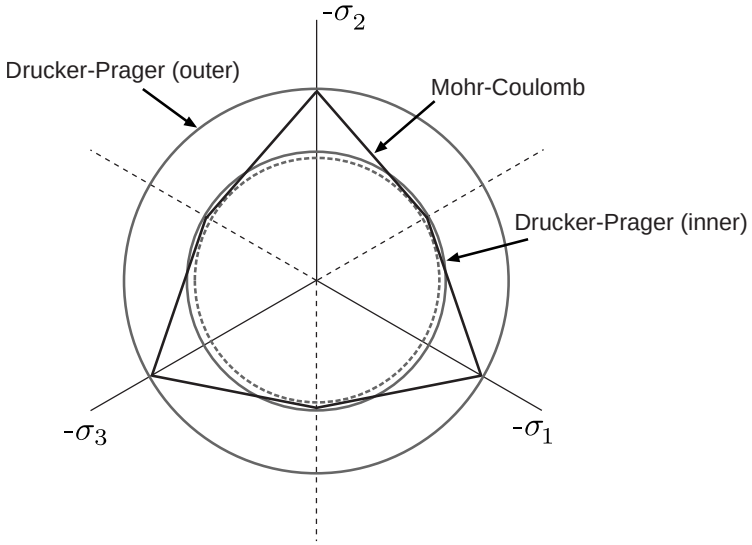

Figure 3.3: Matching between the Mohr-Coulomb and Drucker-Prager yield surfaces in the deviatoric plane

Both the Mohr-Coulomb and the Drucker–Prager are suited to model frictional materials such as polymers. The former is better to capture the different behavior under tension and compression. However, the latter is more robust when implemented in a computational code.

Epoxy micromechanics damage

Understanding the nature and origin of damage at the various constituents is necessary while modeling damage in a UD composite. The polymer matrix and the fiber/matrix interface, in particular, are the weakest parts of the microstructure, acting as a trigger for composite degradation and failure. Understanding the concepts of crack initiation and propagation necessitates a solid understanding of fracture mechanics. For that reason, some fundamental concepts, such as the concept of quasi-brittle material and the various methods of modeling damage used in computational micromechanics, are briefly explained in the following paragraphs.

Inglis [134] made the first mathematical attempt to study material fracture in 1913 by analyzing the case of an elliptical hole in a plate subjected to a remote tensile stress perpendicular to the major axis of notch. He demonstrated that

the maximum stress occurs at the vertex of the major axis, where the radius of curvature is the smallest. Furthermore, when the elliptical notch is collapsed into a perfect crack, the stress field is singular. Since real materials can only withstand finite stresses, this result indicated that a cracked component cannot sustain any loading if the maximum stress criterion is used, which contradicted the experimental findings.

Griffith [135] investigated the propagation of cracks using energy conservation principles. Griffith proposed that solids have surface energy, and that in order for a crack to propagate, the externally added energy must exceed the surface energy associated with the new area created during crack propagation. Griffith introduced the concept of fracture energy of a material G_c, which was only applicable to perfectly brittle materials. Experimental measurements of the energy required to propagate a crack were orders of magnitude greater than theoretical estimates. Plastic deformation occurs at the tip of the notch, according to experimental observations of crack surfaces, even in brittle materials.

This led Irwin [136] followed by Orovan [137] to theorize the theory of the Fracture Process Zone (FPZ) for the region surrounding the crack tip. This zone was distinguished by progressive softening, in which stress decreases with increasing deformation. The FPZ is surrounded by a nonsoftening nonlinear region characterized by plasticity, with stress remaining constant as deformation increases. The extension of the FPZ depends on the material microstructure and nature and was defined by Hilleborg according to a characteristic length:

$$l_{FPZ} = \frac{EG_c}{\sigma_t^2} \tag{3.7}$$

in which E is the elastic modulus and σ_t is the tensile strength of the material. There are three types of fracture behavior that can be distinguished based on the relative size of the FPZ with respect to the plastic zone and to the structure size, Figure 3.4. In the case of brittle materials, such as ceramics or glass, both the FPZ and the plastic region are very small, and thus small strain increments cause the microcracks to quickly coalesce into a macroscopic one that grows. Linear elastic fracture mechanics (LEFM) is specially suited for this case. The second type of behavior includes situations in which the nonlinear zone is caused by the material's plastic yielding and the size of the actual fracture process zone

remains small. This type of behavior is common in ductile metals and is typically treated using elasto-plastic fracture mechanics (EPFM). Finally, the third type of behavior occurs when a large part of the nonlinear region is damaged due to material softening caused by crazing, void formation, interface breakages, and other similar phenomena. This type of behavior is observed in many quasi-brittle materials [138], such as concrete, rocks, and toughened ceramics.

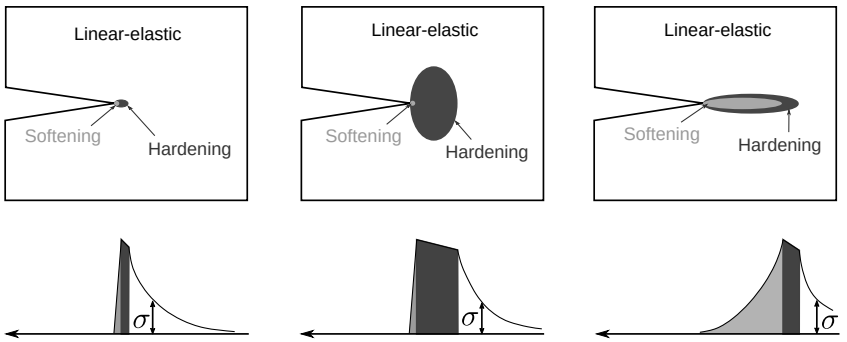

Figure 3.4: Types of fracture according to the FPZ relative dimensions. From left to right: brittle, ductile and quasi-brittle material. Stress distribution along the crack line is shown at the bottom. From Bazant and Planas [138].

The epoxy matrix fails in tension with very limited elongation, and this brittle behavior has classically been treated with LEFM [123]. Nevertheless, when considering a perfectly brittle material, theoretical fracture toughness usually underestimates observations [139]. This was confirmed by fractographic observations, which revealed massive plastic deformations caused by shear banding and crazing around the crack tip [140]. These findings confirmed that toughening mechanisms are involved during the fracture of the epoxy resin and that they can be treated as quasibrittle materials. Two simplified approaches can accurately describe the fracture process in these materials: cohesive crack models and continuum damage models.

Damage-plasticity model

Cracking process in quasi-brittle materials is caused by a continuous nucleation and coalescence of microcracks, as well as the evolution of microcrack density, which results in a macroscopical softening of the material [123, 141]. Epoxy,

like other quasi-brittle materials, behaves differently depending on whether it is loaded in tension or compression. Although the difference between compression and tension strength for an epoxy is not as large as it is for other quasi-brittle materials like concrete, the amount of plastic strain and thus the failure mechanisms are completely different.

Among the various constitutive equations available in the literature, the damage-plasticity model has a number of properties that make it highly suitable for modeling quasi-brittle materials such as epoxy polymers. Lubliner et al. [142] were the first to use the plastic-damage approach to model the mechanical behavior of quasi-brittle materials, which was later modified by Lee and Fenves [143]. The yield function can be expressed in terms of effective stresses and equivalent plastic strains as:

$$F(\sigma, \bar{\varepsilon}_c^{pl}) = \frac{1}{1-\alpha}\left(\sqrt{3J_2} + \alpha I_1 + \beta(\sigma_I) - \gamma\langle -\sigma_I\rangle\right) - \sigma_{yc}(\bar{\varepsilon}_c^{pl}) = 0 \quad (3.8)$$

where I is the first invariant of the equivalent stress tensor, J is the second invariant of the equivalent deviatoric stress tensor, α is the pressure-sensitivity parameter of the original Drucker-Prager yield criterion, σ_I is the maximum principal stress and β is a function of the tensile $\sigma_t(\bar{\varepsilon}_t^{pl})$ and compressive $\sigma_c(\bar{\varepsilon}_c^{pl})$ yield stresses defined as:

$$\beta = \frac{\sigma_c(\bar{\varepsilon}_c^{pl})}{\sigma_t(\bar{\varepsilon}_t^{pl})}(1-\alpha) - (1+\alpha) \quad (3.9)$$

The yield surface under plane stress conditions is plotted in Figure 3.5. This model is a modified version of the pressure-dependent Drucker-Prager plasticity yield criterion [144], allowing for the definition of various tension and compression behavior. However, it employs the concepts of isotropic damaged elasticity in conjunction with isotropic tensile and compressive plasticity to represent the quasibrittle material's inelastic behavior, including the irreversible process that occurs during fracturing.

For compression loading condition, the quasi-brittle material yields according to the standard Drucker-Prager yield criterion. However, under tension loads, the criterion predicts a yielding that is primarily controlled by the maximum principal stress, similar to the Rankine model used for perfectly brittle materials.

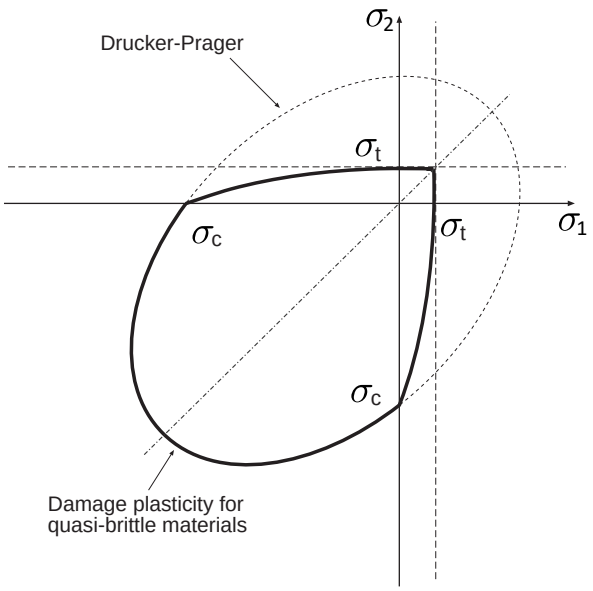

Figure 3.5: Yield surface in plane stress.

The model assumes two main irreversible deformation mechanisms: tensile cracking (microcracking coalescence) and compressive shear banding (followed by compressive crushing). The evolution of the yield surface is governed by two internal damage variables, $(\bar{\varepsilon}_t^{pl})$ and $(\bar{\varepsilon}_c^{pl})$, which are determined by the failure mechanisms under tension and compression loading, respectively.

Under uniaxial tension, the material behaves as an elastic solid until the failure stress σ_{t0} is reached. This point, corresponds to the onset of material degradation, in the form of microcracking, as can be seen in Figure 3.6a. Increasing the displacement causes continuous nucleation and coalescence of microcracks, resulting in a macroscopic softening of the material by decreasing the yield stress. Under uniaxial compression the response of the material is linear and elastic until the value of the compression strength σ_{c0} which corresponds with the onset of the plastic regime. Typically, material experiences some hardening until the ultimate compression stress is reached. This point corresponds to the onset of compression damage (crushing). Typically, some hardening occurs until the ultimate compression stress σ_{cu} is reached. This is when compression damage begins (crushing), as can be seen in Figure 3.6b.

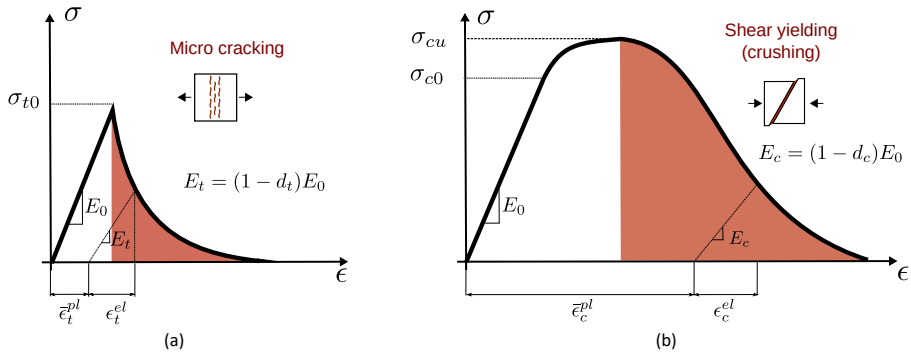

Figure 3.6: Response of quasi-brittle material to uniaxial loading in: a) tension and b) compression.

Epoxy micromechanical modelling

The epoxy matrix is modelled using the isotropic damaged/plasticity model, named as concrete damaged plasticity included in Abaqus [145]. The main features of this constitutive model are the pressure dependent yield surface and the distinction between tensile and compressive damage evolution. This model requires not only the definition of the uniaxial tensile and compressive mechanical response, but also the evolution of the yield surface (plasticity) and material degradation (damage), as described in detail in the Mohr-Coulomb and Drucker-Prager yield criterion.

Although multiaxial tests are required to calibrate this model, Naya [146] demonstrated that the representative behavior of the polymer matrix can be captured using the elastic modulus E^m, compression yield limit σ_{yc}^m, and internal friction angle ϕ^m, if the right values are assumed for some of the parameters describing the yield surface evolution and material damage. The model assumes that damaged plasticity characterizes the uniaxial tensile and compressive response, and thus the evolution of tensile plastic strain ($\bar{\varepsilon}_t^{pl}$) and compressive equivalent plastic strain ($\bar{\varepsilon}_c^{pl}$). Based on this assumption, the first thing that must be defined is the epoxy's uniaxial stress-strain response and damage evolution (Figure 3.7).

Under uniaxial tension, the epoxy behaves as a linear elastic solid. Its tensile strength corresponds to the onset of material degradation, which manifests as microcracking. As the displacement is increased, continuous nucleation and coalescence of microcracks occurs, resulting in a macroscopic softening of the

material that is visible in the strength decay. In this study, a linear decay in the tensile stress profile was chosen.

Under uniaxial compression, the the stress-strain relation is linear and elastic up to the initial compressive yield (σ_{yc}). Then, plastic hardening occurs until the ultimate stress value at the critical plastic strain (σ_{uc}) is reached. Material collapse begins at this point which is modeled by means of stress decay.

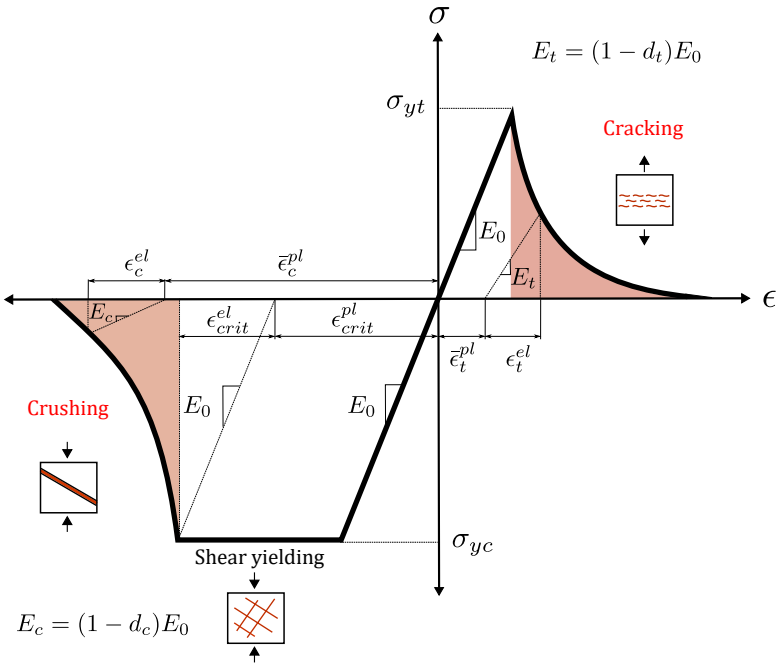

Figure 3.7: Schematic of the stress-strain curves used to model the epoxy uniaxial tension and compression response. Damage modes are highlighted in red.

In addition, two linear damage evolution laws in both tension ($d_t = d_t \bar{\varepsilon}_t^{pl}$) and compression ($d_c = d_c \bar{\varepsilon}_c^{pl}$) were specified. Under tension loading, fracture energy is used to model polymer postfailure behavior. The brittle behavior of concrete is characterized by a stress-displacement response rather than a stress-strain response using this approach. In order to implement the stress-displacement concept in a finite element model, a characteristic length associated with an integration point must be defined. Abaqus [145] performs this element size regularization automatically based on the element geometry and formulation. The equivalent stress-strain relationship is calculated using this element length and the polymer fracture energy.

The damaged/plasticity model requires five additional inputs to predict plastic flow and yield function evolution, including: the dilation angle ψ, the eccentricity parameter ε, the initial biaxial to uniaxial compression strength ratio σ_{b0}/σ_{c0}, the tensile and compressive meridian yield condition ratio K_c, and the viscosity parameter μ_c. The values selected for these parameters are shown in Table 3.2.

Table 3.2: Input parameters of the matrix damaged/plasticity model for the plastic flow and yield surface evolution [146].

ψ	ε	σ_{b0}/σ_{c0}	K_c	μ_c
29	0.1	1.29	1.0	0.0001

To summarize, the epoxy elasto-plastic behavior is presented in this work using a damage-plasticity model based on the Drucker-Prager plasticity criterion. Table 3.3 exhibits these parameters. Regarding the parameters, the elastic modulus E^m is used here to model the elastic response, the compression strength σ_{yc}^m is used to determine the onset of the plastic regime under compression loading, and the polymer internal friction angle ψ is introduced in the yield surface evolution through the biaxial/uniaxial compression ratio. The remaining parameters are either taken from the literature or are default Abaqus values.

Table 3.3: Parameters of the damaged/plasticity model of the 8552 epoxy matrix under uniaxial tension and compression [146].

E^m [GPa]	ν^m [ ]	α^m [$10^{-6}{}^{\circ}C^{-1}$]	σ_{t0}^m [MPa]	G_t^m [J/m^2]	σ_{yc}^m [MPa]	σ_{uc}^m [MPa]
5.07	0.35	52	121	90	176	180

3.1.3 Fibre-matrix interface

Fibre-matrix interface debonding (decohesion) is one of the main damage mechanisms in FRPs because it leads to significant reductions of the strength, ductility and toughness of the material [147]. Interface damage initiates by the nucleation of a crack as the stress at the interface exceeds the interfacial strength. Damage progresses as the crack propagates along the fibre-matrix interface and reduces the amount of load transferred from the matrix to the reinforcement. Finally, the fracture of the composite can occur by the coalescence of interface cracks connected by shear bands in the matrix. For these reasons, the fiber-matrix

decohesion is considered a key mechanism which should be taken into account to analyze the overall composite behavior.

Despite the benefits of continuum damage models, cohesive damage models are well-suited to simulate progressive interface damage at the interface between dissimilar materials due to the well-defined crack path. Various methods, such as extended finite elements, cohesive zone model, strong embedded discontinuities, etc, can be used to implement the cohesive crack in finite element codes.

In this work, fiber/matrix interface failure was taken into account using the cohesive zone method [148, 149]. The cohesive surfaces are inserted at the fiber/matrix interface following a mixed-mode traction-separation law. The cohesive surface has zero or negligible thickness. The traction separation law considers initial linear elastic behavior, followed by damage initiation and evolution. The relative displacement along the interface surface is denoted as δ, and the traction separation behavior of the cohesive zone can be represented in Figure 3.8.

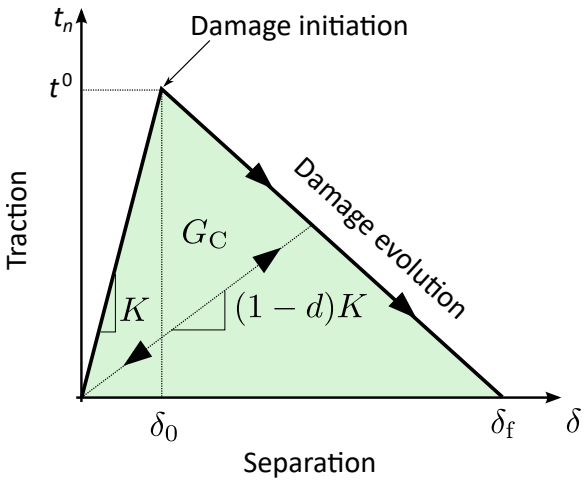

Figure 3.8: Schematic of the pure-mode bilinear traction– separation law used to model the cohesive zone interface.

The elastic behavior can be represented as:

$$t = \begin{Bmatrix} t_n \\ t_s \\ t_t \end{Bmatrix} = \begin{bmatrix} K_{nn} & K_{ns} & K_{nt} \\ K_{ns} & K_{ss} & K_{st} \\ K_{nt} & K_{sn} & K_{tt} \end{bmatrix} \begin{Bmatrix} \delta_n \\ \delta_s \\ \delta_t \end{Bmatrix} = K\delta \tag{3.10}$$

where t denotes the traction vector, K represents the contact stiffness that describes the linear-elastic behavior of the interface prior to damage initiation, and under any compressive normal tractions, which are assumed not to cause damage to the interface. The subscripts n, t, and s depict the normal, tangential, and shear, respectively. The tractions acting at the interface can be represented as:

$$t_{(n,s,t)} = (1-d)\bar{t}_{(n,s,t)} \tag{3.11}$$

The variable d, represents the irreversible damage, with d = 0 and d = 1 depicting no damage and completely damage states, respectively. To represent the damage under the combined mode of loading with both normal and shear components acting across the interface, an expression for effective separation is defined as:

$$\bar{\delta} = \sqrt{\langle \delta_n \rangle^2 + \delta_s^2 + \delta_t^2} \tag{3.12}$$

Where $\langle\rangle$ is the Macauley bracket, δ_n, δ_s, and δ_t represent the normal and the two shear displacement, respectively. The Macaulay brackets indicate that the displacement jump in the normal direction is only taken into account when it leads to crack separation. In other words, normal compression loading has no effect on the interface damage propagation.

Mixed mode debonding

It is commonly found that a mixture of Mode I and II loading occurs in advanced composite structures (Figure 3.9). Under mixed-mode loading, damage initiation and softening behaviour may occur before the respective individual parameters are reached. Therefore, Abaqus [150] includes various criteria for mixed mode debonding onset and propagation [148].

Damage initiation

Damage initiation under mixed-mode loading can be described by a quadratic interaction function based on the nominal stress ratio:

$$\left(\frac{\langle t_n \rangle}{t_n^o}\right)^2 + \left(\frac{t_s}{t_s^o}\right)^2 + \left(\frac{t_t}{t_t^o}\right)^2 = 1 \tag{3.13}$$

subscript n represents Mode I component while subscripts s and t represents in-plane shear and out-of-plane shear that is represented together as a Mode II component, as shown in Figure 3.9.

Damage evolution

The damage evolution is dependent on the energy released during the surface separation process. The energy dissipated during the process is called fracture energy and is equal to the area under the traction separation curve (Figure 3.8. The dependence of fracture energy (G_c) on mixed-mode can be represented either by a power-law or by the Benzeggagh-Kenane (BK) criterion [148]. We used BK law [151] to compute the energy dissipation by:

$$G^c = G_n^c + (G_s^c - G_n^c)\left(\frac{G_S}{G_T}\right)^\eta \tag{3.14}$$

where η is the BK power exponent, G_n^c and G_s^c are the normal and shear fracture energies, respectively, and G_S and G_T the reciprocal work under mixed mode propagation.

Interface micromechanical modelling

The debonding between fibers and matrix is modeled by means of the cohesive zone method coupled with frictional behavior. This coupled cohesive-friction approach is implemented in the kinematics of surface contact interactions in Abaqus/Standard [145]. This model is used to account for the significant effect of friction during and after fibre/matrix debonding. The shear stresses caused by friction at the interface are ramped up progressively and proportionally to the degradation of the interface, thus once the interface is fully debonded, the surface interaction is uniquely governed by a pure Coulomb model. Furthermore, as shear stresses ramp with the interface damage variable, friction affects the

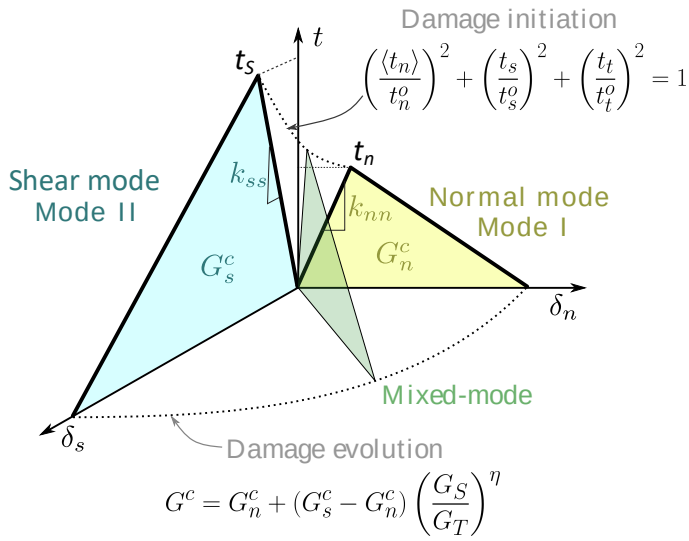

Figure 3.9: Schematic of bilinear traction– separation law for mixed-mode loading based on the BK fracture criterion

cohesive response, as illustrated in Figure 3.10. This increases the interface shear resistance, which is a function of the normal compressive tractions used.

Damage initiation is implemented by a quadratic interaction criterion (Eq. 3.13) that is determined by the fiber/matrix interface strength values. Once interface debonding is initiated, the cohesive tractions transferred through the interface decrease linearly to zero using the energy-based BK damage propagation criterion (Eq. 3.14).

In terms of interface parameters, it will be assumed that the properties in the transverse shear direction (t) are the same as those in the longitudinal shear direction (s). As a result, two interface strengths (t_n and t_s), two interface energies (G_n^c and G_s^c), two penalty stiffnesses (K_{nn} and K_{ss}), and the BK exponent (η) need to be defined. The penalty stiffness, K_{nn} and K_{ss}, are non-physical parameters that should be large enough to ensure displacement continuity in the absence of interface damage while minimizing convergence difficulties due to ill-conditioned stiffness matrix. The interface shear strength, t_s, was determined experimentally from push-in tests [152]. While the normal interface strength is set to $t_n = 2t_s/3$ as stated by Ogihara and Koyanagi [153].

To the best of the author's knowledge, there are no reliable experimental methods

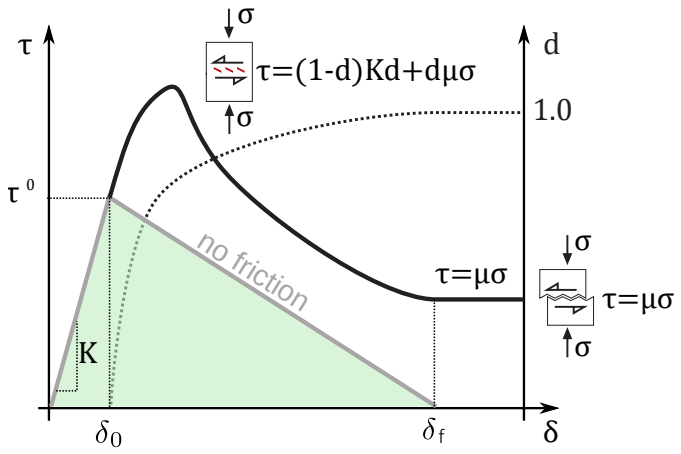

Figure 3.10: Schematics of the shear response of the damage-friction model for fiber/matrix interfaces.

for measuring interface fracture energies. Setting the fracture energy values according to parametric studies that aim at reproducing macroscopic experimental results was the approach followed by Canal et al. [105]. Nevertheless, the fracture energies obtained in this way comprise other dissipation mechanisms together with the pure interface debonding process, essentially matrix plasticity and fiber bridging. In the case of the normal separation mode, this could result in an overestimation of the true interface fracture energy. For instance, assuming a value of $G_n^c = 150\ J/m^2$ and linear softening, the ultimate separation at failure would be $\delta_f = 2G_n^c/t_n \approx 70\ \mu m$, which is around ten times the carbon fiber diameter. In view of this, the mode I fracture energy is assumed to be $G_n^c = 2\ J/m^2$. Similar values are reported in the literature [128, 154].

For the shear fracture energy, G_s^c, a value of $100\ J/m^2$ was assumed such that the separation at failure was $\delta_s = 1\ \mu m$. This energy is lower than that of the matrix, representing the brittle nature of the fiber/matrix interface. Finally, from Lopes et al. [155], the BK exponent was set to 1.2. The interface parameters used in the simulations are presented in Table 3.4.

Table 3.4: Material properties of AS4/8552 fiber/matrix interface [156].

t_n [MPa]	t_s [MPa]	k_{nn} [GPa/μm]	k_{ss} [GPa/μm]	G_n^c [J/m^2]	G_s^c [J/m^2]	η [ ]
42	63	100	100	2	100	1.2

3.2 Representative volume element

The mechanical behavior of composite materials can be analysed through the finite elements simulation of a representative volume element (RVE) of the microstructure. The RVE was first defined by Drugan and Willis [157] as the smallest material volume element of an heterogeneous material for which the average stress and strain microfields converge to an asymptotically constant value which is size independent and represents the effective macroscopic constitutive response. As a result, the RVE should be larger than a certain size in order to ensure that the simulation results are independent of the size and spatial distribution of the reinforcements within the microstructure. There are no procedures for predicting the size of the RVE for a specific composite analysis, but it should be confirmed by an a posteriori assessment of the statistical error. If a large RVE was required to represent the composite, performing the numerical computation would be impossible or costly. Fortunately, it has been demonstrated that an RVE can accurately simulate the mechanical behavior of metal matrix composites and FRPs in the elasto-plastic regime with only a few dozens of fibers [106, 158, 159].

3.2.1 RVE generation

The artificial generation of representative microstructures is a key feature of the computational micromechanics strategy. In the case of UD fiber-reinforced composites, the microstructure corresponds to the distribution of fiber cross sections. The fiber arrangement is an important factor in the composite's behavior. Square and hexagonal fiber arrangements typically produce unrealistic results [36]. To overcome this difficulty, it is necessary to generate a Representative Volume Element (RVE) that is representative of the material, which means having the correct size and being able to represent the microstructure of the composite material. Many different approaches have been proposed to achieve this goal.

Fiber distributions can be directly determined from a micrograph of the composite cross-section to generate real-like microstructures using image-based reconstruction techniques [160, 161]. Image-based reconstruction techniques provide the best RVE in terms of fidelity to the real microstructure, capturing defects, fiber clusters, and so on. Despite the fact that these methods are rapidly improving, high-quality composite cross-section micrographs are not always available. Furthermore, sample preparation, image processing, and the export process to the FE code are time-consuming and resource-intensive tasks. Besides that, periodic microstructures are not easily found in real micrographs, and enforcing such a condition requires additional effort, rendering the mathematical work unfeasible. As a result, generating a virtual microstructure statistically equivalent to the real one using random distributions is still the quickest way to solve the problem.

Artificial RVE generators based on mathematical algorithms [154, 162–164] are an alternative to image-based reconstruction techniques. Among the various mathematical models, two algorithms stand out above the rest: the Random Sequential Adsorption (RSA) [162, 163] and the Nearest Neighbor Algorithm (NNA) [154]. The RSA technique was employed in this work to generate artificial microstructures of FRPs, and the description of this method is given below.

Rintoul and Torquato [162] developed the RSA algorithm, which was later improved by Segurado and Llorca [163]. The RSA algorithm is robust and fast, even when generating large 3D spherical particle distributions. The RSA generates fiber centers at random and sequentially, and each new fibre is accepted if the distance between neighboring fiber surfaces is greater than a minimum distance ($0.05D$, where D stands for the fibre diameter) to ensure adequate finite element discretization of this region. In addition, the distance between the fiber surface and the RVE edges should be greater than $0.15D$ to avoid distorted finite elements during meshing. Fibers intersecting the RVE edges were split and complemented at the opposite sides of the square RVE to create a periodic microstructure. New fibers were added until the desired volume fraction was reached. If the desired fiber volume fraction is not reached, the unit cell is compressed in several steps. At each step, a fiber is adsorbed towards a specific point, making space for more fibres and eventually increasing the local volume

fraction (Figure 3.11).

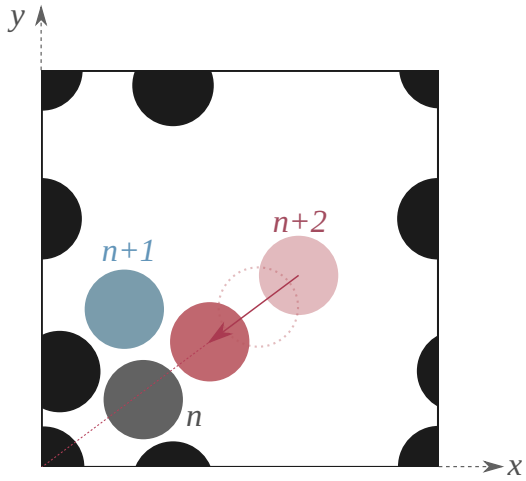

Figure 3.11: Schematic of the periodic fiber distribution generation based on the RSA algorithm. The black fibres guarantee the periodicity of the RVE.

3.3 Micromechanics modelling frameworks

The micromechanical model developed in this section is based on a representative volume element (RVE) containing a periodic and random dispersion of parallel fibers embedded in a polymer matrix, representing an unidirectional composite ply. In this work, the volume fraction of fiber reinforcement was set to 50% in all simulations, a value that is usually attained in manufacturing of common structural FRPs.

The RVE dimensions were large enough to ensure simulation results were size independent in a statistical sense [109], without exceeding the computational resources, to allow fast and efficient computations. The computational micromechanics framework has been implemented in the simulation environment Abaqus/Standard [145] as the main FE platform throughout this study.

3.3.1 Boundary conditions

Periodic boundary conditions (PBC) were used instead of other strategies such as iso-strain or iso-stress approaches to minimize the influence of the boundary conditions on the mechanical response of the model. PBCs provide a balance

between the effective response obtained from imposing displacements (upper limit) and tensions (lower limit) [165]. PBC were imposed between opposite faces of the RVE to ensure the displacement continuity with the neighboring RVEs as a jigsaw puzzle. For a given RVE with dimensions of $L \times H \times W$ (Figure 3.12), PBC are introduced as nodal displacement constraints between opposite RVE faces using the following equations:

$$\begin{aligned} u(L,y,z) - u(0,y,z) &= u^{Mx} - u^{Mo} = u_x \\ u(x,H,z) - u(x,0,z) &= u^{My} - u^{Mo} = u_y \\ u(x,y,W) - u(x,y,0) &= u^{Mz} - u^{Mo} = u_z \end{aligned} \tag{3.15}$$

where x, y, z are the coordinates axis ($0 \leq u_x \leq L$, $0 \leq u_y \leq H$, $0 \leq u_z \leq W$), and u_x, u_y, u_z are the displacements of the master nodes. As a result, three master nodes Mx, My, and Mz are defined in the RVE. The relative displacement of a couple of nodes laying on opposite faces is equal to the displacement between the corresponding pair of master nodes. The different loading states are introduced, which include any physical homogeneous deformation state within the unit cell and impose displacements on these master nodes. Each master node will contain the reaction force generated by all the nodes laying on its corresponding face. Uniaxial tension or compression in any directions can be imposed to the RVE by applying the appropriate displacements to the master nodes. For example, a uniaxial tension in longitudinal directions (z) is introduced by setting $M\text{x} = (u_x, 0, 0)$, $M\text{y} = (0, u_y, 0)$, and $M\text{z} = (0, 0, \delta)$, where u_x and u_y stand the resulting lateral Poisson contractions, and δ the applied tensile displacement.

3.3.2 Methodology

In this section, a computational micromechanics methodology based on a periodic RVE approach is proposed to predict the longitudinal tensile strength of a UD composite using the constituent properties mentioned in section 3.1. The Weibull parameters, in particular, are critical properties of the model. Depending on the characteristic Weibull fibre strength (σ_0), the size of the RVE must be scaled in order to obtain a reasonable tensile strength value. When fibers larger than those used in the single tensile test are used, a lower value of σ_0 is obtained due to a higher probability of fiber defects and, as a result, a lower value of tensile strength. Using shorter fibers in the tensile test, on the other

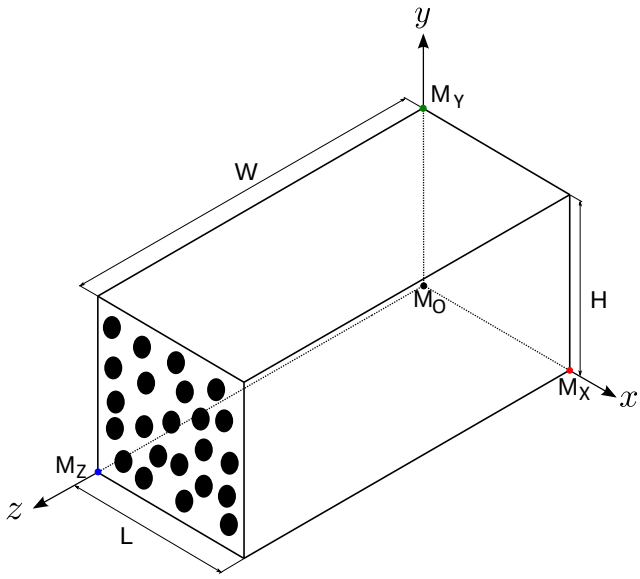

Figure 3.12: Diagram depicting the position of the master nodes used to implement the periodic boundary conditions within the RVE.

hand, predicts a higher value of σ_0 and thus of strength.

The length of the RVE (W) can be defined using the ineffective length obtained from Equation 2.10. In this equation, by replacing σ_f with σ_0, the fiber strength is properly scaled in relation to σ_0. To allow for full stress recovery, the RVE should be at least twice the length of the ineffective length. Then a reasonable σ_0 value is required. If σ_0 is too large as a result, the RVEs will be too large, rendering the computation extremely difficult. Small values of σ_0, on the other hand, will result in small RVEs, where stress recovery cannot be formed.

The length of RVE in the fibre longitudinal direction should be long enough to ensure that the ineffective length will be well captured. Some studies employed RVEs with lengths ranging from $15R$ to $40R$ [18, 166]. However, an RVE using these length values does not guarantee a good prediction of the fibre fragmentation. A congruent RVE length depends on the fibre and matrix elastic properties, as well the ineffective and debonding lengths. Thus, RVEs lengths of several orders of magnitude greater than the ineffective length should be used [99, 167]. Furthermore, size effects may occur. Therefore, the RVE must be large enough to capture the micro-mechanisms of the damage, the stress redistribution around the broken fibres during the failure process, and the

clusters of fibre breaks on the different planes.

Periodic RVE model

A 2D periodic RVE of the unidirectional composite ply is generated, using the in–house developed software, employing the random sequential adsorption (RSA) algorithm to reproduce statistically representative microstructures. The generated ply section has the dimensions length (L) = height (H) = $25 \times R$, where R is the average fibre radius, and contains 107 fibers (see Figure 3.13).

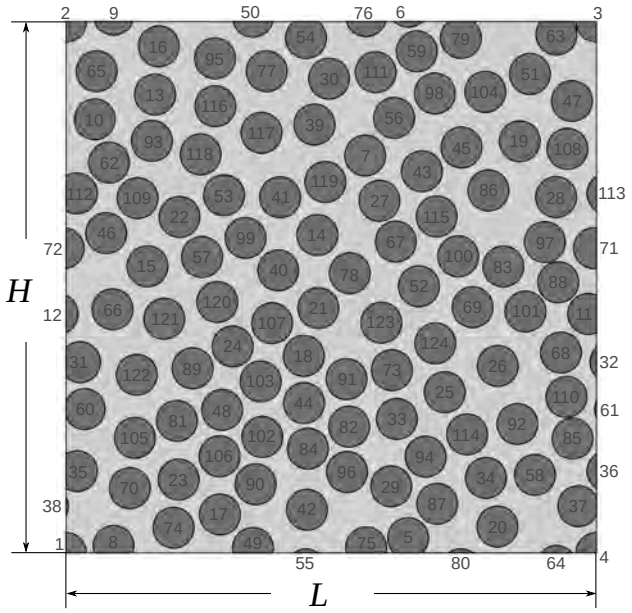

Figure 3.13: Reference RVE section with $V_f = 51\%$, contains 107 fibers. The location and number of each fiber are specified.

This 2D section is extruded along the fiber direction, to a total width $W = 113 \times R$, to achieve the final 3D RVEs (Figure 3.14). This size is sufficient to provide full stress recovery inside the RVE after a fiber is broken while maintaining a local load sharing approach.

The RVE size was selected based on well-informed parametric studies and the proposed methodology described above that targeted the best trade-off between computational effort and proper capturing of the relevant deformation phenomena with minimum interference of model boundaries. The microstructure of the composite ply is idealized as a dispersion of parallel, circular elastic fibers

embedded in the polymer matrix.

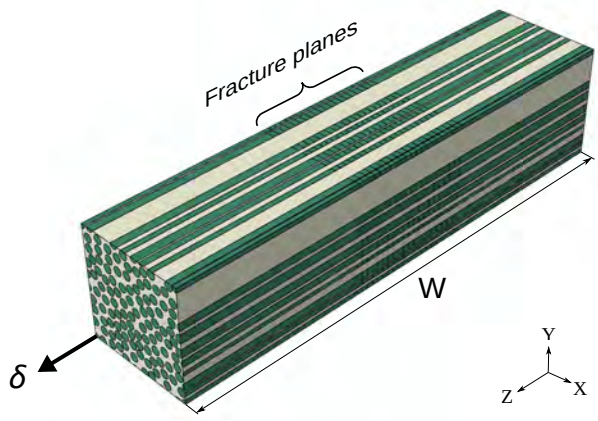

Figure 3.14: Extruded 3D RVE model.

To simulate the micromechanical behavior of RVE, proper damage models that can represent the behavior of the constituents in the RVE must be implemented. Since the RVE is composed of matrix, fibers, and interfaces, three damage models have been implemented in FE model to capture the damage associated with each component. The damage models associated with the matrix and interface are detailed in sections 3.1.2 and 3.1.3, respectively.

To capture the longitudinal failure of the microstructure, the fracture of carbon fibers must be explicitly reproduced. In order to achieve this, a sequence of fracture planes, represented by cohesive surface-based interactions, is introduced in the longitudinal direction of each fiber, as shown in Figure 3.15. The separation of the contacting surfaces is governed by cohesive behaviour to simulate the progressive breakage of the fibres. Figure 3.16 depicts a section of the micromechanical model detailing the location of cohesive surfaces in the fiber and at the fiber/matrix interface.

The distance between the fracture planes (d) must be carefully considered so that the model can capture the stress recovery of the fractured fibre (Figure 3.15). If d is set to an extremely large value, the model will fail to capture the stress recovery. It also cannot be ”extremely” small, because the Weibull distribution would result in extremely large strengths, which would be incorrect.

In this model, the distance between fracture planes corresponds to the length of

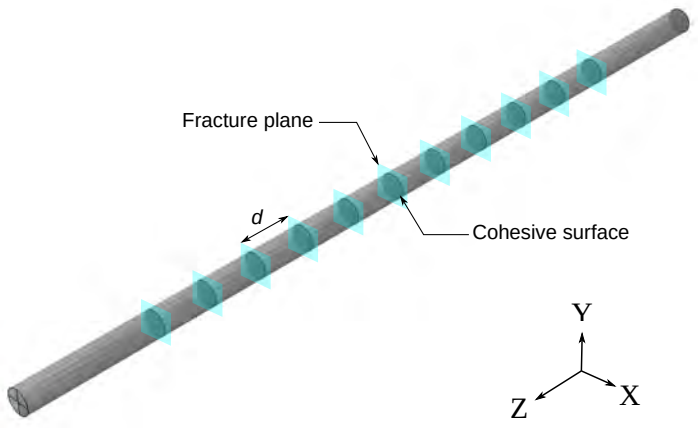

Figure 3.15: An example of the distribution of fracture planes and cohesive surface-based interactions in a fiber. The parameter d denotes the distance between fracture planes.

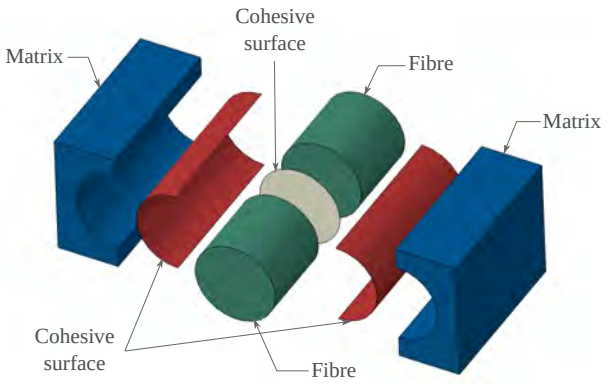

Figure 3.16: A section of the micromechanical model detailing the location of cohesive surfaces in the fiber and at the fiber/matrix interface.

the element (bundle) in the Fibre Bundle Models (FBM). As a result, the size of d can be considered equal to the length of the element used in the FBMs [20, 99, 168–170]. According to the literature [20, 99, 168–170], the best value for this length is in the range of $R \leq d \leq 2R$, where R is the radius of the fibre. For this study, $d = 5\mu m$ was chosen as the ideal distance between the fracture planes.

Another essential aspect that must be addressed is the number of fracture planes in each fibre. It should be sufficient to capture the effect of Weibull distribution in the fiber fracture strength. To this end, we consider that the fracture planes are distributed in such a way that they cover a length equal to the ineffective length. According to Swolfs [36], the effective length of a broken carbon fiber is $\approx 28 \times R$, where R is the radius of the fibre. As a result, by dividing the ineffective length by the distance between fracture planes (d), the number of fracture planes can be estimated. Using this strategy, each fiber requires a total of 20 fracture planes (Figure 3.14).

The RVE has a total of 2140 fracture planes due to the presence of 107 fibers, each with 20 fracture planes. The strength of each fracture plane is assigned randomly using Weibull distribution (Eq. 2.1). The Weibull parameters $\sigma_0 = 4.275\,GPa$ and $L_0 = 12.7\,mm$ [171]. The parameter L is equal to the distance between two fracture planes d. Figure 3.17 depicts the obtained distributions of strength for all the fracture planes.

The micromechanical behaviour of FRP can be affected by the occurrence of post-curing thermo-mechanical residual stresses that arise due to the different thermal expansion coefficients of the fibres and the matrix. To account for these effects, this finite element analysis consists of two steps. In the first one, residual thermal stresses were introduced in the model through an initial elastic thermal step, in which the temperature was homogeneously reduced from the curing temperature (T = 180 °C) down to the room temperature (T = 20 °C) without external constraints. Due to the mismatch of thermo-mechanical properties between fiber and matrix, the residual thermal stresses build up. Afterwards, the longitudinal mechanical loading was simulated in the second step by means of the displacement in z direction.

The 3D RVE is discretized with fully integrated brick (C3D8) and wedge (C3D6)

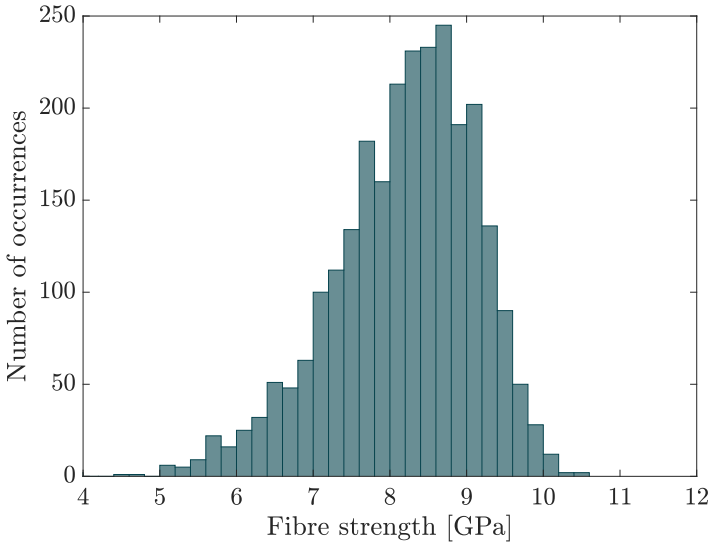

Figure 3.17: Distributions of tensile strength of the 2140 fracture planes in the fibres of the RVE, based on Weibull distribution.

[145] isoparametric elements with an average characteristic length of 1 μm , totalling around 1.1×10^6 elements. This discretization is judged, after parametric analysis and convergence study, to be fine enough to capture the stress gradients around a fibre break. The RVE analyses is extremely demanding and require around 8 days to complete in an HPC cluster of 50 Intel Xeon E5-2670 cores.

3.4 Results and discussion

Figure 3.18 depicts the longitudinal stress-strain curves for the UD AS4/8552 ply under longitudinal tension resulting from the RVE simulation. The stress-strain curve behaves linearly until almost the point of failure. However, in fact, once the first fiber fracture occurs, the system becomes non-linear and non-linearity increases as the number of broken fibers increases.

The micromechanical model predicted a maximum strength of 2164 MPa. This value was compared to the tensile strength of an AS4/8552 composite material from the literature [172], as well as the supplier product data sheet (Hexcel) [173]. Table 3.5 shows that the result of the micromechanical model is in very good agreement with the values obtained experimentally. Minor differences in the results can be attributed to the following factors:

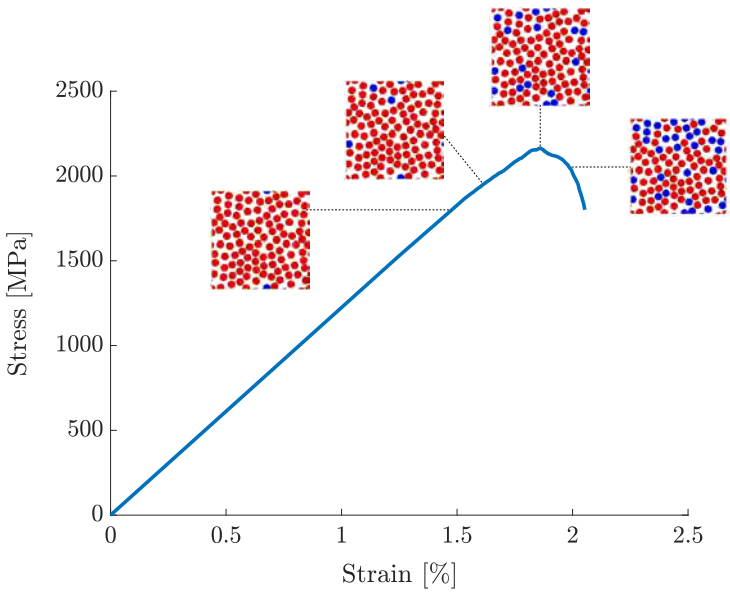

Figure 3.18: Stress-strain curves for the AS4/8552 carbon-epoxy matrix under longitudinal tension. The number of broken fibers at various strains is represented. The blue color represents broken fibers, while the red color represents intact fibers.

- First, the longitudinal tension test is difficult to perform, and there is significant scattering from one coupon to the next, which corresponds to the stochastic distribution of defects. This is evident in the disparity between supplier and literature results.

- Second, the micromechanical analysis prediction corresponds to the value of a single RVE and a single Weibull distribution. In this case, repeating the analysis for different microstructures and fiber strength distributions will result in a more realistic average prediction.

- Finally, the number of fibers in the RVE may not be sufficient to capture the effect of the Weibull distributions. For example, the number of fibers used in experimental testing to obtain the tensile strength reported in the literature, either by Marlett et al. [172] or by the supplier [173], ranges between 136 and 290. Due to computational resource limitations, simulation of an RVE with this number of fibers is not feasible.

As it was expected, the RVE fails due to accumulated fiber failure (cluster) through a plane perpendicular to the loading direction, as shown in Figure 3.18. Despite the large number of fibers (107 fibers) in the RVE, a closer evaluation

Table 3.5: Comparison of predicted micromechanical and experimental results for a AS4/8552 carbon-epoxy.

	Micromechanic	Experimental [172]	Hexcel [173]
Tensile strength (MPa)	2164	1965±83	2205

of the RVE at the time of failure (σ = 2164 MPa and ε = 1.85%) reveals that the number of broken fibers before reaching the maximum stress is only 16 (Figure 3.18). This means that a fracture in just these 16 fibers could be enough to cause the RVE composed of 107 fibers to fail. This group of 16 broken fibers is known as critical fibers, representing only 15% of the total volume fraction of fibers in the RVE. The number of broken fibers at the end of the simulation ($\varepsilon = 2\%$) reaches 30 fibers (28% of the total volume fraction), see Figure 3.19.

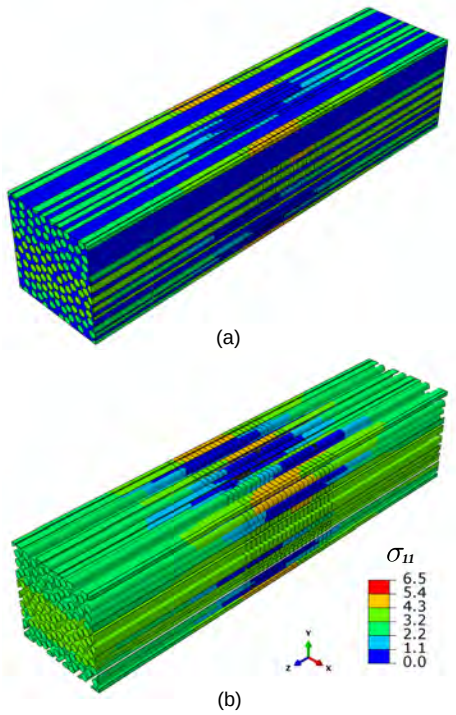

Figure 3.19: Longitudinal stress and failure at $\varepsilon = 2\%$: a) the full RVE, b) the RVE in the absence of a matrix for better illustration.

The fracture sequence can be visualized by isolating the set of broken fibers. This process is shown in Figure 3.20, where the stress and fracture evolution of broken fibres are depicted. For better visualization, the matrix and intact fibres are hidden. Figure 3.21 shows the cluster evolution at various strains. It can

be observed that the first fracture occurs in fibres 75-76 at $\varepsilon = 1.4\%$. Fiber 21 remains the only broken fiber up to $\varepsilon = 1.6\%$, at which fibres 31-32 break. The breakdown of fibers proceeds with increasing strain until strain of 1.85 percent. At $\varepsilon = 1.85\%$, a total of 16 fibers have been broken, including fibers 5-6, 19, 24, 29, 31-32, 35-36, 39, 54-55, 65, 75-76, 93, 95, 101, 102, 106, and 108. As a result, RVE reaches its maximum capacity and collapses.

Although all broken fibers contribute to the failure process, some fibers, particularly those located in the inner region and denser area of the RVE, can play a more effective role in damage propagation. It is also worth noting that fiber failure in the RVE can be classified into two types. In the first type, fiber failure occurs directly as a result of applied stress, with no interference from the fracture of adjacent fibers, such as failure in fibre 75-76. In this case, the fiber breaks as soon as the applied stress equals its strength. In the second type, fiber failure occurs as a result of applied stress and induced stress from adjacent broken fibers. In this case, the fiber breaks before the applied remote stress equals its strength. This is due to the fact that when a fiber breaks, it loses its ability to transfer load. In this case, the stress of the broken fiber is distributed among neighboring fibers based on their distance from the broken fiber. A parameter known as the stress concentration factor can be used to calculate the amount of redistributed stress.

Figure 3.22 depicts a detailed example of this and the RVE model is displayed exactly before and after the first fiber fails. It can be seen in Figure 3.22a before any fiber failure, the stress is distributed uniformly across all the fibres. However, after the failure of the first fiber (periodic fiber 75-76), the stress is no longer uniformly distributed, as shown in Figure 3.22b. In this case, the nearby fibers have a higher stress (range 8 to 20%) than the rest of the fibers and applied stress. This induced stress increases the possibility of failure in these nearby fibers.

The situation is even more complicated for an intact fiber surrounded by several broken fibers, as it is subjected to induced stress from all of them. For example, Figure 3.23 represents some sets of intact fibers that are surrounded by two or more broken fibers. Set A contains an intact fibre surrounded by four broken fibres (13, 16, 93, and 95). This means that, in addition to the applied stress, fiber 116 receives also induced stresses from those fibers. The following expression

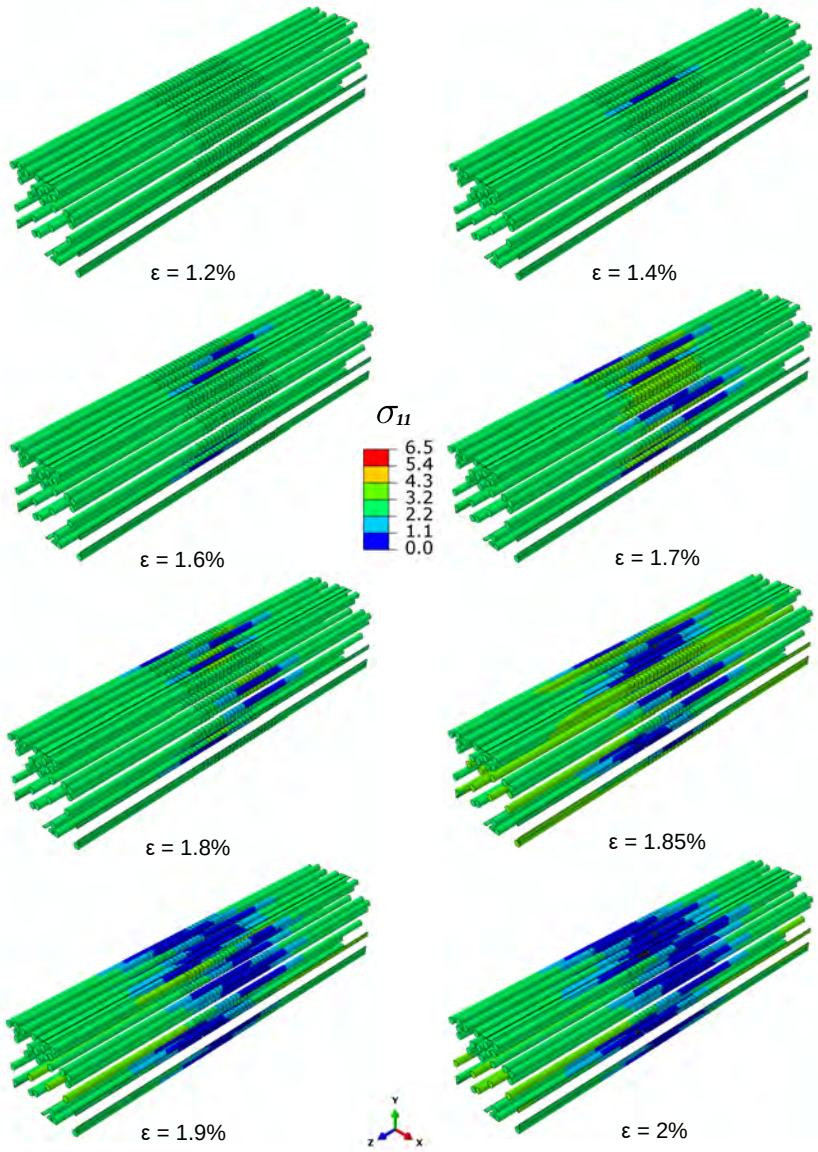

Figure 3.20: Fracture sequence in the group of broken fibers with respect to longitudinal strain. The matrix and intact fibres have been removed for better visibility.

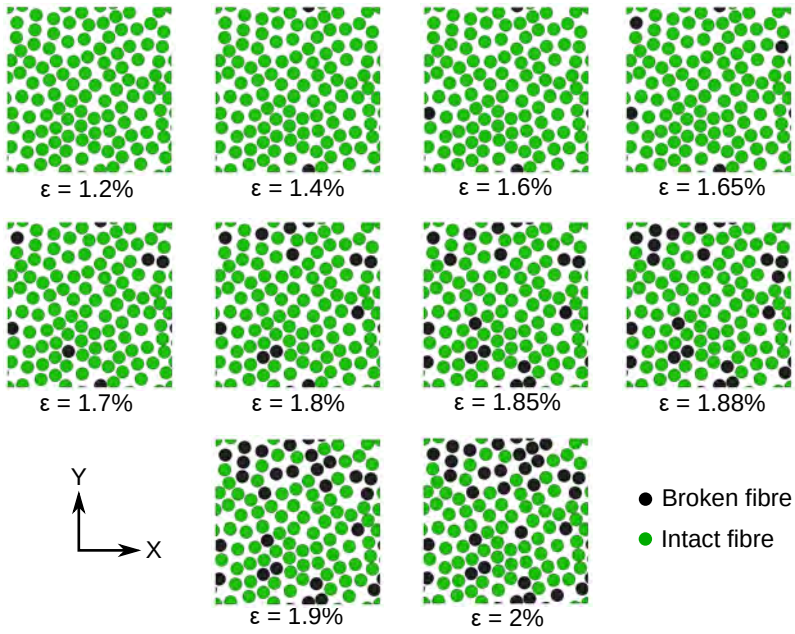

Figure 3.21: The sequence of fiber failure and cluster formation at various strains.

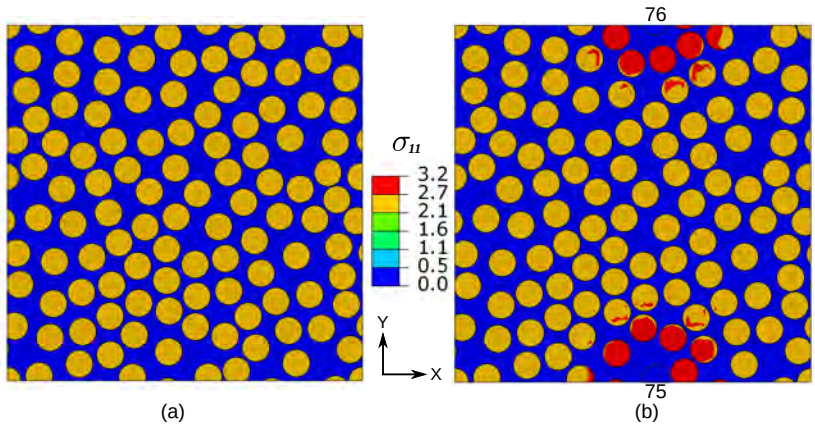

Figure 3.22: Stress distribution in the RVE prior to and after the first fibre breakage.

can be used to express this condition:

$$\sigma^{116} = \underbrace{\sigma}_{\text{Applied stresses}} + \underbrace{\left(k^{13}\sigma^{13} + k^{16}\sigma^{16} + k^{93}\sigma^{93} + k^{95}\sigma^{95}\right)}_{\text{Induced stresses}} \tag{3.16}$$

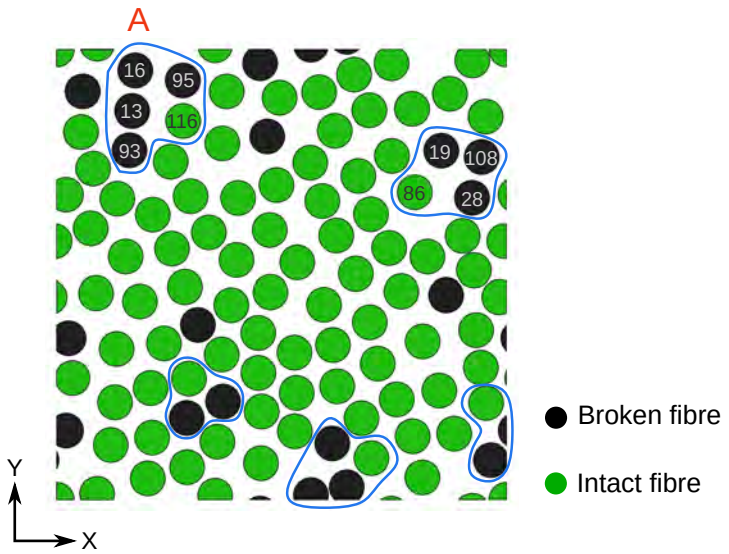

Figure 3.23: The superposition effects of stress distribution around several broken fibres.

It should be noted that not all of the stress carried by the broken fibres (13, 16, 93, and 95) is transferred to fibre 116, but only a fraction of it is transferred. The parameter k represents the fraction of stress that is transferred to fiber 116. This phenomenon is known as superposition, which means that as the number of broken fibers surrounding an intact fiber increases, so does the stress concentration, and the total stress concentration can be calculated by adding the stress concentrations induced by each broken fiber.

Another critical failure mechanism in UD composites is fibre/matrix interface debonding, which our micromechanics model can capture in extreme detail. The fibers, 28, 30, 106 and 116, were chosen for this purpose, and the progression of fiber/matrix interface damage was plotted at various strains. Two of these fibers are broken and two are intact in order to investigate the effect of interface debonding on both broken and intact fibers. Figure 3.24 presents the progression of damage at the fiber/matrix interface for all four fibers.

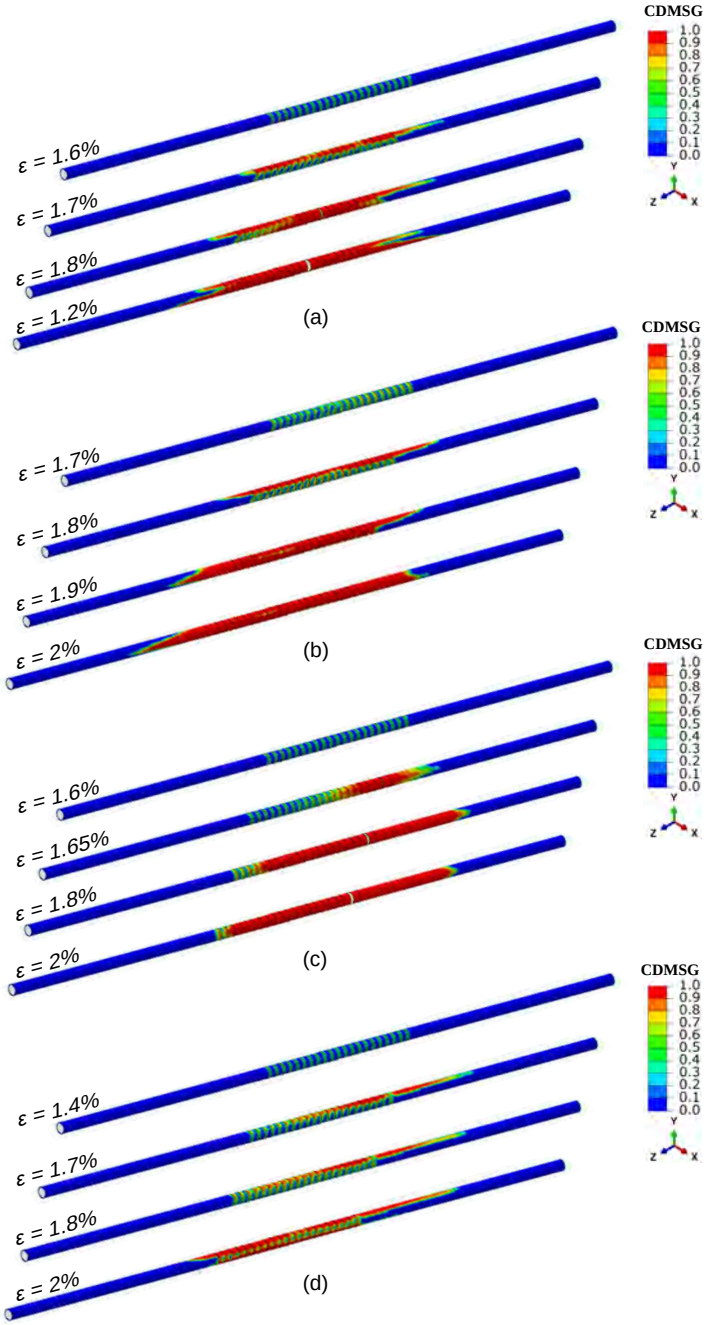

Figure 3.24: The progression of damage at the fiber/matrix interface as a result of longitudinal strain. a) fibre 28, b) fibre 30, c) fibre 101, and d) fibre 116.

Interestingly, it was discovered that some intact fibers, even when not broken, experience interface debonding. Although these fibres do not become completely debonded, the partial decohesion of their interfaces affects the stress redistribution. Partial debonding affects the surface sections of the neighboring fibres facing the broken fibre. The further away the intact fibre is from the broken one, the less affected its interface is.

Figure 3.25 shows the matrix plasticity in various strains. It reveals that plastic deformations form around broken fibers and increase significantly as the number of broken fibers increases (growth in cluster size).

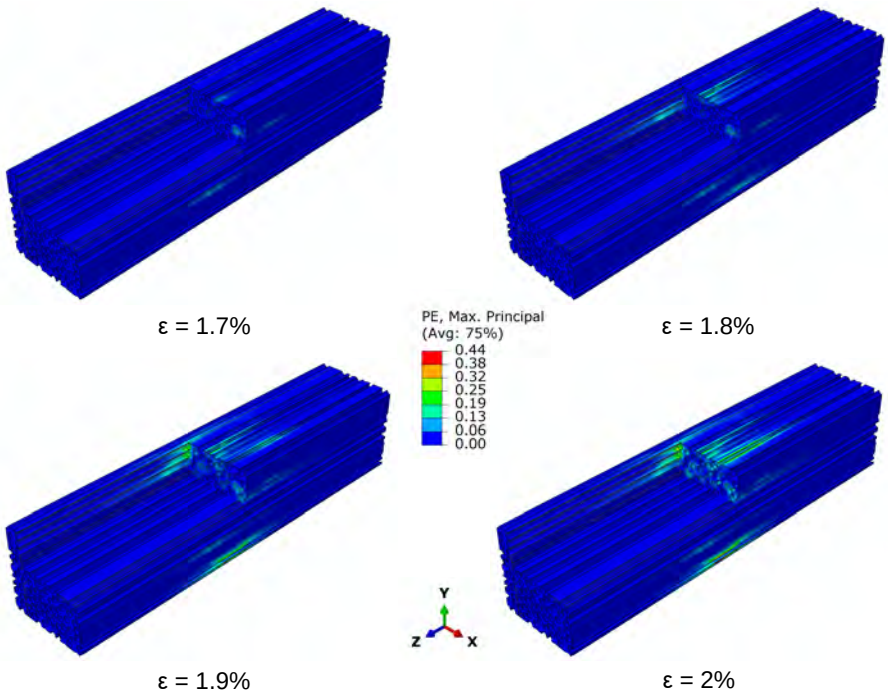

Figure 3.25: Evolution of matrix plasticity as a result of longitudinal strain. A section of the matrix is cut to improve visibility.

The post-curing thermo-mechanical equilibrium resulted in an average longitudinal shrinkage of the RVE of approximately 0.3%. Due to higher thermal expansion, the resin shrinks more than the fiber during the cooling process. In this case, the fiber acquires a positive (tensile) strain while the matrix acquires a negative strain. As a result, when the fibers cool, they become compressed, and the matrix becomes strained in tension. This causes an increase in the

deviatoric stress component of the stress, which has a greater influence on the occurrence of plasticity in the matrix. Nevertheless, this does not sensibly affect the strain-to-failure of the system in the subsequent mechanical load step, which keeps being totally controlled by the breakage of the fibres. However, they have considerable influence on the fibres ineffective lengths and debonding, which will be explored in detail later in Chapter 4.

3.5 Concluding remarks

This chapter was devoted to the micromechanical modelling of the tensile failure in a UD AS4/8552 composite. To predict the failure and longitudinal behavior of UD composites with high accuracy, a computational micromechanics framework based on experimentally characterised material constituents was developed. An exclusive damage model has been implemented for each constituent, such as fiber, matrix, and interface, to capture different types of failure. The models, boundary conditions, RVE generation, and main driving motivations for each parameter are all detailed.

The developed micromechanics model can reproduce the experimentally observed ply behavior in great detail. The result obtained by the micromechanics model was compared with the experimental results from the literature as well as the manufacturer data sheet (Hexcel). The predicted tensile strength was in very good agreement with the experimental results. It was demonstrated that under longitudinal tension, fibre failure is dominated by the presence and distribution of defects in the fibres, and that fibre failure rarely occurs in the same plane, instead failing in multiple plains based on the locations of the weaker regions. The microlevel fracture process has a strong local component related to stress redistribution following fiber breakage. Since the fiber fracture process is stochastic and heavily influenced by the number of fracture planes and fibers present in the RVE, simplified models with a limited number of fibers would not be precise enough.

A micromechanical study was also conducted to investigate the role of the fiber/matrix interface. Debonding began after the first fiber breakage, explaining the small non-linear region present in the stress-strain curve before reaching maximum stress. Some of non-linearity is also related to fibre breakage. However, it has a minor impact when compared to the fiber strength distribution,

which is determined by the Weibull parameters and the number of fibers present in the RVE. Interestingly, it was discovered that some intact fibers, even when not broken, experience interface debonding. Although these fibres do not become completely debonded, the partial decohesion of their interfaces affects the stress redistribution. Partial debonding affects the surface sections of the neighboring fibres facing the broken fibre. The further away the intact fibre is from the broken one, the less affected its interface is.

It was discovered that matrix plasticity forms around broken fibers and increases significantly as the number of broken fibers increases (increase in cluster size). Furthermore, it was noticed that, due to the large difference in fiber and matrix tensile strengths, regardless of the fiber strength distribution, the influence of matrix plasticity in the maximum stress borne by the RVE is low when compared to the influence of the fiber/fiber (cohesive plane in fibre) and fiber/matrix interfaces. During the post-peak regime and dynamic effect, matrix plasticity and damage become significant.

The micromechanics model is extremely accurate but extremely computationally demanding. This prevents it from being used for large RVEs with a large number of fibers. As a result, simplified models that still provide accurate results can be used to improve computational efficiency. In the case of longitudinal tension, for example, matrix plasticity can be ignored because it adds a significant computational cost with not much influence on the mechanical behaviour.

4

Effect of first-fiber failure: Deformation Mechanisms and Stress Concentration Factors

In this chapter, the stress redistribution and damage phenomena in the vicinity of the first-fibre break in unidirectional composites under longitudinal tensile loads are investigated by means of high-fidelity computational micromechanics based on experimentally characterised material constituents. In this framework, periodic microstructures with statistically representative random fibre packings are analysed, and transient dynamic analyses are performed to take into account the progressive failure and recoiling of a breaking fibre. The effects of mechanisms such as curing residual stresses, fibre/matrix debonding and matrix inelastic deformation on the first-fibre failure process are investigated.

4.1 Introduction

It has been shown that induced stress concentrations from a fibre break can have a significant influence on the whole process of longitudinal tensile failure [174, 175]. Therefore, an understanding of the stress distribution mechanisms associated with fibre breakage is a must to improve the current knowledge of composites' failure and improve their performance and applicability.

Along with breakage, a fibre loses its local load-transfer capability. In the process, the surrounding matrix is overloaded. Longitudinally, the matrix transfers the load back to the broken fibre through shear stresses in the fibre/matrix interface along a characteristic distance commonly referred to as the ineffective or recovery length [74, 76]. This mechanism is known as 'shear lag'. If the local shear stresses are sufficiently high they might cause fibre/matrix debonding which further increases the ineffective length. Around the fibre break, the matrix also transfers stresses to the neighboring fibres. The relative increase in induced stresses in intact fibres due to a neighboring fibre break is quantified using stress concentration factors (SCFs). Depending on the magnitude of the SCFs, additional fibre breaks can be triggered in the vicinity of the first broken fibre in a runaway mechanism leading to the formation of localised clusters of fibre breaks. Once a critical cluster size is reached, the fracture process becomes unstable, causing catastrophic failure of the composite [176]. This failure propagation scheme shows the importance of the stress redistribution upon first-fibre breakage.

There are two main approaches to calculate SCFs: i) shear lag modeling (SLM) and ii) finite element analysis (FEA). The first is an analytical methodology that

simplifies many complexities while assuming that all axial loads are carried by the fibres whilst the matrix only carries shear loads. Initially, SLM was used by Hedgepeth [77] for a 1D fibre packing, predicting a maximum SCF of 33%. Later, Hedgepeth and Van Dyke [49] extended this approach to 2D square and hexagonal fibre packings. They calculated a SCF of 14.6% for square and 10.4% for hexagonal packings. Ohno [177] combined SLM with the statistical Weibull distribution for the strength of continuous fibres to predict stochastic failure of unidirectional composites. Ryvkin [178] presented a 3D periodic analytical approach and used it for extensive parametric studies, such as various ratios of the fiber-to-matrix stiffness and fiber volume fractions, to investigate the behavior of a unidirectional FRP containing a broken fiber. Shear lag methods are very attractive because of their efficiency in terms of time and cost, allowing the analysis of large fibre clusters, but they have a significant drawback regarding accuracy because they do not easily account for realistic microstructures and relevant micro-deformation mechanisms such as fibre/matrix interface debonding. Several efforts have been undertaken to mitigate these issues [47, 61, 101] which have led to lower SCF estimations in comparison to Hedgepeth's initial prediction [77].

A more accurate approach to calculate SCFs and failure micromechanisms is FEA, as demonstrated by Xia and Okabe [60]. Three-dimensional FEA is computationally expensive, thus imposing limits on the size of the microstructure that can be analysed. Therefore, FEA is unpractical to tackle the fully representative simulation of the formation of clusters of fibre breaks, and on its own is insufficient to predict the statistical nature of composite strength. This problem can be mitigated by combining FEA and analytical SLM. The SCF profile around the first-fibre break can be numerically predicted based on a small representative volume element (RVE) of the microstructure and then be used as an input in an SLM of a sufficiently large RVE to tackle the failure of fibre clusters [169].

Nedele et al. [179] used FEA on a 2D hexagonal packing of carbon fibres. They assumed that the matrix remains entirely elastic and that a perfect bonding exists between the fibers and matrix, predicting a maximum SCF of 5.8% which is a value much lower than the 10.4% predicted using the SLM approach by Hedgepeth and Van Dyke[49]. Later, Xia et al.[60] showed that fibre shear

deformation, which is not considered in SLM, can affect stress redistribution and be the reason behind this SCF correction.

Van den Heuvel et al. [180] validated the accuracy of the FEA approach to the calculation of SCFs. Their micromechanical model consisted of a planar array of five carbon fibres positioned in the centre of an RVE. By taking into account fibre/matrix interface debonding, they demonstrated that an increase of the debonded length correlated with a decrease of the SCF. Furthermore, the effects of elastic–plastic matrix deformation were investigated leading to the prediction of longer fibre ineffective lengths and higher SCFs as compared with estimations considering elastically deforming matrices.

All previously mentioned studies, either based on SLM or on FEA, were performed on microstructures with regular fibre packings which are not statistically equivalent to fibre distributions in real FRP. Swolfs et al. [18, 67, 181] went a step further by considering random fibre arrangements. They carried out a wide range of studies in the SCF for both mono-fibre and fibre-hybrid unidirectional composites. These studies investigated the influences of several parameters, such as fibre distribution, fibre volume fraction (V_f) and fibre-to-matrix stiffness ratio, have on the SCFs, as well as the effects of matrix microcracks. Circular-section RVEs with random fibre packings, a pre-broken fibre at center and longitudinal symmetry were studied under static loading conditions. Elastically-behaving matrices and perfect fiber/matrix adhesion were assumed. The studies reported SCF values of 16%, 15% and 13%, respectively, for random fibre arrangements with V_f of 30%, 50% and 70%, which were found to be almost twice as high as those calculated for square fibre packings and three times as high as those for hexagonal packings. Moreover, they concluded that V_f and the fibre-to-matrix stiffness ratio exert a significant influence on the fibre ineffective length, although SCFs were little affected by the second parameter. The presence of matrix microcracks was found to have a negligible influence on SCFs and ineffective length [18, 67, 181].

Generally, SLM investigations on SCFs are based on the analysis of pre-broken microstructure-embedded fibers under static loading conditions [49, 77, 177, 178]. Curiously, most FEA on the same subject, although allowing for higher simulation fidelity, consider similar static equilibrium conditions which are unrealistic because the transient phenomena associated with brittle fiber failure

are not taken into account appropriately. The sudden fibre failure and elastic recoil can produce discontinuities in the evolution of stresses and other dynamic effects. Less than a handful of publications on SCFs and on the effects of fibre breakage are based on transient dynamic modeling. A remarkable example is the numerical study of Ganesh et al. [182] which is focused on the analysis of unidirectional glass FRP with 2D RVEs with regular fibre distributions. The dynamic analysis predicted a peak SCF of 30% that compared with a lower value of 13% for the equivalent static case [182].

The present research constitutes a step beyond the state of the art in the investigations of the effects of first-fibre failure in FRP. It explores the use of high-fidelity computational micromechanics modeling by means of 3D RVEs with statistically representative fibre distributions to investigate the transient effects of dynamic fibre failure on deformation mechanisms and SCFs around a progressively breaking fibre. The micromechanical analyses herein are based on a realistic material system, the carbon/epoxy AS4/8552, whose properties have been thoroughly characterized by means of experimental micromechanics in previous studies. Periodic boundary conditions (PBCs) [183] are employed to allow increased model representativeness with reduced computational domains.

In a first set of simulations (Section 4.3.1), the relevant deformation mechanisms associated with first-fibre failure are investigated and an appropriate baseline computational framework is established to analyse this phenomenon. To capture and assess the effects of different micromechanisms, several modeling approaches are explored: transient dynamic fibre failure, fiber/matrix interface debonding, matrix inelastic deformation, and curing residual micro-stresses. A second set of computations (Section 4.3.2) is conducted with the established modeling approach to study the influence of several microstructural parameters on failure phenomena and SCFs: fibre volume fraction, fibre failure probability, fibre-to-matrix stiffness ratio and fibre/matrix interface strength.

4.2 Micromechanics modeling framework

A general computational micromechanics framework, implemented in the commercial software Abaqus/Standard [145], is used throughout the present research.

4.2.1 Periodic RVE approach

A 2D periodic RVE of the unidirectional composite ply is generated, employing the random sequential adsorption (RSA) algorithm, as detailed in Section 3.2.1, to reproduce statistically representative microstructures. The size of the generated ply section is width (W) = height (H) = $12 \times R$, wherein R is the average fibre radius, and contains 34 fibres on average. This section is extruded along the fiber direction, to a total length $L = 84 \times R$, to achieve the final 3D RVEs (Figure 4.1b). The resulting models contain a single fibre allowed to break through a fracture plane set at $z = L/2$. The remaining fibres can only deform elastically. The breaking fibre is always generated at the centre of the RVE, in spite of the different (random) microstructures (Figure 4.1a). The RVE size was selected based on well-informed parametric studies that targeted the best trade-off between computational effort and proper capturing of the relevant deformation phenomena with minimum interference of model boundaries. In this respect, the fulfillment of the following conditions was sought: i) L should be large enough to allow a complete stress recovery in the broken fibre, guaranteeing that the remote stresses at $z = \{0, L\}$ are not influenced by the fibre break, and ii) H and W should be large enough to allow a nearly complete stress redistribution between the broken fibre and its neighbors. The sectional dimensions were firstly estimated based on previous studies which concluded that the SCFs decay to negligible values within distances $d > 2R$ from the broken fibre [18, 181].

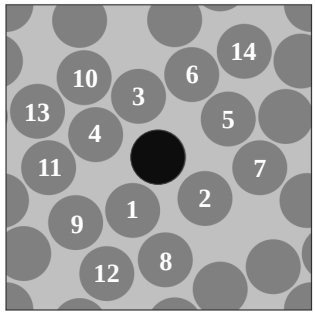

(a)

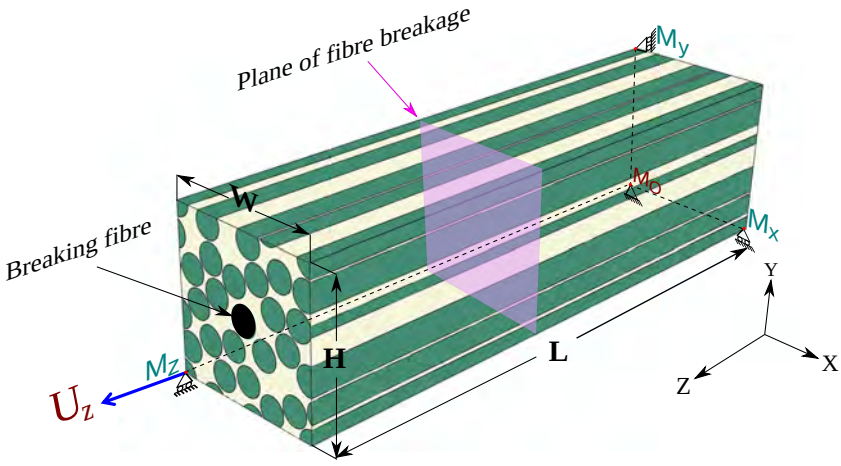

(b)

Figure 4.1: a) Reference RVE section with $V_f = 60\%$. The pre-broken or failing fibre (indicated in black) is always located at the center. Intact neighboring fibres are numbered, based on the distance from broken fibre, for reference in the text. b) Extruded 3D RVE model with details of boundary and initial conditions. The fracture plane of the breaking fibre is always located at $z = L/2$.

Matrix and fibres are modeled as separated geometrical entities that interact by means of cohesive behaviour and contact kinematics explained in Section 3.1.3. To this purpose, the penalty-based general contact algorithm in Abaqus/Standard is coupled with the surface-based cohesive zone method [145]. A similar strategy is used to simulate the breakage of the central fibre which is modeled as two geometrical rods in top-to-top surface contact. The separation of the initially contacting surfaces is governed by cohesive behaviour to simulate the

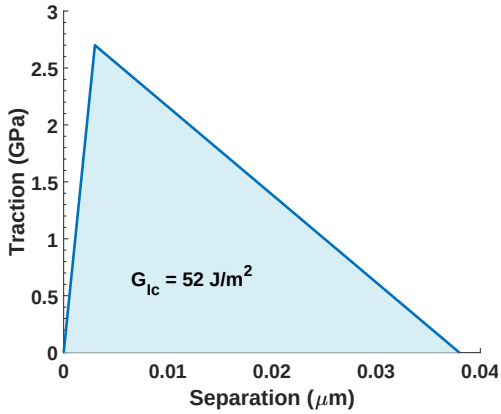

Figure 4.2: Bi-linear cohesive law used to model progressive fiber breakage. The maximum traction is a stochastic value given by the Weibull fibre failure probability distribution function (here σ_f= 2.7 GPa).

progressive breakage of the fibre. Appropriate cohesive laws are coupled to the contact kinematics to simulate either fibre-matrix debonding or fibre breakage. The complete 3D RVE is discretized with fully integrated brick (C3D8) and wedge (C3D6) isoparametric elements with an average characteristic length of 1 μm, totalling around $\geqslant 195,000$ elements. This discretization is judged, after parametric analysis, to be fine enough to capture the high stress gradients around a fibre break. Node positions on opposite faces of the RVE are identically located in order to apply PBCs, and ensure the displacement continuity with the neighboring RVEs. According to the methodology developed by Segurado and LLorca [163], PBCs are introduced as nodal displacement constraints between equivalent nodes at opposite RVE faces, by enforcing the relations:

$$\begin{aligned} \overrightarrow{u}(0,y,z) - \overrightarrow{u}(W,y,z) &= 0 \\ \overrightarrow{v}(x,0,z) - \overrightarrow{v}(x,H,z) &= 0 \\ \overrightarrow{w}(x,y,0) - \overrightarrow{w}(x,y,L) &= U_z \end{aligned} \tag{4.1}$$

through face master nodes $M_O(0,0,0)$, $M_X(W,0,0)$, $M_Y(0,H,0)$, $M_Z(0,0,L)$ (Figure 4.1b). U_i $(i = x,y,z)$ are the arbitrary unidirectional displacements imposed on the master nodes.

Readers are referred to Sádaba et al. [183] for an in-depth description of the use of PBC in multiscale analyses of composites. A longitudinal tensile load

is applied by means of controlled displacement on the front plane master node ($z = L$), $U_z \neq 0$.

An incremental implicit dynamics integration procedure is adopted using Abaqus/Standard [145] for Moderate Dissipation applications. This option is available to introduce a small amount of viscous damping (Rayleigh damping) [184] that enables the numerical convergence of highly nonlinear problems, e.g. involving contacts, without significantly degrading solution accuracy [185]. It provides a convenient abstraction to damp lower (mass-dependent) and higher (stiffness-dependent) frequency range behavior. To this end, a damping matrix C is added to the system. This damping matrix is linearly proportional to mass M and stiffness K matrices [184]:

$$\mathbf{C} = \alpha\mathbf{M} + \beta\mathbf{K} \tag{4.2}$$

C matrices are generated for each material in the model. The damping factors α and β can be estimated using modal analysis [145]. These variables are defined in Abaqus under the Material Properties subsection. Several sources of damping naturally exist in material systems but its right amount is difficult to evaluate. Some simulations were conducted with higher levels of damping that did not lead to significant changes in the results. However, lower levels of damping which could be more realistic were not applicable because they hindered numerical convergence.

Time increment plays a key role in numerical transient dynamic analyses. It should be selected as small as necessary in order to capture the relevant dynamic deformation mechanisms without excessively compromising computation time. The minimum characteristic time of any dynamic deformation event in a continuous medium is given by the the speed of the stress wave, which can be estimated using the Newton-Laplace equation for an equivalent medium of density ρ and homogenized Young's modulus E as $c = \sqrt{E/\rho}$. For an AS4 fibre, the critical constituent in the micromechanics model, this translates into a characteristic time step of $t_c = D/c = 0.63ns$ (D is the diameter of fibre). Such a small time increment is not practical in the present analysis framework. Fortunately, the shortest relevant event in the present analyses, fibre breakage, is orders of magnitude slower than stress wave propagation through the composite medium. By means of preliminary FEA, the characteristic time for complete

breakage of a microstructure-embedded AS4 fibre was predicted to be around 4 μs. The preliminary model to establish the fibre breakage time was, in all respects, based on the main RVE modeling approach, albeit with a much smaller cross section containing a single matrix-embedded fibre which was allowed to break. Because of its numerical efficiency, it allowed to carry dynamic analysis with time increments in the order of *ns*, henceforth simulating the progressive fibre breakage, matrix debonding and recoil process in a very refined way. To allow practical multi-fibre RVE analyses while still capturing the progressive fibre breakage, albeit in a very coarse way, the time increment in those models is fixed at 1 μs.

The number of stress wave interactions during a fibre break, taking into account the reflections on model boundaries, is in the order of 10^3. This means that the physical process is barely controlled by stress wave propagation and that inertial effects are expected to be reduced or damped within a localized region. The process, although transient in nature, is expected to be largely dominated by the conditions of quasi-static equilibrium. It must be noticed that this condition is essential to the consistent application of PBC that enforce 'instantaneous' kinematic constraints across the RVE.

Set with the above-mentioned parameters, the typical RVE analyses require around a day to complete in an HPC cluster of 50 Intel Xeon E5-2670 cores and GPU acceleration.

4.2.2 Model constituents

The aeronautical-grade carbon FRP system AS4/8552, with fibre volume fraction, $V_f \approx 60\%$, was chosen as the reference material for the purpose of demonstrating the methodology. The constitutive models and experimentally-characterized properties of fibre, matrix and interface constituents for this material system have been thoroughly presented in Chapter 3. For the sake of completeness, the essential or distinctive aspects are overviewed herein.

The 8552 epoxy polymer matrix is represented using the isotropic plasticity model included in Abaqus/Standard [145] which is based on pressure-dependent Druker-Prager [144] plastic behaviour coupled with tensile damage degradation to simulate brittle materials [142]. The elasto-plastic-damage properties of the

8552 epoxy matrix follow literature-available values and in-house experimental characterization by means of nanoindentation tests [120] (Table 4.1).

The fibre-matrix interface is modeled using the surface-based implementation of the cohesive zone method in Abaqus/Standard [145] which is coupled with Coulomb frictional behaviour to simulate the sliding of the fibres upon decohesion. A mixed-mode bilinear traction-separation law is used to define the cohesive behaviour. Damage initiation is triggered using a quadratic stress-interactive criterion, and damage propagation is controlled by the Benzeggagh-Kenane criterion [151]. The strength properties of the AS4/8552 fibre/matrix interface follow in-house experimental characterization by means of the push-in tests reported by Naya et al. [120, 156], and are presented in Table 4.1. Without compromising numerical convergence, the elastic stiffness values of the cohesive law are chosen to be sufficiently high in order to maintain the continuity of displacements across the cohesive surface until failure is initiated.

The AS4 fibres, with a measured average diameter $2R = 7.09\ \mu m$, are modeled as linear elastic and transversely isotropic solids. Their thermo-elastic properties were obtained from literature-available data [120] and experimental characterization performed in-house [119] (Table 4.1). The progressive breakage of the central fibre in the RVE is enabled at the defined fracture plane located at $z = L/2$ by means of the surface-based traction-separation behaviour implemented in Abaqus/Standard [145], in a similar fashion to the modeling of fibre-matrix debonding. The bilinear traction-separation law is, in this case (Figure 4.2), governed by the fibre strength and fracture energy values which have been experimentally characterized in-house [119]. Governed by the cohesive law, the predefined crack is allowed to start opening at a specified traction value, corresponding to fibre strength, and to develop progressively until the fracture energy associated with fibre breakage is completely dissipated and the crack surfaces become fully separated. Except where otherwise stated, the interface strength adopted is the average value of the statistical fibre strength distribution which can be described using a two-parameter Weibull probability density function [19] in the following form:

$$P(\sigma_f) = 1 - exp\left[\frac{L}{L_0}\left(\frac{\sigma_f}{\sigma_0}\right)^m\right] \tag{4.3}$$

wherein $P(\sigma_f)$ is the cumulative probability of failure of a fibre of length L at a stress level of σ_f. The parameters σ_0 and m are, respectively, the scale and shape of the Weibull distribution, and L_0 is the reference gauge length. The Weibull cumulative distribution for the strength of AS4 fibres is plotted in Figure 4.3, and is characterized by $P(\sigma_f$=2.7GPa$) = 50\%$. The fracture energy (G_f) of AS4 carbon fibres is 52 J/m^2 [119].

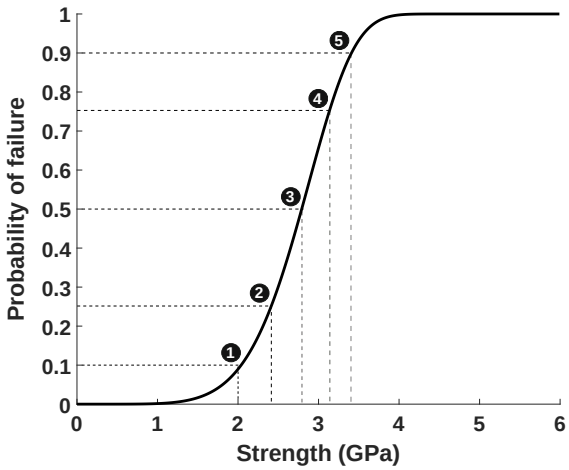

Figure 4.3: Weibull probability of failure distribution of AS4 carbon fibres [119]. Five discrete values are marked (2.0, 2.4, 2.7, 3.1 and 3.4 GPa) corresponding, respectively, to probabilities of failure of 10%, 25%, 50%, 75% and 90%. The reference gauge length is equal to 20 *mm*.

4.2.3 Post-processing of results

The required data are extracted from the evolving 3D stress field in the RVE using a python script. The analyses show that stress distributions across fibre cross-sections are not uniform, and the side of an intact fibre closer to the broken fibre receives a higher induced longitudinal stress than the opposite side, as observed in previous research [18]. It is likely that these stress gradients influence the process of longitudinal tensile failure in unidirectional composites. However, the study of this effect is not within the scope of the present work. For simplification, and following previous studies [18, 67, 181], the average stresses throughout the fibres cross-sections are used. Within each fibre, the average stresses are calculated at 20 equidistant planes parallel to the fracture plane, distributed at z^* coordinates multiple from $2R$. The mean stress in each

Table 4.1: Mechanical properties of materials used throughout the present work: E is the elastic modulus; ν is the Poisson ratio; α is the thermal conductivity; σ_{t0} is the tensile strength; G_t is the fracture energy under tension; σ_{yc} is the compression yield limit; σ_{uc} is the compression strength; N and S are the normal and shear interface strengths; k_{nn} and k_{ss} are the normal and shear interface penalty stiffness values; G_n and G_s are the normal and shear interface fracture energies; η_{BK} is the Benzeggagh Kenane fitting parameter. In general, superscripts ^{f,m} refer to quantities of the fibre and matrix respectively, while subscripts $_{1,2}$ indicate longitudinal and transverse properties.

AS4 carbon fibre							
E_1^f [GPa]	E_2^f [GPa]	ν_{12}^f	ν_{23}^f	G_{12}^f [GPa]	G_{23}^f [GPa]	α_1^f [10^{-6} °C^{-1}]	α_2^f [10^{-6} °C^{-1}]
231	13	0.3	0.46	11.3	4.45	-0.9	7.2
8552 epoxy matrix							
E^m [GPa]	ν^m	α^m [10^{-6} °C^{-1}]	σ_{t0}^m [MPa]	G_t^m [GPa]	σ_{yc}^m [MPa]	σ_{uc}^m [MPa]	
5.07	0.35	52	121	90	176	180	
AS4/8552 fibre-matrix interface							
Interface	N [MPa]	S [MPa]	K_{nn} [GPa/um]	K_{ss} [GPa/um]	G_n [J/m]	G_s [J/m]	η_{BK}
Standard	42	63	100	100	2	100	1.2
Weak	34	52	100	100	2	100	1.2
S2 glass fibre							
E_1^f [GPa]	E_2^f [GPa]	ν_{12}^f	ν_{23}^f	G_{12}^f [GPa]	G_{23}^f [GPa]	α_1^f [10^{-6} °C^{-1}]	α_2^f [10^{-6} °C^{-1}]
85	85	0.2	0.2	35.4	35.4	16	16
MTM44-1 matrix							
E^m [GPa]		G^m [GPa]		ν^m		α^m [10^{-6} °C^{-1}]	
4.0		1.43		0.4		40	
S2/MTM44-1 fibre-matrix interface							
N [MPa]	S [MPa]	K_{nn} [GPa/um]	K_{ss} [GPa/um]	G_n [J/m2]	G_s [J/m2]	η_{BK}	
70	103	100	100	2	100	1.2	

plane is calculated as

$$\bar{\sigma} = \frac{1}{\sum V^e} \int_{V^e} \sigma^e dV \tag{4.4}$$

wherein σ^e is the longitudinal stress in each cross-sectional finite element of volume V^e. Finally, the SCF at a given fibre plane, at z^* distance from fracture plane, is calculated as the relative increase in average stress, $\bar{\sigma}_z$, normalized by the remote average stress ($z = L$) as proposed by Fukuda [186]:

$$SCF(z^*) = \frac{\bar{\sigma}_z(z = z^*) - \bar{\sigma}_z(z = L)}{\bar{\sigma}_z(z = L)} \times 100\% \tag{4.5}$$

4.3 Results and discussion

4.3.1 Relevant micromechanisms associated with first-fibre breakage

This section analyses various deformation micromechanisms associated with first-fibre breakage. To isolate the specific effects of progressive fibre failure, fibre/matrix interface debonding, matrix inelastic deformation, and post-curing residual stresses, variations of the reference modeling approach described above are explored and the respective results correlated. This strategy helps in consolidating the most appropriate computational methodology to predict SCFs and to capture the relevant physical phenomena at play. For the sake of illustration, the single microstructure presented in Figure 4.1 is considered in all studies in this section.

4.3.1.1 Progressive fibre breakage and recoil

This study is based on the comparison between two different modeling and simulation approaches. On the one hand, the reference approach described above, wherein the transient dynamic analysis of the full process of progressive fibre breakage and recoil is simulated and on the other hand, the static analysis of a composite RVE containing a pre-broken fibre, and subjected to incremental loads, corresponding to the approach usually adopted in literature-available investigations. These two cases only differ on the initial integrity state of the central RVE fibre, intact vs. pre-broken (Figure 4.1), and on the solution

procedure: whilst the pre-broken fibre case is analysed considering simplified static equilibrium, the progressive fibre failure analysis is performed by means of implicit dynamic integration. In both cases, the phenomena of fibre/matrix interface debonding and of matrix inelastic deformation are considered.

Figure 4.4 plots the evolution with time of stress in the nearest intact fibre (fibre 1 in Figure 4.1a), for the dynamic case, and compares it with the applied far-field stress. The static and dynamic evolutions of the SCF in the same fibre with increasingly applied strains are compared in Figure 4.5a. The line corresponding to the static analysis shows that the SCF rapidly grows from the initial load stages up to 14.9% at an applied strain of $\varepsilon \approx 0.3\%$ and then gradually decreases. In contrast, the dynamic SCF is zero until the fibre breaking strain is reached ($\varepsilon \approx 1.2\%$), at which point it suddenly jumps to a maximum value of 15.4%; much higher than the static SCF for this level of applied strain. This peak is short ($\approx 15\mu s$) and rapidly fades away (zoom-in box in Figure 4.4). Within 60 μs, and after a few rapidly damped oscillations, the evolution of the dynamic SCF converges to that of the static analysis. It must be noted that this oscillatory behaviour is dependent on the amount of damping used in the dynamic analyses which, in the present work, is not supported by physical characterization. However, even admitting a reasonable level of uncertainty, it is safe to state that the processes occurring within this window of transient behaviour are still much slower than stress wave propagation throughout the material, allowing for a number of stress wave reflections and interactions in the order of 10^4. Therefore, after an initial stress peak where inertial effects play a significant role, the fibre failure process can be assumed to be dominated by force equilibrium.

At $\varepsilon \approx 2.3\%$, inflections of the SCF behaviours are observed for both static and dynamic cases (Figure 4.5a), which denote interference of the model boundaries with the stress distribution, i.e. the domain affected by the stress redistribution due to the first-fibre break extends to the model boundaries. Hence, the numerical predictions beyond this applied strain are considered invalid.

The behaviours of SCFs for the nearest neighboring intact fibres (Figure 4.1a) are drawn in Figure 4.5b, which gives a broad overview of the SCF discrepancy between counterpart fibres in dynamic and static analyses. The most notable phenomenon is the decay of the dynamic stress concentration peak towards the

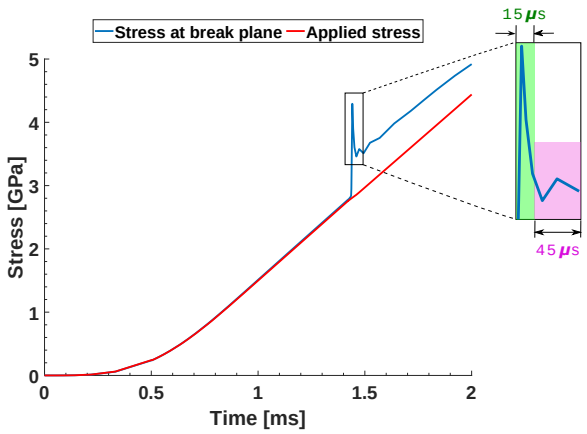

Figure 4.4: Evolution with time of average stress in the nearest intact fibre (fibre 1 in Figure 4.1a) for the dynamic case.

fibres furthest away from the first-fibre break. Fibres that are distanced more than d from the breaking fibre feel immediate stress increases that converge to the values expected from static behaviour without overshooting. Another interesting observation is that the maximum static SCFs at fibres away from the fibre break occur at higher applied strains, although they decrease in value. This is because, with increasing applied load, the stress redistribution progressively involves a larger volume of material around the broken fibre.

The profiles of maximum SCF for each fibre as a function of the distance to the broken fibre, in the plane containing the fibre break, are plotted in Figure 4.6a for the static and dynamic cases. The presented values correspond to the occurrence of the peak SCF in each case ($\varepsilon \approx 0.3\%$ in the static analysis and $\varepsilon \approx 1.2\%$ in the dynamic analysis). The dynamic SCFs are higher than the static values but not significantly, specially in the nearest intact fibres where the difference is only of about 4%. The increasing difference is the result of the different deformation micro-mechanisms around the broken fibre.

The ineffective length is usually taken as the distance along the broken fibre required to recover 90% of the applied far-field stress, σ_L. Figure 4.6b correlates the stress recovery profiles between the dynamic and static cases, at the respective instants of maximum SFCs. It can be observed that the ineffective length is 20% higher for the dynamic case i.e. the stress-affected fibre length is underpredicted with the static analysis. This difference is, again, the result of

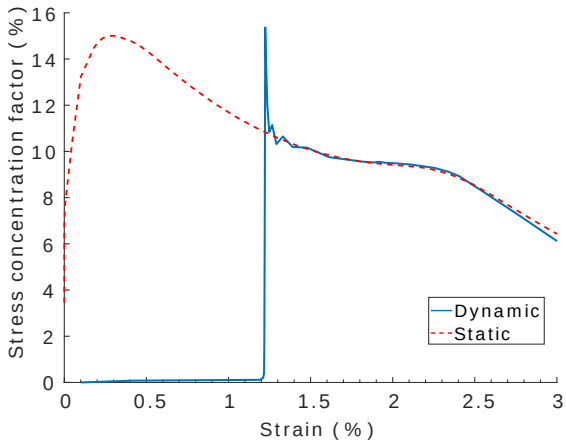

(a)

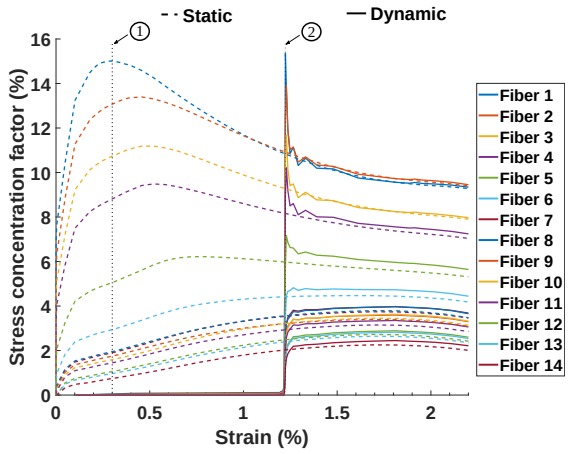

(b)

Figure 4.5: a) Evolutions of SCFs with applied strain for nearest intact fibre (fibre 1 in Figure 4.1a) in static and dynamic analyses. b) Behaviour of SCFs for several neighboring intact fibres in static and dynamic cases. Marks 1 and 2 indicate the strain levels at which SCF profiles are extracted for static and dynamic cases.

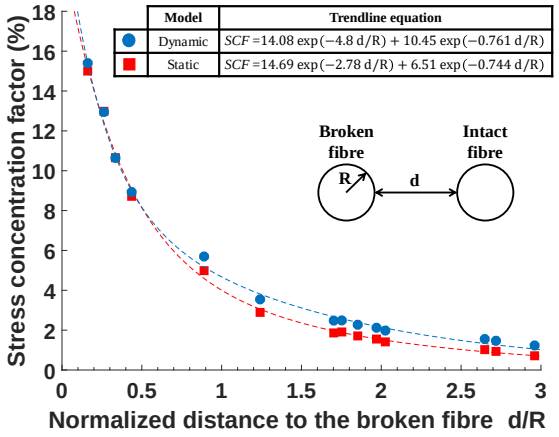

(a)

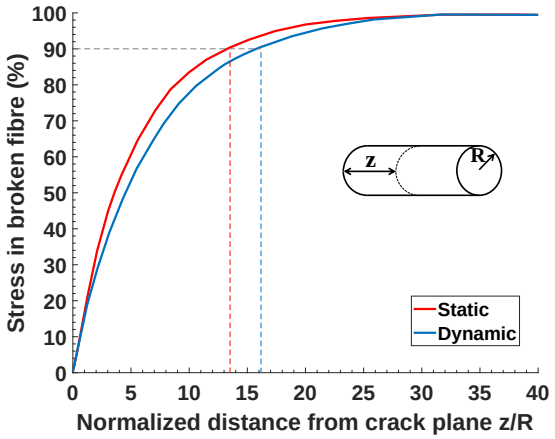

(b)

Figure 4.6: a) SCF profiles corresponding to maximum stress concentrations in static and dynamic analyses (marks 1 and 2 in Figure 4.5b). Each data point represents one intact fibre. b) Stress recovery profiles in broken fibres for static and dynamic cases.

the different deformation micro-mechanisms around the first-fibre break.

The relevant micromechanisms that affect stress distribution characteristics such as SCFs and ineffective length, are fibre/matrix interface debonding and matrix inelastic deformation. Figure 4.7a correlates the predicted interface damage and interface debonding length in the broken fibre between the static and dynamic analyses, at corresponding instants of maximum SCF. The fibre debonding predicted by the dynamic simulation is approximately six times longer than what is computed with the static analysis. The progresses of fibre debonding with applied strain are depicted in Figure 4.7b. The growth of debonding is slow but steady in the static simulation, roughly linearly increasing with applied strain. In the dynamic case, the fibre/matrix interface is kept intact until the moment of fibre breakage. At this point the fibre starts to debond very rapidly as it recoils in the matrix. This instant is equal to the duration of the stress peak (Figure 4.5a). The debonding process is rapidly arrested and the debonding behaviour with applied strain converges to the linear evolution predicted by the static analysis. The linear behaviour is lost for $\varepsilon \geq 2.3\%$, corresponding to inflections in the evolution of SCFs (Figure 4.5a), because the debond fronts approach the RVE boundaries ($z = 0$, $z = L$). Therefore, the simulation results are not valid at such high applied strains.

Figure 4.8 shows that whilst the level of matrix plastic deformation predicted in the static case is negligible, it is quite relevant in the dynamic case, with the plasticized region spreading towards the neighboring fibres. This is the reason why the stress-affected volume of matrix around the fibre grows wider in the dynamic case, requiring longer radial distances for the SCFs to fade (Figure 4.6b). In contrast, the dynamic SCFs in the fibres that interfere with the matrix inelastic region are relatively lower compared to what they would be in case where the matrix behaves elastically, hence the small increase in SCF in the fibres close to the break when compared to the static analysis.

In summary, the static pre-broken fibre analysis leads to a maximum SCF for an applied remote strain that is lower than that required to break the fibre. Therefore, the realistic stress redistribution and deformation mechanisms are only captured when progressive first-fibre breakage is considered by means of dynamic analysis. The fibre debonding length and matrix inelastic deformation at the instant of maximum stress concentration are significantly more pronounced

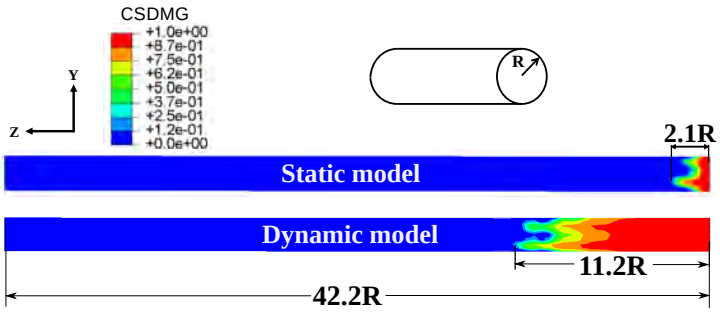

(a)

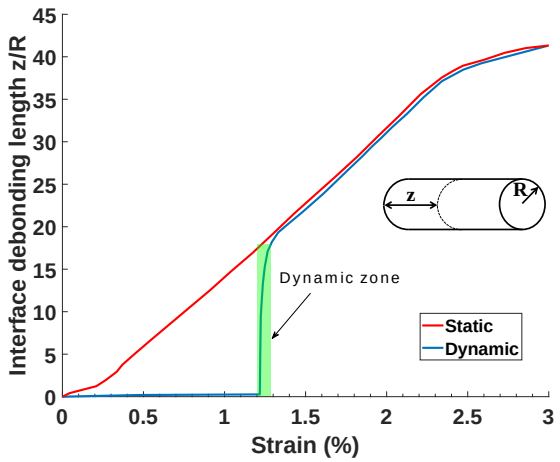

(b)

Figure 4.7: a) Broken-fibre/matrix interface damage predictions by static and dynamic simulations at respective moments of maximum SCF values ($\varepsilon \approx 0.3\%$ and $\varepsilon \approx 1.2\%$ for static and dynamic models, respectively). b) Broken fibre debonding length vs. applied strain for static and dynamic cases.

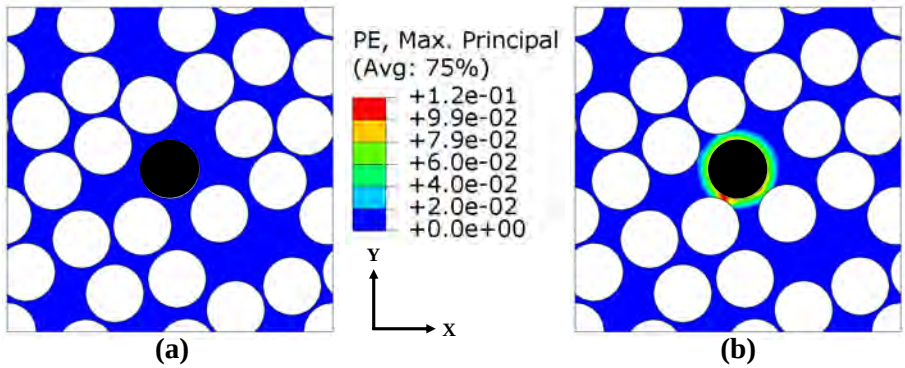

Figure 4.8: Comparison of matrix plasticity levels in the plane containing the fibre break between (a) static and (b) dynamic analyses, for respective maximum SCF values ($\varepsilon \approx 0.3\%$ and $\varepsilon \approx 1.2\%$ for static and dynamic cases, respectively).

in the dynamic case. As a result, the broken fibre ineffective length and the peak SCF are also higher. The conclusion is that static analysis is an oversimplified methodology to study the longitudinal failure mechanism and SCFs. Hence, the following studies on first-fibre breakage are based on dynamic progressive failure simulations.

4.3.1.2 Fibre/matrix interface debonding

To study the effects of fibre/matrix interface debonding on failure micromechanisms and SCFs around a broken fibre, the results of the reference dynamic modeling approach described above are compared with the ones of equivalent numerical simulations in which perfect fibre/matrix adhesion is considered.

The SCF distributions for both cases are compared in Figure 4.9a. At similar distances to the broken fibre, the SCFs are about 50% lower for the case of perfect interfaces. It is noteworthy that this trend is the opposite to what was reported in previous publications based on static analyses [180] that concluded that the SCFs decrease with the occurrence of debonding of the broken fibre. However, those studies reported a maximum SCF of approximately 14% for a perfect fibre/matrix interface which is substantially higher than the current prediction for similar conditions.

The current result can be interpreted by analysing the stress recovery profiles shown in Figure 4.9b. A perfect interface leads to a much higher gradient of stress recovery and a substantially shorter ineffective length (about 30%). Hence,

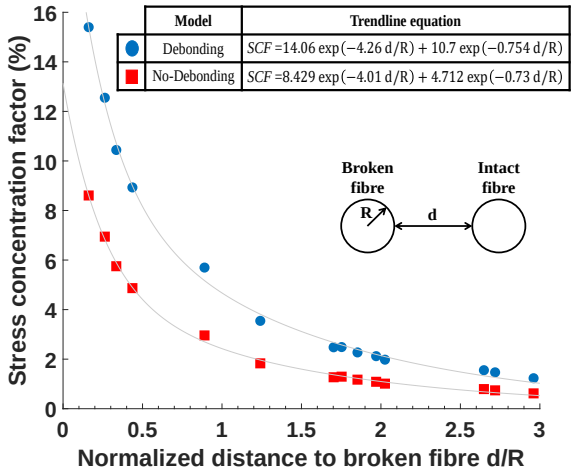

(a)

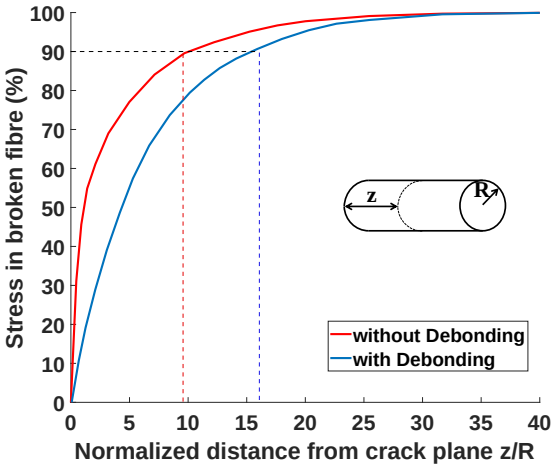

(b)

Figure 4.9: a) Maximum SCF values predicted by simulations considering perfect and imperfect fibre/matrix interfaces. b) Broken-fibre stress recovery profiles for both cases.

the stress loss is less pronounced when the interface of the broken fibre is perfect, and the SCFs in neighboring intact fibres are lower.

Fibre/matrix interface damage in the broken fibre at the moment of maximum SCFs ($\varepsilon \approx 1.2\%$) is represented in Figure 4.7a. This study reveals that, in addition to the debonding of the broken fibre, interface damage also occurs in its neighbors (Figure 4.10). Although these fibres do not become completely debonded, the partial decohesion of their interfaces affects the stress redistribution. Partial debonding affects the surface sections of the neighboring fibres facing the broken fibre. The further away the intact fibre is from the broken one, the less affected its interface is. In the present case, only interface sections within a distance $2R$ from the broken fibre are affected (R is the radius of fibre). The fading effects with distance are both in terms of the arc surface section and length of the affected fibre. It is remarkable that the partial debond can be as long as the broken-fibre full-debond length (Figures 4.7a vs. 4.10b).

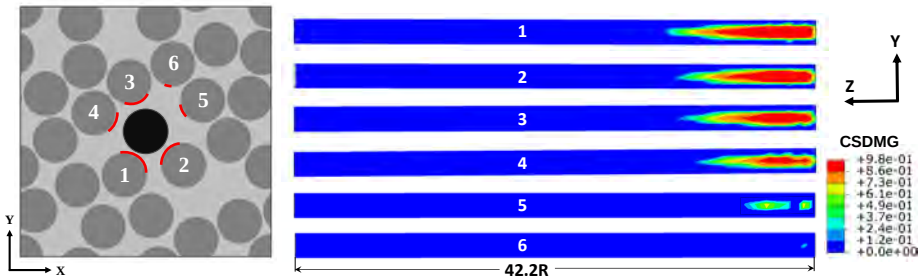

(a) (b)

Figure 4.10: a) Sectional view of the integrity of the interfaces of broken-fibre neighbors (fibre debonds indicated in red) at the moment of maximum SCFs ($\varepsilon \approx 1.2\%$). b) Longitudinal view of fibre debonding on the same fibres (approximate debonding lengths of $11.2R$, $10.8R$, $10.6R$, $9.2R$, $5.4R$ and $1.1R$ for fibres 1 to 6, respectively).

Figure 4.11 shows that the extent of the matrix plastic deformation around the broken fibre is higher when it is allowed to debond. This is the result of the more pronounced unloading of the broken fibre and the transfer of higher shear loads to the matrix.

It can be extrapolated from this study that the SCFs would be predicted to be even lower if, in addition to perfect interfaces, the matrix is considered to behave elastically. Nevertheless, the major conclusion is that the simulation of fibre/matrix debonding is essential for the realistic simulation of the effects of

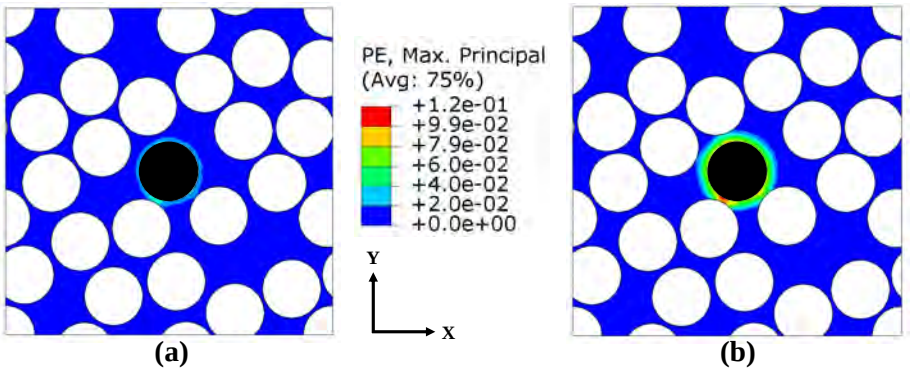

Figure 4.11: Correlation of matrix plastic deformation levels ($\varepsilon \approx 1.2\%$) for simulations a) without interface debonding and b) with interface debonding.

first-fibre breakage.

4.3.1.3 Matrix inelastic deformation

To investigate the effect of matrix inelastic deformation, i.e. plasticity and microdamage, on the consequences of first-fibre breakage, the reference simulation approach is compared with a simplified one wherein the matrix behaves linear-elastically. All remaining modeling aspects are kept similar.

Figure 4.12a compares the SCF profiles predicted by both approaches. The simplified model results in SCF values up to 10% higher, especially around the fibre break. The difference to the reference SCF profile fades out as the distance to the broken fibre increases. This indicates that matrix inelastic deformation has a local stress shielding effect, a conclusion that is corroborated by the results in Figure 4.13 which illustrates the cross-sectional region of matrix plasticity, in the reference model, just after first-fibre breakage. The stress shielding effect only affects the nearby fibres, typically those located within $d/R \leqslant 1$.

The ineffective and debonding lengths are, respectively, about 10% and 12% higher for the simulations that take into account matrix inelastic deformation micromechanisms, as represented in Figure 4.12b. It can be concluded that the higher matrix straining around the broken fibre also contributes to fibre/matrix debonding, hence elongating its ineffective length.

In summary, an elastic matrix allows the concentration of higher stresses around the fibre break. This leads to higher stresses in the plane of the breakage but

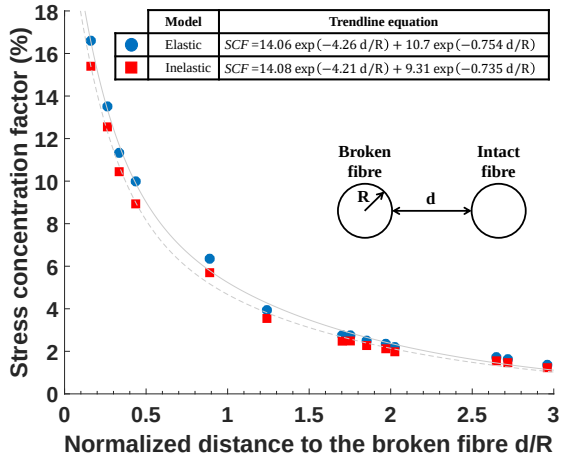

(a)

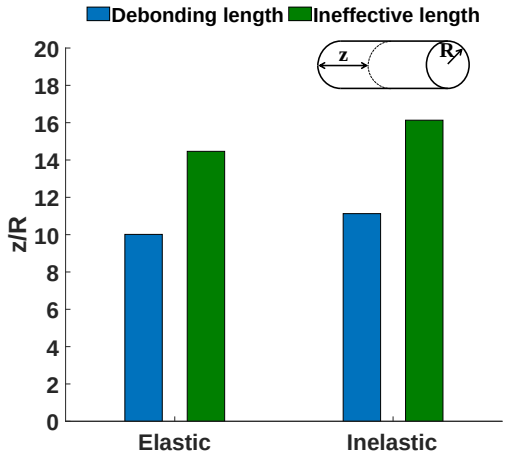

(b)

Figure 4.12: a) Maximum SCF values for simulations with elastic and inelastic matrices. b) Ineffective and interface debonding lengths, corresponding to maximum SCFs, for both cases.

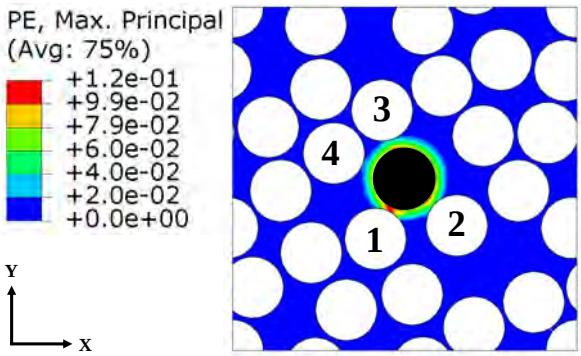

Figure 4.13: Maximum matrix plasticity levels predicted by the reference simulation ($\varepsilon \approx 1.2\%$). The numbered fibres are those most affected by matrix inelastic deformation.

also allows their decay over shorter distances along the longitudinal direction, resulting in shorter ineffective and debonding lengths. Matrix inelastic deformation has a stress shielding effect but contributes to longer fibre debonding and ineffective length.

4.3.1.4 Residual curing stresses

The micromechanical behaviour of FRP can be affected by the occurrence of post-curing thermo-mechanical residual stresses that arise due to the different thermal expansion coefficients of the fibres and the matrix.

To account for these effects, the reference numerical procedure is modified by applying a thermo-mechanical loading step before the standard progressive longitudinal mechanical loading. In the thermo-mechanical step, the temperature of the system is varied from the material curing temperature ($T_c = 180°C$ for AS4/8552) down to room temperature ($T_r = 20°C$). The thermo-mechanical coupling and equilibrium are governed by the fibre and matrix thermal expansion coefficients, α. The resulting equilibrium stress state is the baseline for the application of longitudinal mechanical loading.

In the case of the AS4/8552 micromechanical system, post-curing thermo-mechanical equilibrium results in an average longitudinal shrinkage of the RVE of approximately 0.3%. Nevertheless, this does not sensibly affect the strain-to-failure of the system in the subsequent mechanical load step, which keeps being totally controlled by the breakage of the central fibre at $\varepsilon \approx 1.2\%$.

Figure 4.14a shows that the through-the-width SCF profiles resulting from both simulation procedures are very similar, differing only by 2% at most, and no significant stress shielding effect is generated. However, the fibre ineffective and debonding regions are predicted to be, respectively, 11% and 16% longer when residual stresses are taken into account (Figure 4.14b). The level of inelastic deformation in the matrix around the broken fibre is also higher in this case (Figure 4.15). Hence, residual curing stresses affect the matrix inelastic deformation and fibre/matrix adhesion. This can be explained by the different thermal expansion coefficients of matrix and fibres, especially in the longitudinal direction (Table 4.1). Under curing cool-down, the 8552 matrix undergoes isotropic shrinking while AS4 fibres tend to expand longitudinally because of their negative thermal expansion coefficient (Figure 4.16). Equilibrium is established by means of longitudinal fibre compression that counteracts matrix tensile stress. This mismatch creates residual fibre/matrix interface shear stresses that decrease its adhesion integrity, and the increase in the deviatoric stress components that promote the occurrence of plasticity in the matrix.

In summary, residual curing stresses do not significantly change SCFs but have appreciable effects on fibre ineffective and debonding lengths. Although these mechanisms should not be neglected, for the sake of computational efficiency, the reference simulation case, which is the basis for subsequent analysis, does not include the thermo-mechanical loading step. To mitigate this shortcoming, a practical and conservative assessment could be to account for the cumulative effects of residual stresses and other loading mechanisms.

4.3.2 Influence of microstructural parameters on failure mechanisms and SCFs

This section is dedicated to studying the influence of relevant microstructural parameters on first-fibre failure mechanisms and SCFs: fibre volume fraction (V_f), fibre-to-matrix stiffness ratio, strength of the breaking fibre and fibre/matrix interface properties. Except where specifically noted, each of these parametric analysis will follow the reference modeling approach outlined in Section 4.2 and will be conducted on five statistically representative random volume elements, hence taking into account the stochastic nature of the microstructure.

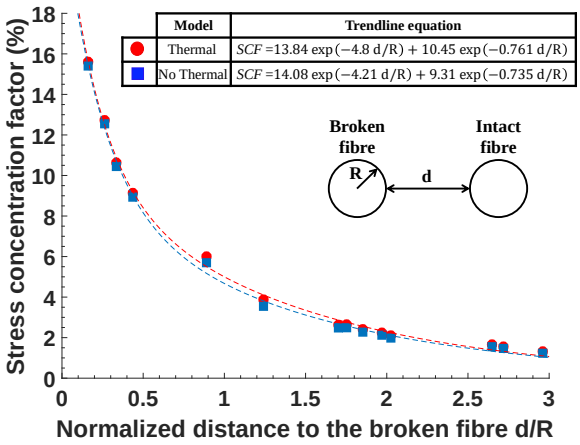

(a)

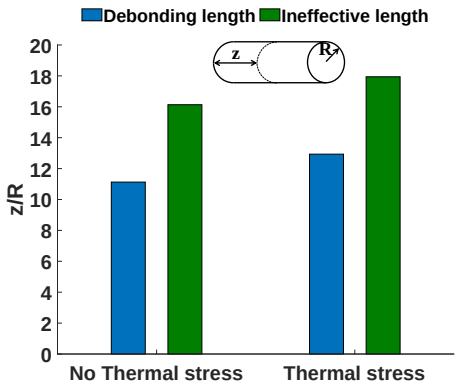

(b)

Figure 4.14: a) Maximum SCF values for simulations with and without residual curing stresses. b) Levels of ineffective and interface debonding lengths, corresponding to maximum SCFs, for both cases.

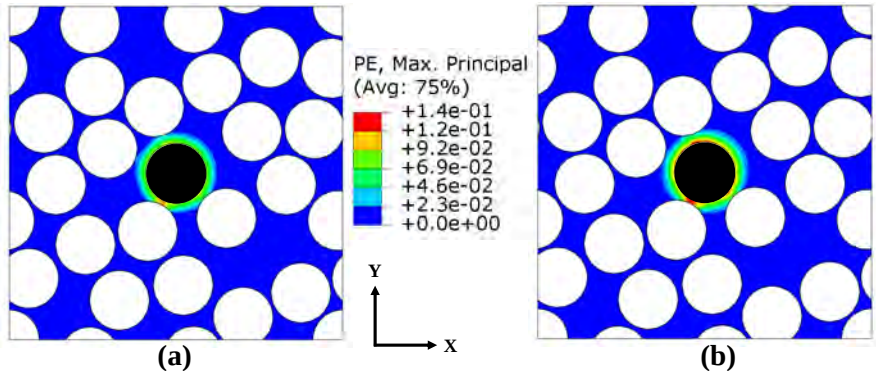

Figure 4.15: Matrix plasticity levels, corresponding to maximum SCFs ($\varepsilon \approx 1.2\%$), in the absence (a) and inclusion (b) of curing residual stress.

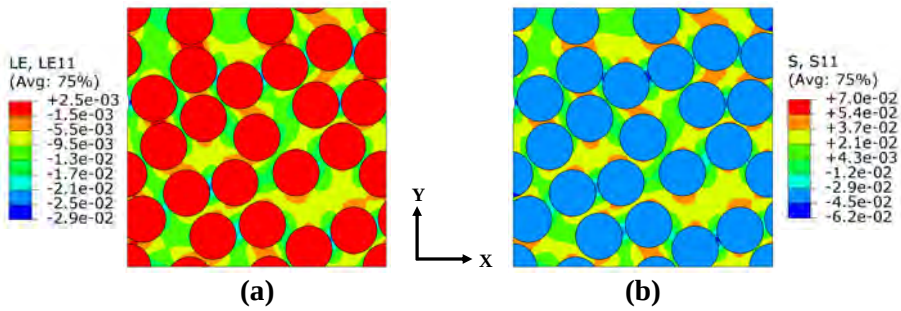

Figure 4.16: Longitudinal strain (a) and stress (b) fields, at maximum SCFs, in the case including residual curing stresses.

4.3.2.1 Fibre volume fraction

The stochastic simulations for V_f values of 50%, 60% and 70% (Figure 4.17a) show that denser microstructures result in lower maximum SCFs in all neighbors of the broken fibre. Average maximum SCFs of 20.6%, 16.1% and 14.2% are predicted for each of these V_f levels, respectively. The SCF values for $V_f = 50\%$ are roughly 45% higher than for $V_f = 70\%$. This trend, in agreement with the results obtained by Swolfs et al. [18, 67, 181], is due to the redistribution of the the stress concentration by a larger number of fibres in denser microstructures. Previous studies [60, 179, 180], however, led to the opposite conclusion because they were based on RVEs with regularly distributed microstructures and did not consider the effect of the distance between intact and broken fibres. In such regular fibre arrangements, lower V_f values inevitably result in higher distances between the broken fibre and its neighbors, which led to a lower SCF. Hence, the conclusion was misguided by the fact that, for typical FRP material systems, the increasing distance to the fibre break has a stronger softening effect on the SCF than the enhancing effect of the decrease in V_f. In randomly distributed RVEs, inter-fibre distance and V_f are less strongly coupled, and the effect of fibre density can be appreciated.

Statistically representative predictions of broken-fibre ineffective and interface debonding lengths (Figure 4.17b, average value with standard deviation) show that both parameters decrease with V_f, although the effect is more pronounced on the ineffective length. Similar to the decrease in SCFs, a higher number of fibres available for load redistribution around the fibre break lead to narrow stress and damage affected regions, and shorter stress recovery lengths.

Figure 4.18 shows that the volume of plasticised matrix around the broken fibre decreases with V_f. Again, this is due to the stronger load support given by a larger amount of surrounding fibres. However, due to the tendentiously thinner matrix ligaments in the microstructure, the local plastic deformation levels increase with V_f.

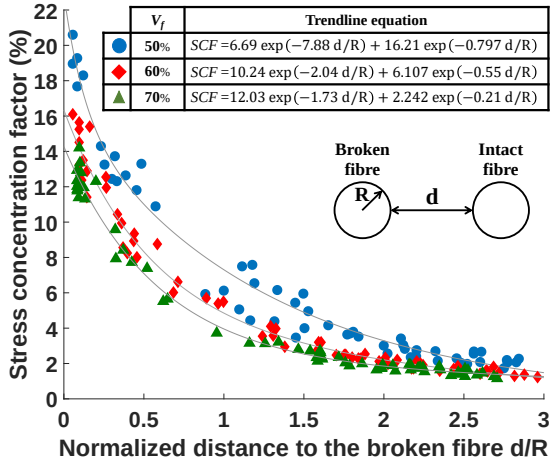

(a)

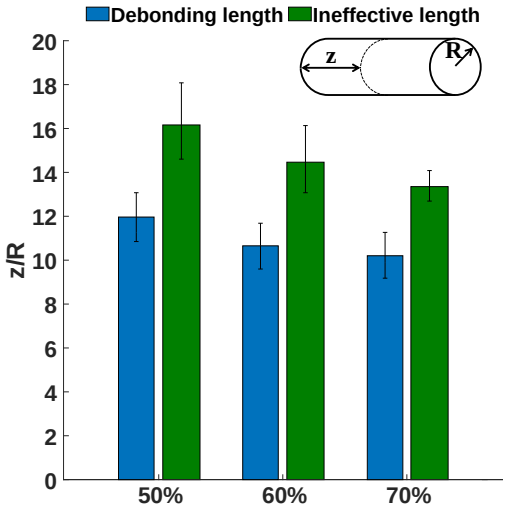

(b)

Figure 4.17: a) Maximum SCF values for five statistically representative microstructures with V_f = 50%, 60% and 70%. b) Corresponding stochastic predictions of broken-fibre ineffective lengths ($z/R = [12 \pm 1.1, 10.7 \pm 1.1, 10.2 \pm 1]$) and debonding lengths ($z/R = [12 \pm 1.1, 10.7 \pm 1.1, 10.2 \pm 1]$), respectively, for $V_f = [50\%, 60\%, 70\%]$.

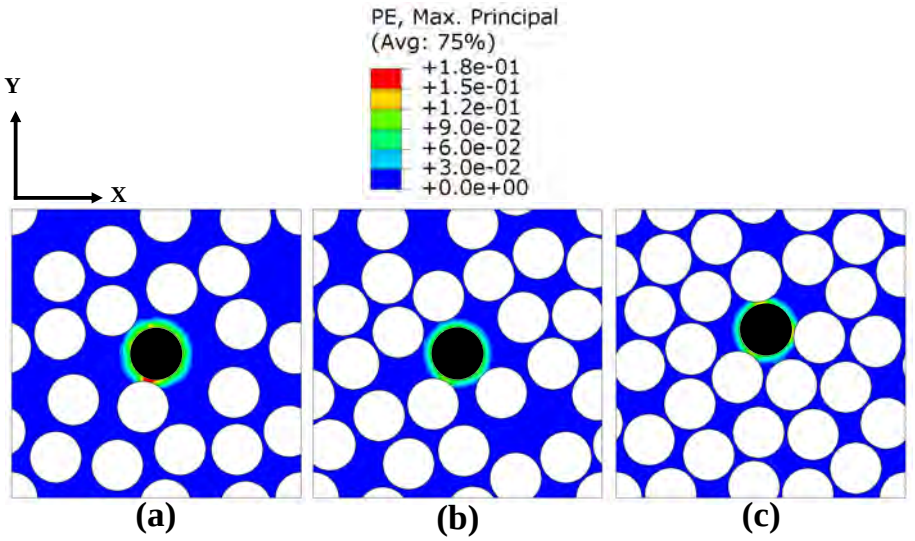

Figure 4.18: Matrix plasticity levels, for maximum SCF values, for representative microstructures with V_f = 50%, 60% and 70%.

4.3.2.2 Fibre-to-matrix stiffness ratio

To study the influence of the fibre-to-matrix stiffness ratio on the failure phenomena and SCFs, two realistic FRP systems are compared: the carbon/epoxy AS4/8552 ($E_1^f/E^m \approx 46$) and the glass/epoxy S2/MTM44-1 ($E_1^f/E^m \approx 21$). The respective constituent properties are given in Table 4.1 following experimental characterisation [156]. In both cases, V_f is 60% and, for the sake of efficiency, the resin matrices behave linear elastically.

Figure 4.19a reveals that the SCFs on intact fibres close to the broken fibre are higher for the system with the highest stiffness ratio. This is because the relatively stiffer fibres attract a higher share of the load redistributed as a result of the fibre breakage. However, after a certain distance to the broken fibre ($d/R > 1.4$) this trend is reversed. This means that, although the SCFs reach higher levels, the stress-affected section is narrower for material systems with higher stiffness ratios, likely leading to similar stress concentration resultants (volume integration of SCFs). Similar to the other previous cases, in this context the lower SCFs also correlate with shorter ineffective and debonding lengths (up to 30%), as shown in Figure 4.19b.

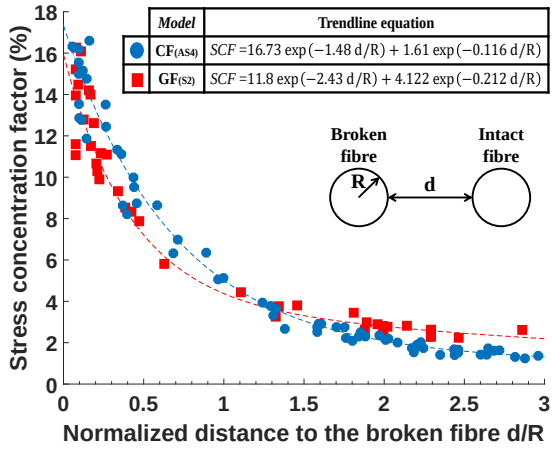

(a)

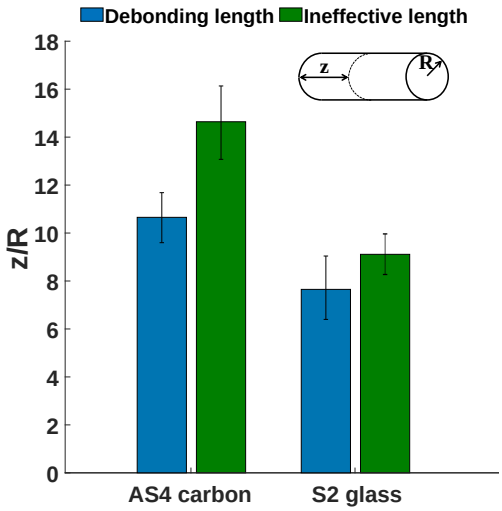

(b)

Figure 4.19: a) Maximum statistical SCF values (five outcomes) for first-fibre breakage in AS4/8552 and S2/MTM44-1 composites (applied strains $\varepsilon \approx 1.2\%$ and $\varepsilon \approx 3.3\%$, respectively). b) Corresponding predictions of broken-fibre ineffective lengths ($z/R = [14.7 \pm 1.4, 9.2 \pm 0.8]$) and debonding lengths ($z/R = [10.7 \pm 1.1, 7.6 \pm 1.4]$), respectively, for [AS4/8552, S2/MTM44-1] material systems.

4.3.2.3 First-fibre breaking strength

The effects of fibre strength on the failure mechanisms and SCFs associated with first-fibre failure are analysed herewith by considering five representative strength values from the Weibull fibre failure probability distribution function (σ_f= 2.0, 2.4, 2.7, 3.1 and 3.4 GPa) corresponding respectively to $P(\sigma_f)$=10%, 25%, 50%, 75% and 90% (Figure 4.3). Except for different fibre breaking strengths, which also correspond to distinct strain-to-failure values, the entire study is based on the reference model of the AS4/8552 material system with the single microstructure represented in Figure 4.1b ($V_f = 60\%$).

It can be appreciated (Figure 4.20a) that stronger breaking fibres result in lower peaks in the SCF profiles. Nevertheless, this difference is only as high as 12% and fades away with the distance to the fibre break (Figure 4.20b).

Figure 4.21a illustrates that both ineffective and debonding lengths increase roughly linearly with σ_f although the increase is steeper for fibre-matrix debonding. Figure 4.22 shows that the volume and maximum levels of matrix plasticity also increase with σ_f, with the evolution being non-linear (Figure 4.21b).

From these results it can be concluded that the decrease in SCFs with the increase in strength of the breaking fibre is due to the relatively lower increase in fibre/matrix interface and matrix load transfer capabilities because of the accumulation of inelastic deformation (plasticity, microdamage and debonding) in both constituents. This is compensated by longer ineffective lengths and larger volumes of matrix inelastic deformation.

4.3.2.4 Fibre/matrix interface strength

The effect of fibre/matrix interface strength on micromechanisms and SCFs is studied by analysing first-fibre break behaviours in AS4/8552 systems with two different sets of fibre/matrix interface properties. The first is the standard set used in all previous analyses and corresponds to properties measured at room temperature and dry conditions. The second set corresponds to interface properties that have been weakened by high temperature (70°C) and humidity conditions (85%) [120] (Table 4.1). Other than interface behaviour, it is assumed that the properties of fibres and matrix are unaffected. A single microstructure is considered (Figure 4.1b).

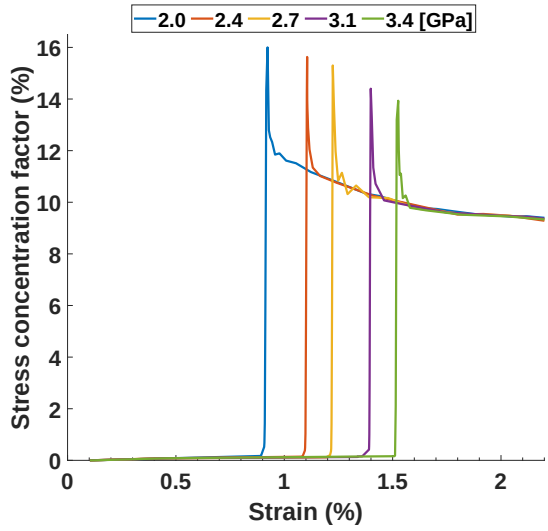

(a)

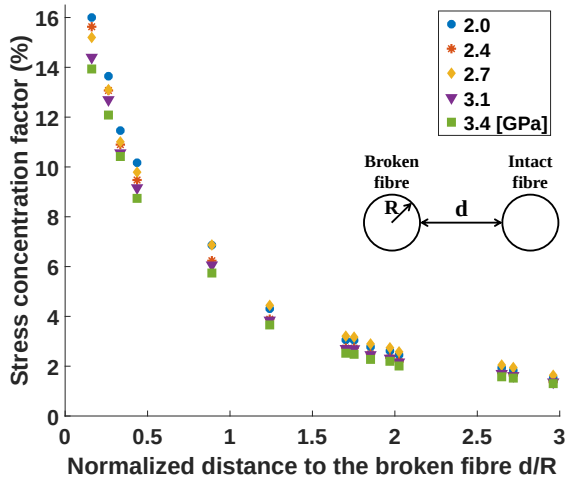

(b)

Figure 4.20: a) SCF vs. strain in nearest intact fibre for different fibre strengths. b) SCF profiles transverse to the broken fibre for different fibre strengths.

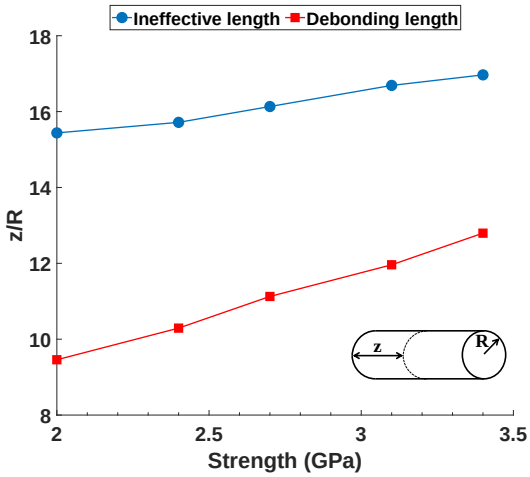

(a)

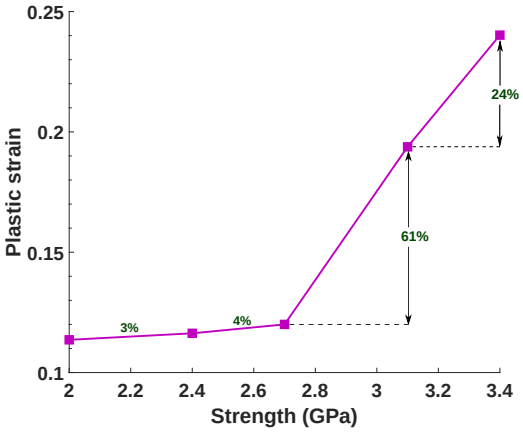

(b)

Figure 4.21: a) Broken-fibre ineffective and interface debonding lengths as function of strength. b) Evolution of peak matrix plasticity levels with fibre strength.

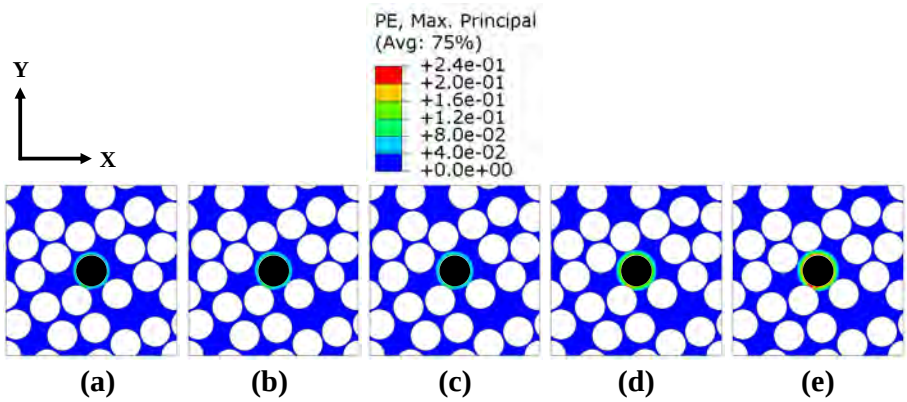

Figure 4.22: Matrix plasticity levels corresponding to maximum SCF values, and for different fibre strengths : a) σ_f = 2.0 GPa, b) σ_f = 2.4 GPa, c) σ_f = 2.7 GPa, d) σ_f = 3.1 GPa and e) σ_f = 3.4 GPa

The predicted SCF profiles are similar in both cases, as shown in Figure 4.23a. The debonding length increases for the weaker interface (Figure 4.23b) while a decrease of the levels of matrix inelastic deformation is observed (Figure 4.24). However, the ineffective length is almost unaffected, as shown in Figure 4.23b.

In summary, while the interface strength affects the damage micromechanisms, it has little influence on the fibre ineffective length and SCFs.

4.4 Concluding remarks

The deformation micromechanisms and stress redistribution in the vicinity of the first fibre break in unidirectional composites subjected to longitudinal tensile loads were simulated by means of high-fidelity computational micromechanics supported by experimentally characterised material constituents. Transient dynamic analyses were adopted to take into account the progressive failure and recoiling of a breaking fibre. Periodic microstructures with statistically representative random fibre packings were analysed. The relevance of several phenomena on the SCF, such as curing residual stresses, fibre-matrix debonding, matrix inelastic deformation, and their effects was investigated.

The profiles of SCFs around a progressively failing fibre were demonstrated to be different from those evolving under static equilibrium around a pre-broken fibre, although their maximum values were within close range. Moreover, the deformation micromechanisms are significantly different wherein longer fibre

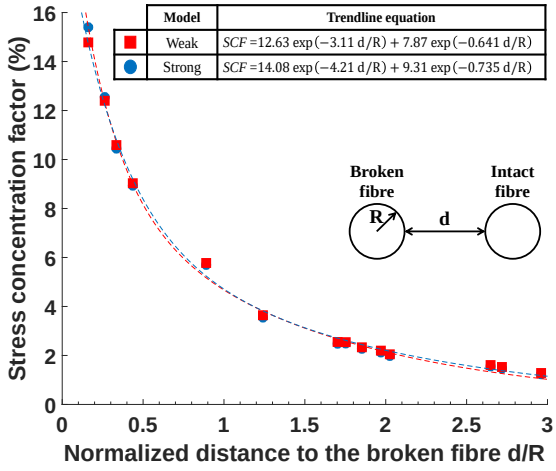

(a)

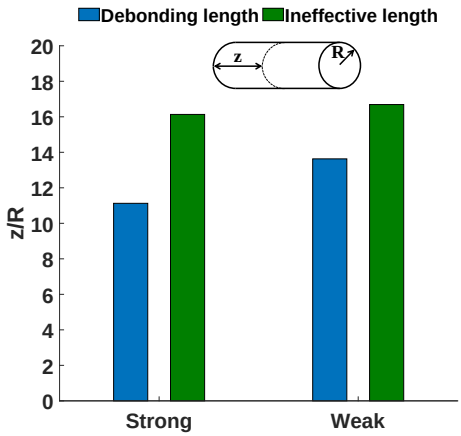

(b)

Figure 4.23: a) Maximum SCF predictions for weak and strong fibre/matrix interfaces. b) Corresponding broken-fibre ineffective and debonding lengths.

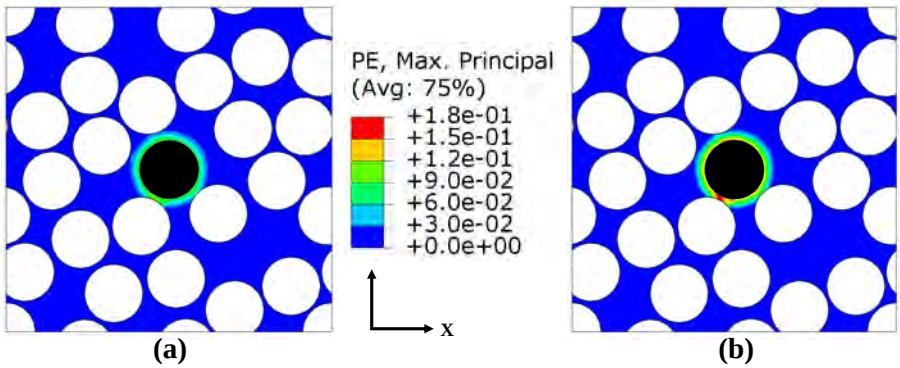

Figure 4.24: Matrix plasticity levels, corresponding to maximum SCF values, for a) weak and b) strong fibre/matrix interfaces.

debondings and higher levels of matrix inelastic deformation are predicted in realistic dynamic first-fibre failure. Hence, it is relevant to consider the process of progressive fibre failure and recoil as well as the micromechanisms of fibre/matrix debonding and matrix inelastic deformation, which have significant effects on SCFs and on the ineffective lengths of the broken fibre. Moreover, it was found that interface damage occurs not only in the broken fibre but also in its intact neighbors. The effects of residual thermal stresses were found to be negligible.

The transient dynamics computational micromechanics framework was used to investigate the influences of microstructure parameters such as fibre volume fraction, stochastic fibre breaking strength, fibre-to-matrix stiffness ratio and fibre/matrix interface properties. It was demonstrated that weaker breaking fibres, lower fibre volume fractions, or higher fibre-to-matrix stiffness ratios lead to higher SCF. Moreover, the effects of these parameters on the deformation micromechanisms are significant. The fibre/matrix interface strength has a relatively small influence on the longitudinal tensile failure process.

Overall, this work brings new insights into the mechanisms controlling longitudinal tensile failure of unidirectional composites. Firstly, the current high-fidelity dynamic analyses do not lead to SCF predictions significantly different from previous simplified static models reported in the literature. This is essentially because the progressive breaking of a fibre is slow compared to the stress wave propagation speed. This means that fibre breakage can be approximated to a quasi-static process. However, the fact that the maximum SCF's occur at higher

strain levels than previously assumed signifies that the resulting over-stresses on intact fibres are more likely to promote their failure, since they are closer to their stress limit. This is a second major insight gained in this work. It can signify a stronger fibre breakage cascading effect than what was previously predicted, resulting in the rapid failure of neighbouring fibres and larger clusters of broken fibres. This hypothesis will be tested by feeding efficient shear-lag-based fibre fragmentation models with a larger number of fibres [169] with the inputs resulting from the current high-fidelity analyses. Thirdly, the high-fidelity simulations reveal that the secondary damage micro-mechanisms of fibre/matrix interface debonding and matrix plasticity have opposite effects on SCF's. The former enhances the SCF's while the later mitigates them, as if matrix plasticity has a stress shielding effect. Finally, another relevant finding is that the SCF's generated by a fibre break depend on its specific stress-to-failure in the strength probability distribution. The stronger the fibre the lower the generated SCF's because of the stronger shielding effect from matrix plasticity. These findings will also be fed to efficient fibre fragmentation models to evaluate their implications on the longitudinal tensile failure of unidirectional composites.

5

Implications of matrix on fibre failure mechanisms: Stress Intensity Factor and Ultimate Strength

The current analytical or numerical determination of the stress intensity factor (SIF) in cracked bodies typically assumes that the body is isolated. However, in fibre reinforced composites, the main load carrying component, the fiber, is embedded in a matrix. In this chapter, we propose a micromechanical finite element model of a fibre embedded in an isotropic matrix and compute the SIF using the J-integral method to clarify the effect of the embedding matrix on the SIF and ultimate strength of the fiber. A parametric analysis based on dimensionless variables further investigates the effect of the fibre-matrix stiffness ratio and the degree of elastic orthotropy of the fibre.

5.1 Introduction

Composites reinforced with technical fibres (carbon, glass, etc.) exhibit the best mechanical performance among structural materials in terms of specific properties (stiffness and strength to weight ratio).

In spite of the small diameter of technical fibres, typically below 15 microns, their very high strength leads to Irwin's lengths much smaller than the diameter, that is, they behave like brittle materials. In this scenario, the Stress Intensity Factor, SIF or K_I, which depends on the existing surface flaws, load, geometry and the fibre toughness (referred to as critical SIF or K_{IC}), governs the fibre strength [187].

Commonly, the strength of brittle fibres such as glass or carbon is obtained by means of single fibre tensile tests, where a dry fibre (without being embedded in a matrix) is tested under tension [20]. A Weibull distribution [19] is then fitted to characterise the strength scatter, and this is used as input data into micromechanical strength models to predict the tensile failure of composite materials [188]. Recent detailed comparison between numerical models and experimental data shows that models strongly overpredict the fibre break density at low applied strains compared with experimental data, suggesting that the Weibull statistics used by the models is not accurate [188]. One possible reason to explain this gap between models and experiments is that the strength of dry fibres (without a matrix) may be different than the strength of the fibres *in-situ* (embedded in the matrix) [188]. From a theoretical point of view, the matrix may act as a crack constraint, thus reducing the SIF of the fibre and increasing the fibre strength.

The critical SIF of fibres, K_{IC}, has been investigated by combining experimental methods and some type of numerical approach to determine the SIF [119, 189–204]. For instance, Ogihara et al. [189] introduced various types of notches with straight fronts on carbon fibre mono-filaments using a focused ion beam machining system. Then, the authors used the virtual crack closure method to calculate the SIF of the free carbon fibre under tensile load in both isotropic and orthotropic cases to perform the data reduction of the experimental results. Herraez et al. [119] used a different numerical approach based on the J-integral to compute the SIF for several crack lengths. Then, they characterized strength and toughness of carbon AS4, E-glass and Kevlar KM2 via tensile tests on notched and un-notched fibres. The strength of the un-notched fibres was characterized in terms of the Weibull statistics, whereas the residual strength of the notched fibres was used to determine their apparent toughness. In both cases, the SIF was computed by assuming a free mono-filament, that is, the effect of the matrix was not considered.

A single fibre in a composite under longitudinal tension can be idealized as a cylinder loaded axially embedded in a homogeneous material, the matrix. Currently, there is a large amount of studies investigating the SIF of isotropic cracked bars, rods or beams with cylindrical cross-sections, loaded in tension or bending, and either under static or fatigue loading [190–204]. However, to the authors' best knowledge, the effect that embedding the fibre in a matrix has on the SIF and fibre strength has not been explored. Because of that, the present work makes use of high-fidelity computational micromechanics modelling, to compute the SIF along the crack front for a straight edge crack in a fibre subjected to tension loading, while embedded in an isotropic matrix.

First, the numerical approach proposed is verified by comparing the results for a free isotropic fibre with existing published results. Next, we present a parametric study to investigate the influence the fibre-matrix stiffness ratio has on the SIF of an isotropic fibre embbeded in a matrix. After that, we investigate the influence the fibre orthotropy (longitudinal-to-transverse stiffness ratio) has on the SIF. Finally, the results of this investigation are used to modify an existing Weibull distribution dataset of a 34-700 carbon fibre [205] that was obtained from single fibre tensile tests by other authors. The modified data is fed into a state-of-the-art micromechanical strength model [168–170, 206] able to

predict the damage accumulation and failure of composite materials. By using the modified Weibull distribution data, the fibre break density predicted by the model becomes significantly closer to the experimental observations. The results of this investigation prove that the matrix has a significant impact on the SIF and fibre strength. In addition, the results provided contribute to the understanding of the fracture of elastic bodies that goes beyond composite materials. Indeed, the work provides closed-form equations to describe the SIF for cylindrical shaped cracked elements surrounded by an elastic and homogeneous media. These equations are relevant for other practical cases such as the glass fibre composite rebars reinforcing concrete. The remaining of this paper is organised as follows: firstly, we present the micromechanical model to evaluate the SIF and secondly, the micromechanical strength model is summarised. Finally, the results and conclusions are presented.

5.2 Linear elastic fracture mechanics

Many engineering structures contain flaws or crack-like defects arising from manufacturing and fabrication techniques or initiation during service. Manufacturing flaws exist as imperfections in the materials' microstructure such as sites of porosity, second phase particles and impurities. Flaws created during fabrication are often associated with harsh processing procedures such as machining and drilling. The initial size of flaws may be small, even microscopic, but have a propensity to grow, or new cracks develop, due to the action of a variable service load or environmental conditions (moisture and corrosion). The presence and size of cracks in a component have a profound adverse affect upon its static (residual) strength. If the residual strength reduces sufficiently then loss of structural integrity occurs under normal operating conditions. The analysis of failure in cracked bodies may involve the determination of:

- Crack growth rates (from an initial flaw size to a critical size)
- Residual strength as a function of crack size
- Critical crack size tolerable by a structure
- Appropriate inspection schedules for cracked components
- Size of pre-existing flaws in the manufactured state

Fracture mechanics is an engineering discipline that assesses the state of cracks or cracked structures to quantitatively evaluate the phenomena listed above. A quantitative assessment allows engineering optimisation of many areas of structural and component management including design, material selection, inspection schedules, maintenance procedures, and decisions on remedial action.

Engineering materials, such as CFRP, have high fracture toughness, a material property gauging the resistance to crack propagation. Structures with cracks made of such materials ultimately fail due to a rapid separation mechanism known as brittle fracture, as opposed to plastic collapse or rupture. Linear Elastic Fracture Mechanics (LEFM) assumes that the material may be considered to be linear and elastic to describe the stress field in the region of a crack embedded in a loaded body. Though plasticity occurs at the crack tip, the principles of LEFM remain valid if the plasticity is confined to a zone small in size compared to the overall dimensions of the crack and cracked body.

Initial attempts to characterise fracture of materials were based on an energy balance theory, formulated by an English aeronautical engineer, Griffith [135] during World War I. Thereafter, Irwin [207] developed an energy approach for cracked systems defining a term for the elastic energy release rate, G quantifying the energy available for an increment of crack extension as:

$$G = -\frac{d\Pi}{dA} \tag{5.1}$$

The energy release rate G is the rate of change of potential energy Π, with crack growth area A. This crack driving force was used to determine the growth of stable and unstable cracks. In situations where crack tip plasticity is considerable, Rice's J-integral method [208], provides a more representative crack characterising parameter. It may be viewed as an equivalent energy release rate for cracks that follow a non-linear elastic material behaviour. The J-integral is suitable for calculating G by numerical methods and hence is useful in LEFM analysis. Though energy approaches provided great possibilities, subsequent development focused on a more practicable and tangible stress-field approach.

Cracks embedded in brittle materials can be characterised by a single parameter, the stress intensity factor, SIF, describing the crack tip stress field. It is a function of the load on the cracked configuration, crack size and shape and other geomet-

rical boundaries. The SIF is employed in many aspects of fracture mechanics such as to quantify critical flaw size, fatigue and stress corrosion cracking. The application of such analyses to practical problems requires knowledge of the SIF solution for the given geometrical configuration under the specified loading. Solutions for many configurations are available from various sources. These are typically confined to simple, idealised geometries under simple load cases and are mostly restricted to two-dimensional geometries as three-dimensional solutions are more difficult to calculate.

Many practical engineering problems are concerned with complex geometries under complex loading arrangements. The available SIF solutions are often inappropriate, as their usage invariably constitutes an approximation to the physical problem, which may incur in unacceptable errors. Contrary to the judgement of many, that there are sufficient SIF solutions applicable to the vast range of physical problems, design engineers continually strive to generate new reliable and accurate SIF solutions. Furthermore, engineering optimisation and defect assessment requires SIF solutions that have broad limits of validity and that can be rapidly calculated. The difficulty in calculating SIF solutions that meet the criteria stated above is widely recognised and constitutes a longstanding limitation common to many fracture mechanics analyses.

5.2.1 Stress intensity factor

The basis of LEFM theory is the stress intensity factor (K) concept, which relates the local elastic stress field near the crack tip to the known global stress or displacement field [209]. It predicts very accurately the stress state (stress intensity) near the tip of a crack caused by a remote load or residual stress. SIF is a theoretical construct usually applied to a homogeneous, linear elastic material and is useful for providing a failure criterion for brittle materials, and is a critical technique in the discipline of damage tolerance. The concept can also be applied to materials that exhibit small-scale yielding at a crack tip.

The SIF analysis was carried out by Williams [210] in 1957, taking into account Westergaard's work [211]. By using a coordinates system centred in the crack tip and according to William's analysis [210], the near crack tip components of the stress field are proportional to $K/r^{\frac{1}{2}}$, where K is the stress intensity factor. The crack opening may correspond to one of three basic cases, the opening mode,

the sliding mode and the tearing mode, or to any of their combination; thus, there are three basic stress intensity factor values denoted with the subscripts I, II and III.

For each mode, relations for the SIF can be derived by calculating the stress or displacement field, in the crack tip local coordinate frame, as functions of the distance r and angle θ, see Figure 5.1. The stress field in a small region surrounding the crack tip can be calculated using the expressions [212, 213]:

$$\begin{aligned}
\sigma_i^I(r,\theta) &= \frac{K_I}{\sqrt{2\pi r}} f_i(\mu,\theta) \\
\sigma_i^{II}(r,\theta) &= \frac{K_{II}}{\sqrt{2\pi r}} g_i(\mu,\theta) \\
\sigma_i^{III}(r,\theta) &= \frac{K_{III}}{\sqrt{2\pi r}} h_i(\mu,\theta)
\end{aligned} \tag{5.2}$$

where f_i, g_i and h_i are geometrical functions defining the angular dependency of the stress field. For the anisotropic case the stress field also depends on the roots μ_i of the characteristic equation, which is defined below. For example, in an infinite plate containing a crack with length $2a$ and loaded by a normal stress σ_y and shear stresses τ_{xy} and τ_{yz}, the stress intensity factors are defined as:

$$\begin{aligned}
K_I &= \sigma_y \sqrt{\pi a} \\
K_{II} &= \tau_{xy} \sqrt{\pi a} \\
K_{III} &= \tau_{yz} \sqrt{\pi a}
\end{aligned} \tag{5.3}$$

For any situation deviating from this ideal situation (infinite plate) the value of K is modified by adding a factor $\beta(a)$ as:

$$K_I = \sigma_y \sqrt{\pi a}.\beta(a) \tag{5.4}$$

where $\beta(a)$ is a function of the geometry. A number of handbooks are available [214–216] in which the function $\beta(a)$ is supplied for most common problems, but it can also be obtained from a finite element analysis by comparing the calculated displacement field with the displacement field around a crack in an infinite plate loaded in plane tension.

For isotropic materials the functions f_i, g_i and h_i can be related directly to

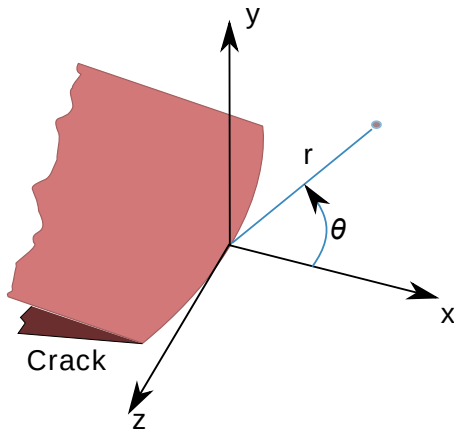

Figure 5.1: Definition of the variables r and θ and the crack tip local coordinate frame.

the material properties E and ν. However, for anisotropic materials, they are functions of the complex roots μ_i. Sih and Irwin [212] derived this function as:

$$a_{11}\mu^4 - 2a_{16}\mu^3 + (2a_{12} + a_{66})\,\mu^2 - 2a_{26}\mu + a_{22} = 0 \tag{5.5}$$

where the coefficients a_{ij} are the (compliance) elements of the elastic constitutive matrix, relating the stresses and strains according to

$$\varepsilon_i = a_{ij}\sigma_j \qquad (i,j = 1,...,6) \tag{5.6}$$

The SIF is used to determine the fracture toughness of most materials. Fracture toughness is an indication of the amount of stress required to propagate a pre-existing flaw. It is a very important material property since the occurrence of flaws is not completely avoidable in the processing, fabrication or service of a material/component. Flaws may appear as cracks, voids, metallurgical inclusions, weld defects, design discontinuities or some combination thereof. Since engineers can never be totally sure that a material is flawless, it is common practice to assume that a flaw of chosen size will be present in some number of components and use the LEFM approach to design critical components. This approach uses the flaw size and features, component geometry, loading conditions and the material property called fracture toughness to evaluate the ability of a component containing flaw to resist fracture.

5.2.2 SIF determination methods

The SIF can be calculated using stress and strain analysis or parameters that measure the energy released by crack growth. The estimation of SIF can be done by analytical or numerical techniques. Normally, the analytical ones are more complex but they have the advantage of their applicability to a wide range of crack lengths. For complex structures, it is difficult to perform an analysis taking into account all boundary effects near the crack tip, so the numerical calculation of K has some advantages for these structures. The evolution of computing hardware and software permit the use of more complex numerical techniques and to obtain solutions with smaller calculation time. Hence, the numerical techniques for estimating stress intensity factors are nowadays more popular than the analytical techniques. The following are some of the numerical methods for determining SIF.

5.2.2.1 Compounding method

The compounding method was proposed by Cartwright and Rooke in 1974 [217]. This method is used for determining SIF in complex structures starting from available solutions for simpler solutions. This method consists of decomposing a cracked structure with N boundaries into N ancillary configurations, each one containing one boundary and for which stress intensity factor solutions are available. The SIF for a crack tip can be expressed as a function of the N ancillary by:

$$K_{1N} = K_0 + \sum_{n=1}^{N} (K_n - K_0) + K_e \tag{5.7}$$

where K_0 is the SIF for the same body without the boundaries, K_n is the SIF for the cracked body having only the $n-th$ boundary and K_e is a SIF term corresponding to boundary-to-boundary interaction. K_e term takes action when boundaries interact one to another. In this case, stresses at the location of these boundaries will be different, leading to an increase or decrease of stress intensity factor values. The compounding technique give reasonable results for relatively simple geometries, however, it becomes excessively time consuming for geometries of great complexity or when interaction between their boundaries exists.

5.2.2.2 Displacement extrapolation

The displacement extrapolation method was developed by Paris and Sih [218], in order to obtain crack tip singular stresses and SIF using only nodal displacements of elements around the crack tip. The near crack tip displacement field may be expressed as a series in function of the SIFs, distance to the crack tip and the angle with the propagation direction. The displacements for mode I, II and III can be determined by

$$\begin{aligned} u_x &= \frac{K_{II}}{2G}\sqrt{\frac{r}{2\pi}}\,(1+k) \\ u_y &= \frac{K_I}{4G}\sqrt{\frac{r}{2\pi}}\,(1+k) \\ u_z &= \frac{K_{III}}{G}\sqrt{\frac{r}{2\pi}} \end{aligned} \tag{5.8}$$

where G is the shear modulus, r is a variable distance from the crack tip along the x axis, u_x, u_y and u_z are the displacements in the x , y and z directions, respectively (refer to Figure 5.1). The parameter k is:

$$k = \begin{cases} 3-4\nu & \text{in plane stress} \\ \frac{3-\nu}{1+\nu} & \text{in plane strain} \end{cases} \tag{5.9}$$

From these equations, a relationship between displacements and the apparent stress intensity factor K_0 is obtained. Using a linear extrapolation to $r = 0$, the stress intensity factor at the crack tip can be estimated with a high accuracy. The extrapolation method produces consistent results with reasonable accuracy and is highly efficient in terms of computational effort, however it is better suited for the models with simple geometry.

5.2.2.3 Force method

The force method is an alternative to the displacement method. It uses nodal reactions obtained in a finite element model. This method was first developed by Raju and Newman [219] in 1977. Based on the first term of Williams series expansion of the stress, it is possible to estimate the SIF value using extrapolation

as:

$$\begin{aligned}\sigma_{xx} &= \frac{K_I}{\sqrt{2\pi r}} \\ \sigma_{yy} &= \frac{K_I}{\sqrt{2\pi r}} \\ \tau_{xx} &= \frac{K_{II}}{\sqrt{2\pi r}}\end{aligned} \tag{5.10}$$

Analyzing the forces along a distance r, the following expressions for the forces transmitted along the x and y direction, are obtained by:

$$\begin{aligned}F_x &= \int_0^{x_c} \tau_{xy} dy = K_{II}\sqrt{\frac{2x_c}{\pi}} \\ F_y &= \int_0^{x_c} \sigma_{yy} dy = K_I\sqrt{\frac{2x_c}{\pi}}\end{aligned} \tag{5.11}$$

Finally, the Modes I and II SIF values can be determined as a function of the distance r by:

$$\begin{aligned}K_I{}' &= \sqrt{\frac{\pi}{2x_c}}\sum_{i=1}^{n} F_{y,i} \\ K_{II}{}' &= \sqrt{\frac{\pi}{2x_c}}\sum_{i=1}^{n} F_{x,i}\end{aligned} \tag{5.12}$$

where x_c is the distance from the crack tip to the intermediate location between the node under consideration and the next node. F_x and F_y are forces in x and y direction, respectively, obtained from the finite element results at various x_c locations. The force method produces accurate results, however, it necessitates the preparation of a suitable finite element mesh in the crack front.

5.2.2.4 J-integral

The J-integral is a contour integral that characterizes the strain energy release rate of an elastic non-linear material. The theoretical concept of J-integral was developed in 1967 by Cherepanov [220] and independently in 1968 by James R. Rice [208], who demonstrated that an energetic contour path integral was independent of the path around a crack. The stress field is related to the strain

energy density as follows:

$$\sigma_{ij} = \frac{\partial W}{\partial \varepsilon_{ij}} \tag{5.13}$$

where σ is the stress, ∂W is the strain energy density and ε is the strain. Based on the definition of potential energy along a contour, work theorem and the previous equation, Rice [208] defined an integral independent of the integration contour Γ around the crack tip as:

$$J = \int_{\Gamma} \left(W dy - t \cdot \frac{\partial u}{\partial x} ds \right) \tag{5.14}$$

where W is the strain energy density, x, y are the coordinate directions, $\mathbf{t} = [\sigma]\mathbf{n}$ is the surface traction vector, $\mathbf{n}$ is the normal to the curve Γ, $[\sigma]$ is the Cauchy stress tensor, and $\mathbf{u}$ is the displacement vector.

For linear or non-linear elastic materials, the J-integral is equal to the strain energy release rate (G) [209] for a crack in a body subjected to monotonic loading. This is generally true, under quasistatic conditions, only for linear elastic materials. For materials that experience small-scale yielding at the crack tip, J-integral can be used to compute the energy release rate under special circumstances such as monotonic loading in mode III (antiplane shear). The strain energy release rate can also be computed from J for pure power-law hardening plastic materials that undergo small-scale yielding at the crack tip.

5.2.2.5 Finite crack extension method

The finite crack extension method [221] relies on calculation of the strain energy release rate, using the energy variation under an infinitesimal crack length extension:

$$G = \frac{\partial U}{\partial a} \tag{5.15}$$

This method can be divided into two categories:

i) Crack closure technique

This technique was first presented by Rybicki and Kanninen [222] in 1977. This method is also called two-step crack closure technique, as it requires two steps FE analysis in order to calculate the strain energy release rate for a specific crack length. The crack is physically extended, or closed, during two complete FE analyses as shown in Figure 5.2. The crack closure technique (CCT) is based on Irwin's crack closure integral [223, 224]. The method relies on the assumption that the energy ΔE released when the crack is extended by Δa from a (Figure 5.2a) to $a+\Delta a$ (Figure 5.2b) is identical to the energy required to close the crack between location i and j. For a crack modeled with two-dimensional four node elements (5.2) the work E required to close the crack along one element side can be calculated as:

$$\Delta E = \frac{1}{2}\left[X_{1i}\,.\,\Delta u_{2i} + Y_{1i}\,.\,\Delta w_{2i}\right] \tag{5.16}$$

where X_1 and Y_1 are the shear and opening forces at nodal point i to be closed and Δu_2 and Δw_2 are the differences in shear and opening nodal displacements at node i as shown in Figure 5.2. The crack closure method establishes the original condition before the crack was extended. Therefore, the forces required to close the crack are identical to the forces acting on the upper and lower surfaces of the closed crack. The forces X_1 and Y_1 may be obtained from a first finite element analysis where the crack is closed. The displacements u_2 and w_2 are obtained from a second finite element analysis where the crack has been extended to its full length $a+\Delta a$.

ii) Virtual crack closure technique

The Virtual Crack Closure Technique (VCCT) is based on the same assumptions as the crack closure method [222]. However, it is assumed that a crack extension of Δa from $a+\Delta a$ (node i) to $a+2\Delta a$ (node j) does not significantly alter the state at the crack tip, as seen in Figure 5.3. This implies that the displacements of a region close to the crack tip, when the tip is at specific node, are approximately the same as the displacements at the same location when the tip is at the previous node. Using Figure 5.3 as an example, it is assumed that the displacements at node i will be approximately equal to the displacements at node l when the crack

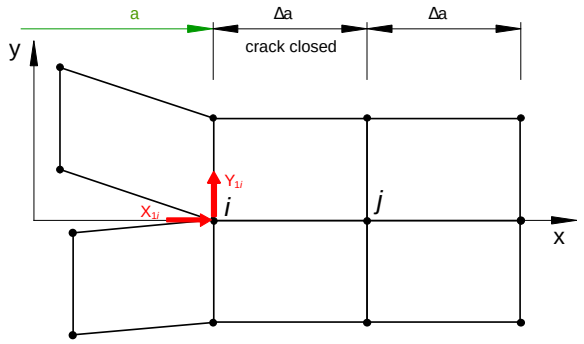

(a) First FE analysis step: crack closed

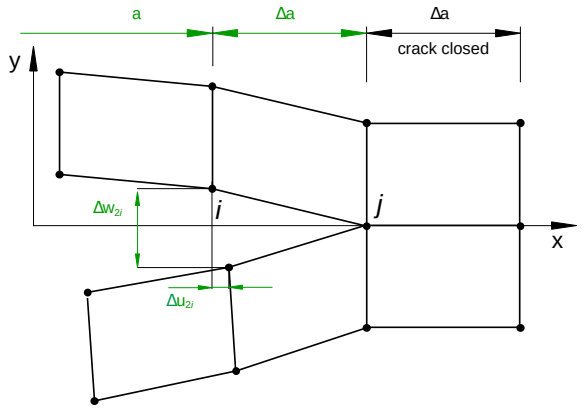

(b) Second FE analysis step: crack extended

Figure 5.2: Two steps crack closure technique.

extends from node i to node j.

Further, the energy E released when the crack is extended by Δa from $a+\Delta a$ to $a+2\Delta a$ a is identical to the energy required to close the crack between location i and k, and can be calculated by:

$$\Delta E = \frac{1}{2}\left[X_i \,.\, \Delta u_l + Y_i \,.\, \Delta w_l\right] \tag{5.17}$$

where X_i and Z_i are the shear and opening forces at nodal point i and Δu_l and Δw_l are the shear and opening displacements at node l. Therefore, the information required for the calculation of the energy variation is obtained from a single finite element analysis. After obtaining the energy variation, the energy release rate G is calculated as:

$$G = \frac{\Delta E}{\Delta A} \tag{5.18}$$

where ΔA is the surface area created by a crack propagation of; in the case of plates with a thickness b, this area is $\Delta a.b$. The VCCT is a more straightforward calculation than CCT, just requiring that the two elements behind and in front of the crack tip are identically. However, this method is not suitable for models with several domains.

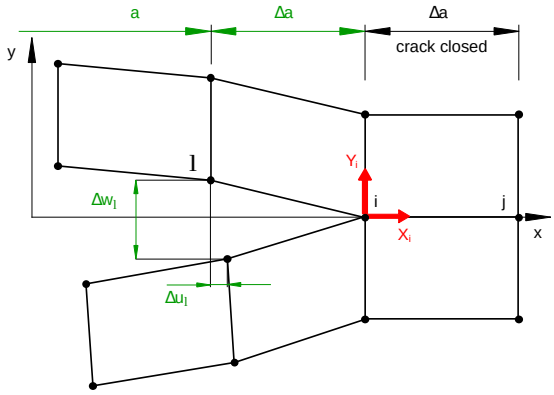

Figure 5.3: FE model with details of the boundary conditions and finite-element meshing of the crack tip region.

In summary, and based on the following requirements, the j-integral was chosen to compute the SIF: K values are consistent when using the J-integral method;

the presence of plasticity in the model; the J-integral is an appropriate method to determine accurate K values for both 2D and 3D cracks. Local errors are minimized because J-integral is domain independent and can be applied to a domain with multiple elements.

5.3 Methodology

5.3.1 Numerical evaluation of SIF

To compute the SIF of fibres embedded into a matrix, this work relies on a micromechanics finite element simulation performed in Abaqus Standard 2020 [150]. The model consisted of a notched fibre embedded in an isotropic matrix, subjected to a tensile axial force (Figure 5.4a), while the lateral surface area was free from stresses. The fibre included a straight-fronted edge crack at $x_1 = L/2$, with varying depth (a), as indicated by the grey area in Figure 5.4b. Matrix and fibres are modelled as elastic materials with a perfect fibre/matrix adhesion using tie constraints at the interface.

The size of the model was decided based on a parametric study that targeted the best trade-off between computational effort and accuracy. The axial length, L, had to be long enough to guarantee that the remote stresses at the upper and bottom faces, were not influenced by the presence of the crack. This led to $L = 10D$, where D is the fibre diameter. We selected a large enough thickness of the surrounding matrix, t, to avoid severe deformation in the boundaries of the matrix around the crack region. This criterion prevailed over achieving a realistic fibre volume fraction for the composite (not the purpose of this study), and led to $t = D$.

To reduce the computational costs, only one-quarter of the model was simulated by taking advantage of the symmetry boundary conditions along the x_1 and x_3 axes (Figure 5.5). A uniform normal traction stress, σ, was imposed in the upper part of the model. The fibre and matrix were meshed separately. We used a swept and structured mesh around the crack tip to enrich the discretization and capture the high stress gradients therein (Figure 5.5). The element size, after a convergence study, varied in the range of $D/1500$ (at crack tip) to $D/100$ (in far-field). To account for the stress singularity, quadratic isoparametric elements (C3D20) with the inverse square root singularity were used at the crack tip.

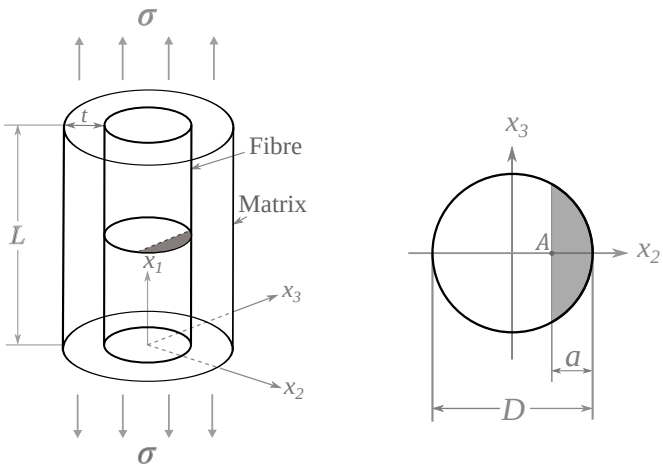

Figure 5.4: A notched fibre with straight-fronted edge crack (indicated in grey) embedded in a matrix. a) 3D geometry of the model and b) the fibre cross-section at crack plane.

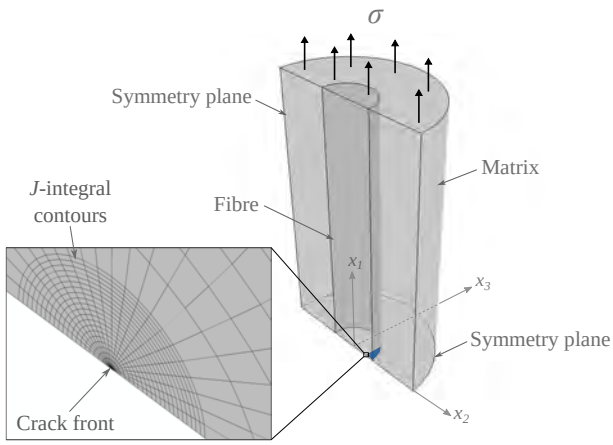

Figure 5.5: FE model with details of the boundary conditions and finite-element meshing of the crack tip region.

The stress intensity factor evaluation was carried out by means of the J-integral method, as described in Section 5.2.2.4. In this approach, the energy release rate is obtained by integration along the contour Γ around the crack tip (Figure 5.6) with

$$J = \int_{\Gamma} \left(W dx_1 - t \cdot \frac{\partial u}{\partial x_2} ds \right) \tag{5.19}$$

where x_1 and x_2 are rectangular coordinates to the crack front, x_1 being perpendicular to the crack surface, W is the elastic strain density, t is the traction vector, u is the displacement vector, and ds is an increment of arc length along any contour Γ. Due to the geometry of the model, the J-integral values are not constant along the crack front. Thus, this work concentrated on the maximum value attained at the crack tip (point A in Figure 5.4b). For linear elastic problems of crack opening in mode I, the J-integral equals the energy release rate (G_I). The path independence [208] of J-integral was checked and a total of 21 concentric contours surrounding the crack tip were used, as shown in Figure 5.5 (magnified area).

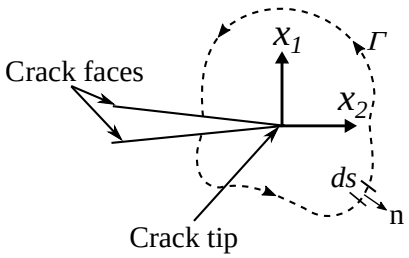

Figure 5.6: Definition of the contour path around the crack tip to compute the J-integral.

For an isotropic material, the stress intensity factor in mode I, K_I, can be calculated from the J-integral by

$$J = \frac{{K_1}^2 (1 - \nu^2)}{E} \tag{5.20}$$

where E is the fibre Young's modulus and ν the Poison's ratio. For an orthotropic material, the J-integral and the K_I are related through the following equation

[212]

$$J = {K_I}^2 \sqrt{\frac{a_{11}a_{22}}{2}} \left[\sqrt{\frac{a_{22}}{a_{11}}} + \frac{2a_{12} + a_{66}}{2a_{11}} \right]^{1/2} \tag{5.21}$$

where a_{ij} stands for the compliance tensor of the orthotropic solid under plane strain

$$a_{11} = \frac{1}{E_{11}},\ a_{22} = \frac{1}{E_{22}},\ a_{66} = \frac{1}{G_{12}},\ a_{12} = -\frac{\nu_{12}}{E_{11}} \tag{5.22}$$

and E_{11} and E_{22} are the fibre Young's modulus in longitudinal and transverse directions, respectively, and G_{12} is the fibre shear's modulus. Finally, the non-dimensional stress intensity factor (f) is calculated by

$$f = \frac{K_I}{\sigma\sqrt{\pi a}} \tag{5.23}$$

where σ is the far-field stress, and a is the crack length.

5.3.2 Non-dimensional Parametric Analysis

A parametric non-dimensional analysis was defined to investigate the effect of embedding a fibre in a matrix for different material parameters.

For an embedded isotropic fibre, the independent elastic constants that have an effect on the SIF are the modulus of elasticity and the Poisson's ratio of the fibre, E^f and ν^f, and of the matrix, E^m and ν^m. The non-dimensional analysis is based on the definition of the parameter α, representing the fibre-to-matrix stiffness ratio:

$$\alpha = \frac{E_1^f - E^m}{E_1^f + E^m} \tag{5.24}$$

with α ranging between $\alpha = -1$ (stiffness of the fibre negligible with respect to that of the embedding material, $E^f \ll E^m$) and $\alpha = 1$ ($E^f \gg E^m$, which corresponds to the free fibre). For $\alpha = 0$, the fibre and matrix have the same modulus of elasticity, so this case corresponds to an homogeneous cylindrical material with an internal crack.

In an orthotropic fibre, the number of elastic constants increases to nine: modulus of elasticity (E_1^f, E_2^f, E_3^f), Poisson's ratios ($\nu_{12}^f, \nu_{13}^f, \nu_{23}^f$) and shearing moduli ($G_{12}^f, G_{13}^f, G_{23}^f$). The subscripts 1, 2 and 3 refer to longitudinal and the two

transverse directions, respectively. For the sake of simplification, the fibre was considered transversely isotropic ($E_2^f = E_3^f$, $\nu_{12}^f = \nu_{13}^f$, $G_{12}^f = G_{13}^f$), and some of the elastic constants took a fixed value ($\nu_{12}^f = 0.3$, $\nu_{23}^f = 0.4$, $G_{12}^f = 11.3$, $\nu_{12}^f = \nu^m = 0.3$) [121]. Therefore, the elastic constants involved in the parametric study were E_1^f, E_2^f and E^m, which were combined in the non-dimensional parameters α, defined above in Eq. 5.24, and β:

$$\beta = \frac{E_1^f - E_2^f}{E_1^f + E_2^f} \tag{5.25}$$

where β ranges between $\beta = -1$ ($E_1^f \ll E_2^f$) to $\beta = 1$ ($E_1^f \gg E_2^f$). The case $\beta = 0$ corresponds to the isotropic fibre.

Due to the positive-definiteness of the strain energy, the elasticity tensor (compliance matrix) in linear elastic materials must be positive-definite [225]. To assure this, some constraints must be applied to the engineering elastic constants:

$$E > 0, G > 0, -1 < \nu < 0.5 \tag{5.26}$$

for isotropic elasticity, and

$$\begin{gathered} E_1, E_2, E_3, G_{12}, G_{13}, G_{23} > 0 \\ |\nu_{12}| < \left(\frac{E_1}{E_2}\right)^{1/2} \\ |\nu_{13}| < \left(\frac{E_1}{E_3}\right)^{1/2} \\ |\nu_{23}| < \left(\frac{E_2}{E_3}\right)^{1/2} \\ 1 - \nu_{12}\nu_{12} - \nu_{23}\nu_{32} - \nu_{31}\nu_{13} - 2\nu_{21}\nu_{32}\nu_{13} > 0 \end{gathered} \tag{5.27}$$

for the orthotropic elastic case. These constrains arise due to thermodynamic admissibility; their violation leads to a non-positive strain energy for certain load cases. Based on the linear elastic conditions, stability restricts β to $-0.5 \leqslant \beta < 1$.

5.3.3 Micromechanical Progressive Failure Model

To investigate the effect that a modified Weibull distribution fibre strength dataset (taking into account the presence of the matrix) has on the tensile failure and damage development of composite materials, the Progressive Failure Model (PFM) developed by J. M. Guerrero et al. [168–170] is employed. The PFM [21, 168–170, 206] is a micromechanical strength model that considers an RVE of width a, height b and length L containing a random distribution of fibres of a certain radius. The fibres are split into elements (tensile springs) of length l along the longitudinal direction, thus leading to a succession of springs that work in series with the other elements of the same fibre and in parallel with the elements of the surrounding fibres. Figure 5.7 presents a schematic representation of the model.

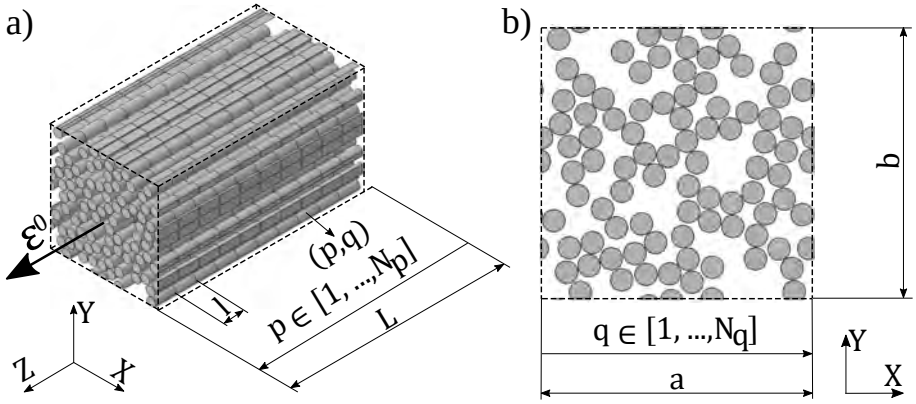

Figure 5.7: Schema of the progressive failure model. a) 3D view and b) cross-section view. Fibres are denoted by $q \in [1, ..., N_q]$, while planes are denoted by $p \in [1, ..., N_p]$, where N_q and N_p are the number of fibres and planes, respectively.

At the beginning of a new simulation, a stochastic strength is assigned to each element, p, q of the model, following a statistical distribution representative of the fibres (usually a Weibull distribution). Following this, a uniaxial strain is slowly applied by increasing the strain, ε^0, in steps. At each step, the stress of an element p, q is computed with [21, 168, 170, 206, 226]

$$\sigma_{p,q} = \frac{SCF_{p,q}}{\Omega_p} E_q \left(1 - D_{p,q}\right) \left(\varepsilon_p + \varepsilon_q^{\mathrm{r}}\right) \tag{5.28}$$

where $SCF_{p,q}$ is the Stress Concentration Factor (SCF) supported by element p, q, E_q is the Young's modulus of fibre q, $D_{p,q}$ is a damage factor which is

equal to 0 for intact elements, equal to 1 for broken elements and in between for elements in any stress recovery, ε_p is the mechanical strain of plane p, $\varepsilon_q^{\mathrm{r}}$ is the fibre's thermal residual strain resulting from the curing of the matrix, and Ω_p is a stress ratio to enforce load equilibrium [21, 168–170, 206].

After computing the element stresses, these are compared with the strength. If no element fails, a new step starts and the applied strain, ε^0, is increased. Otherwise, if a new element breaks, a damage factor equal to 1 is assigned to the failed element. Moreover, this damage is progressively decreased from 1 (at the plane of the breakage) down to zero at the end of the ineffective length of the broken fibre. This approach simulates the loss of stiffness due to the break. In addition, the stress loss through all this region is redistributed to the surrounding intact fibres in form of stress concentration. All this stress redistribution is computed with analytical equations [21, 168–170, 206]. After this, the element stresses are recalculated and the model checks if new elements fail. This iterative process continues until failure is triggered either due to the unstable propagation of a cluster or because all fibres in a plane are broken.

The PFM captures the progressive fragmentation of fibres and the formation of clusters of broken fibres. Thanks to the use of analytical equations, the model is computationally efficient, allowing the simulation of RVEs with thousands of fibres. Deep details of the model formulation can be found elsewhere [21, 168–170, 206].

5.4 Finite element model validation

The numerical approach presented in Section 5.3.1 was verified using two cases of isolated cylindrical bars for which the corresponding SIF has been previously published (free isotropic bar with a surface crack [189, 190, 227] and a bar with internal crack [215]). This verification is described in detail in this section.

5.4.1 Free fibre model

First, the SIF results of the FE model for a single isotropic free fibre (no mesh/material surrounding it) were compared with the literature (Astiz and Elices [227], Daoud et al. [190] and Ogihara et al. [189]), obtaining a good agreement (Figure 5.8). Our dimensionless SIF data was fitted using the follow-

ing equation:

$$\frac{K_I}{\sigma\sqrt{\pi a}} = 1.023 + 0.4448\left(\frac{a}{D}\right) - 1.4\left(\frac{a}{D}\right)^2 + 13.23\left(\frac{a}{D}\right)^3 \tag{5.29}$$

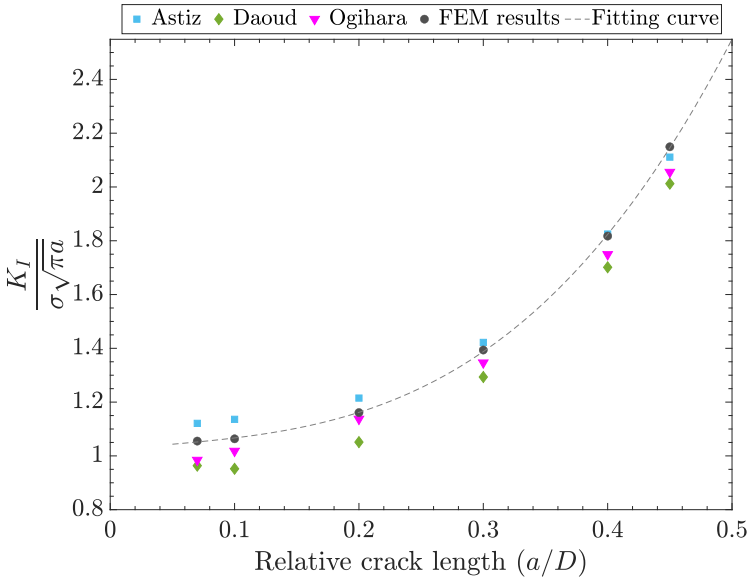

Figure 5.8: Comparison of the non-dimensional stress intensity factor of an isotropic free fibre subjected to uniform tension obtained in this work (FEM), with Astiz [227], Daoud et al. [190] and Ogihara et al. [189].

5.4.2 Embedded fibre model with very low stiffness matrix

Second, the complete computational model, including fibre and the embedding matrix, was used to reproduce the free fibre case. To that purpose, the stiffness of the matrix was defined to be close to 0 ($\alpha = 0.999999$). Notice that an exact value of zero cannot be given since the finite element material model needs a non-zero stiffness. Figure 5.9 compares the results of the computational model (dots) with the equation 5.29 and demonstrates that the embedded fibre model captures this case well.

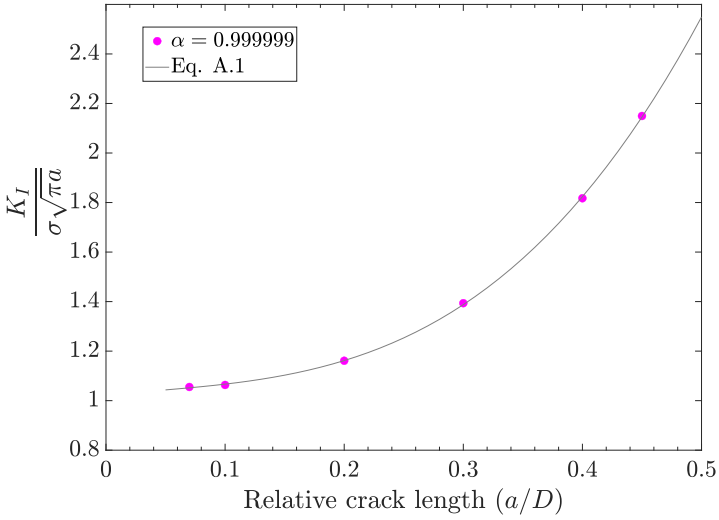

Figure 5.9: Non-dimensional SIF of an isotropic free fibre resulting from a computational model of the isolated fibre (line) and with embedding material of nearly zero stiffness (dots).

5.4.3 Comparison with an analytical model

The third verification case consisted of a cylinder with an internal circular crack under axial tension, for which an analytical model exists [215]. To reproduce this case, the computational model was defined so that the fibre and the matrix had the same elastic properties and the whole fibre cross-section acted as the crack (grey area in Figure 5.10).

The analytical SIF solution for this crack geometry is given by [215]

$$K_I = \frac{2}{\pi} 6\sqrt{\pi a} F\left(a/b\right) \tag{5.30}$$

where

$$F\left(a/b\right) = \frac{1 - 0.5\left(a/b\right) + 0.148\left(a/b\right)^3}{\sqrt{1 - a/b}} \tag{5.31}$$

where a is the crack radius and b is the radius of the cylinder. The SIF and Crack Opening at Center (COAC) were calculated for both analytical and FE models and compared, showing a good agreement (SIF = 2.59 and COAC = 0.051 for analytical model, whereas SIF = 2.53 and COAC = 0.051 for the FE model).

These three verification cases demonstrate the reliability of the proposed compu-

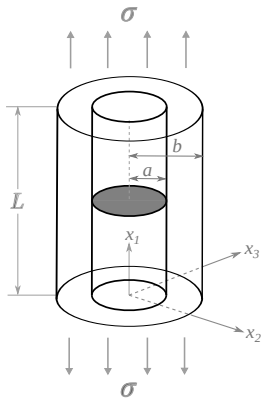

Figure 5.10: Geometric illustration of a model consisting of a broken fibre embedded in a matrix as a solid cylinder with central circular crack. The fibre is broken in the middle ($x_1 = L/2$) and shown as the grey area.

tational approach.

5.5 Results and discussion

5.5.1 Isotropic fibre embedded in a matrix

Figure 5.11 plots the evolution of the non-dimensional SIF for an isotropic fibre embedded in a matrix for different fibre/matrix stiffness ratios (α equal to -0.95, -0.5, 0.0, 0.5, 0.8, 0.95 and 0.98) and relative crack lengths (a/D equal to 0.07, 0.1, 0.2, 0.3, 0.4, and 0.45). The SIFs of an isotropic free fibre (grey continuous line) were added as a baseline, for comparison. For better visualization, Figure 5.12 shows a 3D surface plot of non-dimensional SIF.

The trend is that an increase in matrix stiffness (decrease in α) leads to a significant drop in the SIF of the cracked fibre, especially for longer cracks. Even for a low stiffness matrix ($\alpha = 0.98$ or $E^m = 0.01E^f$), the SIF is reduced by 7% when $a/D = 0.2$ or by 25% when $a/D = 0.4$, with respect to the free fibre case. Figure 5.13 depicts the percentage change of SIF for different fibre/matrix stiffness ratios (α), compared to the free fibre.

Figure 5.14 shows the maximum non-dimensional crack mouth opening displacement (CMOD) for the embedded fibre with α being equal to 0.98 and -0.95, as well as that of the free fibre (grey continuous line) for reference. The trends of the curves are very similar to those of the SIF, and indicate that the surrounding

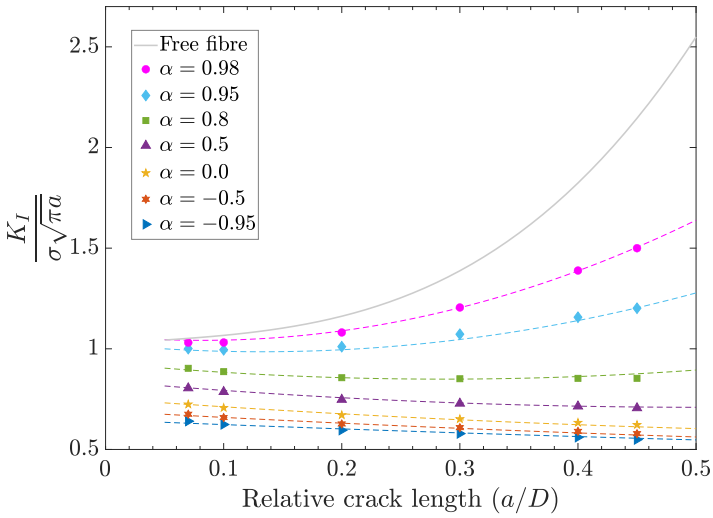

Figure 5.11: Non-dimensional SIF for an isotropic fibre embedded in a matrix for different fibre/matrix stiffness ratios, α. The dots refer to the FEM results and the dashed lines to the fitting curves according to Equation 5.32. The continuous grey curve corresponds to the SIF for a free fibre ($\alpha = 1$).

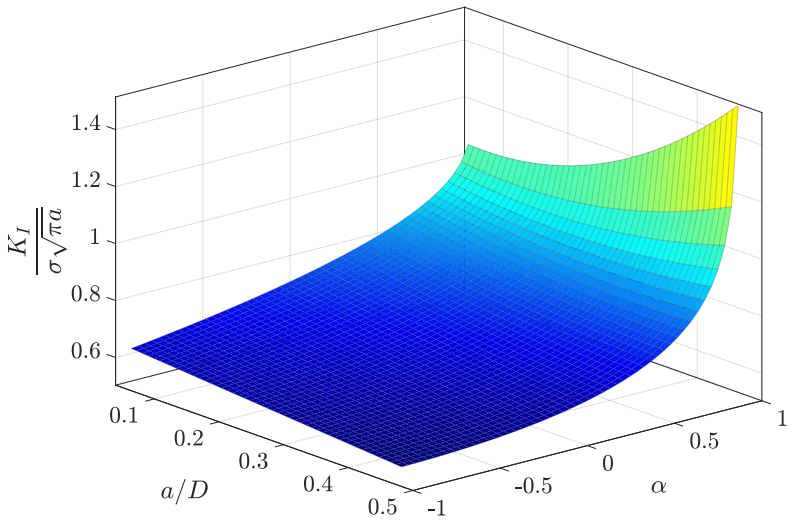

Figure 5.12: 3D surface plot of non-dimensional SIF for an isotropic fibre embedded in a matrix for different fibre/matrix stiffness ratios (α) and crack lengths (a/D).

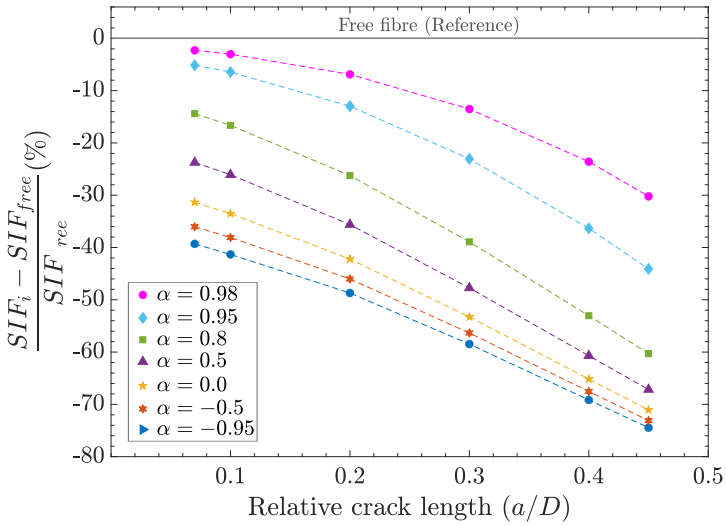

Figure 5.13: Relative reduction of the non-dimensional SIF for an isotropic fibre embedded in a matrix with respect to the free fibre (continuous grey line).

material restricts the crack opening even in the case of a low stiffness matrix. In fact, the CMOD is negligible when the matrix stiffness is large compared with that of the fibre ($\alpha = -0.95$, Figure 5.14).

The non-dimensional SIF for an isotropic fibre embedded in a matrix, as a function of the α parameter, can be approximated by the following equation, which was obtained by fitting the results of this investigation:

$$\begin{aligned} \frac{K_I}{\sigma\sqrt{\pi a}} &= A + B\left(\frac{a}{D}\right) + C\left(\frac{a}{D}\right)^2 \\ A &= A_1 + \frac{A_2}{(1-\alpha)^{A_3}} \\ B &= B_1 + \frac{B_2\,\alpha}{(1-\alpha)^{B_3}} \\ C &= C_1 + \frac{C_2}{(1-\alpha)^{C_3}} \end{aligned} \tag{5.32}$$

The use of Equation 5.32 produces data that deviates by less than 2.8% from any of the FE data points we have examined. The values of the coefficients of Equation 5.32 are listed in Table 5.1. The usefulness of this equation extends to elastic cylindrical cracked bars surrounded by a homogeneous and isotropic

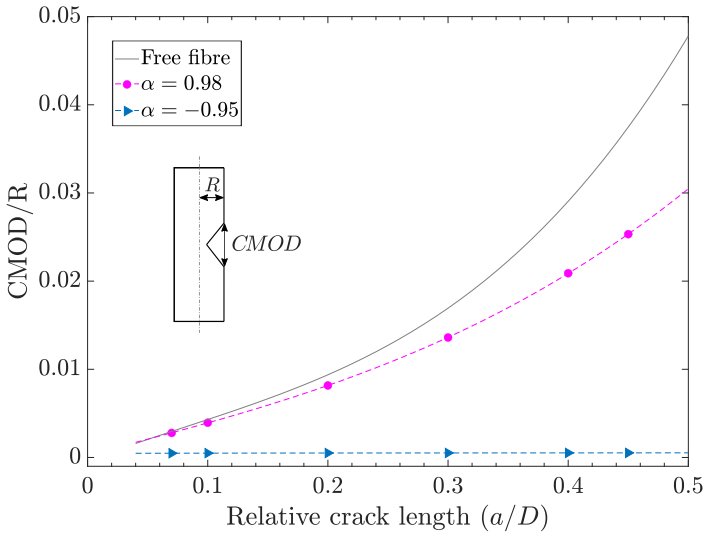

Figure 5.14: Non-dimensional CMOD for an isotropic fibre embedded in a matrix for different fibre/matrix stiffness ratios, α. The continuous grey curve corresponds to the CMOD for a free fibre ($\alpha = 1$).

material, provided that the elastic constraints specified in the previous section are obeyed.

Table 5.1: Coefficients for the fitting equation given in Equation 5.32.

A_1	1.187	B_1	-0.4268	C_1	-0.4647
A_2	-0.4349	B_2	-0.1893	C_2	0.7246
A_3	-0.3255	B_3	-0.07555	C_3	0.4295

5.5.2 Orthotropic free fibre

Figure 5.15 shows the non-dimensional SIF for an orthotropic free-fibre, for different longitudinal/transverse stiffness ratios (β equal to -0.5, 0.0, 0.5, 0.8, 0.9, and 0.99) and relative crack lengths (a/D equal to 0.07, 0.1, 0.2, 0.3, 0.4, and 0.45). The case β = 0 corresponds to the free fibre with isotropic modulus (the fibre is not completely isotropic as $\nu_{23} = 0.4$ and $\nu_{12} = \nu_{13} = 0.3$). The explored range of β involves transverse modulus, E_2^f, ranging from 3 times the axial one ($\beta = -0.5$) to being negligible ($\beta = 1$). Figure 5.16 depicts a 3D surface plot of non-dimensional SIF for better readability.

The curves indicate that the degree of orthotropy has a strong influence on the

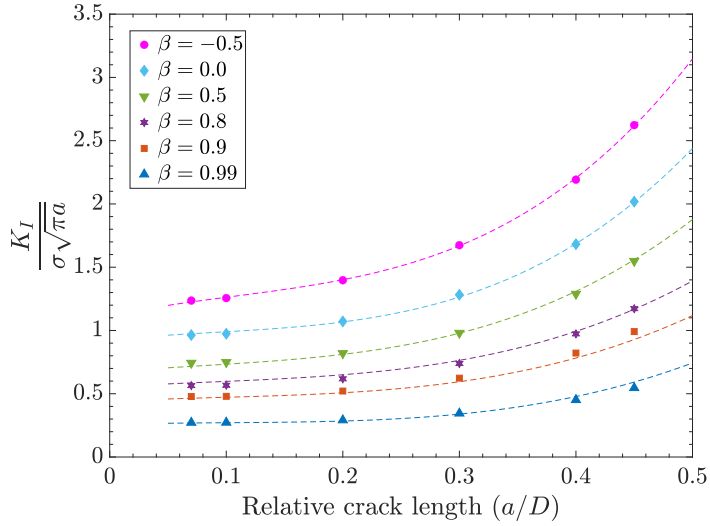

Figure 5.15: Comparison of non-dimensional stress intensity factor of an orthotropic free fibre for different longitudinal/transverse stiffness ratio, β. The dots refer to the FEM results and the dashed lines indicate the fitting results.

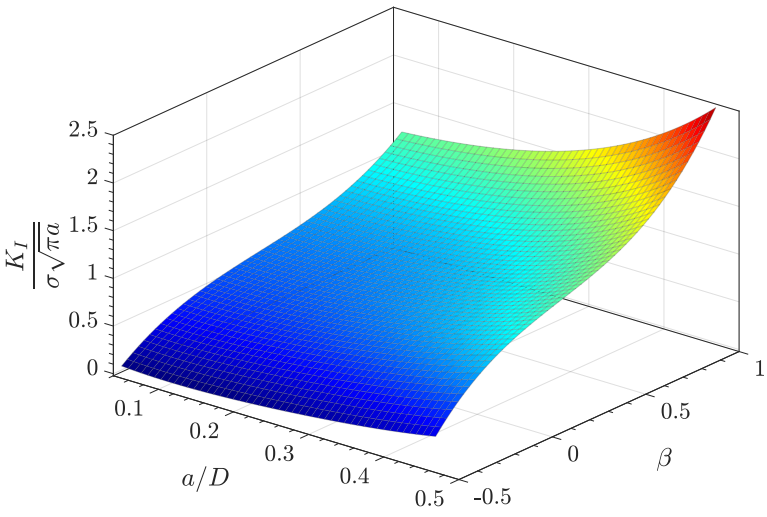

Figure 5.16: 3D surface plot of non-dimensional SIF for an orthotropic free fibre for different longitudinal/transverse stiffness ratios (β) and crack lengths (a/D).

SIF, and that the trend is opposite depending on whether the transverse modulus is smaller ($\beta > 0$) or higher ($\beta < 0$) than the axial modulus. For example, for $\beta = -0.5$ ($E_2^f = 3E_1^f$) the SIF is increased by +30% over the isotropic case; while $\beta = 0.5$ ($E_2^f = 0.33E_1^f$) involves a decrease of -25%. The relative change in the SIF of orthotripc fibres with respect to the isotropic case does not depend significantly on the crack length (Figure 5.17).

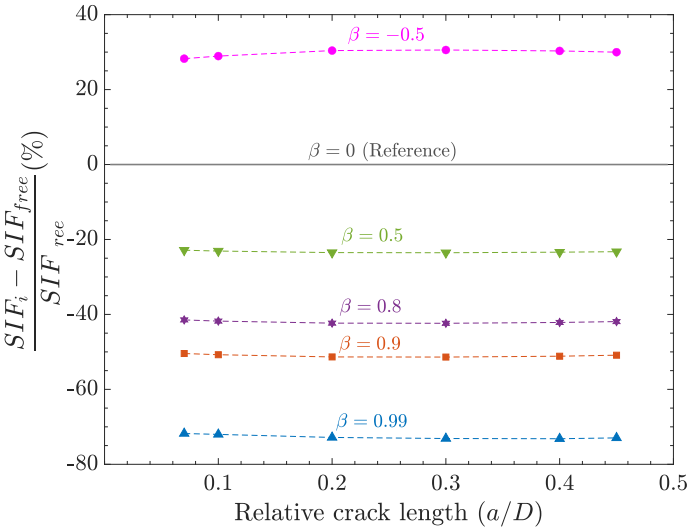

Figure 5.17: Percentage of non-dimensional stress intensity factor changes of an orthotropic free fibre for different longitudinal/transverse stiffness ratio, β. The percentage change was calculated with respect to the model with $\beta = 0$ ($E_1 = E_2$) as the reference.

The finite element results of the non-dimensional SIF for an orthotropic free fibre were fitted to the following equation:

$$\begin{aligned} \frac{K_I}{\sigma\sqrt{\pi a}} &= 0.9257 + A + B\left(\frac{a}{D}\right) + C\left(\frac{a}{D}\right)^2 + D\left(\frac{a}{D}\right)^3 \\ A &= A_1\beta + A_2\beta^2 + A_3\beta^3 + A_4\beta^4 \\ B &= B_1 + B_2\beta^1 + B_3\beta^2 + B_4\beta^3 \\ C &= C_1 + C_2\beta + C_3\beta^2 \\ D &= D_1 + D_2\beta \end{aligned} \tag{5.33}$$

The fitting employed with Equation 5.33 produces data that deviates by less than 2.0% from any of the FE data points we have examined. The values of the coefficients of Equation 5.33 are listed in Table 5.2. The application of this

equation can be extended to elastic cylindrical cracked bars with orthotropic properties, provided that the elastic constraints specified in Equation 5.27 are met.

Table 5.2: Coefficients for the fitting of equation given in Equation 5.33.

A_1	-0.9022	B_1	0.932	C_1	-4.647	D_1	17.67
A_2	0.3677	B_2	-0.7516	C_2	4.415	D_2	-10.7
A_3	1.833	B_3	1.81	C_3	-1.928		
A_4	-1.993	B_4	-1.727				

5.5.3 Orthotropic fibre embedded in a matrix

This subsection presents the effect a surrounding material has on the SIF of an orthotropic cracked fibre. This study involves both parameters α and β (β equal to -0.5, 0.0, 0.5, 0.8, and 0.9). We investigated two cases of fibre/matrix stiffness ratios: α equal to -0.95 and 0.95.

The outcome of this study (Figure 5.18) reinforces the trends presented in the previous cases: i) the presence of the matrix reduces the SIF and this effect scales with the stiffness of the matrix, and ii) the degree of orthotropy of the fibre has a strong influence on the SIF, increasing or decreasing it depending on whether the transverse stiffness is higher or lower, respectively, than the axial stiffness.

The strong observed effect of the surrounding material on the SIF should be attributed to the constrain imposed by the matrix on the opening of the crack (Figure 5.14).

The complete set of presented results have a direct application to the understanding of failure in unidirectional fibre reinforced composites. For instance, a widely-used structural carbon composite combines an AS4 carbon fibre with an epoxy matrix. For that case, $\alpha = 0.95$ and $\beta = 0.89$ (carbon fibres are non-isotropic [228]). An expoxy reinforced with glass fibres (i.e., S2/MTM44-1) corresponds to the case $\alpha = 0.91$ and $\beta = 0.0$ (glass fibres are elastically isotropic). For example, the finite element results of the non-dimensional SIF for a carbon fibre embedded in an elastic epoxy matrix were fitted to the following

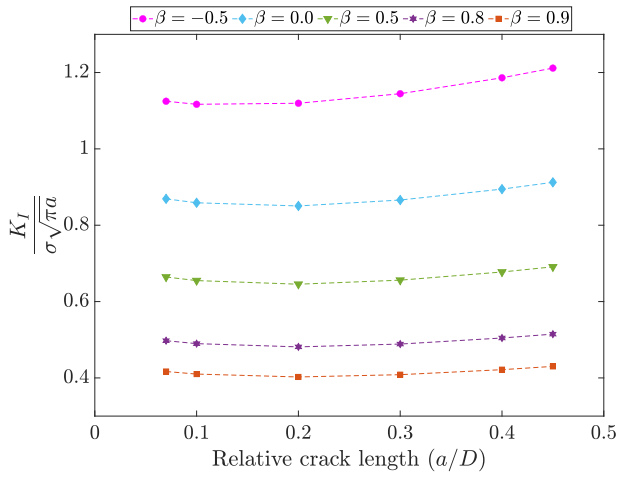

(a) $\alpha = 0.95$

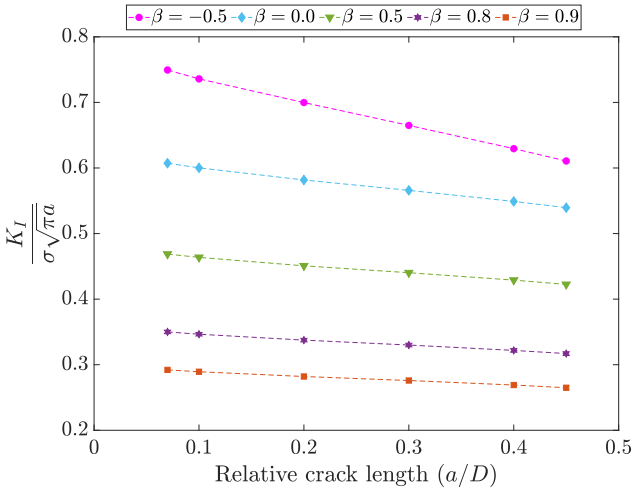

(b) $\alpha = -0.95$

Figure 5.18: Comparison of non-dimensional stress intensity factor of an orthotropic fibre embedded in a matrix, for different fibre longitudinal/transverse stiffness ratios (β) and fibre/matrix stiffness ratios (α). a) $\alpha = 0.95$ and b) $\alpha = -0.95$.

equation:

$$\frac{K_I}{\sigma\sqrt{\pi a}} = 0.4411 - 0.2258\left(\frac{a}{D}\right) + 0.5661\left(\frac{a}{D}\right)^2 \tag{5.34}$$

However, the computational model relies on a strong simplification of the physics of the real problem. Fibre (albeit not carbon fibres) and matrix are considered homogeneous elastic materials. The fibre is assumed to be surrounded by a homogeneous material with the mechanical properties of the matrix. In reality, the fibre is surrounded by a heterogeneous material including nearby fibres which will lead to a higher equivalent stiffness of the embedding material, accentuating the crack opening constraint we have described and, thus, further reducing the SIF. Therefore, we can presume that the presence of neighbouring fibres in the vicinity of the cracked fibre affects the SIF. However, it should not alter the overall trends derived from Figure 5.11. Studying the effect of adding intact fibres surrounding the cracked fibre is challenging due to the increased complexity in the geometry and all the possible combinations of material properties that may affect the outcomes of the results. Hence, this case will be considered separately in a future study. Further to this, the matrix is assumed to surround the fibre, while in reality, it will not only surround the fibre but it will also penetrate the small surface notches or defects present in the fibres and thus, further constraining the crack opening and reducing the SIF.

Another key-point is that the model assumes that the matrix is elastic and the fibre-matrix interface cannot debond. However, typical polymer matrix composites exhibit matrix yielding and fibre-matrix debonding [20]. The developed finite element model can be sophisticated for a more accurate modelling of micromechanisms by introducing fibre/matrix interface debonding and/or matrix plasticity. The effect of these phenomena will be studied in a future paper. In addition, the situation described in this investigation, a cylindrical surface-notched specimen surrounded by a material of different stiffness, goes beyond the field of fibre reinforced composites, since we provided the equations to predict the SIF of a cracked cylindrical fibre for different material properties.

In spite of all simplifications, analytical or numerical models of fibre failure and/or fragmentation in a composite, relying on the stress intensity factor, will benefit from the information presented. For example, current fragmentation

models rely on the experimental characterization of the fibre strength using a Weibull distribution [188]. This characterization is commonly performed on dry isolated fibres [20]. The present work demonstrates that this characterization can not be transferred to the fragmentation model while ignoring the effect of the matrix, since the expected strength of dry fibres will be different than that of the fibres *in-situ* as proven by the SIF. These findings may explain why the current fragmentation models predict an incorrect fibre break density evolution compared with experimental data [188]. This issue is explored in detail following in sections 5.5.4 and 5.5.5.

5.5.4 Effect on the fibre strength

In this section, the effect that embedding the fibre on a matrix has on the ultimate strength of the fibre is investigated and compared with the free fibre (i.e. without being embedded in the matrix). For this purpose, the experimental data of 34-700WD carbon fibres from Breite et al. [188, 205] is used. This experimental set provides information on the strength (σ^u) and diameter (D) of each fiber. In Breite et al. [188, 205], the strength of 34-700WD fibre was measured experimentally by means of single fibre tensile tests, and a Weibull distribution was then fitted onto the data. Therefore, we will use the same data, but we will modify the fibre strengths based on the SIF difference between dry and embedded fibres obtained in the previous sections. With this modifications, we will approximate the actual strength of the fibres in-situ (being embedded onto the matrix), and fit a new Weibull distribution to this data. The idea is to compare how different is the fibre strength distribution of the 'embedded' fibres compared with the 'free' fibres.

The approach assumes that the measured fibre strength is related to surface defect in the fibre. From the knowledge of the fibre toughness and individual strength, we compute the critical defect size that caused failure. Then, we assume that the same defect will be the critical one for the failure of the embedded fibre.

To do this, first, the crack length in free fibers is computed when failure occurs. The failure of the fibre is triggered when the stress intensity factor (K_I) reaches

the critical SIF (K_{IC}):

$$\begin{aligned} K_I &= K_{IC} \\ \sigma_i^u \cdot f\left(a_i/D_i\right) \cdot \sqrt{\pi a_i} &= K_{IC} \qquad i : \text{the i fibre} \end{aligned} \tag{5.35}$$

where σ^u is equal to the experimental strength of free fibre given in Breite et al. [188, 205], $f(a/D)$ is the non-dimensional SIF for free carbon fibre obtained by Eq. 5.34, and the critical SIF (K_{IC}) is taken equal to 2.12 $MPa\sqrt{m}$, as calculated by Herraez et al. [119]. By solving Equation 5.35, the critical crack length (a_i) that supposedly broke the free fibres is obtained. In the next step, the objective is to calculate the strength (σ) of the embedded fibres. To do so, Eq. 5.35 is solved with the following inputs: $f(a/D)$ given by Eq. 5.32 (which corresponds to the non-dimensional SIF for an embedded fibre), the critical crack length (a_i) is the same as that obtained for free fibers, and K_{IC} is again 2.12 $MPa\sqrt{m}$.

The approach proposed assumes that the crack length that broke the fibre is the same for the dry and embedded fibre. In addition, the critical SIF used (= 2.12 $MPa\sqrt{m}$) was computed for a fibre different than the one used in this work. Nevertheless, the authors believe that this approach is representative enough to study the implications of embedding the fibre or not on the fibre strength.

Figure 5.19 depicts the strength distribution histogram for both free fibre and embedded fibre. It is observed that the strength of the fibres embedded in the matrix is increased (on average, 11%) compared to the free fibres, so that both diagrams are shifted one in respect to the other. Further to this, a unimodal Weibull distribution [19] was fitted onto both datasets using the maximum likelihood estimator. The Weibull plots for both free and embedded fibers are shown in Figure 5.20, together with the scale parameter (σ_0) and Weibull modulus (m).

Results show that the scale parameter of the embedded fibres is larger than that of the dry fibres, which is coherent with the observations seen with the SIF. We also note that there is a slight increase in the Weibull modulus, indicating a narrower strength scatter. With the embedded Weibull distribution, we can expect that the fibre break density evolution will be delayed compared with the Weibull distribution obtained from the dry fibers. This will be studied next in Section 5.5.5.

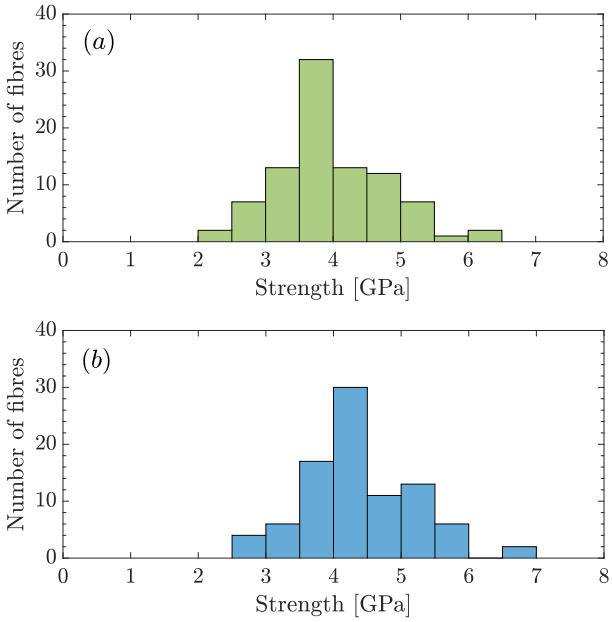

Figure 5.19: The histograms of the tensile strength distribution of the fibres: (a) free fibres, (b) fibres embedded in an elastic matrix.

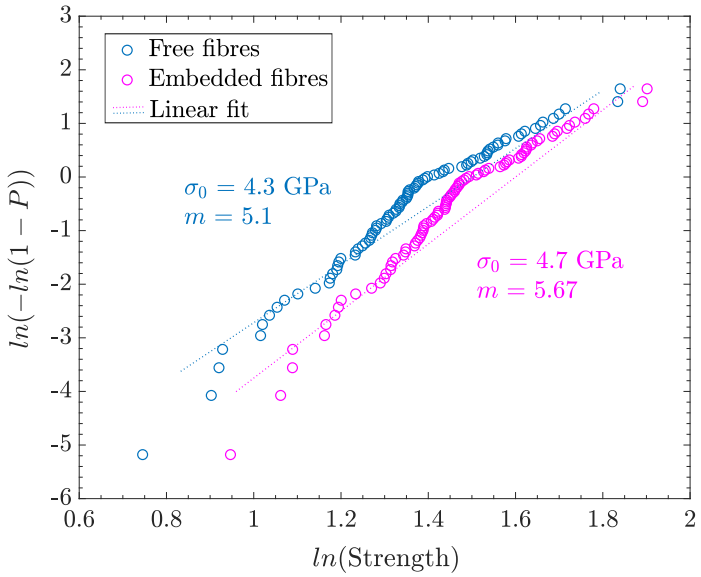

Figure 5.20: Logarithmic Weibull plot diagram (P is the probability of failure), for eighty-nine $34-700WD$ carbon fibers being either free or embedded in a matrix.

5.5.5 Progressive failure and cluster development

The PFM (Section 5.3.3) is used to investigate the impact of using the Weibull distribution modified with the SIF (i.e. embedded fibres), compared with the Weibull distribution without this modification (i.e. measured from dry fibres). To do so, the unidirectional 34-700WD carbon fibre composite material with 736LT epoxy matrix is simulated under longitudinal tension using each Weibull distribution, and the results are compared against experimental data of this material from Breite etal. [188]. Table 5.3 presents the material properties of the fibre. The matrix Young's modulus E_m, Poison's ratio ν_m, and shear yield stress τ_m, are 3.15 GPa, 0.39 and 60.4 MPa, while the fibre volume fraction, V_f, is 48.32%. Notice that in Breite etal. [188], we already simulated such composite with the PFM using the unmodified Weibull distribution from dry fibres and compared the results with the experimental data. Therefore, only the results using the modified Weibull distribution are new. Details of the experimental campaigns are provided in depth in Breite etal. [188], while all experimental data can be found in a data-in-brief paper [205].

Table 5.3: Material properties for the 34-700WD carbon fibre.

Engineering constants and geometrical properties						Weibull parameters (free / embedded fibres)		
E_{11}	$E_{22} = E_{33}$	$G_{12} = G_{13}$	G_{23}	ν	R_f	σ_0	L_0	m
[GPa]	[GPa]	[GPa]	[GPa]	[-]	[μm]	[MPa]	[mm]	[-]
234	15	13.7	6	0.25	3.26	4306 / 4700	12 / 12	5.1 / 5.67

Figure 5.21 shows the average failure strain and strength, as well as the average stress-strain curve from 50 simulations with each Weibull distribution, compared against the experimental measurements. There is little difference in the predicted failure strain and strength by using the modified Weibull distribution or not. The modified Weibull shows larger strength since the strength distribution was shifted to larger strengths (see Fig. 5.19), but the effect is small. In this regard the model is very far from the experimental result as previously outlined in [188].

On the other hand, Fig. 5.22 illustrates the fibre break density evolution as a function of the applied stress. The fibre break density was computed as the number of element breaks divided by the material volume [168]. While the modelling predictions using the original Weibull distribution are extremely off from the experimental data, the results using the Weibull distribution modified

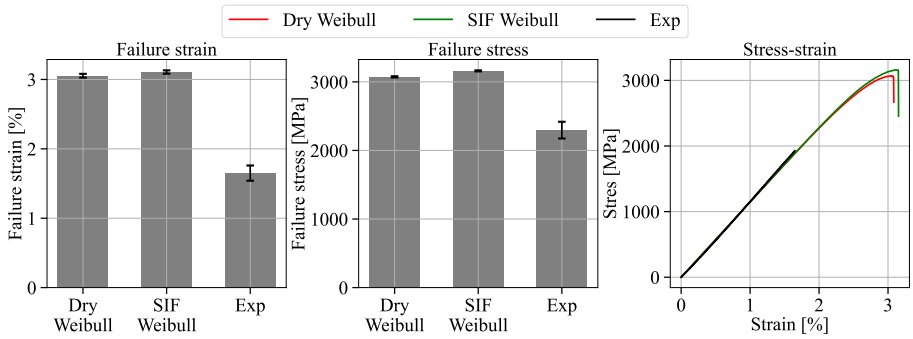

Figure 5.21: Ultimate average failure strain and stress, and stress-strain curve predicted by the PFM from 50 runs (using the Weibull distribution from single fibre tests, and the distribution modified by SIF), compared with the experimental data.

by the SIF is significantly closer to the experimental data points.

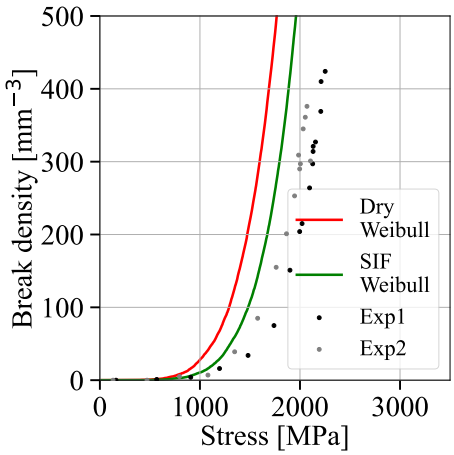

Figure 5.22: Average fibre break density as a function of the applied stress predicted by the PFM from 50 runs (using the Weibull distribution from single fibre tests, and the distribution modified by SIF), compared with the experimental data of two specimens (indicated as Exp1 and Exp2).

These findings suggest that testing dry fibres to obtain the Weibull distribution is not appropriate, since the strength of the fibres in-situ (i.e. embedded into the matrix) is not the same. The difference that still occurs between the model and experiments can be attributed to different things. Firstly, the Weibull distribution modified to account for the matrix was obtained using the fracture toughness of an AS4 carbon fibre, which is different than the 34-700WD fibre simulated here. Secondly, our equations to compute the SIF of the fibre assume the presence of a straight-fronted edge crack in the fibre. In reality the critical crack in the

fibre may have much more complex shapes. The strong difference in strength is probably due to the presence of defects in the experimental samples that were not accounted for in the models. The fibre is considered an homogeneous material, despite the fact that the real microstructure is far more complex [229].

Finally, as outlined previously in Section 5.5.3, simplifications in the FE model such as the omission of matrix plasticity or fibre-matrix debonding may affect the computation of the SIF. For instance, adding matrix plasticity will tend to lower the stress transfer in the matrix, thereby lowering further the SIF and shifting the fibre break density predictions of the PFM even closer to the experimental data.

Finally, Figure 5.23 shows the maximum cluster size of broken fibres, and the 2-plet and 3-plet density as a function of the applied stress. In this work, two fibres are part of the same cluster if their centre-to-centre radial distance was equal to or lower than two fibre diameters and the axial distance was equal to or lower than fifteen fibre diameters [188]. The maximum cluster size is therefore, the number of broken elements contained by the largest cluster. The 'i-plet' density can be understood as the number of clusters containing 'i' broken elements and divided by the RVE volume [170]. Results show that using the modified Weibull distribution causes the cluster size and the i-plet density to increase later than when using the unmodified distribution. However, the trends are the same, hence there is no clear worsening or improvement of the predictions compared with the experimental data. Besides this, we also monitored the formation of co-planar clusters (clusters where all breaks are in the same plane) and found no difference by using one Weibull distribution or the other. Currently, this is one of the weakest points of strength models, since these show a tendency to underestimate co-planarity compared with experimental data [188].

In summary, the change of the fibre strength distribution only affected the point of failure initiation. Using the modified Weibull distribution, accounting for the presence of the matrix, caused the fibres to start failing later, therefore, the break density got considerably closer to experimental data. The cluster formation was not altered significantly, and thus the results did not change in this regard. It is worth noting that the failure strain and strength increased slightly compared to the original weibull distribution.

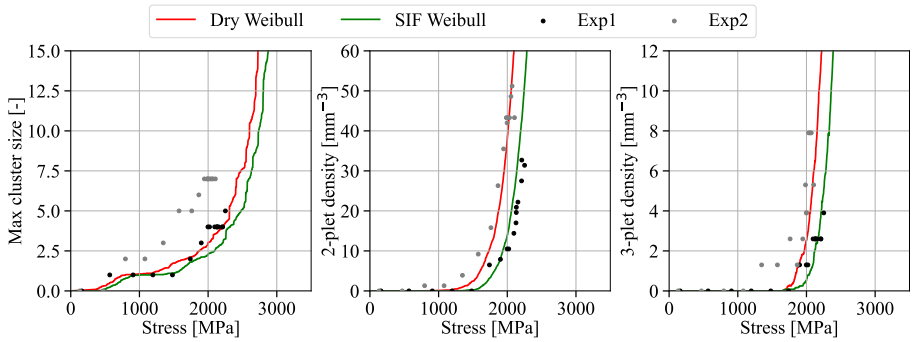

Figure 5.23: Average max cluster size, formation of 2-plet and 3-plet as a function of the applied stress predicted by the PFM from 50 runs (using the Weibull distribution from single fibre tests, and the distribution modified by SIF), compared with the experimental data of two specimens (indicated as Exp1 and Exp2).

5.6 Concluding remarks

In this work a micromechanical finite element model was developed to analyse the stress intensity factor of a single fibre with a straight-fronted edge crack. The fibre was considered elastic and either isotropic or orthotropic, and free or embedded in an elastic material of different stiffness. The study was performed using non-dimensional variables for the fibre/matrix stiffness ratio and fibre longitudinal/transverse stiffness ratio. Only the modulus of elasticity of fibre and matrix were explored, the rest of the elastic parameters were kept constant throughout the study. The stress intensity factor evaluation was carried out using the J-integral. Then, the results obtained from the finite element model were used as input to calculate the Weibull parameters and the rate of change in the ultimate strength of the embedded fibres compared with the dry fibres. Finally, a semi-analytical progressive failure analysis was conducted to illustrate the impact of these changes on the tensile failure and damage development of a unidirectional carbon composite material.

Embedding the fibre in an elastic matrix reduced the SIF over the free fibre case (i.e. without being embedded into a matrix). The higher the matrix stiffness was, the more substantial the decrease in SIF. This effect is due to the constraint of the matrix over the crack opening. For instance, for the model with a very low stiffness matrix ($E^m = 0.01E^f$) the SIF is reduced by -7% at a/D = 0.2 or by -25% at a/D = 0.4, with respect to the free fibre case. We proposed a general non-dimensional equation for the non-dimensional SIF as a function

of the non-dimensional crack length and the ratio between the stiffness of the cracked cylinder and that of the surrounding material.

The elastic orthotropy of the fibre greatly affected the SIF in that it increased for the case of a transverse stiffness higher than that of the axial, and decreased for the opposite case. For example, for a fibre with $E_2^f = 3E_1^f$, the SIF is increased by +30% over the isotropic case ($E_2^f = E_1^f$); while a fibre with $E_2^f = 0.33E_1^f$ involves a decrease of -25%. An equation obtained by fitting was also provided for this case.

It was found that the presence of the matrix enhances the strength of the fibers and alters the Weibull strength distribution parameters, resulting in the fibers failing at higher strains. A modified Weibull distribution taking into account such effect due to the presence of the matrix was computed. The progressive failure of a unidirectional carbon composite was simulated using this Weibull distribution. The fibre break density predicted by the model became significantly closer to the experimental observations, showing that the presence of the matrix must be accounted for obtaining the strength of the fibres.

Although the study presented here was motivated by an interest in improving the understanding of fibre failure in fibre reinforced composite materials, the findings and the equations provided also contribute to the general field of SIF in elastic cracked bodies.

6

In situ stress intensity factor of a carbon fibre embedded in an epoxy matrix

This chapter expands the content of Chapter 5 by focusing on carbon fibers and to account for material non-linearities. The aeronautical-grade carbon fibre reinforced plastic AS4/8552 was chosen for the purpose of demonstration of the methodology. This study proposes a high fidelity micromechanic modelling approach to predict the in situ SIF of a single carbon fibre with an edge crack, embedded in an epoxy matrix. Beyond that, the effects of fibre/matrix interface debonding and matrix plasticity have on the SIF were studied.

6.1 Introduction

In CFRP composites, the carbon fibres are surrounded by a matrix which acts as a binder, maintains the orientation of the fibres and protects them from environmental destructive effects. Hence, the properties of CFRP composites are essentially controlled by the corresponding properties of their constituents, including fibre, matrix and fibre/matrix interface. Nevertheless, current numerical and experimental studies commonly determine the SIF of fibres without considering a matrix, therefore being the fibre isolated [119, 189–192, 194–197, 199, 202, 204, 215]. This is not realistic in CFRP composites since the presence of the matrix could modify the stresses around the crack tip, thereby affecting the SIF. In line with this, the strength of fibres, which is usually employed by micromechanical strength models to predict failure [20, 103, 167, 168, 170, 230–232] is commonly obtained from single fibre tests, without the fibre being embedded into a matrix. If the SIF of a fibre embedded into a matrix differs from the free fibre, one could expect that the strength is also different. This could have major consequences for the micromechanical modelling of composites.

In the previous Chapter, we carried out a comprehensive parametric study of the SIF of a single generic fibre embedded in an isotropic matrix. The effect that several parameters, including the fibre/matrix stiffness ratio and fibre orthotropy (fibre longitudinal/transverse stiffness ratio), have on the SIF were investigated. It was found that the matrix diminishes the SIF of a cracked fibre and the magnitude of this effect is directly related to the fibre/matrix stiffness ratio. For instance, an increase in the matrix stiffness severely reduced the fibre SIF. Further studies revealed that elastic orthotropy (longitudinal/transverse stiffness ratio) of a fibre greatly affected the SIF. The SIF increased when the transverse stiffness was higher than the axial one, and decreased for the opposite case. Based on

these findings, it can be expected that the SIF of carbon fibres embedded in a matrix differs from the free fibre, and consequently, the presence of the matrix cannot be neglected in fibre fragmentation studies of composites. This however, remains to be proven.

In addition to the parameters studied previously in Chapter 5, failure mechanisms in fiber composites also depend on other parameters such as matrix inelastic deformation and interface debonding [121]. These phenomena play an important role in composite crack propagation and failure [169], however, their influence on the SIF of a fibre are unknown. A deeper understanding about the SIF could improve the prediction of the strength of unidirectional CPRF composites in the direction of the fibres, which is crucial for the design and analysis of composite materials.

To further elucidate the knowledge in this topic, the present study proposes a high-fidelity computational micromechanics finite element model to compute the SIF for a straight edge crack in a carbon fibre subjected to tension loading, while embedded in an epoxy matrix in the presence of matrix plasticity and interface debonding. Unlike Chapter 5, the micromechanical analyses herein are based on a realistic material system, the carbon/epoxy AS4/8552, whose properties have been thoroughly characterized by means of experimental micromechanics in Section 3.1. This study is organized as follows. First, we investigate the impact of considering a carbon fibre as an isotropic or orthotropic material on the SIF. Next, the effect that embedding the carbon fibre in an epoxy matrix has on the SIF is investigated. Finally, we study the influence the fibre/matrix interface debonding and matrix plastic deformation have on the SIF. The results indicate that the SIF of an embedded carbon fibre is lower than the free fibre. Taking into account matrix plasticity increases the SIF compared with a perfectly elastic matrix, but still reduces the SIF compared with a free fibre. The presence of debonding had a similar effect. Results demonstrate that the surrounding matrix cannot be neglected.

6.2 Methodology

6.2.1 Finite element micromechanics modelling

The computational micromechanics simulations were performed in Abaqus/Standard [150]. The model is based on the one presented in Chapter 5, which has been validated through various approaches. The micromechanical finite element model consisted of a notched carbon fibre embedded in an isotropic epoxy matrix, subjected to a remote tensile axial force, while the lateral surface was stress free (Figure 6.1a). The carbon fibre included a straight-fronted edge crack at $x_1 = L/2$ as indicated by the grey area in Figure 6.1a, with changeable crack length (a). Matrix and fibre were modelled as elastic materials in the reference model, with a perfect fibre/matrix adhesion using tie constraints at the interface. Depending on the phenomenon to study, more complex models, including matrix plasticity and/or fibre-matrix debonding are simulated as well as later clarified. The matrix is modelled as isotropic, whereas the carbon fibre is orthotropic. We will however also perform one case with an isotropic carbon fibre to observe the effect of the carbon fibre orthotropy.

The length of the model (L) had to be long enough to guarantee that the remote stresses are not affected at the upper and bottom faces, by the presence of the crack. This prerequisite led to $L = 10D$, where D is the fibre diameter. The thickness of the surrounding matrix (t) was selected large enough to avoid severe deformation in the boundaries of the matrix around the crack region. This criterion prevailed over achieving a realistic composite fibre volume fraction, and led to $t = D$. Although this thickness of the surrounding matrix can be seen as unrealistically large for common carbon/epoxy composites, this is not a significant issue for the purpose of this study. In any case, we will also show results for different thicknesses to assess its effect. The size of the model was decided based on parametric studies that targeted the best trade-off between computational cost and precision.

To reduce the computational costs, only one-quarter of the model was simulated by taking advantage of the symmetry boundary conditions along the x_1 and x_3 axes as shown in Figure 6.1a. A uniform normal traction stress σ was applied in

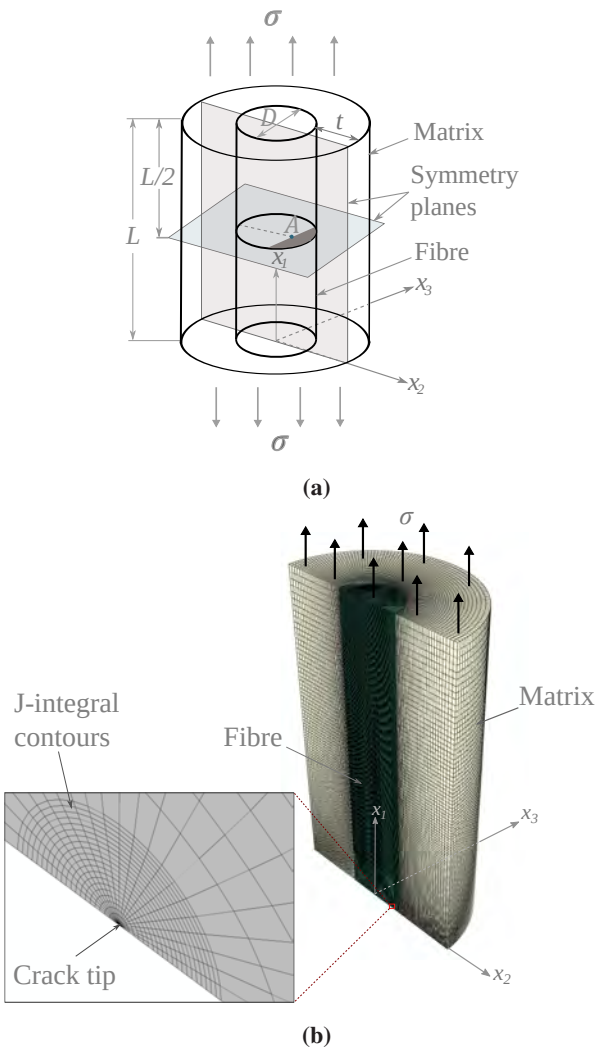

Figure 6.1: Geometrical illustration of the finite element model. a) A notched carbon fiber with a straight-fronted edge crack (indicated in grey) embedded in an epoxy matrix and b) the FE model with details of boundary conditions and finite-element meshing.

the upper part of the model.

The fibre and matrix were meshed separately to achieve an optimal meshing. A combination of swept and structured meshes were used around the crack tip to enrich the discretization and capture the high stress gradients therein (Figure 6.1b). The size of the elements were selected in the range of $D/1500$ (around crack tip) to $D/100$ (in far-field), based on a convergence study. To account for the stress singularity (infinite stress), quadratic isoparametric elements (C3D20) with the inverse square root singularity were used at the crack tip.

6.2.2 Numerical evaluation of SIF

The stress intensity factor evaluation was carried out using the J-integral [208] method, which is the standard approach in characterizing the energy release rate associated with a potential crack growth. In this approach, the energy release rate is obtained by integration along the contour Γ around the crack tip with

$$J = \int_{\Gamma} \left(W dx_2 - t \cdot \frac{\partial u}{\partial x_1} ds \right) \tag{6.1}$$

where x_1 and x_2 are rectangular coordinates to the crack front, x_1 being perpendicular to the crack surface; W is the elastic strain density, t is the traction vector, u is the displacement vector, and ds is an increment of arc length along any contour Γ. Although the J-integral is path independent, a total of 21 concentric contours surrounding the crack tip were used to increase the accuracy (see Figure 6.1b). In addition, due to the geometry of the model and crack, J-integral values are not constant along the crack front, thus the finite element model is focused on the maximum value attained at point A (Figure 6.1a). For linear elastic problems, J-integral equals to the energy release rate (G_I) under a single mode condition. The stress intensity factor in mode I, K_I, was calculated from J-integral by employing Eq.(6.2) and Eq.(6.3) for the isotropic and orthotropic cases, respectively.

$$J_{ISO} = \frac{{K_1}^2(1-\nu^2)}{E} \tag{6.2}$$

$$J_{ORT} = {K_I}^2 \sqrt{\frac{a_{11}a_{22}}{2}} \left[\sqrt{\frac{a_{22}}{a_{11}}} + \frac{2a_{12} + a_{66}}{2a_{11}} \right]^{1/2} \tag{6.3}$$

In the isotropic case, the SIF depends only on the fibre Young's modulus E and the Poison's ratio ν, while in the case of orthotropic, the compliance tensors a_{ij} are also involved. The reader is referred to Chapter 5 for in-depth details.

6.2.3 Model constituents

The aeronautical-grade CFRP system AS4/8552, which has a wide application in industries, was chosen as reference material for the purpose of demonstrating the methodology. Table 6.1 presents the constitutive models and experimentally-characterized properties of the fibre, matrix, and interface constituents for this material system, which have been thoroughly discussed in Chapter 3. For the sake of completeness, the essential or distinctive aspects are overviewed herein.

Table 6.1: Mechanical properties of materials used throughout the simulations.

AS4 carbon fiber						
E_1^f [GPa]	E_2^f [GPa]	ν_{12}^f	ν_{23}^f	G_{12}^f [GPa]	G_{23}^f [GPa]	
231	13	0.3	0.46	11.3	4.45	
8552 epoxy matrix						
E^m [GPa]	ν^m	α^m [10^{-6} °C^{-1}]	σ_{yt}^m [MPa]	G_t^m [GPa]	σ_{yc}^m [MPa]	σ_{uc}^m [MPa]
5.07	0.35	52	121	90	176	180
AS4/8552 fiber-matrix interface						
N [MPa]	S [MPa]	K_{nn} [GPa/um]	K_{ss} [GPa/um]	G_n [J/m]	G_s [J/m]	η_{BK}
42	63	100	100	2	100	1.2

6.2.3.1 Fibre and matrix

The AS4 fibre is modeled as linear elastic and transversely isotropic solid. The 8552 epoxy polymer matrix is represented using the isotropic plasticity model included in Abaqus/Standard [145], which is based on pressure-dependent Druker-Prager [144] plastic behaviour, coupled with tensile damage degradation

to simulate brittle materials [142].

6.2.3.2 Fibre/matrix interface

The fiber-matrix interface is modelled using the surface-based implementation of the cohesive zone method which is coupled with Coulomb frictional behaviour to simulate the sliding of the fibres upon decohesion. A mixed-mode bilinear traction-separation law is used to define the cohesive behaviour. Damage initiation is modeled using a quadratic stress-interactive criterion and damage propagation occurs under the Benzeggagh-Kenane law [151]. Matrix and fibres are modelled as separated geometrical entities which interact by normal and sliding contact kinematics. To this purpose, the penalty-based general contact algorithm is used. Cohesive laws are coupled to the contact surface relations to simulate fibre-matrix debonding.

6.3 Results and discussion

6.3.1 Effect of isotropy and orthotropy

Figure 6.2 illustrates the non-dimensional SIFs for an isotropic and orthotropic free AS4 carbon fibre (i.e., without being embedded into a matrix) for different relative crack lengths (a/D equal to 0.07, 0.1, 0.2, 0.3, 0.4, and 0.45). In the case of isotropic, $E_2^f = E_1^f$ and $\nu_{23}^f = \nu_{12}^f$.

The results indicate that considering a carbon fibre as an orthotropic or isotropic material has a strong influence on the SIF. In the orthotropic carbon fibre, the SIF is reduced by 54% compared to the isotropic case. The relative change in the SIF of orthotripc fibre with respect to the isotropic case does not depend significantly on the crack length as it is approximately equal to 54% for all the crack lengths. The results are consistent with our previous study in Chapter 5, which demonstrated that the degree of orthotropy (longitudinal/transverse stiffness ratio) has a strong influence on the SIF. These results therefore prove that simplifying the fibre as isotropic instead of orthotropic is not correct when the SIF is to be taken into account. This is an important fact, since many modelling works simplify the fibres as isotropic [103, 168, 232].

The non-dimensional SIF for an isotropic free carbon fibre can be approximated

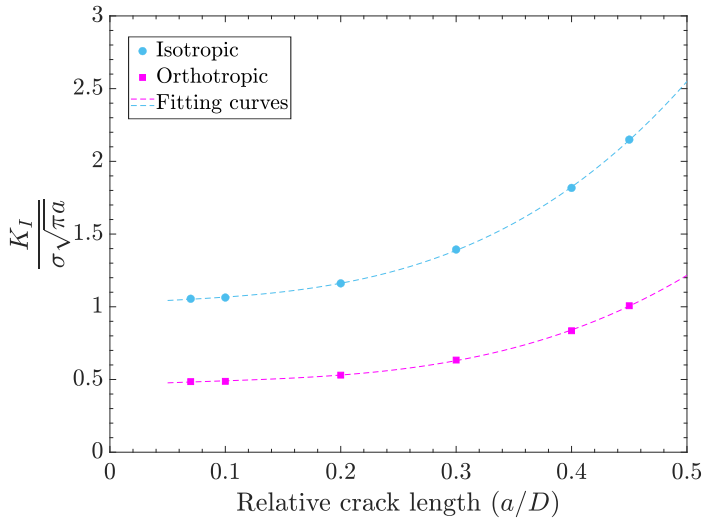

Figure 6.2: Non-dimensional SIF of a free carbon fibre with isotropic or orthotropic elastic properties.

by the following equation, which was obtained by fitting the results of this investigation:

$$\frac{K_I}{\sigma\sqrt{\pi a}} = 1.023 + 0.4448\left(\frac{a}{D}\right) - 1.4\left(\frac{a}{D}\right)^2 + 13.23\left(\frac{a}{D}\right)^3 \tag{6.4}$$

and for the orthotropic case as:

$$\frac{K_I}{\sigma\sqrt{\pi a}} = 0.458 + 0.4709\left(\frac{a}{D}\right) - 2.296\left(\frac{a}{D}\right)^2 + 8.774\left(\frac{a}{D}\right)^3 \tag{6.5}$$

where a is the crack length and D is the diameter of carbon fibre. Equations 6.4 and 6.5 can therefore be used to estimate the SIF for a free carbon fibre with an error of $\leqslant 1.0\%$.

6.3.2 Orthotropic carbon fibre embedded in a matrix

Figure 6.3 plots the evolution of the non-dimensional SIFs for an orthotropic carbon AS4 fibre embedded in an 8552 elastic epoxy matrix for different relative crack lengths (a/D equal to 0.07, 0.1, 0.2, 0.3, 0.4, and 0.45). The model was run for different matrix thicknesses (t equal to $D/4$, $D/2$, and D). Perfect adhesion is considered between the fibre/matrix interface. The SIFs of an orthotropic free fibre (grey line) were added as a baseline, for comparison.

A drastic drop in the SIFs can be seen in the embedded carbon fibre compared to its free counterpart, especially in the larger cracks. For instance, for the embedded case with matrix thickness $t = D$, the SIF is reduced by 11% with a crack length $a/D = 0.1$ and by 55% with a crack length $a/D = 0.45$, compared with the free fibre case. This SIF reduction is directly dependent on the thickness of the matrix. It can be seen that the embedding effect is intensified by increasing the thickness of the matrix, especially in larger cracks. The thickness of the matrix significantly affects the SIF, but only up to a certain value. For thicknesses larger than the fibre diameter (D) the effect was seen to be negligible.

The fact that embedding the fibre into a matrix reduces the SIF was already observed in Chapter 5 with a fictitious fibre, and can be attributed to the fact that the matrix constraints the fibre crack opening, reducing the SIF. Further, the influence of crack length on the SIF is reduced significantly in the presence of the matrix unlike the free fibre which increases exponentially with crack length. Results prove that omitting the presence of the matrix to compute the SIF is not appropriate.

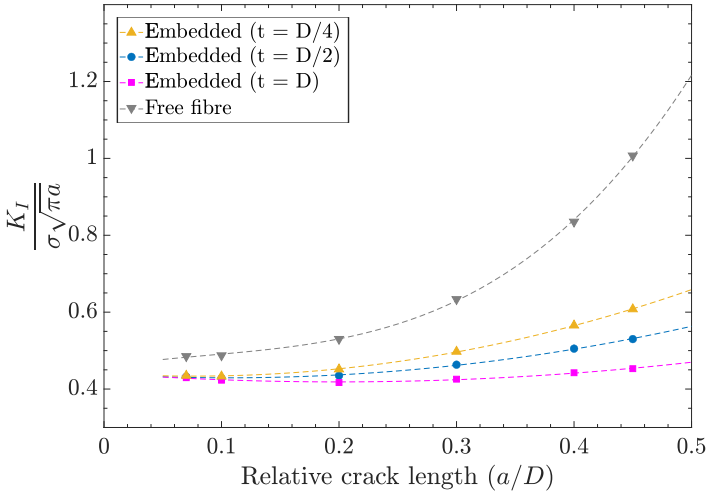

Figure 6.3: Comparison of the non-dimensional SIFs of an orthotropic carbon fibre embedded in a linear-elastic matrix for different matrix thicknesses (t). The results of a free carbon fibre are added as the reference for comparison. The parameter D is the fibre diameter. The markers represent the FE results and dashed lines represent the fitting results.

It is also worth remarking that these findings are obtained by embedding a single

carbon fibre into a matrix. In reality, a composite material contains millions of fibres. Therefore, we can presume that the presence of fibres neighbouring the cracked fibre will influence the SIF, but it should not alter the trends derived from Figure 6.3. Studying the effect of adding fibres surrounding the cracked one is challenging due to the increased complexity in the geometry and all the possible material properties combinations that may affect the outcomes of the results. Consequently, this will be studied separately in future work.

By fitting onto the finite element model results, the non-dimensional SIF for an orthotropic carbon fibre embedded in an elastic matrix with thickness of D, with perfect fibre/matrix adhesion, can be approximated by the following equation

$$\frac{K_I}{\sigma\sqrt{\pi a}} = 0.4411 - 0.2258\left(\frac{a}{D}\right) + 0.5661\left(\frac{a}{D}\right)^2 \tag{6.6}$$

This equation produces data that deviates by less than 1.0% from any of the FE data points we have examined.

6.3.3 Fibre/matrix interface debonding

Figure 6.4 depicts the results of the non-dimensional SIFs for an orthotropic AS4 carbon fibre embedded in an elastic 8552 epoxy matrix for different relative crack lengths (a/D equal to 0.07, 0.1, 0.2, 0.3, 0.4, and 0.45), in the presence of interface debonding. The fibre/matrix interface debonding was modelled based on the cohesive zone model approach, as described in section 6.2.3. The results are compared with the ones obtained previously in section 6.3.2 considering perfect fibre/matrix adhesion.

The carbon fibre with interface debonding presents higher SIFs compared to the model with perfect interface adhesion. The difference is minimal with smaller cracks, while it becomes more pronounced as the crack length increases. This is due to the separation of the fibre/matrix interface in the vicinity of the crack, which reduces the matrix constraint on the fiber crack opening. As a result of the debonding, the fibre and the matrix separate, and consequently the fiber crack opening is allowed to move more independently than the matrix, behaving more

similar to a free fibre and leading to an increase of the SIF. This fact is proved by Figure 6.5, which shows the comparison of the non-dimensional Crack Mouth Opening Displacement (CMOD) for both cases. The CMOD in the model with interface debonding grows faster and has a linear correlation with crack length compared to the model without debonding. Therefore, in this respect, stronger interfaces are preferable since they will decrease the possibility of debonding and decrease the SIF. Nevertheless, we note that, even for the largest crack length used in this work, the SIF with debonding is still considerably smaller than the free fibre, proving again the importance of taking into consideration the presence of the matrix.

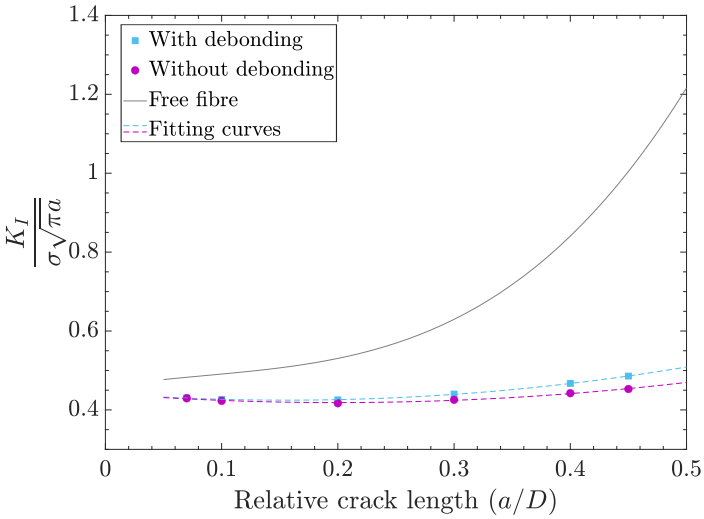

Figure 6.4: Comparison of the non-dimensional SIFs of an embedded orthotropic carbon fibre with interface debonding and perfect adhesion. Free fibre curve added for comparison reference.

Figure 6.6 depicts the evolution of the maximum interface debonding length (i.e., the length extension between fibre and matrix that has debonded) with respect to the relative crack length (a/D). Results show that the interface debonding length grows with an increase in the crack length. It is worth noting that the half of the interface debonding is depicted since the model is symmetrical. This fact explains why the SIF with debonding interface increases with larger crack lengths. Since increasing the crack length increases the debonding length, there is a larger region between the fibre and matrix that separates. Consequently, as the debonded length increases, the matrix restrains less the crack opening,

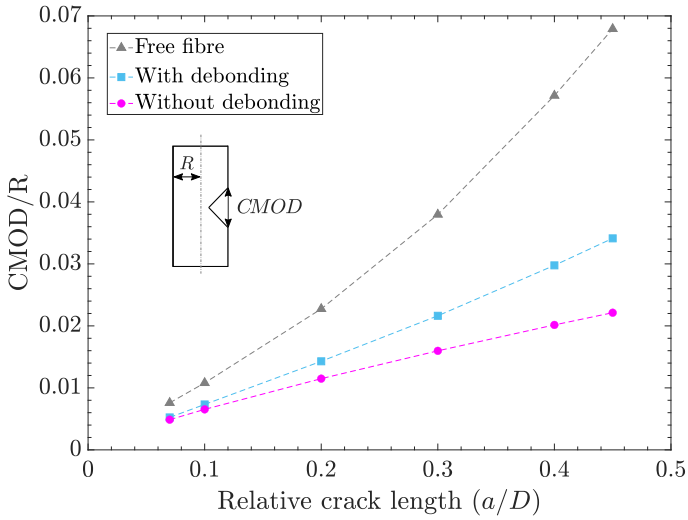

Figure 6.5: Evolution of non-dimensional CMOD for the model with interface debonding and the model without interface debonding, as a function of the relative crack length (a/D).

increasing the SIF. Since the debonding length is generally small (about few times the fibre radius), the presence of the matrix is still significant, hence leading to much smaller SIF than the free fibre.

A further interesting point is that the SIF trends do not seem to correlate with the observations found regarding the Stress Concentration Factor (SCF) around broken fibres seen in the literature [121]. While the SCF in intact fibres around broken fibres is known to decrease when debonding appears, the opposite occurs with the SIF. Even though both properties are different, they are both related with the failure of composites. This can be important for micromechanical strength models that attempt to model the failure of composite materials [18, 103, 169, 181, 231], especially if such models attempt to combine fracture mechanics approaches with strength-based failure criteria.

The non-dimensional SIFs for an orthotropic carbon fibre embedded in an elastic matrix, with interface debonding can be approximated by

$$\frac{K_I}{\sigma\sqrt{\pi a}} = 0.442 - 0.2214\left(\frac{a}{D}\right) + 0.7096\left(\frac{a}{D}\right)^2 \tag{6.7}$$

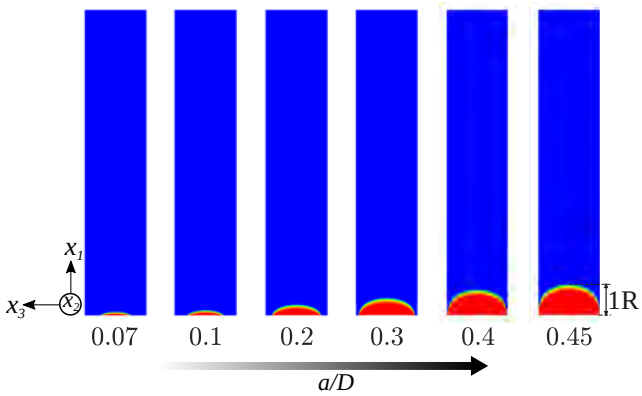

Figure 6.6: Evolution of the interface debonding as a function to the relative crack length (a/D). Only half of the interface debonding is depicted as the model is symmetric. The approximate debonding lengths (relative to the fibre radius) are 0.11R, 0.17R, 0.35R, 0.56R, 0.82R, and 1R from left to right, respectively.

6.3.4 Fibre/matrix interface strength

Due to the importance of the debonding effect found in previous section 6.3.3, this section studies the effect the fibre/matrix interface strength has on the SIF.

Figure 6.7 shows the evolution of the SIFs for an orthotropic AS4 carbon fibre embedded in a elastic 8552 matrix for different interface strength including standard, weak and strong. The standard refers to the reference model based on the properties listed in Table 6.1. The weak and strong employ half and double the strength of the standard case, respectively. The rest of the modelling parameters are left unchanged.

The results show that an increase in interface strength leads to a small drop in the SIF of the cracked fibre, especially for shorter cracks, although the difference between the three SIFs is generally small. The difference in the SIF levels are more prominent for small cracks and then progressively decrease as the crack lengths deepen. Figure 6.8 plots the non-dimensional length of interface debonding for each case. It can be seen that interface debonding length decreases significantly with increasing interface strength, since an increase in interface strength reinforces the matrix constraints on the fibre crack opening. The reason why the SIF predicted with the three interface strength becomes more similar with an increase in crack length is because the relative difference in debonding length between the three interface strength decreases as the crack

length increases (see Figure 6.8). For example, the debonding length relative difference between the weak and strong interfaces is equal to 400% for $a/D = 0.1$, but reduces to 180% for $a/D = 0.4$.

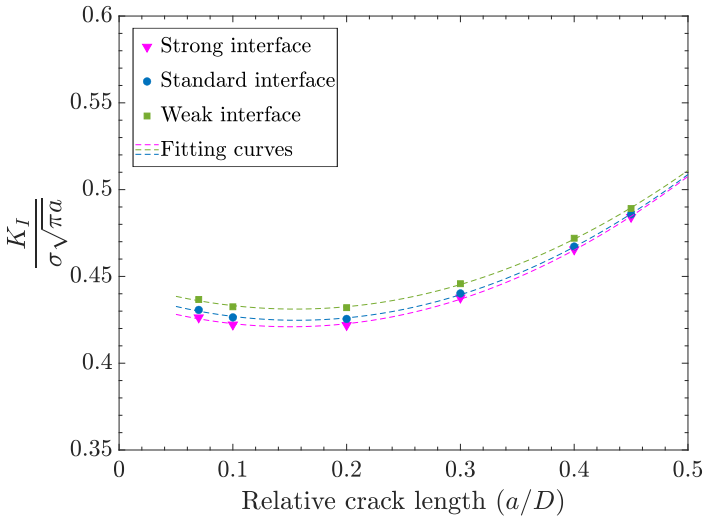

Figure 6.7: Comparison of non-dimensional SIFs of an orthotropic carbon fibre embedded in a elastic matrix for different interface strengths including strong, standard, and weak interface.

6.3.5 Matrix plasticity

Figure 6.9 shows the results of the non-dimensional SIFs for an orthotropic AS4 carbon fibre embedded in a non-linear inelastic 8552 epoxy matrix. The model with matrix yielding is compared against the model assuming a perfect elastic matrix, shown in earlier section 3.2. All remaining modeling aspects are kept as previously, except that perfect adhesion is considered between fibre and matrix.

The carbon fibre embedded in an inelastic matrix results in a higher SIF compared to the one with a linear-elastic matrix (Figure 6.9). The higher is the crack length, the larger the difference becomes. Thus, the elastic or inelastic behavior of a matrix, directly affects the scale of the matrix constraints (shielding effect) on fibre crack opening. This can be understood as follows. In the model with an inelastic matrix, when the matrix reaches the yield stress, it undergoes a larger deformation than the perfectly elastic matrix, specially around the crack zone. This larger deformation reduces the matrix shielding effect on the crack, and allows the crack to move more freely apart from the constraints imposed

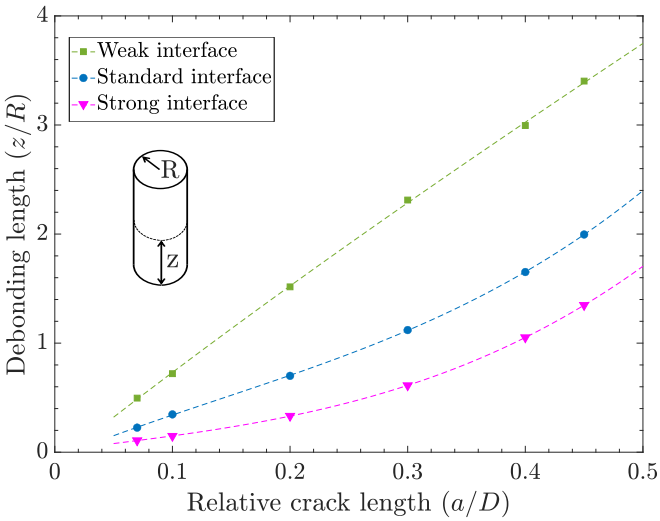

Figure 6.8: Non-dimensional interface debonding length for an orthotropic carbon fibre embedded in a matrix for the different interface strength. Where parameter z is the debonding length and R is the fibre radius.

by the matrix, effectively causing the fibre to behave closer to the free fibre. Consequently, this increase in the fibre crack opening leads to the increase in the SIF. Still, we note that the SIF with an inelastic matrix is much smaller than the free fibre.

Figure 6.10 depicts the evolution of the matrix plastic strain around the crack area. It is observed that the plastic strain increases significantly with the growth of the crack and covers a larger area around the crack zone. This explains why the difference in the SIF increases between the elastic and inelastic matrices with longer crack lengths as follows. If the crack length is longer, the area of the matrix that undergoes plastic deformation increases. Effectively, this means that the matrix has a lower capacity to constraint the crack opening, hence, reducing the efficiency of embedding the fibre and increasing the SIF.

Similar to previous section 6.3.3, results obtained in this section are opposite to the trends of the stress concentration factor in the literature. While the SCF has a tendency to decrease with matrix yielding [103, 231], the SIF shows the opposite. Again, this is an important fact for the micromechanical modelling of composites.

The non-dimensional SIF for an orthotropic carbon fibre embedded in an inelas-

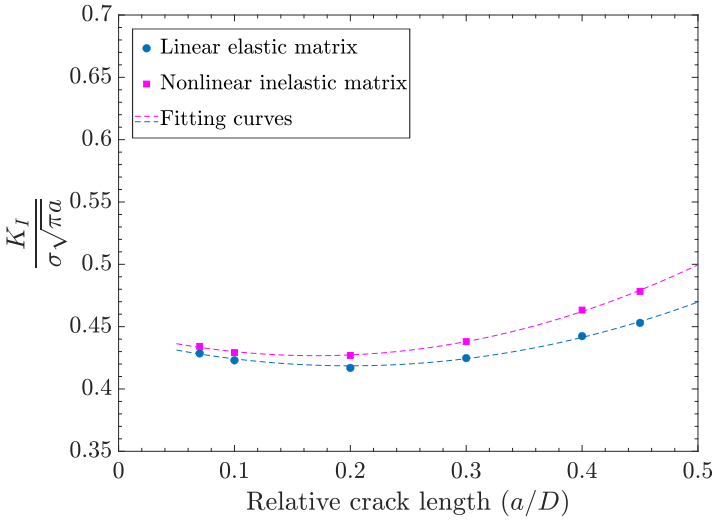

Figure 6.9: Non-dimensional SIFs of an orthotropic carbon fibre embedded in an elasto-plastic epoxy matrix. The results of a model with linear-elastic matrix is added as the reference for comparison.

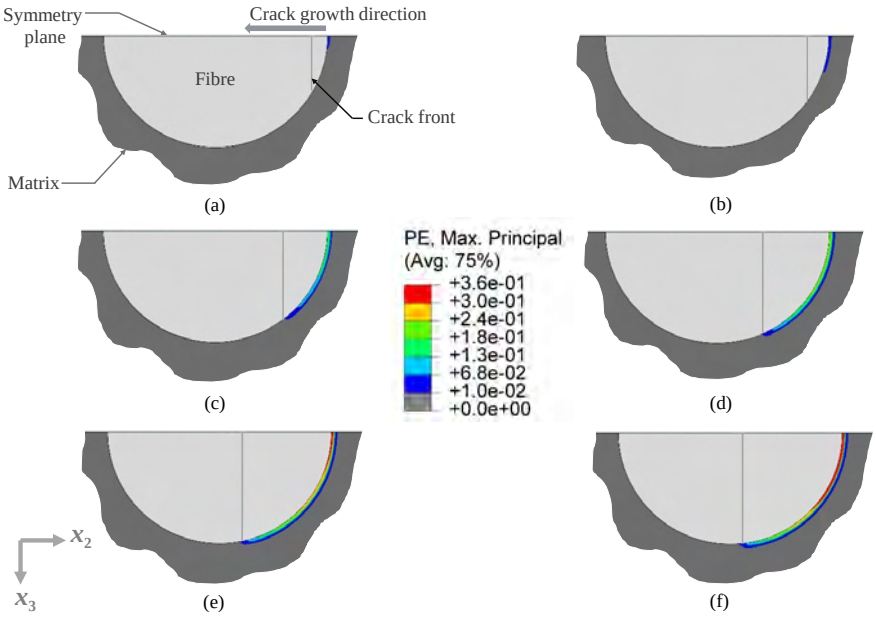

Figure 6.10: Evolution of the matrix plastic strain around the cracked area, with respect to the relative crack length: a) $a/D = 0.07$, b) $a/D = 0.1$, c) $a/D = 0.2$, d) $a/D = 0.3$, e) $a/D = 0.4$, and f) $a/D = 0.45$. Due to the symmetry of the model, only half of the model is presented.

tic matrix, with perfect adhesion, can be approximated by

$$\frac{K_I}{\sigma\sqrt{\pi a}} = 0.446 - 0.2272\left(\frac{a}{D}\right) + 0.6688\left(\frac{a}{D}\right)^2 \tag{6.8}$$

6.3.6 Matrix yield stress

The effect that the matrix yield stress has on the SIF is here investigated. Three models with different matrix yield stress were simulated. Firstly, the standard model with the default yield stress (σ_{yt}) presented in Table 6.1, and secondly, two models which have a yield stress equal to $\sigma_{yt}/2$ and $\sigma_{yt} \times 2$, respectively. Perfect adhesion is considered between fibre/matrix interface for all the cases.

Figure 6.11 depicts the non-dimensional SIFs for an orthotropic carbon fibre embedded in an inelastic matrix for different matrix yield stresses. The results show that an increase in the matrix yield stress leads to a decrease in the SIFs. This outcome can be related to the correlation of the matrix yield stress and shielding effect. A matrix with lower yield stress reaches the yield stress much faster and hence, loses its shielding effect around the crack area easily which ultimately leads to larger fibre crack openings and larger SIF.

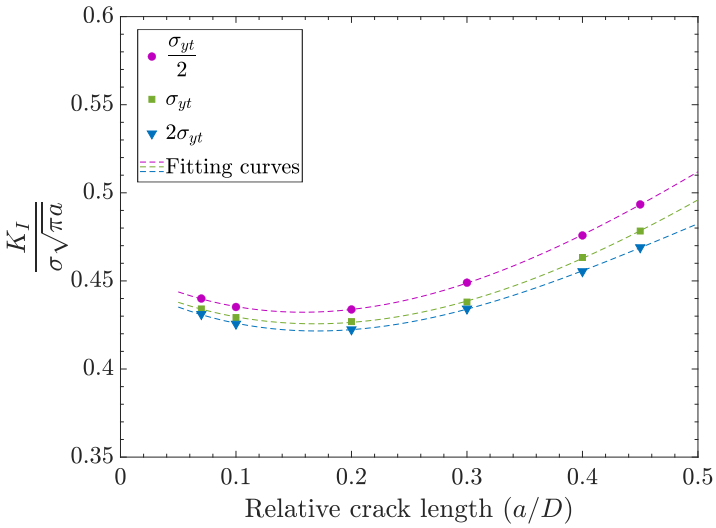

Figure 6.11: Comparison of non-dimensional SIFs for an orthotropic carbon fibre embedded in an non-linear inelastic matrix for different matrix yield stress (σ_{yt}).

6.3.7 Matrix plasticity and interface debonding

This section investigates the simultaneous effect both matrix plastic deformation and interface debonding have on SIF. To do so, the AS4/8552 carbon/epoxy composite is simulated including an inelastic matrix and cohesive interface properties altogether using the default material data presented in Table 6.1.

Figure 6.12 shows the simultaneous effects of both matrix plasticity and interface debonding on the SIF, also compared with the case that considers an inelastic matrix with perfect cohesion (without debonding). At the beginning, a slight difference is observed in which the model without interface debonding has a slightly higher SIF over the model with interface debonding. The difference fades away gradually with longer crack lengths, so that both curves end up overlapping. Therefore, this discloses that simultaneous presence of interface debonding and matrix inelastic deformation do not enhance the effects on the SIF. It can be concluded that accounting for matrix plasticity includes the effect of debonding in some way. As a result, to save computational cost, simply including matrix plasticity in the model is sufficient; debonding is not required if the matrix yields.

Further to this, it was observed that the matrix yields after the start of interface debonding. To further understand this phenomenon, Figure 6.13 depicts a visual representation of the interface debonding and matrix plasticity scale for a relative crack length (a/D) of 0.45. Results show that the area of the interface debonding (indicated in dark grey) has completely dominated the area of the matrix inelastic deformation. Hence, the addition of matrix yielding is negligible. Nonetheless, it is worth mentioning that these findings could be different with other material properties, depending whether the interface debonds before or after the matrix yields, and whether the matrix yield stress is large compared with the interface strength and viceversa.

6.4 Concluding remarks

This study presented a computational micromechanics analysis of the stress intensity factor of a single carbon fibre with a straight-fronted edge crack. The fibre was considered linear-elastic and either free or embedded in an epoxy matrix. Furthermore, the effect micromechanical failure mechanisms such as

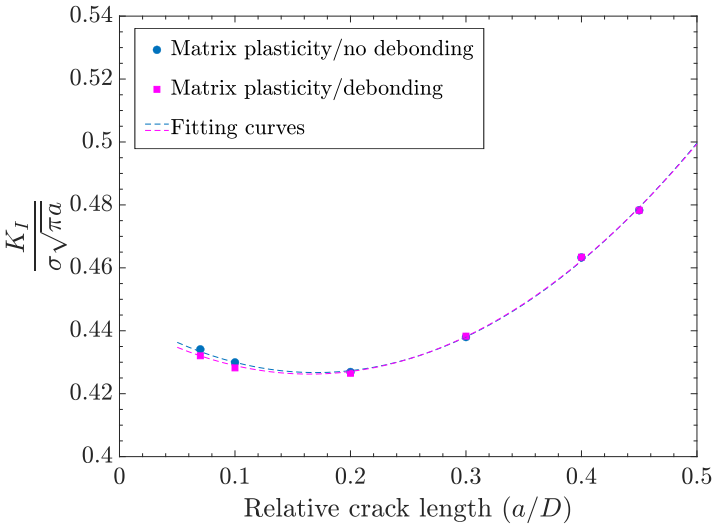

Figure 6.12: Non-dimensional SIFs of an orthotropic carbon fibre embedded in a non-linear inelastic matrix in the presence of interface debonding. The model is compared with a model with perfect interface adhesion.

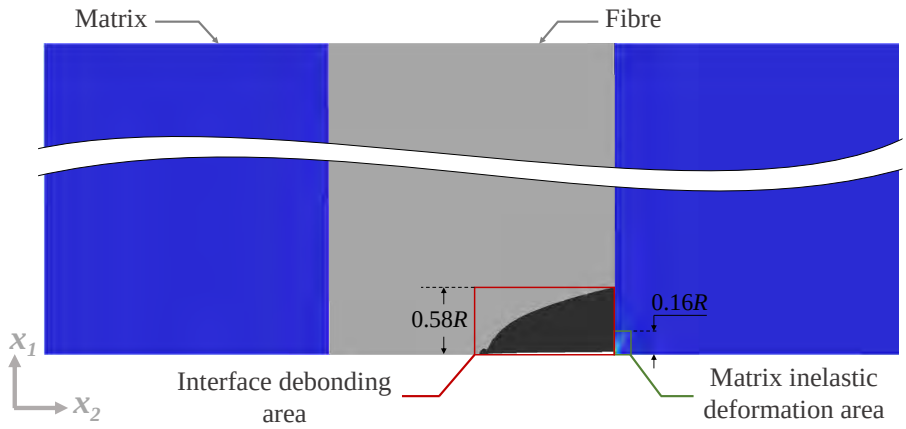

Figure 6.13: Comparison of the size of the interface debonding and matrix inelastic deformation area around the crack region for $a/D = 0.45$.

the fibre/matrix interface debonding and matrix plasticity have on the SIF was investigated. Carbon fibre reinforced plastic AS4/8552 was used as the reference material and stress intensity factor evaluation was carried out using the J-integral method.

Considering a carbon fibre as an orthotropic or isotropic material affects significantly the SIF. Taking into account the orthotropic behaviour of the carbon fibre led to a 55% lower SIF than the isotropic case. Moreover, embedding the carbon fibre in a matrix reduced the SIF drastically over the free fibre case. When the fibre was embedded in an elastic epoxy matrix, the SIF was reduced by 11% with a relative crack length $a/D = 0.1$ and by 55% with $a/D = 0.45$, with respect to the free fibre case. This effect is due to the constraint of the matrix over the crack opening.

Further study revealed that the constraint of the matrix on the fibre crack varies depending on whether it is considered as an elastic or inelastic material. If the fibre is embedded in an inelastic matrix, and the load is high enough to cause matrix yielding, the constraint on the fibre crack opening is reduced due to a larger deformation of the matrix around the crack tip. This leads to a larger crack opening and an increase in the SIFs compared to an elastic matrix. Since the matrix plastic deformation is controlled by the yield stress, any increase in matrix yield stress reduces the SIFs and vice versa.

In addition, the presence of debonding between the fibre/matrix interface also has a notable effect on the SIF of carbon fibre. Similar to the effect of matrix yielding, the presence of debonding led to higher SIF compared with a perfect fibre/matrix adhesion. This is because the matrix constraint on the fibre crack opening is reduced as the interface separates. An increase in the interfacial strength reduces the SIFs and vice versa. Further to this, combining matrix yielding and debonding altogether did not further affect the SIF than considering both phenomena separately.

Overall, this work brings new insights into the mechanisms controlling the SIF of a carbon fibre embedded in a matrix and, in consequence, fibre failure. In addition to improving the understanding of fibre failure in carbon fibre reinforced composite materials, this study also provided the non-dimensional equations which can be used to approximate the SIF of a carbon fibre in different situations.

Future work will expand this study by embedding the fibre in a composite with several surrounding fibres.

7 Conclusions and future work

This chapter summarizes the thesis's main conclusions, as well as reporting the main developments and results obtained. Future research to extend knowledge in the field of micromechanical modeling is also proposed.

7.1 Conclusions

- A high-fidelity computational micromechanics framework was developed in order to accurately predict the failure and longitudinal behavior of UD composites. The result obtained from the micromechanics model was compared to experimental results from the literature and to the manufacturer data sheet (Hexcel). The predicted tensile strength was in very good agreement with the experimental results.

  To accurately capture the mechanisms of failure, each constituent of the composite (fibers, matrix, and interfaces) was modeled. The fracture of carbon fibers was explicitly reproduced to capture the longitudinal failure of the microstructure. To accomplish this, a sequence of fracture planes were introduced in the longitudinal direction of each fiber via cohesive surface-based interactions. The epoxy polymer matrix was represented using the isotropic plasticity model included in Abaqus/Standard which is based on pressure-dependent Druker–Prager plastic behaviour coupled with tensile damage degradation to simulate brittle materials. The fibre–matrix interface was modeled using the surface-based implementation of the cohesive zone method in Abaqus/Standard which was coupled with Coulomb frictional behaviour to simulate the sliding of the fibres upon decohesion.

- Stress redistribution and damage phenomena in the vicinity of the first-fibre break in unidirectional composites under longitudinal tensile loads were comprehensively studied by means of high-fidelity computational micromechanics based on experimentally characterised material constituents. In this framework, periodic microstructures with statistically representative random fibre packings were analysed, and transient dynamic analyses were performed to take into account the progressive failure and recoiling of a breaking fibre. The effects of mechanisms such as curing residual stresses, fibre/matrix debonding and matrix inelastic deformation on the first-fibre failure process were investigated.

The results showed that dynamic fiber failure can better reproduce the failure process in a real fibre and provides more realistic stress distribution. Increases in fibre volume fraction decrease the SCF and ineffective length, but increase the debonding length and matrix damage-plasticity.

- The stress intensity factor of a single fibre with a straight-fronted edge crack and embedded in a matrix was studied using a micromechanical finite element model. The fibre was considered elastic and either isotropic or orthotropic, and free or embedded in an elastic material of different stiffness. The study was performed using non-dimensional variables for the fibre/matrix stiffness ratio and fibre longitudinal/transverse stiffness ratio. The J-integral was used to calculate the stress intensity factor.

  Embedding the fibre in an elastic matrix reduced the SIF over the free fibre case. The higher the matrix stiffness was, the more substantial the decrease in SIF. This effect is due to the constraint of the matrix over the crack opening. The elastic orthotropy of the fibre greatly affected the SIF in that it increased for the case of a transverse stiffness higher than that of the axial, and decreased for the opposite case. It was discovered that the presence of the matrix enhances the strength of the fibers and alters the Weibull strength distribution characteristics, resulting in the fibers failing at higher strains and slightly narrowing the distribution. A modified Weibull distribution taking into account such effect due to the presence of the matrix was computed. The progressive failure of a unidirectional carbon composite was simulated using this Weibull distribution. The fibre break density predicted by the model became significantly closer to the experimental observations, showing that the presence of the matrix must be included for obtaining the strength of the fibres.

To summarize, the computational micromechanics models developed in this thesis shed light on the characterization of the damage and fracture processes of FRPs.

7.2 Future work

In this section various research lines to further extend the research conducted in this thesis are presented:

- The dynamic fibre failure phase needs to be explored deeper. Towards that end, the use of a proper characteristic time increment is critical to capture the essentials of dynamic fiber failure mechanisms.
- Modeling the fracture in the fiber, matrix, and material heterogeneities using a micromechanics model based on the Extended Finite Element Method (X-FEM). In comparison to standard finite element, X-FEM would produce less computationally expensive, more accurate, and mesh-independent results.
- The use of continuum damage mechanics (CDM) to model the failure in fibre at the micro level, since it is less computationally demanding. In this case, CDM can be used instead of cohesive planes to capture the fracture in fibre.
- Computational micromechanics models, as noted, are very accurate but extremely demanding. These models must be optimized in order to achieve a balance between accuracy and computational efficiency. One approach is to combine them with some analytical models such that the finite element can be used for a small model to collect data with high accuracy, and then fed it into the analytical model to simulate a larger model. Similar to the scenario in Chapter 5, where the Finite Element model results were utilized as inputs for a semi-analytical progressive damage model.
- Formulation of meso-scale models based on the results obtained with the micromechanical simulations. These models should encompass both elastic and damage behavior.
- Determine the SIF of a cracked fibre when surrounded by other fibres, reproducing the microstructure of a composite.

Bibliography

[1] J. Llorca, C. Gonzalez, J. Molina-Aldareguıa, J. Segurado, R. Seltzer, F. Sket, M. Rodrıguez, S. Sadaba, R. Munoz, L. Canal, Multiscale modeling of composite materials: a roadmap towards virtual testing, Advanced materials 23 (2011) 5130–5147.

[2] H. Schurmann, Konstruieren mit Faser-Kunststoff-Verbunden, Springer Berlin Heidelberg (2007).

[3] M. Hinton, A. Kaddour, P. Soden, Failure criteria in fiber reinforced composites: The World-Wide Failure Exercise, Elsevier Science (2004).

[4] Z. Hashin, Failure criteria for unidirectional fibre composites, Journal of Applied Mechanics 47 (1980) 329–334.

[5] S. Kyriakides, R. Arseculeratne, E. J. Perry, K. M. Liechti, On the compressive failure of fiber reinforced composites, International Journal of Solids and Structures 32 (1995) 689–738.

[6] A. Puck, H. Schurmann, Failure analysis of FRP laminates by means of physically based phenomenological models, Composites Science and Technology 58 (1998) 1045–1067.

[7] C. Davila, N. Jaunky, S. Goswami, Failure Criteria for FRP Laminates in Plane Stress, 44th AIAA/ASME/ASCE/AHS/ASC Structures, Structural Dynamics and Materials Conference, Virginia (2003) 5379–5389.

[8] C. Davila, P. Camanho, C. Rose, Failure criteria for FRP laminates, Journal of Composite Materials 39 (2005) 323–345.

[9] G. J. Dvorak, N. Laws, Analysis of progressive matrix cracking in composite laminates ii: first ply failure, Journal of Composite Materials 21 (1987) 309–329.

[10] S. Pinho, C. Davila, P. Camanho, L. Iannucci, P. Robinson, Failure Models and Criteria for FRP Under In-Plane or Three-Dimensional Stress States Including Shear Non-linearity, Technical Report NASA/TM-2005-213530 (2005).

[11] S. Pinho, R. Darvizeh, P. Robinson, C. Schuecker, P. Camanho, Material and structural response of polymer-matrix fibre-reinforced composites, Journal of Composite Materials 46 (2012) 2313–2341.

[12] S. Pinho, L. Iannucci, P. Robinson, Physically based failure models and criteria for laminated fibre-reinforced composites with emphasis on fibre kinking. Part II: FE implementation, Composites Part A: Applied Science and Manufacturing 37 (2006a) 766–777.

[13] P. Camanho, A. Arteiro, A. Melro, G. Catalanotti, M. Vogler, Three-dimensional invariant-based failure criteria for fibre-reinforced composites, International Journal of Solids and Structures 55 (2014) 92–107.

[14] E. Totry, C. Gonzalez, J. LLorca, Failure locus of fiber-reinforced composites under transverse compression and out-of-plane shear, Composites Science and Technology 68 (3-4) (2008a) 829–839. doi:10.1016/j.compscitech.2007.08.023.

[15] M. Romanowicz, A numerical approach for predicting the failure locus of fiber reinforced composites under combined transverse compression and axial tension, Computational Materials Science 51 (2012) 7–12.

[16] A. R. Melro, P. Camanho, F. M. Andrade Pires, S. T. Pinho, Micromechanical analysis of polymer composites reinforced by unidirectional fibres: Part II-Micromechanical analyses, International Journal of Solids and Structures 50 (11-12) (2013) 1906–1915. doi:10.1016/j.ijsolstr.2013.02.007.

[17] A. Argon, "statistical aspects of fracture," in Composite Materials: Fatigue and Fracture, New York: Academic Press 5 (1974) 153–190.

[18] Y. Swolfs, L. Gorbatikh, V. Romanov, S. Orlova, S. V. Lomov, I. Verpoest, Stress concentrations in an impregnated fibre bundle with random fibre packing, Composites Science and Technology 74 (2013) 113 – 120.

[19] W. Weibull, A statistical distribution function of wide applicability, Journal of Applied Mechanics 18 (1951) 293 – 297.

[20] Y. Swolfs, I. Verpoest, L. Gorbatikh, A review of input data and modelling assumptions in longitudinal strength models for unidirectional fibre-reinforced composites, Composite Structures 150 (2016) 153–172. doi:10.1016/j.compstruct.2016.05.002.

[21] R. P. Tavares, J. M. Guerrero, F. Otero, A. Turon, J. A. Mayugo, J. Costa, P. P. Camanho, Effects of local stress fields around broken fibres on the longitudinal failure of composite materials, International Journal of Solids and Structures 156-157 (2019) 294–305. doi:10.1016/j.ijsolstr.2018.08.027.

[22] T. Okabe, N. Takeda, Size effect on tensile strength of unidirectional CFRP composites-experiment and simulation, Composites science and technology 62 (15) (2002) 2053–2064. doi:10.1016/S0266-3538(02)00146-X.

[23] J. Watanabe, F. Tanaka, H. Okuda, T. Okabe, Tensile strength distribution of carbon fibers at short gauge lengths, Advanced Composite Materials 23 (5-6) (2014) 535–550. doi:10.1080/09243046.2014.915120.

[24] A. S. Watson, R. L. Smith, An examination of statistical theories for fibrous materials in the light of experimental data, Journal of Materials Science 20 (9) (1985) 3260–3270. doi:10.1007/BF00545193.

[25] J. Gutans, V. Tamuzs, Strength probability of unidirectional hybrid composites, Theoretical and Applied Fracture Mechanics 7 (3) (1987) 193–200. doi:10.1016/0167-8442(87)90036-X.

[26] I. J. Beyerlein, S. Phoenix, Statistics for the strength and size effects of microcomposites with four carbon fibers in epoxy resin, Composites Science and Technology 56 (1) (1996) 75–92. doi:10.1016/0266-3538(95)00131-X.

[27] S. Phoenix, P. Schwartz, H. Robinson, Statistics for the strength and lifetime in creep rupture of model carbon/epoxy composites, Composites Science and Technology 32(2) (1988) 81–120.

[28] M. H. Berger, D. Jeulin, Statistical analysis of the failure stresses of ceramic fibres: dependence of the weibull parameters on the gauge length, diameter variation and fluctuation of defect density, Journal of Materials Science 38 (2003) 2913–2923.

[29] W. A. Curtin, Tensile strength of fiber-reinforced composites: III. Beyond the traditional Weibull model for fiber strengths, Journal of Composite Materials 34 (15) (2000) 1301–1332. doi:10.1177/002199830003401503.

[30] R. Gulino, S. Phoenix, Weibull strength statistics for graphite fibres measured from the break progression in a model graphite/glass/epoxy composite, Journal of Materials Science 26(11) (1991) 3107–3118.

[31] J. Watanabe, F. Tanaka, T. Okabe, The tensile strength distribution of carbon fibers at short gauge length, 38th Conference of the Japan Society for Composite Materials (2013).

[32] H. Peterlik, D. Loidl, Bimodal strength distributions and flaw populations of ceramics and fibres, Engineering Fracture Mechanics 68 (3) (2000) 253–261. doi:10.1016/S0013-7944(00)00110-7.

[33] K. Goda, H. Fukunaga, The evaluation of the strength distribution of silicon carbide and alumina fibres by a multi-modal Weibull distribution, Journal of Materials Science 21 (12) (1986) 4475–4480. doi:10.1007/BF01106574.

[34] J. W. Hitchon, D. C. Phillips, The dependence of the strength of carbon fibres on length, Fibre Science and Technology 12 (3) (1979) 217–233. doi:10.1016/0015-0568(79)90032-0.

[35] D. Harlow, S. Phoenix, Probability distributions for the strength of composite materials II: A convergent sequence of tight bounds, International Journal of Fracture 17 (6) (1981) 601–630. doi:10.1007/BF00681559.

[36] Y. Swolfs, Hybridisation of self-reinforced composites: Modelling and verifying a novel hybrid concept, PhD thesis, KU Leuven 150 (2015) 153–172.

[37] Y. Swolfs, I. Verpoest, L. Gorbatikh, Issues in strength models for unidirectional fibre-reinforced composites related to Weibull distributions, fibre packings and boundary effects, Composites Science and Technology 114 (15) (2015) 42–49.

[38] M. R. Wisnom, Size effects in the testing of fibre-composite materials, Composites Science and Technology 59 (13) (1999) 1937–1957. doi:10.1016/S0266-3538(99)00053-6.

[39] M. Wisnom, B. Khan, S. Hallett, Size effects in unnotched tensile strength of unidirectional and quasi-isotropic carbon/epoxy composites, Composite Structures 84(1) (2008) 21–28.

[40] M. Wisnom, S. Hallett, C. Soutis, Scaling effects in notched composites, Journal of Composite Materials 44(2) (2010) 195–210.

[41] S. Pimenta, S. T. Pinho, Hierarchical scaling law for the strength of composite fibre bundles, Journal of the Mechanics and Physics of Solids 61 (6) (2013) 1337–1356. doi:10.1016/j.jmps.2013.02.004.

[42] W. Curtin, Dimensionality and size effects on the strength of fiber-reinforced composites, Composites Science and Technology 60(4) (2000) 543–551.

[43] S. Mahesh, I. Beyerlein, S. Phoenix, Size and heterogeneity effects on the strength of fibrous composites, Physica D: Nonlinear Phenomena 133(1-4) (1999) 371–389.

[44] S. Mahesh, S. Phoenix, I. Beyerlein, Strength distributions and size effects for 2d and 3d composites with weibull fibers in an elastic matrix, International Journal of Fracture 115(1) (2002) 41–85.

[45] S. Hallett, B. Green, W. Jiang, M. Wisnom, An experimental and numerical investigation into the damage mechanisms in notched composites, Composites Part A: Applied Science and Manufacturing 40(5) (2009) 613–624.

[46] V. Calard, J. Lamon, Failure of fiber bundles, Composites Science and Technology 64 (5) (2004) 701–710. doi:10.1016/j.compscitech.2003.07.003.

[47] C. Landis, R. McMeeking, Stress concentrations in composites with interface sliding, matrix stiffness and uneven fiber spacing using shear lag theory, International Journal of Solids and Structures 36(28) (1999) 4333–61.

[48] B. W. Rosen, Tensile failure of fibrous composites, AIAA Journal 2 (11) (1964) 1985–1991. doi:10.2514/3.2699.

[49] J. Hedgepeth, P. Van Dyke, Local stress concentrations in imperfect filamentary composite materials, NASA 1(3) (1967) 294–309.

[50] Y. Le Bozec, S. Kaang, P. J. Hine, I. M. Ward, The thermal-expansion behaviour of hot compacted polypropylene and polyethylene composites, Composites Science and Technology 60(3) (2000) 333–344.

[51] S. Batdorf, R. Ghaffarian, Size effect and strength variability of unidirectional composites, International Journal of Fracture 26(2) (1984) 113–123.

[52] A. A. Gusev, P. J. Hine, I. M. Ward, Fiber packing and elastic properties of a transversely random unidirectional glass/epoxy composite, Composites Science and Technology 60(4) (2000) 535–541.

[53] M. Ibnabdeljalil, W. A. Curtin, Strength and reliability of fiber-reinforced composites: localized load sharing and associated size-effects, International Journal of Solids and Structures 34 (21) (1997) 2649–2668. doi:10.1016/S0020-7683(96)00179-5.

[54] K. Naito, J. Yang, Y. Tanaka, Y. Kagawa, The effect of gauge length on tensile strength and weibull modulus of polyacrylonitrile (pan)- and pitch-based carbon fibers, Journal of Materials Science 47(2) (2012) 632–642.

[55] C. M. Landis, I. J. Beyerlein, R. M. McMeeking, Micromechanical simulation of the failure of fiber reinforced composites, Journal of the Mechanics and Physics of Solids 48 (3) (2000) 621–648. doi:10.1016/S0022-5096(99)00051-4.

[56] S. J. Zhou, W. A. Curtin, Failure of fiber composites: A lattice green function model, Acta Metallurgica Et Materialia 43 (8) (1995) 3093–3104. doi:10.1016/0956-7151(95)00003-E.

[57] F. Zhang, T. Lisle, W. Curtin, Z. Xia, Multiscale modeling of ductile-fiber-reinforced composites, Composites Science and Technology 69(11-12) (2009) 1887–1895.

[58] A. E. Scott, I. Sinclair, S. M. Spearing, A. Thionnet, A. R. Bunsell, Damage accumulation in a carbon/epoxy composite: Comparison between a multiscale model and computed tomography experimental results, Composites Part A: Applied Science and Manufacturing 43 (9) (2012) 1514–1522. doi:10.1016/j.compositesa.2012.03.011.

[59] D. R. Aroush, E. Maire, C. Gauthier, S. Youssef, P. Cloetens, H. Wagner, A study of fracture of unidirectional composites using in situ high-resolution synchrotron x-ray microtomography, Composites Science and Technology 66(10) (2006) 1348–1353.

[60] Z. Xia, T. Okabe, W. A. Curtin, Shear-lag versus finite element models for stress transfer in fiber-reinforced composites., Composites Science and Technology 62(9) (2002) 1141–9.

[61] Q. Zeng, Z. Wang, L. Ling, A study of the influence of interfacial damage on stress concentrations in unidirectional composites, Composites Science and Technology 57(1) (1997) 129–35.

[62] I. Beyerlein, C. Landis, Shear-lag model for failure simulations of unidirectional fiber composites including matrix stiffness, Mechanics of Materials 31(5) (1999) 331–350.

[63] S. Behzadi, P. T. Curtis, F. R. Jones, The effect of temperature on stress transfer between a broken fibre and the adjacent fibres in unidirectional fibre composites, Composites Science and Technology 68(13) (2008) 2690–2696.

[64] I. J. Beyerlein, S. Phoenix, Stress concentrations around multiple fiber breaks in an elastic matrix with local yielding or debonding using quadratic influence superposition, Journal of the Mechanics and Physics of Solids 44 (12) (1996) 1997–2036. doi:10.1016/S0022-5096(96)00068-3.

[65] F. Zhao, N. Takeda, Effect of interfacial adhesion and statistical fiber strength on tensile strength of unidirectional glass fiber/epoxy composites. Part I: experiment results, Composites Part A-Applied Science and Manufacturing 31 (11) (2000) 1203–1214.

[66] A. Johnson, F. Zhao, S. Hayes, F. Jones, Influence of a matrix crack on stress transfer to an alpha-alumina fibre in epoxy resin using FEA and photoelasticity, Composites Science and Technology 66 (13) (2006) 2023–2029.

[67] Y. Swolfs, R. M. McMeeking, I. Verpoest, L. Gorbatikh, Matrix cracks around fibre breaks and their effect on stress redistribution and failure development in unidirectional composites, Composites Science and Technology 108 (2015) 16 – 22.

[68] H. Hahn, Residual stresses in polymer matrix composite laminates, Journal of Composite Materials 10 (1976) 265–277.

[69] R. Kim, H. Hahn, Effect of curing stresses on the first ply-failure in composite laminates, Journal of Composite Materials 13 (1979) 2–16.

[70] S. White, H. Hahn, Process modeling of composite materials: residual stress development during cure. Part I. Model formulation, Journal of Composite Materials 26 (1992) 2402–2422.

[71] R. Isaac, Residual stresses in composites, In: Kessler M.R. (ed.), Advanced Topics in Characterization of Composites, Trafford Publishing (2004).

[72] Y. Msallem, F. Jacquemin, A. Poitou, Residual stresses formation during the manufacturing process of epoxy matrix composites: resin yield stress and anisotropic chemical shrinkage, International Journal of Material Forming 3 (2010) 1363–1372.

[73] L. Mishnaevsky, P. Brøndsted, Statistical modelling of compression and fatigue damage of unidirectional fiber reinforced composites, Composites Science and Technology 69 (3-4) (2009) 477–484. doi:10.1016/j.compscitech.2008.11.024.

[74] L. Mishnaevskyjr, P. Brondsted, Micromechanical modeling of damage and fracture of unidirectional fiber reinforced composites, Computational Materials Science 44(4) (2009) 1351–1359.

[75] H. E. Daniels, The Statistical Theory of the Strength of Bundles of Threads. I, Proceedings of the Royal Society A: Mathematical, Physical and Engineering Sciences 183 (995) (1945) 405–435. doi:10.1098/rspa.1945.0011.

[76] W. A. Curtin, Theory of mechanical properties of ceramic–matrix composites, journal of american ceramic society 74(11) (1991) 2837–45.

[77] J. Hedgepeth, Stress concentrations in filamentary structures, NASA (D-882) (1961) 1–36.

[78] D. Harlow, S. Phoenix, The Chain-of-Bundles Probability Model for the Strength of Fibrous Materials I : Analysis and Conjectures, Journal of Composite Materials 12 (2) (1978) 195–214.

[79] D. Harlow, S. Phoenix, The Chain-of-Bundles Probability Model for the Strength of Fibrous Materials II : A Numerical Study of Convergence, Journal of Composite Materials 12 (3) (1978) 314–334.

[80] H. J. Bohm, A short introduction to basic aspects of continuum micromechanics, Technical Report, TU Wien (2008).

[81] J. Eshelby, The determination of the elastic field of an ellipsoidal inclusion, and related problems, Proceedings of the Royal Society A:Mathematical, Physical and Engineering Sciences 241 (1957) 376–396.

[82] R. Hill, Elastic properties of reinforced solids: Some theoretical principles, Journal of the Mechanics and Physics of Solids 11 (1963) 357–372.

[83] E. Kroner, Berechnung der elastischen konstanten des vielkristalls aus den konstanten des einkristalls, Zeitschrift fur Physik 151 (1958) 504–518.

[84] T. Mori, T. Tanaka, Average stress in matrix and average elastic energy of materials with misfitting inclusions, Acta Metallurgica 21 (1973) 571–574.

[85] Y. Benveniste, A new approach to the application of mori-tanaka's theory in composite materials, Acta Metallurgica 6 (1987) 147–157.

[86] R. Christensen, K. Lo, Solutions for effective shear properties in three phase sphere and cylinder models, Journal of the Mechanics and Physics of Solids 27 (1979) 315–330.

[87] R. Roscoe, Isotropic composites with elastic or viscoelastic phases: General bounds for the moduli and solutions for special geometries, Rheologica Acta 12 (1973) 404–411.

[88] Z. Hashin, The differential scheme and its application to cracked materials, Journal of the Mechanics and Physics of Solids 36 (1988) 719–733.

[89] P. P. Castaneda, The effective mechanical properties of nonlinear isotropic composites, Journal of the Mechanics and Physics of Solids 39 (1991) 45–71.

[90] H. Pettermann, A. Plankensteiner, H. Bohm, F. Rammerstorfer, A thermoelastoplastic constitutive law for inhomogeneous materials based on an incremental mori-tanaka approach, Computers and Structures 71 (1999) 197–214.

[91] C. Gonzalez, J. Llorca, A self-consistent approach to the elasto-plastic behavior of two-phase materials including damage, Journal of the Mechanics and Physics of Solids 48 (2000) 675–692.

[92] O. L. Pamies, P. P. Castaneda, On the overall behaviour, microstructure evolution, and macroscopic stability in reinforced rubbers at large deformations: I: Theory, Journal of the Mechanics and Physics of Solids 54 (2006) 807–830.

[93] R. Hill, The elastic behavior of a crystalline aggregate, Proceedings of the Royal Society of London 65 (1952) 349–354.

[94] Z. Hashin, S. Shtrikman, A variational approach to the theory of the elastic behaviour of multiphase materials, Journal of the Mechanics and Physics of Solids 11 (1963) 127–140.

[95] S. Torquato, Effective stiffness tensor of composite media : Ii. applications to isotropic dispersions, Journal of the Mechanics and Physics of Solids 46 (1998) 1411–1440.

[96] H. Fukuda, T. Chou, Monte Carlo Simulation of the Strength of Hybrid Composites, Journal of Composite Materials 16 (5) (1982) 371–385. doi:10.1177/002199838201600502.

[97] W. A. Curtin, N. Takeda, Tensile strength of fiber-reinforced composites: I. Model and effects of local fiber geometry, Journal of Composite Materials 32 (22) (1998) 2042–2059. doi:10.1177/002199839803202203.

[98] S. Behzadi, P. T. Curtis, F. R. Jones, Improving the prediction of tensile failure in unidirectional fibre composites by introducing matrix shear yielding, Composites Science and Technology 69(14) (2009) 2421–2427.

[99] Y. Swolfs, R. M. McMeeking, I. Verpoest, L. Gorbatikh, The effect of fibre dispersion on initial failure strain and cluster development in unidirectional carbon/glass hybrid composites, Composites Part A: Applied Science and Manufacturing 69 (2014) 279–287. doi:10.1016/j.compositesa.2014.12.001.

[100] Y. Swolfs, I. Verpoest, L. Gorbatikh, Maximising the hybrid effect in unidirectional hybrid composites, Materials and Design 93 (2016) 39–45. doi:10.1016/j.matdes.2015.12.137.

[101] T. Okabe, N. Takeda, Y. Kamoshida, M. Shimizu, W. A. Curtin, A 3D shear-lag model considering micro-damage and statistical strength prediction of unidirectional fiber-reinforced composites, Composites Science and Technology 61 (12) (2001) 1773–1787. doi:10.1016/S0266-3538(01)00079-3.

[102] T. Okabe, H. Sekine, K. Ishii, M. Nishikawa, N. Takeda, Numerical method for failure simulation of unidirectional fiber-reinforced composites with spring element model, Composites Science and Technology 65 (6) (2005) 921–933. doi:10.1016/j.compscitech.2004.10.030.

[103] R. Tavares, F. Otero, A. Turon, P. Camanho, Effective simulation of the mechanics of longitudinal tensile failure of unidirectional polymer composites, International Journal of Fracture 208 (1-2) (2017) 269–285. doi:10.1007/s10704-017-0252-9.

[104] R. P. Tavares, F. Otero, J. Baiges, A. Turon, P. P. Camanho, A dynamic spring element model for the prediction of longitudinal failure of polymer composites, Computational Materials Science 160 (October 2018) (2019) 42–52. doi:10.1016/J.COMMATSCI.2018.12.048.

[105] L. Canal, J. Llorca, C. Gonzalez, J. Segurado, Intraply fracture of fiber-reinforced composites: Microscopic mechanisms and modeling, Composites Science and Technology 72 (2012) 1223–1232.

[106] E. Totry, J. M. Molina-Aldareguia, C. Gonzalez, J. Llorca, Effect of fiber, matrix and interface properties on the in-plane shear deformation of carbon-fiber reinforced composites, Composites Science and Technology 70 (2010) 970–980.

[107] M. Sautter, C. Dietrich, M. Poech, S. Schmauder, H. Fischmeister, Finite element modelling of a transverse-loaded fibre composite: Effects of section size and net density, Computational Materials Science 1(3) (1993) 225–233.

[108] J. Wulf, T. Steinkopff, , H. Fischmeister, FE-simulation of crack paths in the real microstructure of an Al(6061)/SiC composite, Acta Materialia 44 (1996) 1765–1779.

[109] C. Gonzalez, J. Llorca, Numerical simulation of the fracture behavior of ti/sic composites between 20 ∘c and 400 ∘c, Metallurgical and Materials Transactions A: Physical Metallurgy and Materials Science 38 (2007) 169–179.

[110] S. Aoki, Y. Moriya, K. Kishimoto, S. Schmauder, Finite element fracture analysis of wc-co alloys, Engineering Fracture Mechanics 55 (1996) 275–287.

[111] Z. Xia, W. A. Curtin, P. W. Peters, Multiscale modeling of failure in metal matrix composites, Acta Materialia 49 (2) (2001) 273–287. doi:10.1016/S1359-6454(00)00317-7.

[112] Q. Yang, L. Tang, H. Chen, A new method of predicting effective properties of inclusion media, Finite Elements in Analysis and Design 17 (1994) 247–257.

[113] T. Chen, Exact moduli and bounds of two-phase composites with coupled multifield linear responses, Journal of the Mechanics and Physics of Solids 45 (1997) 385–398.

[114] L. P. Canal, J. Segurado, J. LLorca, Failure surface of epoxy-modified fiber-reinforced composites under transverse tension and out-of-plane shear, International Journal of Solids and Structures 46 (11-12) (2009) 2265–2274. doi:10.1016/j.ijsolstr.2009.01.014.

[115] J. Aboudi, Micromechanical analysis of composites by the method of cells, Applied Mechanics Reviews 42 (1989) 193–221.

[116] G. Dvorak, Transformation field analysis of inelastic composite materials, Proceedings of The Royal Society of Landon 437 (1992) 311–327.

[117] J. Aboudi, M. Pindera, S. Arnold, Linear thermo-elastic higherorder theory for periodic multiphase materials, Journal of Applied Mechanics 68 (2001) 697–707.

[118] J. Aboudi, M. Pindera, S. Arnold, Higher-order theory for periodic multiphase materials with inelastic phases, International Journal of Plasticity 19 (2003) 805–847.

[119] M. Herráez, A. Fernandez, F. Naya, C. S. Lopes, C. Gonzalez, Strength and toughness of structural fibres for composite material reinforcement, Philosophical Transactions of the Royal Society of London 374 (2016) 1–12.

[120] F. Naya, C. González, C. S. Lopes, S. V. der Veen, F. Pons, Computational micromechanics of the transverse and shear behavior of unidirectional fiber reinforced polymers including environmental effects, Composites Part A: Applied Science and Manufacturing 92 (2017) 146–157.

[121] M. Barzegar, J. Costa, C. S. Lopes, High-fidelity computational micromechanics of first-fibre failure in unidirectional composites: Deformation mechanisms and stress concentration factors, International Journal of Solids and Structures 204-205 (2020) 18–33.

[122] B. W. Cherry, K. W. Thomson, The fracture of highly crosslinked polymers, Journal of Material Science 16 (1981) 1925–1934.

[123] A. J. Kinloch, R. J. Young, Fracture behavior of polymers, Elsevier Applied Science (1983).

[124] B. Fiedler, M. Hojo, S. Ochiai, K. Schulte, M. Ando, Failure behavior of an epoxy matrix under different kinds of static loading, Composites Science and Technology 61 (2001) 1615–1624.

[125] A. F. Yee, J. Du, M. D. Thouless, Toughening of epoxies. in: Polymer blends, John Wiley Sons (2000) 225–267.

[126] J. Labuz, A. Zang, Mohr-coulomb failure criterion, Rock Mechanics and Rock Engineering 45 (2012) 975–979.

[127] D. Drucker, W. Prager, Soil mechanics and plastic analysis for limit design, Quarterly of Applied Mathematics 10 (1952) 157–165.

[128] A. R. Melro, P. Camanho, F. M. Andrade Pires, S. T. Pinho, Micromechanical analysis of polymer composites reinforced by unidirectional fibres: Part I-Constitutive modelling, International Journal of Solids and Structures 50 (11-12) (2013) 1897–1905. doi:10.1016/j.ijsolstr.2013.02.009.

[129] L. Yang, Y. Yan, Y. Liu, Z. Ran, Microscopic failure mechanisms of fiber-reinforced polymer composites under transverse tension and compression, Composites Science and Technology 72 (2012) 1818–1825.

[130] K. Mogi, Fracture and flow of rocks under high triaxial compression, Journal of Geophysical Research 76 (1971) 1255–1269.

[131] L. Zhang, P. Cao, K. C. Radha, Evaluation of rock strength criteria for wellbore stability analysis, International Journal of Rock Mechanics and Mining Sciences 47 (2010) 1304–1316.

[132] G. Arslan, Sensitivity study of the drucker-prager modeling parameters in the prediction of the nonlinear response of reinforced concrete structures, Materials and Design 28 (2007) 2596–2603.

[133] R. Quinson, J. Perez, M. Rink, A. Pavan, Yield criteria for amorphous glassy polymers, Journal of Materials Science 32 (1997) 1371–1379.

[134] C. E. Inglis, Stresses in a plate due to the presence of cracks and sharp corners, Transactions of the Institute of Naval Architects 55 (1913) 219–241.

[135] A. A. Griffith, The phenomena of rupture and flow in solids, Philosophical Transactions of the Royal Society of London 221 (1921) 163–198.

[136] G. R. Irwin, Fracture dynamics: Fracturing of metals, ASM publication (1948) 147–166.

[137] E. Orowan, Energy criterion of fracture, Welding Journal 34 (1955) 1575–1605.

[138] Z. Bazant, J. Planas, W. Chen, Fracture and size effect in concrete and other quasibrittle materials, Purdue University (1998).

[139] J. B. Berry, Brittle behavior of polymeric solids, fracture process in polymeric solids, Interscience, New York, 1964.

[140] R. L. Patrick, The use of scanning electron microscopy, in treatise on adhesion and adhesives, Marcel Dekker, New York (1973) 3.

[141] P. Metha, P. J. M. Monteiro, Concrete:structure, properties and materials, Englewood Cliffs, N.J., Prentice-Hall (1993).

[142] J. Lubliner, J. Oliver, S. Oller, E. Onate, A plastic-damage model for concrete, International Journal of Solids and Structures 25 (1989) 299–326.

[143] J. Lee, G. L. Fenves, Plastic-damage model for cyclic loading of concrete structures, Journal of Engineering Mechanics 124 (1998) 892–900.

[144] D. C. Drucker, W. Prager, Soil mechanics and plastic analysis on limit design, Journal of Applied Mathematics 10 (1952) 157–165.

[145] Simulia, Abaqus/standard user's manual, version 6.14 (2016).

[146] F. Naya, Prediction of mechanical properties of unidirectional frp plies at different environmental conditions by means of computational micromechanics, Ph.D. thesis, Universidad Politecnica de Madrid (2017).

[147] J. Llorca, Void formation in metal matrix composites. in: Comprehensive composite materials, vol. 3. metal-matrix composites, Pergamon, Amsterdam (2000) 91–115.

[148] P. Camanho, C. Davila, Mixed-mode decohesion finite elements for the simulation of delamination in composite materials, Technical Report, NASA Langley Research Center Hampton (2002).

[149] A. Turon, P. Camanho, J. Costa, C. Davila, A damage model for the simulation of delamination in advanced composites under variable-mode loading, Mechanics of Materials 38 (2006) 1072–1089.

[150] Simulia, Abaqus/standard user's manual (2020).

[151] M. Benzeggagh, M. Kenane, Measurement of mixed-mode delamination fracture toughness of unidirectional glass/epoxy composites with mixed-mode bending apparatus, Composites Science and Technology 56(4) (52) (1996) 439–446.

[152] M. Rodriguez, J. Molina-Aldareguia, C. Gonzalez, J. Llorca, A methodology to measure the interface shear strength by means of the fiber push-in test, Composites Science and Technology 72 (2012a) 1924–1932.

[153] S. Ogihara, J. Koyanagi, Investigation of combined stress state failure criterion for glass fiber/epoxy interface by the cruciform specimen method, International Journal of Solids and Structures 70 (2010) 143–150.

[154] T. J. Vaughan, C. T. McCarthy, A combined experimental-numerical approach for generating statistically equivalent fibre distributions for high strength laminated composite materials, Composites Science and Technology 70 (2) (2010) 291–297. doi:10.1016/j.compscitech.2009.10.020.

[155] C. S. Lopes, P. P. Camanho, Z. Gürdal, P. Maimi, E. V. González, Low-velocity impact damage on dispersed stacking sequence laminates. part ii: Numerical simulations, Composites Science and Technology 69 (2009) 937 – 947.

[156] F. Naya, J. M. Molina-Aldareguía, C. S. Lopes, C. González, J. Llorca, Interface characterization in fiber-reinforced polymer-matrix composites, JOM 69 (1) (2017) 13–21.

[157] W. J. Drugan, J. R. Willis, A micromechanics-based nonlocal constitutive equation and estimates of the representative volume element size for elastic composites, Journal of the Mechanics and Physics of Solids 44 (1996) 497–524.

[158] A. Eckschlager, W. Han, H. J. Bohm, A unit cell model for brittle fracture of particles embedded in a ductile matrix, Computational Materials Science 25 (2002) 85–91.

[159] J. Segurado, C. Gonzalez, J. LLorca, A numerical investigation of the effect of particle clustering on the mechanical properties of composites, Acta Materialia 51 (2003) 2355–2369.

[160] D. Trias, J. Costa, A. Turon, J. E. Hurtado, Determination of the critical size of a statistical representative volume element (SRVE) for carbon reinforced polymers, Acta Materialia 54 (13) (2006) 3471–3484. doi:10.1016/j.actamat.2006.03.042.

[161] V. Romanov, S. V. Lomov, Y. Swolfs, S. Orlova, L. Gorbatikh, I. Verpoest, Statistical analysis of real and simulated fibre arrangements in unidirectional composites, Composites Science and Technology 87 (2013) 126–134. doi:10.1016/j.compscitech.2013.07.030.

[162] M. Rintoul, S. Torquato, Reconstruction of the structure of dispersions, Journal of Colloid and Interface Science 186 (1997) 467–476.

[163] J. Segurado, J. Llorca, A numerical approximation to the elastic properties of sphere-reinforced composites, Journal of the Mechanics and Physics of Solids 50 (10) (2002) 2107 – 2121.

[164] A. R. Melro, P. P. Camanho, S. T. Pinho, Generation of random distribution of fibres in long-fibre reinforced composites, Composites Science and Technology 68 (2008) 2092–2102.

[165] S. Hazanov, C. Huet, Order relationships for boundary conditions effect in heterogeneous bodies smaller than the representative volume, Journal of the Mechanics and Physics of Solids 42 (1994) 1995–2011.

[166] R. Tavares, A. R. Melro, M. A. Bessa, A. Turon, W. K. Liu, P. Camanho, Mechanics of hybrid polymer composites: analytical and computational study, Computational Mechanics 57(3) (2016) 405–421.

[167] Y. Swolfs, H. Morton, A. E. Scott, L. Gorbatikh, P. A. S. Reed, I. Sinclair, S. M. Spearing, I. Verpoest, Synchrotron radiation computed tomography for experimental validation of a tensile strength model for unidirectional fibre-reinforced composites, Composites Part A: Applied Science and Manufacturing 77 (2015) 106–113. doi:10.1016/j.compositesa.2015.06.018.

[168] J. M. Guerrero, J. A. Mayugo, J. Costa, A. Turon, A 3D Progressive Failure Model for predicting pseudo-ductility in hybrid unidirectional composite materials under fibre tensile loading, Composites Part A: Applied Science and Manufacturing 107 (February) (2018) 579–591. doi:10.1016/j.compositesa.2018.02.005.

[169] J. M. Guerrero, R. P. Tavares, F. Otero, J. A. Mayugo, J. Costa, A. Turon, P. P. Camanho, An analytical model to predict stress fields around broken fibres and their effect on the longitudinal failure of hybrid composites, Composite Structures 211 (2019) 564 – 576.

[170] J. M. Guerrero, J. A. Mayugo, J. Costa, A. Turon, Size effects in hybrid unidirectional polymer composites under longitudinal tension : A micromechanical investigation, Composites Part A 140 (October 2020) (2021) 106186. doi:10.1016/j.compositesa.2020.106186.

[171] W. A. Curtin, N. Takeda, Tensile strength of fiber-reinforced composites: II. application to polymer matrix composites, Journal of Composite Materials 32 (22) (1998) 2060–2081.

[172] K. Marlett, Y. Ng, J. Tomblin, E. Hooper, Ncamp test report: Cam-rp-2010-002 rev a, Technical report, National Institute for Aviation Research (2011).

[173] www.hexcel.com/products/resources/1664/hextow-laminate-properties-in-hexply-8552.

[174] P. W. J. V. den Heuvel, Y. J. W. V. der Bruggen, T. Peijs, The influence of carbon fibre surface treatment on fibre-fibre interactions in multi-fibre microcomposites, Advanced Composites Letters 3(6) (1994) 197–208.

[175] K. D. Jones, A. T. DiBenedetto, Fiber fracture in hybrid composite systems, Composites Science and Technology 51(1) (1994) 53–62.

[176] Y. Swolfs, L. Gorbatikh, I. Verpoest, Fibre hybridisation in polymer composites, Composites Part A: Applied Science and Manufacturing 67 (2014) 181–200.

[177] N. Ohno, S. Okabe, T. Okabe, Stress concentrations near a fiber break in unidirectional composites with interfacial slip and matrix yielding, International Journal of Solids and Structures 41(16-17) (2004) 4263–77.

[178] M. Ryvkin, J. Aboudi, Three-dimensional continuum analysis for a unidirectional composite with a broken fiber, International Journal of Solids and Structures 45 (2008) 4114–29.

[179] M. R. Nedele, M. R. Wisnom, Three-dimensional finite element analysis of the stress concentration at a single fibre break, Composites Science and Technology 51(4) (1994) 517–24.

[180] P. W. J. V. den Heuvel, M. K. Wubbolts, R. J. Young, T. Peijs, Failure phenomena in two-dimensional multi-fibre model composites: 5. a finite element study, Composites Part A-Applied Science and Manufacturing 29(9-10) (1998) 121–135.

[181] Y. Swolfs, L. Gorbatikh, I. Verpoest, Stress concentrations in hybrid unidirectional fibre-reinforced composites with random fibre packings, Composites Science and Technology 85 (2013) 10 – 16.

[182] R. Ganesh, S. Sockalingam, B. Haque, J. J. Gillespie, Dynamic effects of single fiber break in unidirectional glass fiber-reinforced composites, Journal of Composite Materials 51 (9) (2017) 1307 – 1320.

[183] S. Sadaba, M. Herráez, F. Naya, C. González, J. Llorca, C. S. Lopes, Special-purpose elements to impose periodic boundary conditions for multiscale computational homogenization of composite materials with the explicit finite element method, Composite Structures 208 (2019) 434 – 441.

[184] L. Rayleigh, Theory of Sound (two volumes), Dover Publications, New York, 1945 re-issue 31 (1877) 105–124.

[185] H. M. Hilber, T. J. R. Hughes, R. L. Taylor, Improved numerical dissipation for time integration algorithms in structural dynamics, Earthquake Engineering and Structural Dynamics 5 (1997) 283–292.

[186] H. Fukuda, Stress concentration factors in unidirectional composites with random fiber spacing, Composites Science and Technology 22(2) (1985) 153–163.

[187] P. Paris, , F. Erdogan, A critical analysis of crack propagation laws, ASME J. Basic Eng. 85 (1963) 528–533.

[188] C. Breite, A. Melnikov, A. Turon, A. de Morais, F. Otero, F. Mesquita, J. Costa, J. Mayugo, J. Guerrero, L. Gorbatikh, L. McCartney, M. Hajikazemi, P. Camanho, R. Tavares, S. Lomov, S. Pimenta, W. Van Paepegem, Y. Swolfs, Blind benchmarking of seven longitudinal tensile failure models for two virtual unidirectional composites, Composites Science and Technology 202 (2021) 108555. doi:https://doi.org/10.1016/j.compscitech.2020.108555.
URL https://www.sciencedirect.com/science/article/pii/S0266353820323472

[189] S. Ogihara, Y. Imafuku, R. Yamamoto, Y. Kogo, Direct evaluation of fracture toughness in a carbon fiber, 17th International Conference on Composite Materials, ICCM-17, Edinburgh, United Kingdom (2009).

[190] O. E. K. Daoud, D. J. Cartwright, M. Carney, Strain-energy release rate for a single-edge-cracked circular bar in tension, Journal of Strain Analysis for Engineering Design 13 (1978) 83–89.

[191] J. Bush, Stress intensity factors for single-edge-crack solid and hollow round bars loaded in tension, J. Test. Eval. 9 (1981) 216–223.

[192] F. Ouchterlony, Extension of the compliance and stress intensity formulas for the single edge crack round bar in bending, Fracfure Mechanics for Ceramics, Rocks and Concrete 745 (1981) 237–256.

[193] A. Carpinteri, Stiffness loss and fracture resistance of a cracked beam with circular cross-section, Meccanica 18 (1983) 156–162.

[194] T. L. Mackay, B. J. Alperin, Stress intensity factors for fatigue cracking in high-strength bolts, Engineering Fracture Mechanics 21 (1985) 391–397.

[195] A. Athanassiadis, J. M. Boissknot, P. Brevet, D. Francois, A. Raharinaivo, Linear elastic fracture mechanics computations of cracked cylindrical tensioned bodies, Int. J. Fracture 17 (1981) 553–566.

[196] A. S. Salah el din, J. M. Lovegrove, Stress intensity factors for fatigue cracking of round bars, International Journal of Fatigue 3 (3) (1981) 117–123.

[197] O. E. K. Daoud, D. J. Cartwright, Strain energy release rates for a straight-fronted edge crack in a circular bar subject to bending, Engng Fracture Mech. 19 (1984) 701–707.

[198] K. Nezu, S. Machida, H. Nakamura, Sif of surface cracks and fatigue crack propagation behaviour in a cylindrical bar, Proc. 25th Japan Congr. Mater. Res. MelaN. Mater. (1982) 87–92.

[199] G. G. Trantina, H. G. de Lorenzi, W. W. Wilkening, Three-dimensional elastic-plastic finite element analysis of small surface cracks, Engng Fracfure Mech. 18 (1983) 925–938.

[200] O. E. K. Daoud, D. J. Cartwright, Strain energy release rate for a circular-arc edge crack in a bar under tension or bending, J. Strain Anal. 20 (1985) 53–58.

[201] I. S. Raju, J. C. Newman, Stress intensity factors for circumferential surface cracks in pipes and rods, Fracture Mechanics 905 (1986) 789–805.

[202] K. J. Nord, T. J. Chung, Fracture and surface flaws in smooth and threaded round bars, Int. J. Fracture 30 (1986) 47–55.

[203] M. Caspers, C. Mattheck, D. Munz, Fatigue crack propagation in cylindrical bars, Z. Werkstofftech. 17 (1986) 327–333.

[204] C. K. Ng, D. N. Fenner, Stress intensity factors for an edge cracked circular bar in tension and bending, International Journal of Fracture 36 (1988) 291–303.

[205] C. Breite, A. Melnikov, A. Turon, A. Morais, F. Otero, F. Mesquita, J. Costa, J. A. Mayugo, J. M. Guerrero Garcia, L. Gorbatikh, N. McCartney, M. Hajikazemi, P. Camanho, R. Tavares, Y. Swolfs, A synchrotron computed tomography dataset for validation of longitudinal tensile failure models based on fibre break and cluster development, Mendeley Data, V1, doi: 10.17632/6f2cv54ym8.1 39 (2020) 107590.

[206] J. M. Guerrero, J. A. Mayugo, J. Costa, A. Turon, Failure of hybrid composites under longitudinal tension: Influence of dynamic effects and thermal residual stresses, Composite Structures 233 (2020) 111732. doi:10.1016/j.compstruct.2019.111732.

[207] G. R. Irwin, Onset of fast crack propagation in high strength steel and aluminium alloys, Sagamore Research Conference Proceedings 2 (1956) 289–305.

[208] J. R. Rice, A path independent integral and the approximate analysis of strain concentration by notches and cracks, J. Appl. Mech. 35(2) (1968) 379–386.

[209] T. L. Anderson, Fracture mechanics: Fundamentals and applications, 3rd edition, Taylor & Francis (2005).

[210] M. L. Williams, On the stress distribution at the base of a stationary crack, Journal of Applied Mechanics 24 (1957) 109–114.

[211] H. M. Westergaard, Bearing pressures and cracks, Journal of Applied Mechanics (1939) A49–A53.

[212] G.C.Sih, P.C.Paris, G.R.Irwin, On cracks in rectilinearly anisotropic bodies, International Journal of Fracture (1965) 189–203.

[213] A. C. Pickard, The application of 3-dimensional finite element methods to fracture mechanics and fatigue life prediction, London: Chameleon Press Ltd. (1986).

[214] D. P. Rooke, D. J. Cartwright, Compendium of stress intensity factors, Uxbridge: The Hillingdon Press (1976).

[215] H. Tada, P. Paris, G. Irwin, The analysis of cracks handbook, ASME Press, New York (2000).

[216] R. Forman, V. Shivakumar, Growth behavior of surface cracks in the circumferential plane of solid and hollow cylinders: Seventeenth volume, J.H. Underwood, R. Chait, C.W. Smith, D.P. Wilhelm, W.A. Andrews and J.C. Newman (Eds.). ASTM STP 905, Philadelphia (1986).

[217] D. J. Cartwright, D. P. Rooke, Approximate stress intensity factors compounded from known solutions, Engineering Fracture Mechanics 6(3) (1974) 563–571.

[218] P. C. Paris, G. C. Sih, Stress analysis of cracks: in fracture toughness testing and its applications, ASTM American Society for Testing and Materials 381 (1965) 30–83.

[219] S. Raju, J. C. Newman, Three dimensional finite-element analysis of finite-thickness fracture specimens, Technical report, Langley Research Center, NASA TN D-8414 (1977).

[220] G. P. Cherepanov, The propagation of cracks in a continuous medium, Journal of Applied Mathematics and Mechanics 31(3) (1967) 503–512.

[221] R. Kruger, M. Konig, T. Schneider, Computation of local energy release rates along straight and curved delamination fronts of unidirectionally laminated dcb- and enf- specimens, 34th AIAA/ASME/ASCE SSDM Conference, La Jolla, CA: American Institute of Aeronautics and Astronautics, Washington (1993) 1332–1342.

[222] E. F. Rybicki, M. F. Kanninen, Finite-element calculation of stress intensity factors by a modified crack closure integrals, Engineering Fracture Mechanics 9(4) (1977) 931–938.

[223] G. R. Irwin, Fracture i, in Handbuch der Physik VI, Flugge 2 (1958) 558–590.

[224] D. Broek, Elementary engineering fracture mechanics, 4th revised ed: Kluwer Academic Publishers (1991).

[225] B. Lempriere, Poisson's ratio in orthotropic materials, AIAA Journal (1968) 2226–2227.

[226] J. M. Guerrero, R. P. Tavares, F. Otero, J. A. Mayugo, J. Costa, A. Turon, P. P. Camanho, An analytical model to predict stress fields around broken fibres and their effect on the longitudinal failure of hybrid composites, Composite Structures 211 (December 2018) (2019) 564–576. doi:10.1016/j.compstruct.2018.12.044.

[227] M. A. Astiz, An incompatible singular elastic element for two- and three dimensional crack problems, International Journal of Fracture 31 (1986) 105–124.

[228] S. M.Rangappa, T. Satishkumar, M. M. M. Cuadrado, S. Siengchin, C. Barile, Fracture failure analysis of fiber reinforced polymer matrix composites, Springer Singapore (2021).

[229] E. Fitzer, L. M. Manocha, Carbon Reinforcements and Carbon/Carbon Composites, Springer Berlin, Heidelberg (1998).

[230] A. Bunsell, L. Gorbatikh, H. Morton, S. Pimenta, I. Sinclair, M. Spearing, Y. Swolfs, A. Thionnet, Benchmarking of strength models for unidirectional composites under longitudinal tension, Composites Part A: Applied Science and Manufacturing 111 (June 2017) (2018) 138–150. doi:10.1016/j.compositesa.2018.03.016.

[231] C. Breite, A. Melnikov, A. Turon, A. B. de Morais, C. Le Bourlot, E. Maire, E. Schöberl, F. Otero, F. Mesquita, I. Sinclair, J. Costa, J. A. Mayugo, J. M. Guerrero, L. Gorbatikh, L. N. McCartney, M. Hajikazemi, M. Mehdikhani, M. N. Mavrogordato, P. P. Camanho, R. P. Tavares, S. M. Spearing, S. V. Lomov, S. Pimenta, W. V. Paepegem, Y. Swolfs, Detailed experimental validation and benchmarking of six models for longitudinal tensile failure of unidirectional composites, Composite Structures 279 (October 2021) (2022) 114828. doi:10.1016/j.compstruct.2021.114828.

[232] S. Pimenta, A computationally-efficient hierarchical scaling law to predict damage accumulation in composite fibre-bundles, Composites Science and Technology 146 (2017) 210–225. doi:10.1016/j.compscitech.2017.04.018.


AMADE
Universitat de Girona